ADVERTIMENT. La consulta d'aquesta tesi queda condicionada a l'acceptació de les següents condicions d'ús: La difusió d'aquesta tesi per mitjà del servei TDX (www.tesisenxarxa.net) ha estat autoritzada pels titulars dels drets de propietat intel·lectual únicament per a usos privats emmarcats en activitats d'investigació i docència. No s'autoritza la seva reproducció amb finalitats de lucre ni la seva difusió i posada a disposició des d'un lloc aliè al servei TDX. No s'autoritza la presentació del seu contingut en una finestra o marc aliè a TDX (framing). Aquesta reserva de drets afecta tant al resum de presentació de la tesi com als seus continguts. En la utilització o cita de parts de la tesi és obligat indicar el nom de la persona autora.

ADVERTENCIA. La consulta de esta tesis queda condicionada a la aceptación de las siguientes condiciones de uso: La difusión de esta tesis por medio del servicio TDR (www.tesisenred.net) ha sido autorizada por los titulares de los derechos de propiedad intelectual únicamente para usos privados enmarcados en actividades de investigación y docencia. No se autoriza su reproducción con finalidades de lucro ni su difusión y puesta a disposición desde un sitio ajeno al servicio TDR. No se autoriza la presentación de su contenido en una ventana o marco ajeno a TDR (framing). Esta reserva de derechos afecta tanto al resumen de presentación de la tesis como a sus contenidos. En la utilización o cita de partes de la tesis es obligado indicar el nombre de la persona autora.

WARNING. On having consulted this thesis you're accepting the following use conditions: Spreading this thesis by the TDX (www.tesisenxarxa.net) service has been authorized by the titular of the intellectual property rights only for private uses placed in investigation and teaching activities. Reproduction with lucrative aims is not authorized neither its spreading and availability from a site foreign to the TDX service. Introducing its content in a window or frame foreign to the TDX service is not authorized (framing). This rights affect to the presentation summary of the thesis as well as to its contents. In the using or citation of parts of the thesis it's obliged to indicate the name of the author

POLITÈCNICA
DE CATALUNYA

Fractal Antennas

by

Carles Puente Baliarda

Rafael Pous Andrés, director

Ph.D. Dissertation
(Tesi Doctoral)

Electromagnetics and Photonics Engineering group
Dept. of Signal Theory and Communications
UNIVERSITAT POLITÈCNICA DE CATALUNYA (UPC)

Barcelona, May 1997

UPC

UNIVERSITAT POLITÈCNICA DE CATALUNYA
Biblioteca
1400265926

BIBLIOTECA
Campus Nord

Aquesta tesi ha estat enregistrada
amb el núm. 158

UPC
Unitat Tècnica de Gestió del Tercer Ci
Jordi Girona, 31 (Torre Girona)
08034 BARCELONA

Qualificada: Apte cum laude

Barcelona, 30 de Gener de 1997

a la Pilar,
als meus pares i a la
meva germana Diana

Jesús Sánchez Miñana
Presidente

Sordo Romeu Rosent
Secretario

Miguel Fernando Bataller
Vocal

Rafael Gómez Martín
Vocal

Dwight Leggard
Vocal

Agraïments

Arriba el que és, sens dubte, el moment més màgic de la tesi. És el moment en què hom mira enrera i independentment del resultat final, contempla amb satisfacció el treball realitzat durant aquests darrers anys. Són aquests uns instants en què es resumeixen, de cop, tots els bons i mals moments viscuts. Sens dubte, el millor d'aquests darrers temps ha esta poder compartir aquesta feina amb tota la gent que m'ha envoltat i a qui ara dedico aquestes ratlles.

Aquesta tesi va començar com aquell qui no vol la cosa, quasi bé com un divertiment, impulsada per la curiostitat que des del principi vàrem compartir amb el qui n'ha estat el seu director, en Rafael Pous. A ell li agraeixo especialment el seu entusiasme inicial així com el seu suport incondicional durant tota la tesi. L'altre persona que ràpidament es va volcar amb il.lusió a aquest projecte ha estat en Jordi Romeu. Tota la part experimental de la tesi s'ha pogut realitzar gràcies al seu suport i als coneixements que en aquest aspecte m'ha anat transmetent. També li vull agraïr especialment la seva predisposició a compartir en qualsevol moment els dubtes anteners i les el.locubracions fractalístiques que han anat sorgint.

Hi ha dues persones que, de forma subtil i segurament sense saber-ho, han influit decisivament que el qui escriu aquestes ratlles acabés fent una tesi sobre antenes. Un d'ells és en Paul E. Mayes de la University of Illinois at Urbana-Champaign. Va ser a la tardor del 1993 durant un dels seus cursos de doctorat, que vaig tenir per primer cop l'oportunitat de desenvolupar algunes idees que des de feina temps em rondaven pel cap. No era fàcil pensar als inicis que un tema a priori tan extravagant com el de les antenes fractals pogués donar tant de si. La seva valoració positiva del treball inicial i el seu encoratjament van ser decisius per evitar que aquella feina quedés arraconada per sempre en algun calaix. L'altra persona que ha tingut un paper determinant és l'Ángel Cardama. Si algun dia, per aquestes casualitats inexplicables que té la vida, aquesta tesi arribés a tenir alguna mena de ressò, podria pensar amb satisfacció que va ser en una de les seves inspiradores classes d'antenes a la primavera del 1990 que a un dels seus alumnes se li va ocórrer pensar en les antenes fractals.

M'agradaria agrair-li a l'Adolf Comerón la seva amistat i que un bon dia decidís enredar-me per fer el doctorat a la UPC. Sens dubte ha estat el millor director de treball que mai he tingut, per una tesi que mai va arribar a ser-ho. El seu exemple com a científic i com a persona seran sempre per mi un punt de referència.

Hi ha tot un munt de companys de treball i col.legues que d'alguna manera o altre han contribuït a aquesta feina: en Josep Claret, en Francesc Sagués i la Marta López Salvans de la Universitat de Barcelona, així com la Nuria Ferrer i la Susana Manrubia de la UPC, en els aspectes més fractalístics; el Rafael Gómez de la Universidad de Granada amb les seves simulacions amb el DOTIG4; en Dwight L. Jaggard de la University of Pennsylvania i en Nathan Cohen de la University of Boston amb els seus comentaris i suggerències. Del nostre grup de recerca, el grup d'Enginyeria Electromagnètica i Fotònica (antic A.M.R.) voldria agrair al Sebastià Blanch, al Joan O'Callaghan, al Joan Manel Rius, al Jordi Mallorquí, a la Núria Duffo i en general a la resta de companys les seves col.laboracions puntuals i precises. També haig d'agrair als tècnics i mestres de laboratori, en Josep Mª Haro, en Joaquim Giner (gràcies per la coliflor !), l'Alfredo Cano, el Juanjo Tomeo i el David i Ramón Esteban el seu suport. A nivell institucional, cal esmentar la col.laboració de la CIRIT de la Generalitat de Catalunya, així com de la Comisión Interministerial de Ciencia y Tecnología que per medi dels projectes MAT95-1038-C02-02, TIC-93-0055-C03-03 i TIC-96-0724-C06-04 ha finançat parcialment aquesta tesi.

Vull dedicar un apartat molt especial i entranyable d'aquests agraïments a tots aquells projectistes que de forma entusiasta tant han col.laborat en aquest treball. A en Xavi García, en Lluís Milà, l'Ana Seguí, el Xavi Fernández, l'Alberto Hijazo, en Roberto Bartolomé, l'Arturo Medina, en Jaume Ramis, la Carmen Borja i a la Mònica Navarro, gràcies pel vostre treball, la vostra il.lusió, la vostra companyia i la vostra amistat. Sense vosaltres aquesta tesi no hauria estat el mateix.

A tots als meus amics, a la meva família, i molt especialment a la meva dona, la Pilar, gràcies per haver estat al meu costat.

El Masnou,

2 de Maig de 1997

Acknowledgments

This is, by far, one of the most rewarding moments of the thesis. It is time to look back and regardless of the final result, to contemplate with satisfaction the work done during last years. Good and bad moments are suddenly summarized at once. The best of those years has been undoubtedly sharing this work with all the people around me to whom I would like to dedicate this words.

This thesis started almost as a hobby, mainly driven by the curiosity I shared from the beginning with the thesis director, professor Rafael Pous. I especially thank him his enthusiastic and unconditional support along all this work. The other person who has enthusiastically contributed to this work is professor Jordi Romeu. He has shared with me all his knowledge and experience in the experimental part of the thesis. I very much appreciate his willingness to share my doubts and thoughts upon fractals and antennas.

Two people have had a subtle but determinant influence on this thesis. The first was, professor Paul E. Mayes from the University of Illinois at Urbana-Champaign. It was during one of his courses in Fall 1993, when for the first time I had the chance to develop some ideas that had been long hanging about my head. It was not that obvious at the very beginning that such an unusual fractal antenna concept could lead anywhere. His positive assessment and encouragement were determinant to avoid the initial work becoming forgotten forever in an office drawer. The second was professor Ángel Cardama. It was during one of his inspiring antenna theory lectures in the Spring of 1990 that one of his students started to think about fractal antennas.

I would like to thank professor Adolf Comerón for his friendship and for convincing me to join a Ph.D. program at the UPC. He has been the best work director I ever had, of a thesis that never was. His example as a scientist and human being will be a reference point to me.

There are a lot of peers and colleagues who have somehow contributed to this work: Josep Claret, Francesc Sagués and Marta López Salvans from the Universitat de Barcelona, together with Nuria Ferrer and Susana Manrubia from the UPC, in the fractal theory area;

Rafael Gómez from the Universidad de Granada with the DOTIG4 computer simulations; Dwight L. Jaggard from the University of Pennsylvania and Nathan Cohen from the University of Boston with helpful suggestions and comments to the work. From our research group, the D3-Electromagnetics and Photonics Engineering Group (the former A.M.R. group) I would like to acknowledge the comments and suggestions of Sebastià Blanch, Joan O'Callaghan, Joan Manel Rius, Jordi Mallorquí, Nuria Duffo and the rest of the group. I am in debt with the laboratory technical staff, Josep Mª Haro, Joaquim Giner, Alfredo Cano, Juanjo Tomeo and David and Ramón Esteban. Also, several institutions have given a partial financial support: the CIRIT of the Catalan Government and the CICYT of the Spanish government through grants MAT95-1038-C02-02, TIC-93-0055-C03-03 and TIC-96-0724-C06-04.

I would like to dedicate a very special part of this acknowledgments to all those students who have enthusiastically contributed to this work. To Xavi García, Lluís Milà, Ana Seguí, Xavi Fernández, Alberto Hijazo, Roberto Bartolomé, Arturo Medina, Jaume Ramis, Carmen Borja and Mònica Navarro, thank you for your work, your eagerness, your fellowship and friendship. This thesis would have never been the same with out your collaboration.

To all my friends, to my family and very especially to my wife Pilar, thank you for being always by my side.

El Masnou,
2nd of May, 1997

Table of Contents

1. Introduction *1*

2. Fractals, Antennas and Fractal Antennas *5*

2.1 - Introduction To Fractals And Multifractals **5**

2.1.1 - Fractals as opposed to Euclidean shapes 6

2.1.2 - Early Fractal structures 7

2.1.2.1 - The Cantor Set 7

2.1.2.2 - Koch Curves and Snowflakes 8

2.1.2.3 - Peano and Hilbert Curves 11

2.1.2.4 - The Sierpinski Gasket 13

2.1.3 - Fractals as solutions of recursive systems 14

2.1.3.1 - Iterated Function Systems (IFS) 15

2.1.3.2 - Iterated Systems in the Complex Domain 18

2.1.4 - Fractal characteristic parameters 21

2.1.4.1 - Self-Similarity and Self-Affinity 21

2.1.4.2 - Fractal Dimension 23

2.1.4.3 - Lacunarity 28

2.1.5 - Introduction to Multifractal Measures 28

2.2 - Common Antennas And Bandwidth Limitations **30**

2.2.1 - Radiation mechanism and main antenna parameters 30

2.2.2 - Linear wire antennas 35

2.2.2.1 - Small Dipole and Monopole 35

2.2.2.2 - Finite Length Dipole and Monopole 36

2.2.3 - Frequency dependence of loop antennas 39

2.2.4 - Fundamental Limits of Small Antennas 40

2.2.5 - Microstrip Antennas 41

2.2.6 - Frequency dependence of antenna arrays 42

2.2.6.1 - Uniformly Spaced Linear Arrays 43

2.3 - Frequency-Independent Antennas 46

2.3.1 - Scaling Properties of Maxwell Equations 46

2.3.2 - Self-complementary Antennas 47

2.3.3 - Cones and Spirals 49

2.3.3.1 - The Biconical Antenna 49

2.3.3.2 - Spiral and conical spiral antennas 50

2.3.4 - Log-periodic antennas and antenna arrays 53

2.3.4.1 - Log-periodic planar structures 53

2.3.4.2 - Log-periodic arrays of dipoles 55

2.4 - Why Fractal Antennas ? 61

2.4.1 - Frequency Scaling Properties of Fractal Shapes 61

2.4.1.1 - The IFS as a convolution operator 61

2.4.1.2 - GIFS and scaling properties of fractal attractors 62

2.4.1.3 - IFS and Maxwell Equations 64

2.4.2 - Small Fractal Antennas 67

2.4.3 - Fractals and Electromagnetics 69

2.4.3.1 - Fractal Electrodynamics 69

2.4.3.2 - Scattering from fractal targets 70

2.4.3.3 - Fractals and Optics 71

2.4.3.4 - Early investigations in fractal arrays 72

2.4.4 - Concluding remarks 73

3. Fractal Arrays and Array Factors 75

3.1 Fractal Arrays 75

3.1.1 - Multiband properties of the ideal Cantor array 75

3.1.2 - Uniform generators and SLR protection 79

3.1.2.1 - The classical uniformly spaced uniform amplitude array 81

3.1.2.2 - Optimum Lacunarity for SLR protection 81

3.1.3 - Non uniform generators for a further SLR protection 85

3.1.4 - The Cantor Fishbone Antenna 86

3.1.5 - Low Side-Lobe Arrays Based on the Cantor Set 90

3.1.5.1 - The binomial array as a particular case of the Cantor array. 90

3.1.5.2 - Uniform amplitude, nonuniformly-spaced arrays for near-binomial pattern design 91

3.2 - Fractal Array Factors **97**

3.2.1 - Multiband behavior of Koch array factors 97

3.2.2 - Analysis of the array element distribution 98

3.2.2.1 - Reducing the number of elements: array truncation 99

3.2.2.2 - Analysis of the array element distribution for Koch-pattern conformation 101

3.2.3 - The Blackman-Koch array factor 105

3.2.4 - Self-similarity and self-affinity in spatial and spectral domains 107

3.2.5 - The Weierstrass array 110

3.3 - Conclusions **114**

4. On the Behavior of the Sierpinski Antenna ***115***

4.1 - Multiband features of the Sierpinski monopole **115**

4.1.1 - Input impedance and return-loss 116

4.1.2 - Radiation patterns 120

4.2 - Comparison with the Euclidean triangular antenna. **125**

4.2.1 - Input impedance and Return-Loss 125

4.2.2 - Dipole Radiation patterns 127

4.2.3 - Current Density distribution 133

4.2.3.1 - The FDTD Sierpinski Antenna Analysis 133

4.2.3.2 - Sierpinski Antenna Current Density Distributions 135

4.3 - Wire Model of the Sierpinski Antenna **144**

4.3.1 - Moments Method and Experimental Analysis 145

4.3.2 - Iterative Transmission Line Network Model 149

4.4 - Conclusions **156**

5. Perturbing the Sierpinski Antenna *157*

5.1 - Variations on the flare angle **157**

5.1.1 - Low frequency input parameters 158

5.1.2 - Input parameters through the bands 159

5.1.3 - The Iterative Network Model 163

5.1.4 - Sierpinski-90 and Sierpinski-30 radiation patterns 166

5.1.5 - The Multiperiodic Traveling Wave V Model 171

5.1.5.1 - The Single V Model 171

5.1.5.2 - The Balanced V Model 175

5.1.5.3 - Propagation Through a Multiperiodic Media 176

5.1.5.4 - Comparison with Experimental Results 179

5.2 - Bending the arms of the Sierpinski Dipole **183**

5.2.1 - Experimental Results on the Inclined Sierpinski Dipole 184

5.2.2 - The Multiperiodic Traveling Wave V Model 187

5.3 - Shifting the operating bands **191**

5.3.1 - Perturbation of the Sierpinski antenna 191

5.3.2 - P3/5SPK and P2/3SPK Input Parameters 193

5.3.3 - P3/5SPK and P2/3SPK Radiation Patterns 194

5.3.4 - The Triangular Honeycomb Antenna 196

5.3.5 - The Triangular Honeycomb Antenna Input Parameters 196

5.3.6 - The Triangular Honeycomb Antenna Radiation Patterns 197

5.4 - The Parany Antenna **200**

5.4.1 - The Parany Antenna Input Parameters 201

5.4.2 - The Parany Antenna Radiation Patterns 202

5.5 Conclusions **204**

6. Random Fractal Tree-Like Antennas *205*

6.1 - DLA Growth of Fractal Structures **206**

6.2 - The Fractal Tree Antenna **208**

6.2.1 - Structure Design and Antenna Construction 208

6.2.2 - Input Parameters 210

6.2.3 - Radiation Patterns Main Cuts 212

6.3 - The Trimmed Version of the Fractal Tree Antenna **216**

6.3.1 - Input Return-Loss 217

6.3.2 - Radiation Patterns and Cross-Polar Ratio 217

6.4 - The Simulated DLA Fractal Antenna **220**

6.4.1 - SDLA Antenna Shape Design Algorithm 220

6.4.2 - SDLA Antenna Input Parameters 222

6.4.3 - SDLA Antenna Patterns 223

6.5 - Conclusions **226**

7. Small Fractal Antennas *227*

7.1 - Some theoretical considerations upon small fractal antennas **229**

7.1.1 - Fundamental Limitations on Small Antennas 229

7.1.2 - Small Fractal Antennas and the Fundamental Limit 233

7.1.3 - An Example: Simple Analysis of the Minkowski Loop. 234

7.2 - The Small Koch Monopole **238**

7.2.1 - Antenna Description 238

7.2.2 - Input Parameters 239

7.2.3 - Drive Resistance and Antenna Efficiency 243

7.2.4 - Antenna Size Compression Features 244

7.2.5 - The Quality Factor 247

7.2.6 - Current Distributions 250

7.2.7 - Radiation Patterns 252

7.3 - The Large Koch Monopole 253

7.4 - The Small Zig-Zag Antenna 254

7.5 - Conclusions 257

8. Conclusions 259

9. References 263

1. Introduction

Telecommunication services have been growing at an exponential rate during the last half century. Many of them rely on radio waves to transport one of the presently most valuable goods: information. Thus, radio, TV and more recently mobile communication systems have converted antennas into an ubiquitous device in our everyday life, which can even compete in diffusion with refrigerators, microwave ovens an other common appliances.

Antennas are one of the bulkiest parts in a telecommunication system. Wavelength imposes a rather tight constrain into the size of the antenna. The antenna performance is usually very sensitive to its geometrical form and size to wavelength ratio. This has two important consequences. First of all, once the antenna has been designed to operate at a particular wavelength, it will be rarely useful at other frequencies. Since telecommunication systems operate at separate frequency (wavelength) bands so that they not interfere with each other, one has to usually account for an individual antenna for every single system. Second of all, given a particular service band, the antenna cannot be made arbitrarily small owing to the same constrain.

Among the different telecommunications systems, mobile communication systems have experimented the fastest relative growth of the present decade, being cellular telephony (TACS, GSM, PCN, etc.) and satellite navigation systems (GPS) among the ones with the strongest social and economic impact. In the near future, some of these and many other services will integrate into the Personal Communication Systems (PCS) which will keep us connected to the world. The wavelength constrain on the antenna performance is of an especial concern in such cases. There is a tough race among companies to achieve small, low weight, low profile devices to be easily incorporated into portable systems. A

proliferation of large, single-service antennas to be mounted over a vehicle surface seems to go exactly in the opposite direction.

But not only the mobile part of such communication systems have to deal with the restrictions on the performance of antennas. Such restriction concern the fixed part of the system as well, that is, the base-station network. The huge growth on the mobile telephone demand imposes a proportional growth on the number of base-stations due to the cellular nature of the system. Also, demand has started to saturate the available radio spectrum such that new bands have to be set to support the service. For instance the GSM system currently operating at 900 MHz is going to be complemented by the PCN system at 1800 MHz. This means that one should expect a broad proliferation of base-stations (and antennas) to cover the increasing number of cells and bands. This fact is especially problematic from the urban planning point of view; being large and quite unsightly, mobile telephone base-stations yield an important visual impact in urban landscapes, which have already concerned several city governments and regulatory institutions.

It becomes manifest that the search of multiband (multiservice) and small size antennas appears as a most interesting topic. Neither of them represents novel research area. In the late 50's and early 60's, several research teams at the University of Illinois, the University of California and Ohio State University introduced the concept of frequency-independent antennas. A few geometrical forms featuring scale independent shapes, such as spirals, cones and other angle defined structures proved that the long believed fundamental wavelength dependence of the antenna behavior could be broken. Some of those early designs have been successfully and still are applied to several wide band communication systems.

Some years prior the development of frequency-independent antennas, L.J.Chu, H.Wheeler and other workers stated a fundamental limit on the performance of small antennas. They concluded that there is a physical constrain on the minimum quality factor and thus on the maximum bandwidth achievable by small antennas. In practice, such fundamental limit has not ever been reached, so the development of small antennas still appears as a rather interesting topic, given the new communication services outlined before.

On the other hand, B.B. Mandelbrot coined in the late seventies the term *fractal* to commonly name a huge variety of strange geometrical shapes and objects, often considered mathematical 'monsters'. He noted that such weird shapes are in fact incredibly common in nature and real life. Nowadays, fractal theory has set up the proper framework where many of such shapes can be properly studied and characterized.

The aim of this thesis is to explore the feasibility of fractal shapes for the design of multiwavelength and small antennas. Fractals are usually self-similar shapes, which means that the object global shape is contained at many different scales within its structure. Given the huge variety and richness of fractal objects, it appears most attractive to exploit their multiscale nature to design multiband antennas. Also, fractals are highly convoluted shapes usually featuring many sudden bends and discontinuities. It is well known that radiation is enhanced by discontinuous and uneven shapes, so it appears natural to assume that fractals can become good antennas.

This thesis summarizes most of the work the author and his coworkers have been carrying out during the last years at the Universitat Politècnica de Catalunya (UPC). The concept of fractal multiband radiating systems was, at the extent known by the author, first publicly introduced by the author of this thesis during a URSI meeting at Las Palmas de Gran Canaria, Spain, in 1994 [131]. Some theoretical considerations on fractal arrays showed that they do hold some multiband features. In Spring of 1995, the author together with R. Pous, J. Romeu and X. Garcia applied for the first patent on Fractal and Multifractal antennas [134], and the first papers regarding multiband fractal antennas and arrays appeared in 1996. On the other hand, Nathan Cohen first suggested in the Summer of 1995 that fractals might indeed become efficient small antennas. He observed surprisingly small resonant frequencies on some small fractal loops which led him to think on fractal shapes as good candidates for reducing antenna sizes. Following that work, some features of small fractal antennas are further analyzed here.

Relying on a rather simple principle, the scaling properties of Maxwell Equations, most of the work has been carried out experimentally. Many fractal antenna prototypes have been built and tested to experimentally demonstrate some of the initial assumptions. Some numerical simulations and theoretical analyses give further insight on the experimental results. Being a novel approach to antenna design, the work is essentially exploratory. This means that rather than focusing in a particular fractal antenna, one has tried to cover to the maximum extent the several aspects concerning fractal antennas and arrays. Of course, owing to the extremely broad scope of the topic, there is a trade-off between broadness and depth which one has tried to balance. It is the hope of the author hope that, at least this work might become a useful starting point for further research in this topic.

The dissertation is organized in eight chapters. Chapter 2 introduces some basic concepts on the fractal geometry and the antenna behavior dependence on the operating frequency. Those who feel already comfortable with basic fractal notions can skip Section 2.1. Similarly, those readers that are familiar with antenna theory, their frequency

dependence and the current work on frequency-independent antennas can go directly to Section 2.4. In this section, the motivation for investigating fractal antennas is introduced. A theoretical approach to the potentiality of fractal shapes for becoming multiband antennas has been essayed, and some of the main issues regarding small antennas are introduced. Also, most of the current work relating fractals and electromagnetics is outlined there.

Chapter 3 is entirely dedicated to fractal arrays. Being a rather simple but representative tool, array theory is used to introduce the basic concepts on multiband fractal radiating systems. The design of multiband arrays is essayed from two distinct points of view: the design of fractal arrays and the design of fractal array factors. Some properties regarding the Side-Lobe Ratio and Main Lobe Width of such arrays are also introduced there. The approach is rather theoretical since one does not consider some practical issues concerning the physical array construction. However, being a rather broad discipline which extends far beyond antenna theory, some of the concepts outlined here are expected to give some insight on the scaling properties of fractal arrays.

The behavior of the first reported multiband fractal antenna, the Sierpinski antenna, is described in chapters 4 and 5. The first describes the equilateral Sierpinski antenna while comparing its behavior to the classical triangular (bow-tie) antenna. The second covers several variations on the basic design to essay the sensitivity of the antenna behavior to structural perturbations. A mechanism for shifting the operating bands is presented, while several non fractal variations are explored too.

Chapter 6 and 7 are devoted to random fractal tree-like structures and small fractal antennas respectively. The former is an attempt at achieving a broad band operation by coupling several bands into a single broad one, while the later is focused on the performance of some fractal antennas in the low frequency range. The applicability of the classical fundamental limit to fractal antennas is discussed there as well.

Finally, although conclusions are derived throughout the whole work, most of the main results and their consequences are briefly summarized in the last chapter.

2. *Fractals, Antennas and Fractal Antennas*

Since the early days of the classical era, man has had the need of describing nature and natural phenomena. Geometry has played a key role in this process and has been one of the supports for the development of modern mathematics, physics and other disciplines of science. Modern geometry has its foundation on the ancient work of Euclid who described most basic geometrical forms such as circles, triangles, squares and other polygons, together with curves, lines, planes and regular polyhedral objects. These so called Euclidean shapes has been useful to describe many physical problems that can usually be solved by applying many reasonable approximations. Some of them allow us to model a bottle of glass as a superposition of coaxial cylindrical slices to calculate its volume up to a fair degree of accuracy, or to imagine a point-like rocket over an spherical earth to derive its escape speed. However, nature often appears rich enough and complex to escape from such simple models and it is in such a framework of complexity and even chaotic behavior where fractals emerge as a novel discipline of science. As quoted by Benoît B. Mandelbrot (one of the fathers of fractal theory) in his book The Fractal Geometry of Nature [1], clouds are not spheres, coastlines are not circles, mountains are not cones, and bark is not smooth, nor does lightning travel in a straight line. Fractal theory appears as an alternative way of describing some of these shapes that have been left aside by traditional mathematics as being 'formless' or 'pathological'.

2.1 - Introduction To Fractals And Multifractals

2.1.1 - Fractals as opposed to Euclidean shapes

A classical example is usually used to illustrate the essential difference between fractal and classical shapes and the pitfalls of the Euclidean geometry: the measure of coasts and natural borderlines[1]. When one looks for the length of, for instance, the border between Spain and Portugal in several bibliographic references, substantially different results would come out from the search. An encyclopedia in Spain would claim a length of 616 miles while another one in Portugal would quote 758 miles [1],[2]. A similar result would be obtained for the coast of Britain. One can think that the difference between them is due to a careless measurement procedure which is most unlikely with modern satellite remote sensing systems. The fact is that the measured coastline length is highly dependent on the resolution of the map we use as a reference, or in other words, on the size of the reference yardstick . A finer resolution displays a highly irregular coast with an increased number of bends and wiggles, which results in an increased length. Such an increase of length could be done arbitrarily large by blowing up the contour line to a scale with a proper degree of detail. Thus, it can be concluded that the border between Spain and Portugal has no characteristic length, or in a more mathematical approach, the measure of the length of the border does not converge to a finite value.

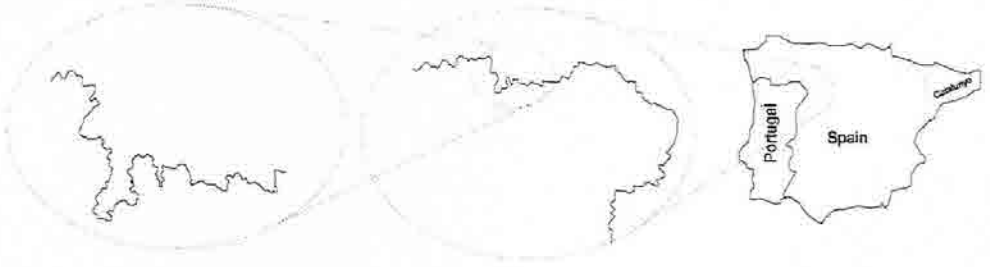

Fig. 2.1 The measure of the border between Spain and Portugal does not converge.

Since length is not a meaningful measure for a coastline and other related fractal curves, it would be interesting to find an alternative parameter to characterize them. Fractal

[1] Borders can be considered fractal shapes when they are defined following the contour lines of natural accidents such as rivers, coasts or mountains. Straight borders defined by man are not fractal.

dimension (see Section 2.1.3) is such a parameter and gives a measure of the roughness, or complexity of a fractal shape.

It is important to emphasize that the coastline example establish a fundamental difference between this kind of shapes and a classical Euclidean one. If we measure the length of a circumference we will not come out with the same problem of the coastline; a polygonal form can be inscribed inside the circumference in such a way that the curve can be approximated by the straight lines of the polygon to any desired degree of accuracy and the length of the first converges to the length of the later. It is precisely due to such kind of fundamental differences between fractal and Euclidean forms that fractal geometry appears as a complementary way of describing some complex problems not successfully described by the classical approach.

2.1.2 - Early Fractal structures

Although fractal theory is a rather novel discipline, many fractal shapes come from the last century. Georg Cantor (1872), Giuseppe Peano (1890), David Hilbert (1891), Helge von Koch (1904), Waclaw Sierpinski (1916), Gaston Julia (1918) or Felix Hausdorff (1919) were some of the pioneers that introduced some 'mathematical monsters' today considered as fractal structures. The value of fractal theory has been to provide a unifying criteria for many of such shapes and a successful way of describing some of the fundamental properties that are common to all of them.

2.1.2.1 - The Cantor Set

The Cantor Set is an infinite set of points in the unit interval [0,1]. It is one of the simplest and less spectacular examples of fractal shapes. Rather than plotting the set, usually its construction algorithm is used to describe it (Fig. 2.2). Let us take the unit interval segment and remove its central part, i.e., the subset (1/3,2/3). Two subsets are left from this initial subtraction, [0,1/3] and [2/3,1]. Now, the same procedure can be applied to the remaining subsets to obtain the segments [0,1/9], [2/9,3/9], [6/9,7/9], [8/9,1]. If such a procedure is carried out an infinite number of times, a set of totally disconnected points will be obtained, the Cantor Set.

The Cantor set holds some interesting properties. First of all it is a self-similar shape. This means that scaled down versions of the whole set can be found within the set itself. That is, if one looks at the left side of the set (Fig. 2.2), a subset which has exactly the

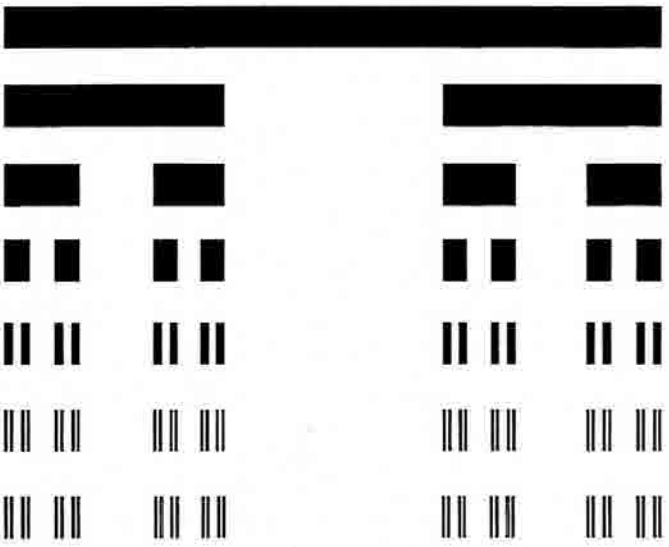

Fig. 2.2 The Cantor Set and its classical generating algorithm

shape of the Cantor set but scaled down a factor of three is found. This property is common to most fractal shapes and plays a key role in the design of the multiband antennas described later on in this thesis. Second of all, although the set is totally disconnected (and thus forms what is also called the 'Cantor dust'), it has the same cardinality as the subset of real numbers within the unit interval. That is, a one to one correspondence can be established between each point of the set and each point belonging to [0,1], which is a kind of counter-intuitive property since the construction of the set lefts an infinite number of gaps within the unit interval. The proof of such a property is beyond the scope of this thesis and can be found in many fractal books [1]-[8], but it is noted here as an example of the singular features of fractal shapes.

The points of the Cantor set can be numbered in a compact way using a triadic notation, i.e., representing the numbers with respect to base 3. It can be seen [2] that the Cantor set is the set of points in [0,1] that only contain numbers 0 and 2 in its triadic expansion. For instance, 0.200220 or 0.022202 are points that belong to the set but 0.201220 is not. Hence, the name of Triadic Cantor Set is also common in the literature [25].

2.1.2.2 - Koch Curves and Snowflakes

The Koch curve is named after the Swedish mathematician Helge von Koch who first introduced it in 1904. The curve can be constructed iteratively in a similar way as the one described for the Cantor set (Fig. 2.3). The central segment of the unit interval is

replaced now by two segments of length 1/3, both forming the upper part of an equilateral triangle. The same procedure can be iterated an infinite number of times, each time replacing the central part of the remaining segments by a triangular cap, to obtain the ideal Koch curve.

Some special features characterize this fractal form. The Koch curve is again a self-similar object; many exact copies of the curve scaled down by a factor of three are found within the structure. Also, the curve is nowhere differentiable, i.e., no point of the ideal curve has a defined tangent [4]. Actually, the curve was first introduced as another example for the discovery of Karl Weierstrass who first described, in 1872, a non-differentiable curve.

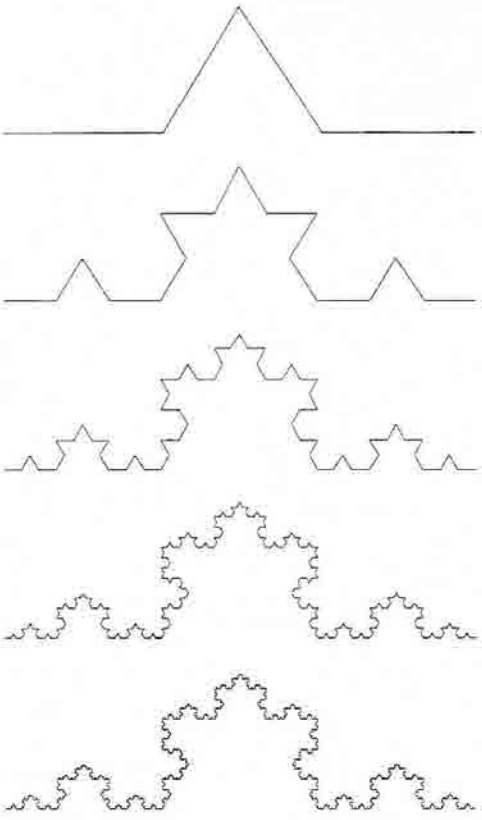

Fig. 2.3 The Koch curve at the fifth stage of its construction algorithm

Other striking properties regard the length and area of the curve. Although its shape looks basically the same when the number of iterations is large enough, the curve increases

its length at each iteration up to an infinite length for the ideal fractal shape. That is, the length l_n^{Koch} of the n^{th} iteration of the Koch curve is given by

$$l_n^{Koch} = a \cdot \left(\frac{4}{3}\right)^n \qquad l_n^{Koch} \xrightarrow[n\to\infty]{} \infty \tag{2.1}$$

where a is the length of the initial segment if, in a more general case, the interval $[0,a]$ is taken instead of the unit interval.

On the other hand such an infinite curve covers a finite area. This can be proved by summing the area of the triangles that are added at each new iteration. The area at each stage can be written as the following succession

$$\begin{aligned} A_1 &= \frac{1}{12\sqrt{3}}a^2 \\ A_2 &= A_1 + A_1 \cdot \frac{4}{9} \\ A_2 &= A_1 + A_1 \cdot \frac{4}{9} + A_1 \cdot \left(\frac{4}{9}\right)^2 \\ &\vdots \\ A_n &= A_1 \cdot \sum_{i=0}^{n-1} \left(\frac{4}{9}\right)^i = \frac{a^2 \cdot \sqrt{3}}{20}\left(1 - \left(\frac{4}{9}\right)^n\right) \end{aligned} \tag{2.2}$$

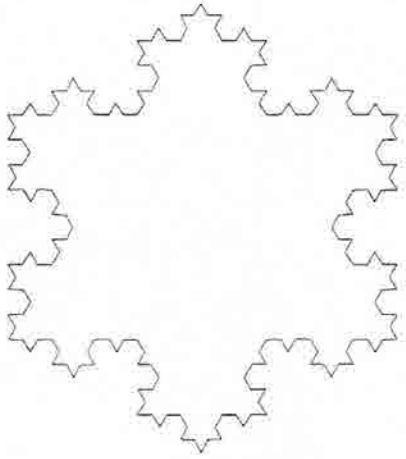

Fig. 2.4 The Koch island, also called Koch snowflake.

which converges to

$$A_{\infty}^{Koch} = \frac{\sqrt{3}}{20} a^2 \tag{2.3}$$

Three Koch curves can be stuck to the three sides of an equilateral triangle of side a to form a Koch island or snowflake (Fig. 2.4). Again, the area $A_{\infty}^{\text{K.I.}}$ of this island is finite

$$A_{\infty}^{K.I.} = \frac{2\sqrt{3}}{5} a^2 \tag{2.4}$$

although it has a coastline with an infinite length, which is a common feature to natural islands and coastlines as discussed in the previous section.

2.1.2.3 - Peano and Hilbert Curves

In the late nineteenth century, Giusseppe Peano and David Hilbert [2] introduced another set of self-similar curves. The iterative construction algorithm is quite similar to the one of the Koch curve. The central part of a segment is iteratively replaced by an '8' pattern in the Peano Curve, while a 'c' pattern is scaled, rotated and shifted several times at each iteration in the Hilbert curve (see examples in Fig. 2.5 and Fig. 2.6).

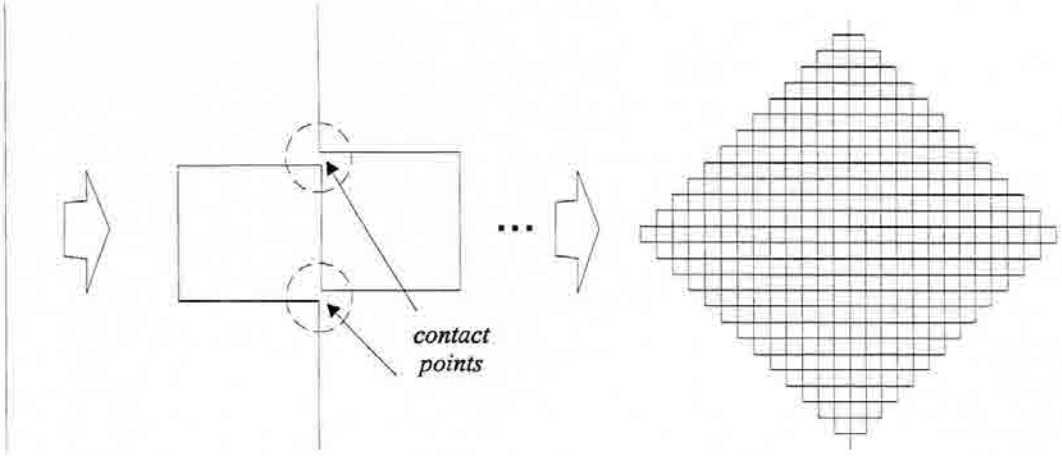

Fig. 2.6 The Peano curve and its construction algorithm

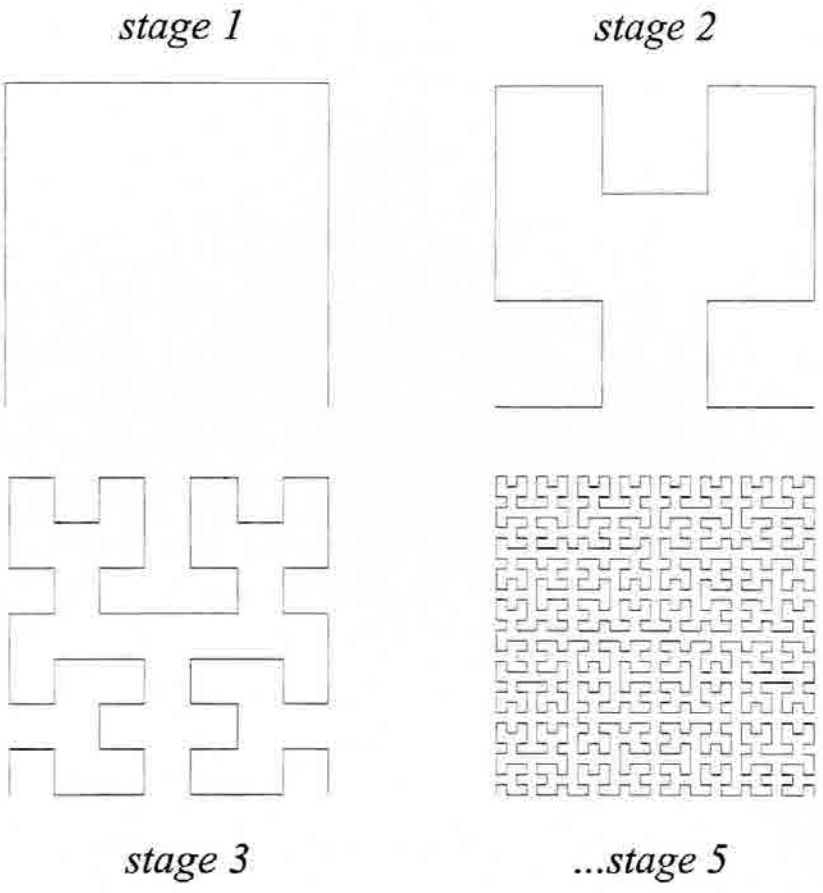

Fig. 2.5 The self-avoiding space-filling Hilbert curve

Both curves share several interesting properties. Although they can be inscribed in a finite square area, they have an infinite length (it is easy to see that the Peano curve grows as 3^n, where n is the number of the stage in the construction algorithm). Moreover, they are both space-filling curves, which means that they pass through every point in the squared region they are inscribed in. The only relevant difference between both curves is that, while Peano's one crosses twice some points in the plane, the Hilbert one is self-avoiding, i.e., it does not intersect with itself anywhere in the plane. Such an space-filling property suggests that any point in the plane can be addressed by a single parameter (its position on a Peano or Hilbert curve) instead of a pair of them. This is a kind of a surprising fact if we take into account that a curve is a one-dimensional object while the square region in the plane is two-dimensional; hence, it seems that our intuitive way of recognizing the dimensional properties of an object should be reviewed. As a matter of fact, fractal theory extends the concept of dimension to take into account the special properties of this kind of objects (see section 2.1.3).

Just to finish the introduction to the Peano and Hilbert curves, we should mention that one could think on a simpler way to fill and area with a curve; for instance, we could draw a zig-zag curve as shown in Fig. 2.7, and try to fill the two-dimensional space by successively compressing the angle between lines. We would cover each point of the plane this way; however, the limit object of such an algorithm is not a curve (see [2] for more details), while Peano and Hilbert objects are indeed curves even when the construction algorithm is carried out an infinite number of times.

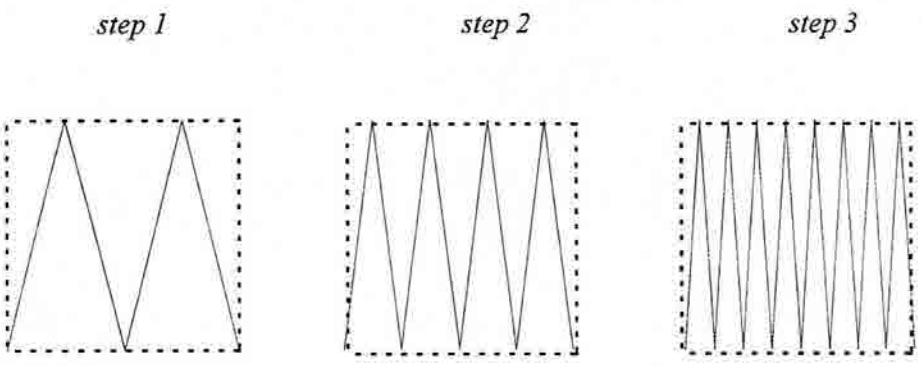

Fig. 2.7. The limit object is not a space-filling curve.

2.1.2.4 - The Sierpinski Gasket

Another classical fractal shape is the Sierpinski gasket or Sierpinski triangle, named after the Polish mathematician Waclaw Sierpinski (1882-1969) who introduced it. Rather than the curve-like appearance of the Koch, Peano and Hilbert curves, the Sierpinski gasket has a surface-like look, although such an intuitive view will have to be carefully re-examined due to the particular features of fractal shapes. The classical construction algorithm (Fig. 2.8) can reveal some interesting properties: in a first step the gasket is obtained by subtracting an inverted equilateral triangle from the center of a larger one. The same scheme is repeated in the next steps on the remaining smaller triangles, leading to the

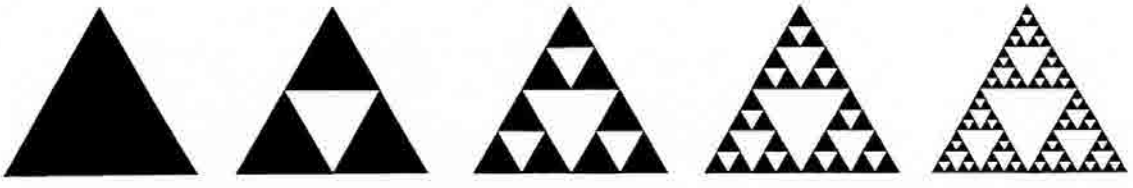

Fig. 2.8 Constructing the Sierpinski gasket.

ideal fractal shape when the iterative procedure is carried out through an infinite number of steps. The final structure has 3 exact copies of the whole shape scaled down by a factor of 2, 3^2 copies scaled down by a factor of 2^2 and so on. Thus, it is said that the Sierpinski gasket is a self-similar object.

It becomes apparent that the final object is at half way between the original triangular two-dimensional surface and a one-dimensional, wired object (it is clear that at least the sides of all the triangles that appear at each iteration remain untouched at the end of the subtraction process). The dimensional problem for this particular shape is left for section 2.1.3, although some one-dimensional features of the structure can be glimpsed in Fig 2.9.

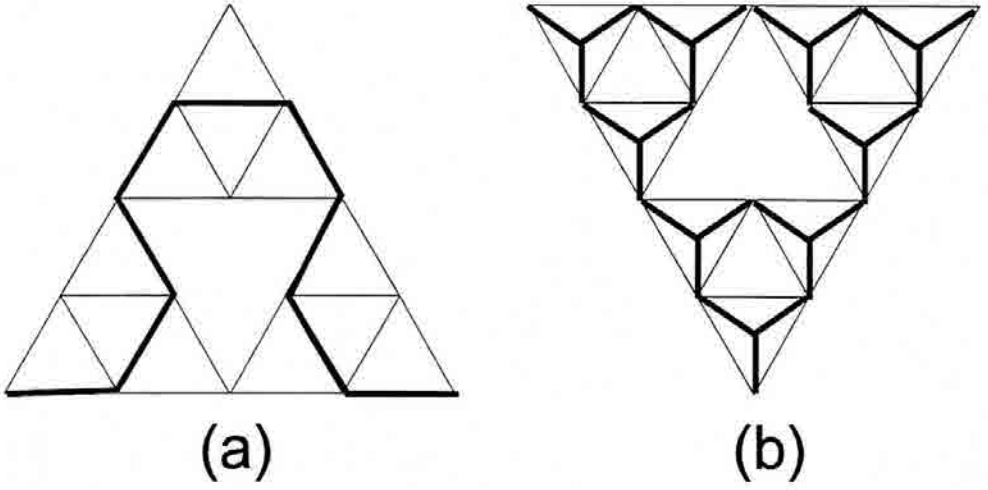

Fig. 2.9 The Sierpinski gasket reviewed either as a continuous curve (a) or as an infinitely branched one (b).

The fractal shape can be either seen as a continuous curve [2] or as an infinitely branched one [6]. In both cases, all the points belonging to the ideal gasket are crossed at least once by the curves in Fig 2.9.

2.1.3 - Fractals as solutions of recursive systems

At this point it becomes apparent that many fractal shapes are generated by means of an iterative procedure. In this section a formal description of such iterative procedures are introduced, and it is shown how most fractals can be seen as characteristic solutions of some recursive systems. Basically, two different recursive systems are used for fractal generation,

the first based on geometrical transformations and the second on polynomial functions in the complex domain.

2.1.3.1 - Iterated Function Systems (IFS)

The first family of recursive systems applies to most classical fractals as those described in Section 2.1.2. It is based on a set of geometrical transformations called linear and affine transformations. The systems introduced here are described in a two-dimensional space to allow a convenient graphical representation of the procedures; the generalization to a three or higher order dimensional space is straightforward.

First of all, let us define a subset (A) of a plane (the subset can be thought as a black and white image by assigning black pixels to the points belonging to it). A Hutchinson operator W[A] is a transformation over the subset A as follows:

$$W[A] = w_1[A] \cup w_2[A] \cup \cdots \cup w_N[A] \tag{2.5}$$

where $w_i[A]$ is an affine transformation [2]. An affine linear transformation is a composition of a linear transformation $\boldsymbol{F}$ of the kind

$$\boldsymbol{F} = \begin{pmatrix} r\cos\phi & -s\sin\psi \\ r\sin\phi & s\cos\psi \end{pmatrix} \tag{2.6}$$

plus a translation to a point (x_0,y_0). That is, if (x,y) is a point of the subset A, the point is transformed to (x',y') in the following way:

$$\begin{pmatrix} x' \\ y' \end{pmatrix} = \begin{pmatrix} r\cos\phi & -s\sin\psi \\ r\sin\phi & s\cos\psi \end{pmatrix} \begin{pmatrix} x \\ y \end{pmatrix} + \begin{pmatrix} x_o \\ y_o \end{pmatrix} \tag{2.7}$$

A linear transformation is a contraction if $0<r<1$ and $0<s<1$. An affine linear transformation is a similarity transformation if it is only composed by contractions or expansions (with $r=s$), rotations (with $\phi=\psi$) and translations. One can apply a Hutchinson operator (i.e. a composition of affine linear transformations) iteratively to a subset A in the following way:

$$\begin{aligned} A_1 &= W[A] \\ A_2 &= W[W[A]] \\ &\vdots \\ A_n &= W[A_{n-1}] \end{aligned} \tag{2.8}$$

This iterative process is called an *Iterated Function System* (IFS) and can be understood as a feedback process as shown in Fig. 2.10.

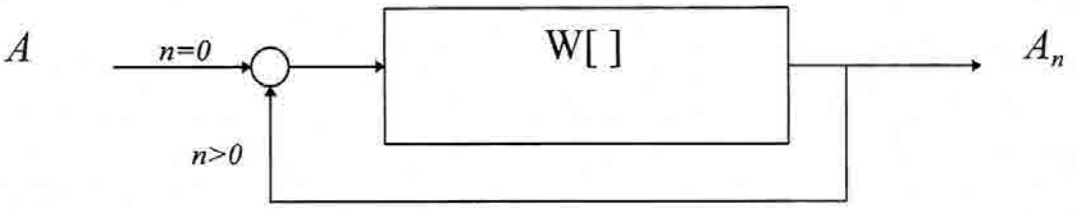

Fig. 2.10 The IFS as a feedback or recursive process

It can be proved [2] that if the Hutchinson operator of an IFS is composed only by contractions, translations and rotations, the sequence $A, A_1 \ldots A_n$ converges to a subset A_∞ when iterated a large number of times ($n \to \infty$).This set A_∞ is called the *attractor* of the IFS and is independent of the initial subset A applied to the IFS. Hence, the attractor can be seen as a characteristic solution of the IFS. The convergence criteria applied here is the Hausdorff distance, i.e., a sequence of subsets A_n converges to a subset A_∞ if the Hausdorff distance between both subsets tends to zero [2].

An important property that follows directly from the convergence of the recursive system is that the attractor holds the invariance property with respect to the Hutchinson operator of the IFS, that is,

$$A_\infty = W[A_\infty] \tag{2.9}$$

An example of and IFS is the one that generates the Sierpinski Gasket. It is composed by three similarity transformations

$$w_1(x,y)=\begin{pmatrix}1/2 & 0\\ 0 & 1/2\end{pmatrix}\begin{pmatrix}x\\ y\end{pmatrix}+\begin{pmatrix}1/4\\ 0\end{pmatrix}$$
$$w_2(x,y)=\begin{pmatrix}1/2 & 0\\ 0 & 1/2\end{pmatrix}\begin{pmatrix}x\\ y\end{pmatrix}+\begin{pmatrix}-1/4\\ 0\end{pmatrix}$$
$$w_3(x,y)=\begin{pmatrix}1/2 & 0\\ 0 & 1/2\end{pmatrix}\begin{pmatrix}x\\ y\end{pmatrix}+\begin{pmatrix}0\\ 1/2\end{pmatrix}$$

$$W_{Sierpinski}[A]=w_1(A)\cup w_2(A)\cup w_3(A) \tag{2.10}$$

Figure. 2.11 illustrates the first stage of the IFS and Fig. 2.12 shows how the Sierpinski attractor is obtained independently of the initial subset A.

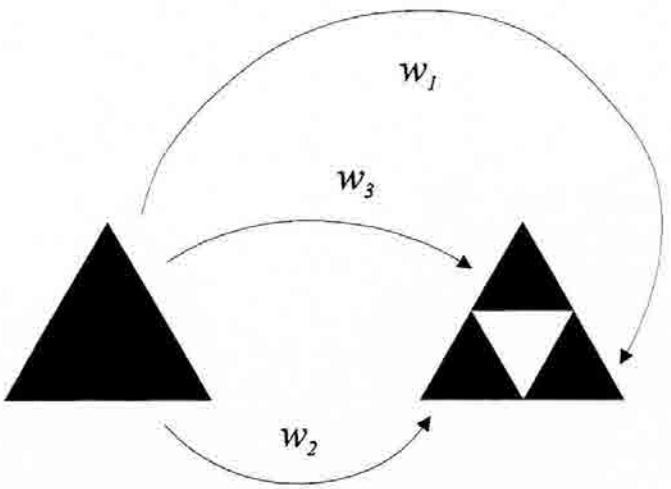

Fig. 2.11 First stage of the IFS that generates the Sierpinski gasket.

The IFS are often named *Multiple Reduction Copy Machines* (MRCM) in the literature. The initial subset A is also named *generator* and the Hutchinson operator as *iterator*. IFSs are most common algorithms for fractal generation; all the fractal shapes described in the previous section can be generated by slightly modifying the Hutchinson operator of the IFS. Other more sophisticated schemes include networks and cascading of IFSs to generate some complex forms such as the Barnsley or Sierpinski ferns [2]-[8].

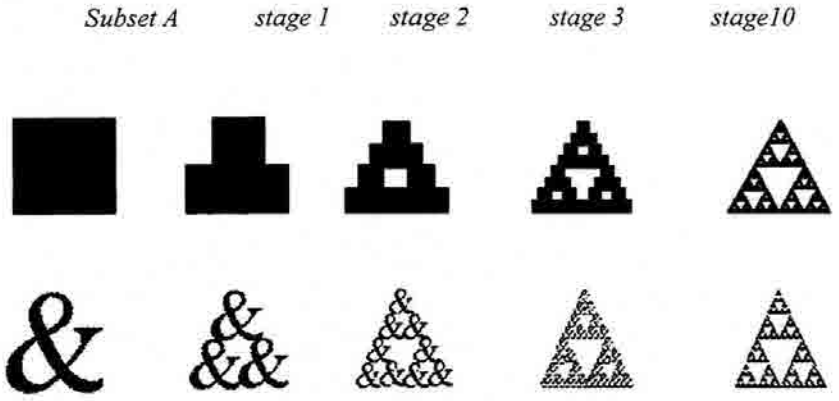

Fig. 2.12 The IFS converges (following the Haussdorf distance criteria) to the same solution despite of the initial subset A.

2.1.3.2 - Iterated Systems in the Complex Domain

A completely different set of fractal shapes are obtained by iterating polynomial functions in the complex domain. The most common are the Julia and the Mandelbrot [1]-[8] sets. The Julia sets are obtained through the recursive equation

$$x_{n+1} = x_n^2 + c \tag{2.11}$$

where c is a fixed complex number and $x_0, x_1, \ldots, x_n$ are the points of a succession in the complex domain. Depending on the initial value x_0 applied to the recursive equation (2.11), the sequence will either become unbounded, i.e., it will leave any circle around the origin, or it will remain bounded, i.e., at least one circle around the origin exists which is never left by x_n no matter how large the value of n is chosen. The set of points x_0 that lead to a bounded sequence are usually called the *prisoner set* for c, while the set of initial points that lead to the unbounded sequence are called the *escape set* for c. Both sets are complementary and the boundary between them is the Julia set. Thus, the prisoner set can be seen as an island (or a set of islands) with a fractal boundary, the Julia set, similarly to the Koch islands described in Section 2.1.2.2. A huge variety of fractal shapes can be obtained by either modifying the characteristic c parameter of the recursive equation or by changing the recursive equation itself. In general, the Julia sets are noted as J_c, being c the parameter of the quadratic equation. A look-up table of prisoner sets (and their associated Julia sets J_c) for several c parameters is shown in Fig. 2.13.

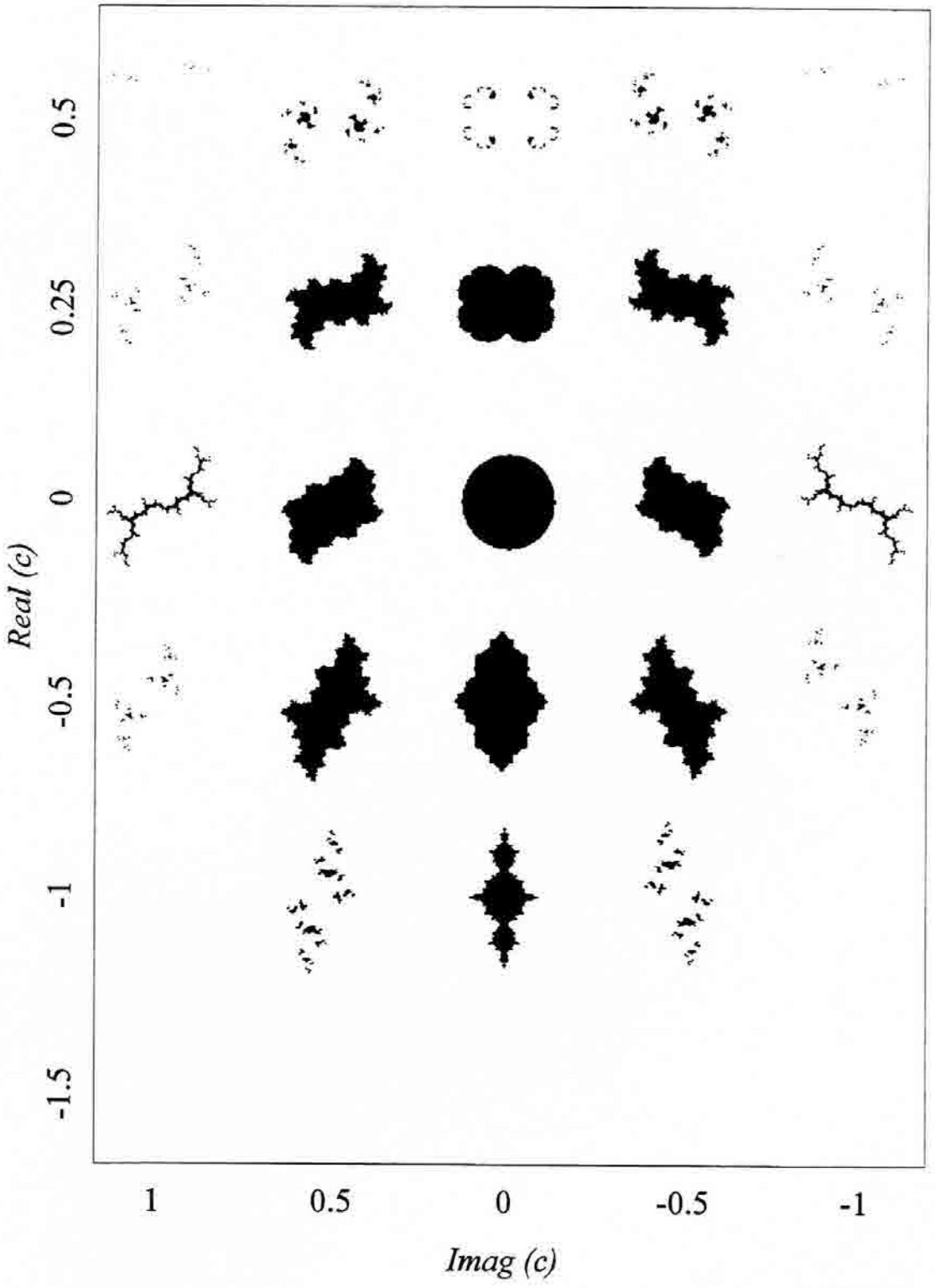

Fig. 2.13 Look-up table of Julia sets.

There is a strong relationship between the IFSs introduced in Section 2.1.3.1 and the recursive complex equations used to compute Julia sets. There is a common procedure to obtain a Julia set which is analogous to the Hutchinson scheme. The procedure is based on iterating backwards equation (2.11). That is, an initial subset A in the complex plane is taken as the initial set; then, for each point x_A belonging to the subset equation (2.11) is reversed as follows

$$\begin{aligned} x_A &\rightarrow x_{n-1}^2 + c \\ x_{n-1} &= \pm\sqrt{x_A - c} \end{aligned} \tag{2.12}$$

when such a procedure is iterated an arbitrary number of times, randomly choosing [2] the positive or negative solution of (2.12) at each step, the Julia set J_c is obtained. Either the plus or minus square root operator in (2.12) can be understood as a transformation analogous to the affine transformations of Section 2.1.3.1; the whole iterative process can be interpreted as an IFS as well and the Julia set can be seen as its attractor. The main difference between both systems is that the one just introduced is composed by non-linear transformations over the complex plane while the previous IFSs were composed only by affine, linear transformations over the real plane.

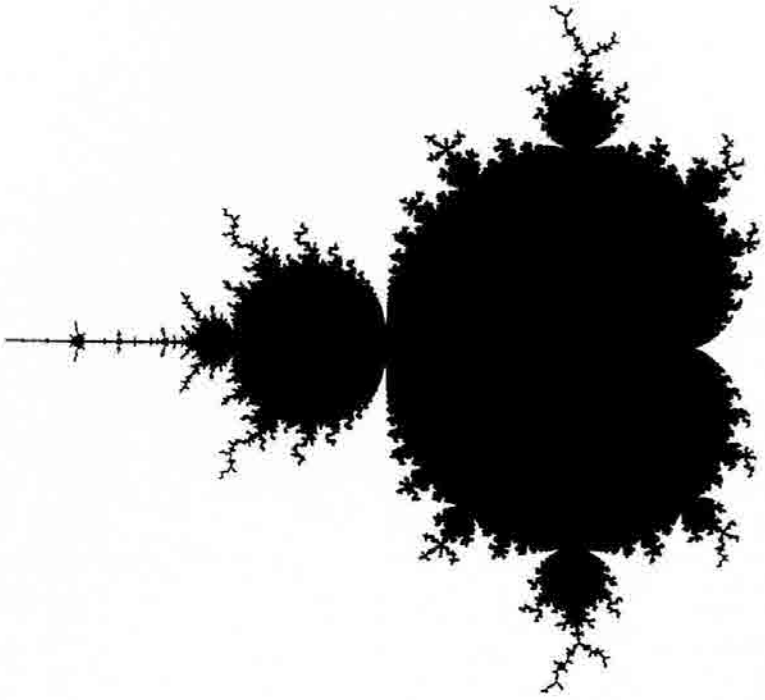

Fig. 2.14 The Mandelbrot set.

In 1979 Mandelbrot made a numerical experiment consisting on determining what c points of the quadratic equation lead to a connected Julia set. The set of such points c are the Mandelbrot set (Fig. 2.14). Thus, it can be seen as an index table where the Julia sets are classified as being connected or disconnected.

The Mandelbrot set is a connected set itself and has a fractal boundary similarly to the other fractal islands as the Julia and Koch islands.

2.1.4 - Fractal characteristic parameters

2.1.4.1 - Self-Similarity and Self-Affinity

Self-similarity is a rather intuitive concept that can be readily understood by taking a look to the geometrical features of the fractal examples introduced up to this point. It is said that an object is *self-similar* when it is composed by smaller copies of itself reduced to a smaller scale. A self-similar object can be decomposed in a set of clusters which are identical to the whole object. Since each cluster is identical to the whole object, it will have to be composed itself by clusters which will be composed by clusters as well, and so on. Hence, an infinite number of small copies of the whole object will be found in some part of the whole structure.

Some times, self-similarity is a too tight concept to describe the similarities found in several parts of an object. Often, the smaller copies of the whole structure are not identical to the whole object but are rather distorted, i.e., they might appear skewed or compressed by a different scale factor with respect axis x and y. In this case, the object is said to be *self-affine* instead of self-similar.

A more precise definition of self-similarity can be given based on the transformation algorithms introduced in Section 2.1.3. An attractor of an IFS is a self-similar object if it the corresponding generating Hutchinson operator is only composed by similarity linear transformations, i.e., translations, rotations, contractions or expansions. It is a self-affine object when the Hutchinson operator is composed by any set of affine-linear transformations as described by equation (2.7) which includes, for instance, reflecting and skewing transformations as well.

Again, these definitions of self-similarity and self-affinity are still to tight to describe some kinds of similarities commonly found in many objects. For instance, we have

seen that Julia and Mandelbrot sets are obtained through a composition of non-linear transformations, leading to objects that have an extremely rich set of similarities within itself but that can not be described by any composition of linear transformations. Therefore, the words self-similar and self-affine are usually applied in a loose sense also to such kind of objects, restricting the attributes *of strict self-similarity* and *strict self-affinity* to describe the properties of the attractors of an IFS. Thus, we will say that, the Cantor set, the Koch curve or the Sierpinski gasket are strictly self-similar objects while the Julia sets are just self-affine (not even strictly self-affine).

There are other kinds of similarity qualities that should be also taken into account. Mainly, these are self-similarity at a point and random self-similarity. The first applies, for instance, to the logarithmic spiral. The spiral is self-similar in the sense that the central part of its shape is a scaled (and rotated) version of the whole spiral, however, if we take a portion of the curve, it does not look as a whole spiral. Strictly speaking, only the central point of the ideal spiral holds the property of similarity, and thus the name of self-similarity at a point. Usually, this kind of objects, which by the way have been broadly used in the design of frequency-independent antennas (see Chapter 2.3), are called self-scaleable objects.

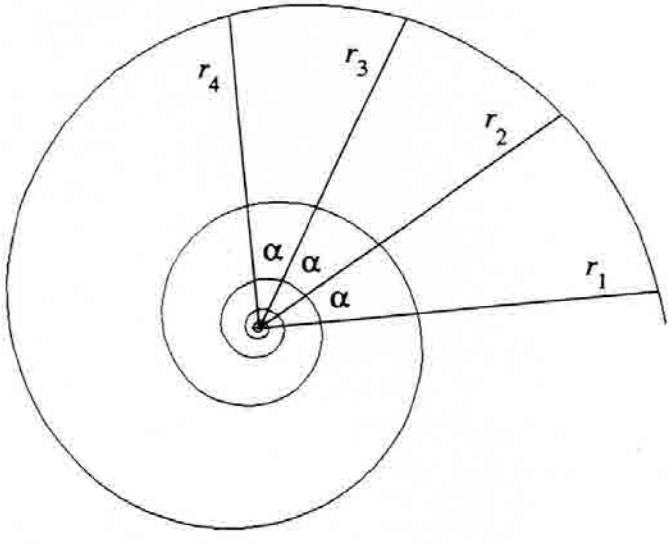

Fig. 2.15 The logarithmic spiral is self-scalable and self-similar at a point.

On the other hand, the *random of statistical self-similarity* property comes from the generalization of the fractal generating schemes to random processes. This can be carried out in many different ways. For instance, a random deviation to the translation or

contraction transformations of a Hutchinson operator could be added at each step of an IFS. But randomness can be introduced through many different ways to generate a whole new family of fractal objects. The most common is the mid-point displacement scheme used to generate the fractional brownian motion random process [5], which is the base for modeling fractal landscapes with random mountains, clouds, and coastlines [1]. If, for instance, we take a piece of random fractal coastline it can not be said that such a piece has the same shape of the whole coastline due to the random nature of its shape, however, both shapes are similar in the sense that they hold the same statistical properties and furthermore, they show the same kind of roughness, the same degree of detail and complexity, and the same richness of sizes and scales. Actually, statistical self-similarity is observed in many natural process and shapes, such as for instance, in cauliflower or broccoli plants, in human kidney, lung or blood vessels, or even in stream or atmospheric turbulence [1]-[8].

We should end this discussion of self-similarity by stressing that this property only applies strictly to ideal mathematical objects. Ideal fractal shapes are obtained through an infinite set of transformations which lead to objects with an infinite set of sizes and scales. Of course, such an idealization can only be approached in the real world by objects that hold some similarity properties up to a certain scale. The resulting truncated versions of the ideal fractal shapes are often named *band-limited fractal shapes* [14].

2.1.4.2 - Fractal Dimension

The common notion of dimension is rather intuitive and self-explanatory: a straight line is a one-dimensional object, a square is two-dimensional while a cube is three-dimensional. We also think of a point as a zero-dimensional object since it does not occupy any space in a straight line which has dimension 1, the same way an infinite number of segments can be fitted in a square, or an infinite number of squares fitted in a cube. In a slightly more mathematical approach, we would describe the dimension of an object as the number of parameters, i.e. coordinates, which are necessary to describe it. However, such an intuitive way of understanding dimension is found in trouble when trying to describe fractal shapes, which we have seen that rather than weird or exceptional objects they are common in every day's life. We have described curves that can be fitted in a finite area but have an infinite length (Koch curves, Julia and natural coastlines ...) and dusts of points that have a one to one correspondence with the all the points in the unit segment (the Cantor set). Furthermore, we have seen how some curves fill higher order two-dimensional objects (Peano and Hilbert curves), and hence how this curves can be used to describe such two-dimensional objects with a single parameter. Therefore, it appears necessary to carefully define the notion of dimension to properly include any kind of geometrical shape. The fact

is that roughly ten different definitions of dimension [2] can be found, all of them with some common features but each of them with its own differences and particularities. Here, we will only introduce the concept of topological dimension, which is the one that better fits our intuitive view of dimension, together with two versions of the fractal dimension: the self-similarity and box-counting dimensions. The later can be seen as a simplification of the Hausdorff dimension, which was the basis of Mandelbrot's work. However, the Hausdorff definition of dimension is often too complex to be evaluated over fractal shapes and the box-counting dimension, although slightly different [2], is broadly used instead in most of the fractal literature. Hence, we hereafter we will take the box-counting dimension as a definition of fractal dimension.

2.1.4.2.1 Topological Dimension

An object X is said to be topologically equivalent to an object Y if there is an homeomorphism h such that,

$$X \xrightarrow{h} Y \tag{2.13}$$

that is, there is a one-to-one and onto mapping h between X and Y that has a continuous inverse mapping h^{-1}. In other words, two objects are topologically equivalent if there is a biunique transformation that allows us to go from one object to the other. For instance, a square can be transformed into a circle or even into a Koch island and thus these three objects are topological equivalents. Henry Poincaré gave an inductive idea of topological dimension (D_T), which also fits our intuition of dimension, in the following way: a point has zero dimension while a curve is one-dimensional because it can be broken in two pieces by subtracting a lower dimensional object, i.e. a point, from it. Then, a square is two-dimensional because it can be broken in two pieces by a straight line and a cube is three dimensional because it can be split by a square. Thus, from the topological point of view, the Koch curve or a circle are both equivalent and one-dimensional objects.

The problem arises when dealing with some objects such as the Peano or Hilbert curves. They have topological dimension one according to Poincaré idea, nevertheless a one-to-one mapping can be established with a surface as the unit square. Thus, the necessity of introducing other definitions of dimension (the fractal dimension) becomes clear.

2.1.4.2.2 Self-Similarity Dimension

A definition of fractal dimension, the self-similarity dimension, directly comes out from the construction of strictly self-similar objects by means of Iterated Function Systems. If an IFS is composed only by contractions by the same reduction factor r ($0<r<1$), and none of the subsets obtained at each transformation overlap, the self-similarity dimension D_s of the fractal attractor can be calculated as

$$D_s = \frac{\log N}{\log(1/r)} \tag{2.14}$$

where N is the number of affine linear transformations that compose the Hutchinson operator of the IFS. In other words, N is the number of small copies of the whole attractor at the first stage, and r is their scale factor with respect to the fractal shape. D_S can be also seen as the exponent of the power-law that relates the number of parts that compose the object and its scale, i.e.,

$$N = r^{-D_s} \tag{2.15}$$

This definition of dimension is consistent with our intuitive idea of dimension as well. For instance, we can consider a square as a composition of 4 squares scaled down by a factor of 1/2. Then, log(4)/log(2)=2, which is also the topological dimension of the square. The same argument could be applied to a cube: it can be broken apart into 8 smaller cubes each one scaled down by a factor of 1/2, which will give a dimension of log(8)/log(2)=3 (see Fig. 2.16).

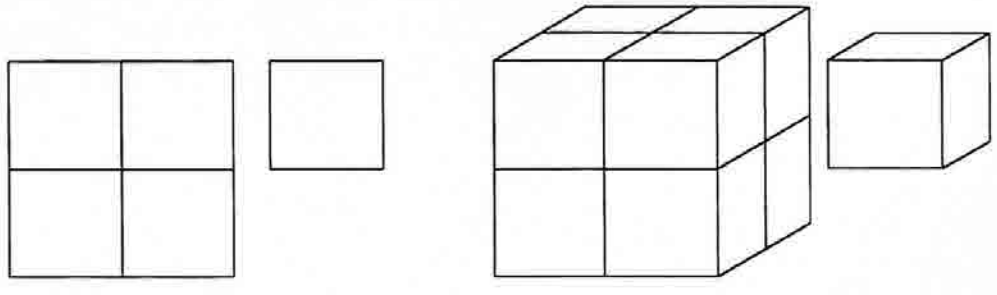

Fig. 2.16 The self-similarity dimension also works for Euclidean shapes.

Now, with this definition in mind, the self-similarity dimension of the classical examples of Section 2.1.2 can be computed as shown in Table 2.1.

Fractal Shape	*N*	*r*	D_S	D_T
Cantor Set	2	1/3	0.631	0
Koch Curve	4	1/3	1.261	1
Peano Curve	9	1/3	2	1
Sierpinski Gasket	3	1/2	1.585	1

Table 2.1 Some fractal shapes and their self-similarity (fractal) and topological dimension (D_S and D_T respectively).

This new definition gives a deeper insight on the nature of the fractal shape. Many of them have a fractional dimension that states a clear difference with common Euclidean shapes. Also, such a fractional dimension gives an idea of the complexity or roughness of the shape. For instance, the Koch curve has a fractal dimension slightly larger than its topological dimension 1; this matches our intuitive idea of a highly convoluted curve that seems to fill a two-dimensional space at least up to a higher degree than a classical Euclidean curve. Similarly, the Cantor set has a fractal dimension which is half way between a zero-dimensional object (a point) and a one-dimensional one (a segment). This is also consistent with the idea of an infinite set of points, that has a one-to-one correspondence with each point on the unit interval segment, though it is still a dust of points, i.e., the set is completely disconnected. Finally, we have a fractal dimension of 2 for the Peano or Hilbert curves since although they are still curves topologically speaking, they completely fill a two-dimensional space.

Such a fundamental difference between fractal and topological dimension is the main characteristic feature of a fractal shape. Although there is not a formal definition of fractal shape (Mandelbrot intentionally left aside this matter to allow a flexible update of the fractal concept), it is broadly accepted that this feature is what distinguishes a classical Euclidean shape from a fractal one.

2.1.4.2.3 Box-Counting Dimension

The definition of dimension just introduced conveniently establishes a fundamental characteristic parameter for a fractal shape. However, this definition is derived directly from the self-similarity property of a fractal and thus not cover fractal shapes which are not strictly self-similar but display self-affinity or statistical self-similarity features. An

alternative definition of fractal dimension, the box-counting dimension, overcomes such a problem.

The definition of box-counting dimension readily comes out from its computing algorithm, which can be described in the following way: firstly, a regular mesh of cell-size s is placed over the object (the mesh will have the proper topological dimension to completely cover the object). Secondly, the number of cells or boxes N_b which contains any part of the object is computed. This procedure is carried out many times scaling the mesh by several box-sizes s, and finally a log-log diagram of the number of boxes $N_b(s)$ as a function of $1/s$ is plotted. The resulting graph is a monotonically increasing function that can be very well approximated by a straight line, which indicates that the number of boxes and their sizes are related by a power-law as

$$N_b(s) \propto s^{-D_b} \tag{2.16}$$

where the exponent is the box-counting dimension D_b. Such a dimension is usually computed as the slope of the line in the log-log plot

$$D_b = \frac{\log(N_b(s))}{\log(1/s)} \tag{2.17}$$

Now, this definition is very similar to the definition on equation (2.14), but has the main advantage that is more general and does not only apply to strictly self-similar objects. For instance, the fractal dimension of the coast of Britain can be computed this way [2] giving a value of D_b=1.31. Thus, although the coast of Britain does not have a meaningful length (it depends on the resolution of our measuring system as discussed before), it does have a meaningful characteristic parameter, its fractal dimension, which also gives us an intuitive idea of a highly intricate, convoluted shape (even more than the Koch curve that has a fractal dimension of 1.261). Finally, we should remark that self-similarity and box-counting dimension are not identical definition, they can turn different values for the same object in some special cases [2] (not for any of the examples in Table 2.1). We will take the box-counting dimension as the fractal dimension due to its wider range of application and due its accordance with the more complete Hausdorff dimension [1]-[2].

2.1.4.3 - Lacunarity

Lacunarity is a rather broad concept that concerns the 'texture' of fractal shapes. Many fractal forms present large gaps within the several parts of its structure and are then said to be highly lacunar[2] objects. Lacunarity appears as a rather different concept than the fractal dimension, since several objects holding the same dimension can have distinct shapes and thus feature a quite different lacunarity.

B. Mandelbrot discusses and suggests in [1] several distinct ways for characterizing fractal lacunarity. They show to be useful definitions of lacunarity depending on the nature of the fractal shape. We shall introduce here an alternative parameter, the lacunarity ratio (L), to characterize the lacunarity of deterministic IFS fractals. It is defined as $L = 1/Nr = \delta/N$, where δ is the inverse of the characteristic scale factor r, i.e., $\delta=1/r$. Although this definition is not specially suitable for unevenly distributed gap fractal shapes, it does give a simple intuitive insight on the average gap to filled structure relation. Also, as it is shown in Chapter 3, such a lacunarity ratio plays a key role on the Side-Lobe Ratio characteristic of fractal arrays.

2.1.5 - Introduction to Multifractal Measures

Some forms can even display a higher degree of complexity than the fractal shapes introduced up to this point. For instance, we can imagine a composition of fractal shapes, each one with its own fractal dimension and characteristic scale factors. A box-counting algorithm will yield only the largest dimension on the whole set, and thus will be an incomplete description of the complexity of the set. Here, the concept of multifractal and multifractal measures arises to allow such a description. A summary of the main concepts regarding multifractals are introduced in this section.

Let us take a measure $\mu(A)$ over a subset A, for instance a fractal attractor. Such a measure can be understood as a probability density function over the support A. A measure $\mu(A)$ can model several physical parameters: the mass distribution over a fractal attractor, the probability of hitting a point on the attractor when a dart is thrown over it, or the current density distribution over a metallic antenna with a fractal shape, to name a few. A point-wise dimension at a point (x,y) can be defined as the exponent α in the power law which

[2] *Lacuna* (related to lake) is Latin for gap, [1].

specifies how fast the measure (i.e. the mass, probability, current etc.) is reduced when a ball $B(x,y)$ of radius r is shrunk around that particular point, i.e., assuming

$$\mu\big(B(x,y)\big) \propto r^{\alpha} \tag{2.18}$$

then the point-wise dimension is

$$\alpha = \lim_{r\to 0} \frac{\mu\big(B(x,y)\big)}{\log r} \tag{2.19}$$

which is also called the *Hölder exponent* at point (x,y). In practical cases, the radius r is never taken to zero to compute (2.19) but a ball (or a cell in a regular mesh) of size ε is used instead; in this case the approximation of (2.19) is called the *coarse Hölder exponent*. A frequency distribution of coarse Hölder exponents of a measure can be computed by covering it with a regular mesh of box-size ε and counting the number of boxes $N_\varepsilon(\alpha)$ that have an exponent within a certain range $\alpha + d\alpha$. Usually, the function $f(\alpha)$ is defined at this point as

$$f(\alpha) = \lim_{\varepsilon\to 0} -\frac{\log N_\varepsilon(\alpha)}{\log \varepsilon} \tag{2.20}$$

which can be loosely interpreted [2] as the fractal dimensions of the subsets in the support having a coarse Hölder exponent α since

$$N_\varepsilon(\alpha) \approx \varepsilon^{-f(\alpha)} \tag{2.21}$$

The function $f(\alpha)$ holds some interesting properties. It is a concave function and lies under the bisector $g(\alpha)=\alpha$. The maximum of the function is equal to the box-counting dimension of the support A of the measure $\mu(A)$. Also, the intersection of $f(\alpha)$ with the bisector, i.e. $f(\alpha)=\alpha$ is the so called information dimension [2],[7].

The concept of multifractal measures can be easily extended to geometrical shapes or images. The trick is to assign a uniform measure (i.e. a uniform distribution of mass or probability) over the fractal support, that is, define an index function which is 1 if a point belongs to the fractal set and 0 otherwise. This way, not only measures but also multifractal shapes can be characterized.

2.2 - Common Antennas And Bandwidth Limitations

2.2.1 - Radiation mechanism and main antenna parameters

An antenna can be viewed as a transition device for electromagnetic waves between an electric circuit or system and free space. The electromagnetic waves are coupled from the electric system to free-space by means of a mechanism called radiation. The behavior of electromagnetic waves, and consequently the behavior of antennas and their radiation mechanism, is fully characterized by Maxwell equations and the boundary conditions. Assuming a time-harmonic behavior in a homogeneous isotropic media, such equations can be written as

$$\begin{aligned} \nabla \times \vec{E} &= -\vec{M} - j\omega\mu\vec{H} \\ \nabla \times \vec{H} &= \vec{J} + j\omega\varepsilon\vec{E} \\ \nabla \cdot \vec{E} &= \frac{\rho_e}{\varepsilon} \\ \nabla \cdot \vec{H} &= \frac{\rho_m}{\mu} \end{aligned} \tag{2.22}$$

where E and H are the electric and magnetic fields, ε and μ the electric permittivity and the magnetic permeability, J and M are electric and magnetic current densities and ρ_e and ρ_m are electric and magnetic charge densities respectively. Both magnetic current and charge densities do not have physical meaning and are thus equal to zero, but they appear as a result of applying the theorem of equivalence. Also, the usual relations among the speed of light c, the wavelength λ and the characteristic impedance of the medium Z_0 should be taken into account

$$c = \frac{1}{\sqrt{\mu\varepsilon}} \qquad k = \frac{c}{f} = \frac{2\pi}{\omega\sqrt{\mu\varepsilon}} \qquad Z_0 = \sqrt{\frac{\mu}{\varepsilon}} \tag{2.23}$$

The frequency dependence of the electromagnetic fields becomes already apparent in the curl equations in (2.22). The dependence of the electromagnetic fields on the antenna size is more clear when the relation between the radiated fields and the current over the antenna is written. In the far field region, i.e., when the distance from the antenna relative to its size to wavelength ratio is large [52],[53], such a relation can be written as

$$\vec{E} = -j\omega\left(A_\theta\hat{\theta} + A_\varphi\hat{\varphi}\right)$$
$$\vec{H} = \hat{r} \times \frac{\vec{E}}{Z_0} \tag{2.24}$$

where A is an auxiliary vector potential function conveniently defined as

$$\vec{A}(\vec{r},\vec{k}) = \frac{\mu}{4\pi}\iiint_V \vec{J}(x',y',z')\frac{e^{-jkR}}{R}\partial V' \tag{2.25}$$

being J the antenna current distribution, V an arbitrary volume enclosing the antenna, k the wave number defined as usual as $k=2\pi/\lambda$, and R the distance of any point (x,y,z) in free-space to any point on the antenna (x',y',z'). Also, when the distance from the source is large enough, equation (2.25) can be approximated as

$$\vec{A}(\vec{r},\vec{k}) = \frac{\mu}{4\pi}\frac{e^{-jkr}}{r}\iiint_V \vec{J}(x',y',z')e^{j\vec{k}\cdot\vec{r}'}\partial x'\partial y'\partial z' = \frac{\mu}{4\pi}\frac{e^{-jkr}}{r}\vec{N}(\vec{k}) \tag{2.26}$$

An auxiliar vector N named the radiation vector has been introduced in (2.26). Such vector can be interpreted as the Fourier transform in the spatial spectrum domain $\{k_X, k_Y, k_Z\}$ of the current distribution over the antenna. Now, the equivalence theorem states that any configuration of electromagnetic fields outside a volume V enclosed in a surface S can be unanimously determined by the tangential components of electric and magnetic fields to the surface S. In particular, such a tangential components are proportional in magnitude to the current density over the antenna when S is taken as the antenna surface [52],[53]. Thus, the electromagnetic fields outside an antenna are fully characterized by its current distribution plus equations (2.24), (2.25) and (2.26). The frequency dependence becomes explicit again in such equations and the dependence with the size of the antenna comes out from the integral domain V which encloses the antenna. For a very small antenna located at the coordinate origin, equation (2.25) can be approximated as

$$\vec{A}(\vec{r},\vec{k}) = \frac{\mu}{4\pi}\frac{e^{-jkr}}{r}\iiint_V \vec{J}(x',y',z')\partial V' \approx \frac{\mu}{4\pi}\frac{e^{-jkr}}{r}\vec{J}_{eq}V_{antenna} \tag{2.27}$$

where r is the distance from the antenna (the origin), $V_{antenna}$ is the volume enclosing the antenna and J_{eq} is an equivalent uniform current distribution conveniently defined to allow the integral over an arbitrary current distribution to be written as the product in (2.27). Now,

by writing ω as $\omega=2\pi c/\lambda$ and substituting (2.27) into (2.24) we find that the magnitude of the electric and magnetic fields are proportional to the antenna volume and wavelength ratio

$$\left|\vec{E}\right| \propto \frac{\left|\vec{J}_{eq}\right| \cdot V_{antenna}}{\lambda} \tag{2.28}$$

Roughly speaking, this means that for a given current magnitude, the size of the antenna has to be comparable to the wavelength to radiate efficiently. The smaller the size of the antenna relative to the wavelength, the smaller will be the radiated electromagnetic fields and their associated radiated power.

The radiation mechanism can be also understood as the natural result from accelerating electric charges. The general time dependence of the far-field electric field can be derived from (2.24) by summing the contributions from all time harmonic components $e^{j\omega t}$, i.e., taking its inverse Fourier transform

$$\vec{E}(\vec{r},t) = \int_{-\infty}^{\infty} -j\omega \cdot \vec{A}(\omega) e^{j\omega t} \partial\omega = -\frac{\partial}{\partial t}\vec{A}(\vec{r},t) \tag{2.29}$$

where the time-dependent vector potential $A(r,t)$ is given by [53]

$$\vec{A}(\vec{r},t) = \frac{\mu}{4\pi}\iiint_V \frac{\vec{J}(\vec{r}',t-R/c)}{R}\partial V' \tag{2.30}$$

The electric current can be seen as a flow of electric charges moving with a velocity v

$$\vec{J}(\vec{r},t) = \rho \cdot v(\vec{r},t) \tag{2.31}$$

where ρ is a volumetric charge density. Then, combining equations (2.29), (2.30) and (2.31), and assuming an homogeneous charge density distribution, the radiated electric field can be written as

$$\vec{E}(\vec{r},t) = \frac{\mu}{4\pi}\iiint_V \frac{1}{R}\cdot\rho\cdot\frac{d}{dt}\vec{v}(\vec{r}',t)dV' = \frac{\mu}{4\pi}\iiint_V \frac{1}{R}\cdot\rho\cdot\vec{a}(\vec{r}',t)dV' \tag{2.32}$$

where $a(r,t)$ is the acceleration of the charge distribution ρ. The simplest example of radiating element is a point-like charge with charge q linearly accelerating in the z direction. In this particular case, the charge density ρ is a delta function which gives the overall charge q inside the volume V when integrated, and the radiated electric field is given by

$$\vec{E}(\vec{r},t) = \frac{\mu q a}{4\pi R}\sin\theta\ \hat{\theta} \tag{2.33}$$

which means that the strength of the radiated electromagnetic fields is directly proportional to the acceleration a (see [109] for a further explanation of this result). Such a result is consistent with the common knowledge that discontinuities, sharp edges, corners and pins, that introduce sudden changes on the current direction and thus to the velocity vector, are to be avoided to prevent radiation when designing low-loss microwave circuits. On the contrary, this fact can be useful when enhancing radiation from antennas.

In general, the performance of an antenna is determined by three main features: its radiation pattern, input impedance and polarization. The radiation pattern $P(\theta,\phi)$ is a normalized function that describes how the antenna spreads the radiated power in free-space and can be calculated from the radiated electromagnetic fields as

$$P(\theta,\phi) = \frac{\mathrm{Re}\left\{\bar{E}\times\bar{H}^{*}\right\}}{\max\left\{\mathrm{Re}\left\{\bar{E}\times\bar{H}^{*}\right\}\right\}} \qquad \left[W/cm^{2}\right] \tag{2.34}$$

Some fundamental properties of the antenna are derived from the radiation pattern such as the *directivity D*, which is the ratio between the maximum radiated power density in a given direction and the power density that would deliver an isotropic antenna that radiated the same total power, and the *side-lobe ratio* (SLR) which is the ratio between the power density in the maximum direction and the power density radiated in the direction of the next relative maximum of the radiation pattern.

The input impedance Z_{in} is the impedance seen by a generator when connected to the antenna terminals. Usually, the input impedance has both resistive and reactive parts, i.e., $Z_{in} = R_{in} + j\,X_{in}$ and the resistive component is due to two effects: the power absorbed and radiated by the antenna into free-space (R_r), and the power absorbed by the antenna and dissipated due to the ohmic losses in its metallic structure (R_Ω). Thus the input resistance is usually written as

$$R_{in} = R_r + R_\Omega \tag{2.35}$$

The ratio between the power delivered to R_r and the total power delivered to R_{in} is the ohmic efficiency of the antenna. The radiation resistance R_r can be computed as,

$$R_r = \frac{2W_r}{|I_{in}|^2} \tag{2.36}$$

where W_r is the total power radiated by the antenna and I_{in} is the the current at the input terminals.

Other interesting parameters related to the input impedance are the normalized input reflection coefficient Γ_{in} and the voltage standing wave ratio *VSWR*

$$\Gamma_{in} = \frac{Z_{in} - Z_0}{Z_{in} + Z_0} \qquad VSWR = \frac{1+|\Gamma_{in}|}{1-|\Gamma_{in}|} \tag{2.37}$$

where Z_o is a reference impedance usually taken to be 50Ω in typical microwave systems. The magnitude of Γ_{in} is called the input return-loss, which is usually expressed in decibels (dB) and gives the ratio between incident and reflected electromagnetic power at the antenna input terminals. A common criteria is to say that an antenna is well matched to a reference impedance Z_o when the input return-loss is below -10dB, more precisely when the voltage standing wave ratio (VSWR) is VSWR<2.

An antenna can be linearly, circularly or elliptically polarized, depending on the polarization status of its radiated waves. Depending on each particular application, a linear or circularly antenna might be preferred. If an antenna is to be linearly polarized, the cross-polar ratio is a figure of merit of the antenna, while if it is to be circularly polarized, the ratio between the left and the right-handed polarization define its performance.

The bandwidth of antenna is the range of frequencies where the antenna characteristics (pattern, input impedance and polarization) are within an acceptable value. Such an acceptable value is completely dependent on the particular application the antenna is designed for, and thus there is not a unanimous definition of bandwidth for an antenna. However, an antenna performance is usually highly frequency dependent as stated in equations (2.22) through (2.28), which often means a narrow-band behavior. In the

following sections, some examples of classical antennas with their main characteristic parameters are introduced to illustrate such a frequency dependence.

2.2.2 - Linear wire antennas

Dipoles and monopoles are among the oldest, simplest and best known examples of antennas. They basically consist on a couple of collinear straight wires (dipole) or a single straight wire over a ground plane (monopole) both fed by a generator with its terminals connected between the two wires or between the wire and the ground-plane respectively.

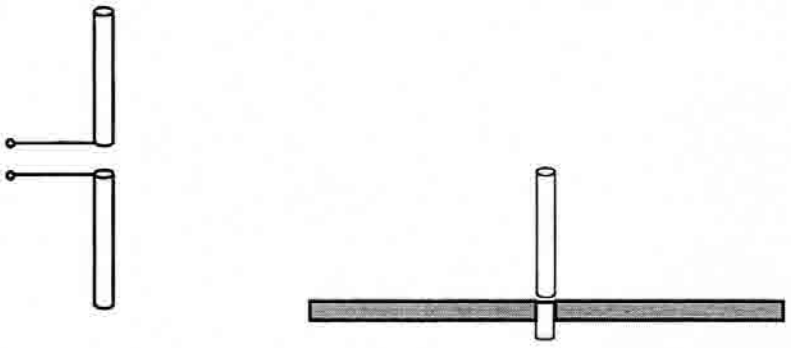

Fig. 2.17 Two simple antennas: the dipole (left) and the monopole (right).

Both antennas have the same performance, that is, they have the same radiation pattern in the upper half-space for the same wavelength; nevertheless the input impedance of the dipole is twice the one of the monopole. In many cases, a monopole is preferred due to its simpler feeding scheme and mechanical simplicity.

2.2.2.1 - Small Dipole and Monopole

A dipole is said to be small when its length it is smaller than one tenth of the operating wavelength [52]. A good approximation of the current over such an antenna is a triangular function, with its maximum at the input terminals and two nulls at the tips of the antenna (a single null in a monopole). The radiation resistance of a small dipole of length l is given by the following equation [52]

$$R_r = 20\pi^2\left(\frac{l}{\lambda}\right)^2 \tag{2.38}$$

where the size to wavelength ratio dependence is clearly stated. The radiation pattern when the antenna is aligned along the z axis is given by

$$P(\theta,\phi) = \sin^2\theta \tag{2.39}$$

which leads to a directivity of D=3/2. The antenna is linearly polarized along the θ direction. It is interesting to notice that the shape of radiation pattern (and thus the directivity) is almost frequency independent, which is a common feature to all small antenna that can be directly derived from the approximation in equation (2.27). Thus, in this particular case the bandwidth of the antenna will be limited by its input impedance behavior.

The small size, poor directivity together with the H-plane omnidirectional pattern makes this kind of antennas suitable for mobile communication systems where the position of the base-station is not known or is changing rapidly. However, special care must be taken regarding to its size: if the antenna is made too small compared to wavelength, the radiation resistance would decay rapidly (2.38) making the antenna highly inefficient. In practical cases, this is the most severe limit to the operation of such small antennas.

2.2.2.2 - Finite Length Dipole and Monopole

A dipole or monopole is no longer small when its length and wavelength are comparable. The current distribution over a finite length dipole or monopole can be approximated by a sinusoidal distribution [52]-[53]. The radiation pattern is proportional to the following expression

$$P(\theta,\phi) \propto \left(\frac{\cos\left(\frac{kl}{2}\cos\theta\right) - \cos\left(\frac{kl}{2}\right)}{\sin\theta} \right)^2 \tag{2.40}$$

which is a function of the operating frequency. The pattern has a characteristic donought shape similar to that of the small dipole (which can be seen now as a particular case of a finite length dipole) when $l \leq \lambda$. When the antenna is made larger, the number of lobes of the pattern begins to increase, which is not a desirable feature since it means that the antenna spreads the radiated power in several directions of space (see Fig. 2.18).

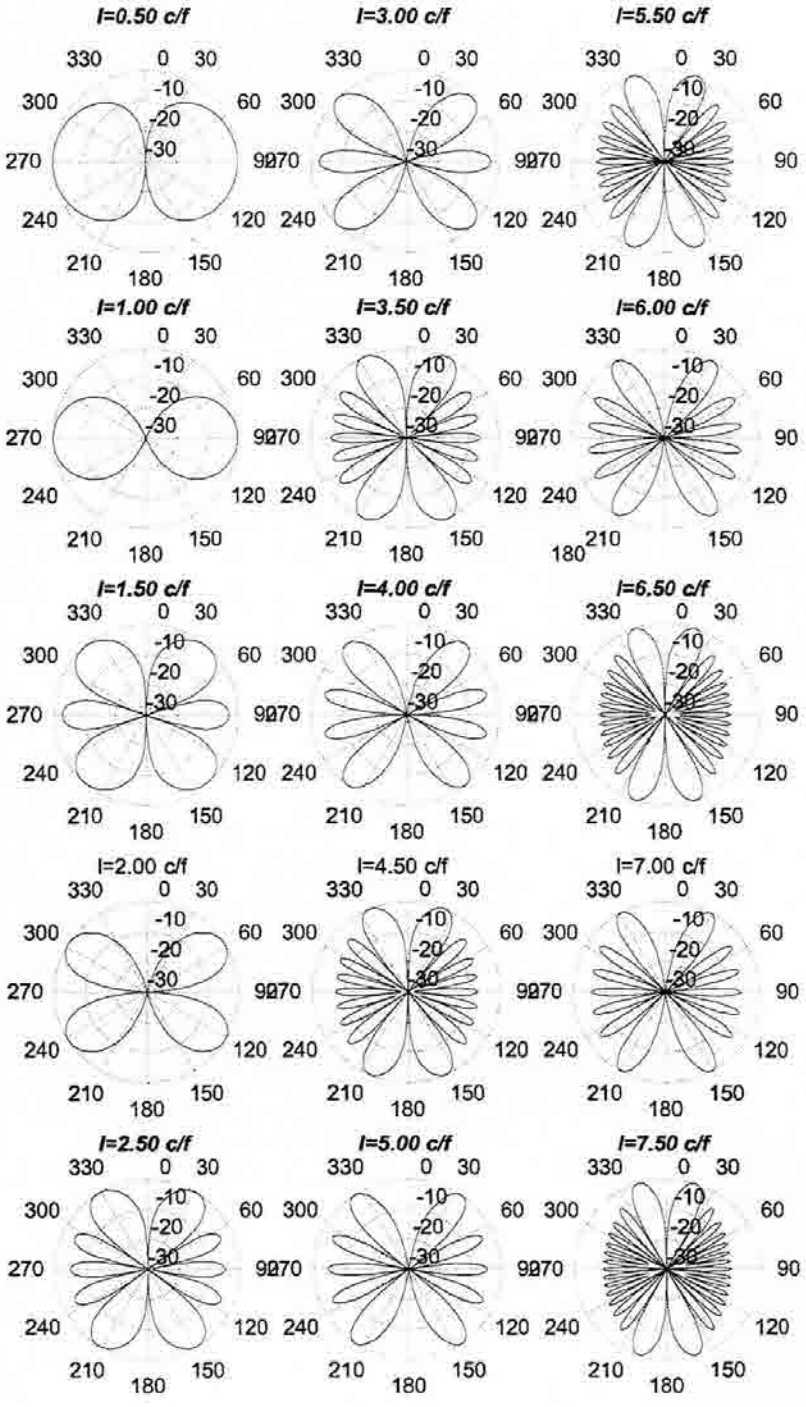

Fig. 2.18 Evolution of the radiation pattern of a finite length dipole with the operating frequency. Sinusoidal current distribution is assumed. Length **l** *is expressed in wavelengths with* 0.5λ *increments (from top to down and left to right)*

The input and radiation resistance of a linear dipole or monopole are highly frequency dependent as well. Such a dependence together with the directivity dependence are illustrated in Fig. 2.19. Usually, a dipole is operated at the first resonance, i.e., when $h \sim \lambda/4$ and the total length of the dipole is a half wavelength. The directivity of such a dipole is slightly larger (D=1.64) than that of a small dipole and its input impedance is real (due to resonance) and equal to 73Ω, which is a very convenient impedance since it is well matched to typical 75Ω and 50Ω coaxial cables. The current distribution has its maximum at the input terminals, so the input impedance and radiation resistance are identical in this case.

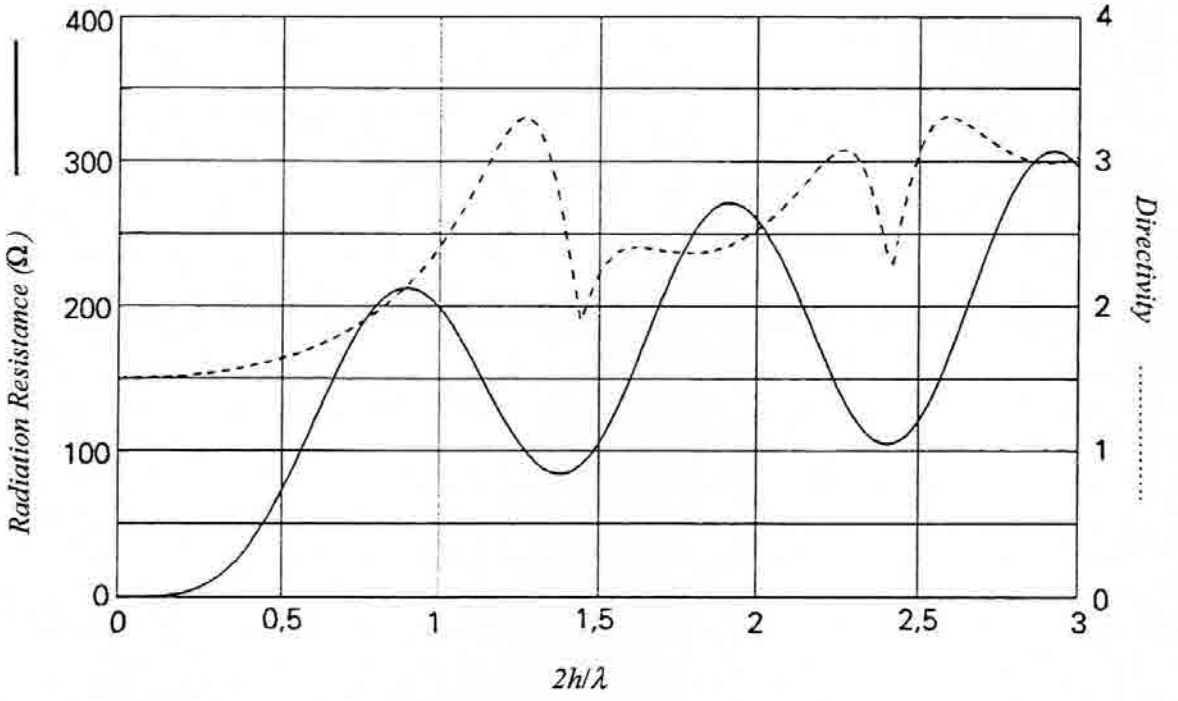

Fig. 2.18. Dependence of a finite length dipole radiaton resistance and directivity with the length (2h) to wavelength ratio.

2.2.3 - Frequency dependence of loop antennas

Another kind of simple, well known antennas are loop antennas. Loop antennas take many different forms (square, circular, triangular,...) being the circular one the most popular one. Loops can also be classified into small loops when its radius a is much smaller than the wavelength, and large loops otherwise. The radiation pattern of a small loop is basically the same of a small dipole, with the only difference that the electric field is linearly polarized along φ. The radiation resistance for a single turn circular loop of radius a is given by

$$R_r = \eta \frac{2\pi}{3}\left(\frac{kS}{\lambda}\right)^2 = 20\pi^2\left(\frac{C}{\lambda}\right)^4 \tag{2.41}$$

where S is the loop area, i.e., $S=\pi a^2$, and C its perimeter ,i.e., $C=2\pi a$. If length was the characteristic size for a dipole, in the loop case, the characteristic size is either the perimeter or the area. Although equation (2.41) is derived for a circular small loop, it also applies for other shapes (square, triangular...), provided the area inside the loop is taken as the characteristic parameter. Again, when the size of the antenna is made small compared to wavelength, the radiation resistance decreases which can be translated in a loss of efficiency as discussed before. However, such a radiation resistance can be made arbitrarily large by stacking multiple loops, i.e., by making a multiturn loop in such a way that the magnetic field crosses all loops. This way, the overall effective area crossed by the magnetic flux is made N times larger (being N the number of turns) and the radiation resistance is increased by a factor of N^2

$$R_r = \eta \frac{2\pi}{3}\left(\frac{kS}{\lambda}\right)^2 \cdot N^2 = 20\pi^2\left(\frac{C}{\lambda}\right)^4 \cdot N^2 \qquad \text{N - turn circular loop} \tag{2.42}$$

Unfortunately, increasing the number of turns also increases the ohmic resistance due to the longer length of the whole wire. Furthermore, the proximity effect between turns produces an additional increase on the ohmic losses which further decreases the overall efficiency. Actually, in practice the efficiency of the antenna can not be made arbitrarily large for very small loops [52] as equation (2.42) seems to suggest.

2.2.4 - Fundamental Limits of Small Antennas

The examples of small dipoles, monopoles and loops that have been just introduced illustrate some limitations of small antennas with respect to their radiation efficiency and frequency behavior. Actually, there has been a thorough analysis of the fundamental limits of small antennas in the literature [58]-[64]. The basic assumption in such an analysis consists on considering a radiansphere (i.e. an sphere of radius $\lambda/2\pi$) enclosing the small antenna and the electromagnetic fields radiated by the antenna as a linear superposition of orthogonal spherical modes. Then, independently of the current distribution over the antenna, both the radiated power flowing across the sphere and the stored reactive energy can be calculated by summing the contribution of each independent mode. The quality factor Q of the antenna can be calculated then as usual in any resonant system as

$$Q = \omega_0 \frac{Energy\ stored\ at\ resonance}{Power\ lost\ in\ a\ oscillation\ period} \tag{2.43}$$

where ω_0 is the resonant frequency. For $Q>>1$, the quality factor can be seen also as the inverse of the fractional bandwidth (FWHM)

$$\frac{FWHM}{f_0} = \frac{\Delta f_{3dB}}{f_0} \approx \frac{1}{Q} \tag{2.44}$$

It has been shown that the higher order modes within a sphere of radius a become evanescent when $ka<1$, then for a very small linearly polarized antenna its Q has the only contribution of the lowest TM mode which reduces to [52],[59],[62]

$$Q = \frac{1}{k^3a^3} + \frac{1}{ka} \overset{ka<<1}{\approx} \frac{1}{(ka)^3} \tag{2.45}$$

The equation above is important because establishes an upper bound to the fractional bandwidth of an small antenna no matter what its shape is. Whether a small antenna reaches such a limit or not depends on how efficiently it utilizes the available volume within the sphere. In practice, common antennas such as small dipoles or loops are far away from such a limit; only some special cases such as the Goubau antenna [60] are about a 65% percent away from it.

2.2.5 - Microstrip Antennas

Microstrip antennas are a special case of antenna which has awaken a great interest due to their particular features [73]-[78] . They basically consist of a metallic patch printed over a dielectric substrate slab which is backed by a metallic ground plane (see Fig. 2.20). The structure is basically the same as that of standard microwave microstrip printed circuits, which is a convenient feature since it allows, in principle, the integration of an antenna and its associated microwave system (i.e., receiver, transmitter, etc.) in a single, compact layout. The shape of the patch can be easily modified without increasing the complexity of manufacture since it is printed using standard photolitographic techniques. Also, the antenna has a very low profile, low weight and it is rather flexible, which are very useful features when the antenna is to be integrated on the surface of a mobile, aerodynamic vehicle.

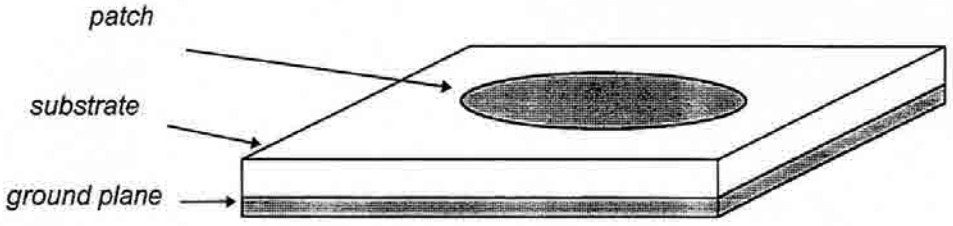

Fig. 2.20 Typical structure of a microstrip antenna.

Nevertheless, some of the main advantages of microstrip antennas are also the source of their major drawbacks. Since the patch is very close to the ground plane, the current flowing over it has an equivalent virtual image at the other side of the plane, which has the opposite sign and thus tends to cancel radiation due to the proximity with the original current source over the patch. Such a phenomenon is clear if one takes into account that the origin of microstrip antennas are microstrip transmission lines and circuits, which tend to confine electromagnetic waves within the substrate (between the printed circuit and the ground plane). Thus, a lot of reactive power is stored under the patch of a microstrip antenna and only a small part of the stored energy is radiated from its leaking border.

With this picture in mind, it is easy to understand that the frequency behavior of a patch antenna is usually analyzed by considering its structure as an energy storage resonant cavity. The equivalent cavity would be bounded by two electric walls (the metallic patch

and ground plane), surrounded by magnetic walls that model the open circuit at the border of the patch. Since the thickness of the substrate is usually much smaller than the operating wavelength, this model can be approached by a two-dimensional resonator with dominant TM_{mn} modes at the lower resonant frequencies. In general, the patch is operated at its fundamental mode, and its corresponding frequency is determined by the cavity model approach [74]. Since the ratio between the stored energy versus the radiated power is large (i.e. the Q factor of the antenna), a patch antenna is usually a very narrowband device, with fractional bandwidths around 1% ~ 2%. This is a major drawback when the antenna is intended to work in a telecommunication system that requires multiple channel operation or a high bit rate, and several systems have been essayed to improve its bandwidth [74],[77]. Among them, the most common consist on either enlarging the spacing between the patch and the ground-plane, or stacking patches of several sizes. Both schemes have shown to be useful to achieve fractional bandwidths up to a 10% ~ 20% [74],[77], but present the awkward problem of increasing the small thickness of the antenna, which was one of its major advantages. Thicker substrates are also related to 'leaky waves' and 'blind angles'.

2.2.6 - Frequency dependence of antenna arrays

An array of antennas is a set of antennas spatially distributed in a set of points. When all the antennas in an array have the same current distribution shape, the array radiated fields can be described in a compact way by means of equation (2.26). That is, if the n^{th} element of the array is located at a points (x_n, y_n, z_n), the overall current distribution can be conveniently written as a convolution of a set of delta functions located at each point of the array with the current distribution of a single element, i.e.,

$$\vec{J}_{Array}(x',y',z') = \vec{J}_{Element}(x',y',z') * \sum_{n=1}^{N} a_n \cdot \delta(x'-x_n, y'-y_n, z'-z_n) \tag{2.46}$$

where a term a_n is included to allow an individual weighting of each element to the overall current of the array. Now, since the Fourier transform of a two-term convolution is the product of the Fourier transform of each term, equation (2.26) can be split in three terms,

$$\vec{A}(x,y,z) = \frac{\mu}{4\pi}\frac{e^{-jkr}}{r} \cdot EF(k_x,k_y,k_z) \cdot AF(k_x,k_y,k_z) \tag{2.47}$$

the first one being the vector potential of an isotropic radiator located at the origin, the second one $EF(k_X, k_Y, k_Z)$ being the so called *element factor* (the Fourier transform of the

current distribution of a single antenna of the array), and the third one being defined as the *array factor* $AF(k_X, k_Y, k_Z)$, which is the Fourier transform of the spatial distribution of elements within the array. Such a compact notation allows an independent analysis and design of the array distribution and its elements. A complete theory has been developed to describe the behavior of arrays and array factors, mainly based on uniform space distribution of elements. In the following subsections, the frequency dependence of this kind of arrays is illustrated for some simple cases.

2.2.6.1 - Uniformly Spaced Linear Arrays

Let us assume a linear array of elements aligned along the z axis, all of them spaced by a common distance d. Although the shape of the current distribution of each element is assumed to be the same, each element can be weighted independently by an amplitude term a_n and phase-shifted by a term β_n. If each element of the array is phase-shifted by the same *progressive phase factor* β with respect the previous element of the array, then the array factor can be rewritten as

$$AF(\Psi) = \sum_{n=0}^{N-1} a_n e^{jn\Psi} \tag{2.48}$$

where Ψ is defined as

$$\Psi \equiv k_z \cdot d + \beta = k \cdot d \cdot \cos\theta + \beta \tag{2.49}$$

Equation (2.48) is formally a Discrete Fourier Transform (DFT) which is commonly used to describe the spectral properties of digital discrete signals [107],[108]. Hence, most signal processing design techniques can be applied to the design of linear arrays. It is well known [107] that the Fourier Transform of a discrete sequence is a periodic function with period 2π, hence the array factor $AF(\Psi)$ is completely characterized by the interval $(-\pi,\pi)$. On the other hand, although the function in equation (2.48) is formally defined for any real value Ψ, equation (2.49) restricts the possible values of Ψ within the interval $(-kd+\beta, kd+\beta)$. This interval is known as the *visible range* of the array factor, and plays a key role in the shape of the radiation pattern of the array.

Figure 2.21 shows the array factor of a uniformly spaced, uniform amplitude distribution, ten-element array in both Ψ and θ domains. It becomes apparent that once the

array factor in the Ψ domain is fully defined through the number of elements and current distribution, the overall shape in the θ domain is mainly dependent on two parameters: the visible range and the progressive phase β. Depending on the size of the visible range, the number of lobes included on the final pattern will be enlarged or reduced, and the main-lobe width will be widened or narrowed as well. Depending on the progressive phase, the main lobe can be steered to point in a θ_0 direction

$$\theta_0 = \arccos\left(\frac{-\beta}{kd}\right) \tag{2.50}$$

Two typical array configurations come out from such a relation: the *broadside* and the *endfire* arrays. A broadside array has its maximum pointing to the orthogonal direction to the array, i.e. θ=90°, and it is achieved by feeding all the elements in phase, i.e., $\beta = 0$. An endfire array has its maximum pointing in the same direction the elements of the array are aligned in (the z-direction in our case), which is achieved by phasing the elements by a

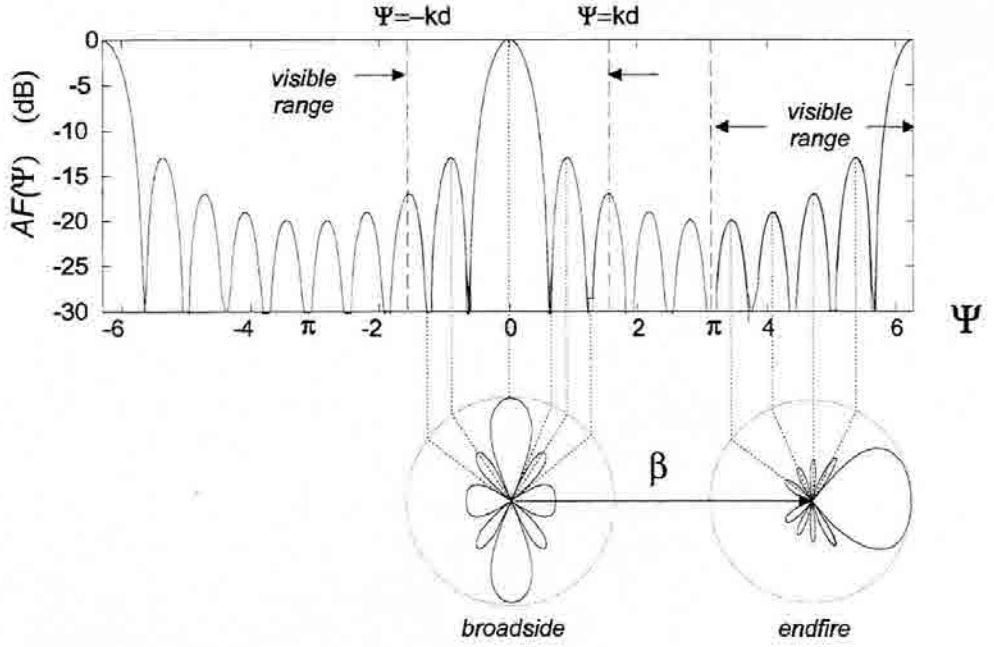

Fig. 2.21 Array factor of a uniformly spaced, uniform amplitude array in Ψ and θ domains.

progressive phase β=-kd. In the particular case of Fig. 2.21, the spacing among elements has been chosen to be $d=\lambda/4$ so the visible range is $(-\pi/2,\pi/2)$ for the broadside case and $(-\pi, 2\pi)$ for the endfire one.

The main point here is noticing that both the direction and shape of the final pattern is clearly dependent on the *kd* product, i.e., on the spacing to wavelength ratio d/λ. In particular, if the spacing is chosen such that $d/\lambda>1$, more than two entire periods in the Ψ domain will be included in the visible range and several grating lobes will appear in the array pattern, which is an undesirable feature since it introduces an ambiguity in the pointing direction and an overall decrease of the array directivity. Hence, an array has to be designed with a particular d/λ in mind, which means that the resulting pattern will be highly frequency dependent. Such a dependence is analogous to the length to wavelength dependence of a dipole or monopole as described in Section 2.2.2.2 , nevertheless, here the spacing between elements rather than the overall length is the characteristic size of the radiating system which conditions the frequency dependence.

2.3 Frequency-Independent Antennas

It was a common belief before the 1950s that the frequency dependence of an antenna behavior upon its characteristic size to wavelength ratio would be a major limitation for their broadband operation. However, several works [39]-[45] mainly carried out at the University of Illinois at Urbana-Champaign and the University of California at Berkeley in the late 1950s and early 1960s, leaded to the invention of some frequency-independent antennas. Such antennas were the demonstration that practical bandwidths of 1:40 could be achieved, which far exceeded the typical 1:2 bandwidths performed by former antennas. In this chapter an overview of the main principles of the frequency-independent antenna design, together with some of the antennas developed are introduced [39]-[50].

2.3.1 - Scaling Properties of Maxwell Equations

The main principle for the design of frequency-independent antennas, the scaling principle, directly comes out from Maxwell Equations. The following development is basically the same as the one described in [45],[48] and establishes a useful sufficient condition for an antenna to be frequency independent. Let us write the rotational Maxwell Equations for a loss-less medium

$$\begin{aligned} \nabla \times \vec{E} &= -j\omega\mu\vec{H} \\ \nabla \times \vec{H} &= j\omega\varepsilon\vec{E} \end{aligned} \tag{2.51}$$

now, let us define a normalized space $\mathbf{R^{3'}}$ with coordinates x', y', z' that are related to the original coordinates x,y,z in $\mathbf{R^3}$ as

$$x' = x/\lambda \qquad y' = y/\lambda \qquad z' = z/\lambda \tag{2.52}$$

where λ is the wavelength. The rotational operators with respect to the (2.52) coordinates in both domains hold the following relationship

$$\nabla' \times \vec{E}(x',y',z') = \lambda \cdot \nabla \times \vec{E}(x',y',z') \tag{2.53}$$

hence, Maxwell Equations can be written in $\mathbf{R}^3$ as

$$\begin{aligned}\nabla'\times\vec{E}(x',y',z') &= -j\omega\mu\vec{H}(x',y',z')\cdot\lambda \\ \nabla'\times\vec{H}(x',y',z') &= j\omega\varepsilon\vec{E}(x',y',z')\cdot\lambda\end{aligned} \tag{2.54}$$

which leads to the Frequency Independent Maxwell Equations

$$\begin{aligned}\nabla'\times\vec{E}(x',y',z') &= -j2\pi Z_0\vec{H}(x',y',z') \\ \nabla'\times\vec{H}(x',y',z') &= j2\pi Z_0\vec{E}(x',y',z')\end{aligned} \tag{2.55}$$

From (2.55) one can conclude that if a particular solution of Maxwell Equations self-scales with wavelength, that is,

$$\begin{aligned}\vec{E}(x,y,z) &= \vec{E}\left(\frac{x}{\lambda},\frac{y}{\lambda},\frac{z}{\lambda}\right) \\ \vec{H}(x,y,z) &= \vec{H}\left(\frac{x}{\lambda},\frac{y}{\lambda},\frac{z}{\lambda}\right)\end{aligned} \tag{2.56}$$

then the solution will be also a solution of the Frequency Independent Maxwell Equations. The equivalence theorem tells us that the fields radiated by an antenna are uniquely determined by the electric and magnetic fields tangential to an arbitrary surface enclosing the antenna. In particular, the antenna surface can be taken as such an arbitrary surface and in this case, the tangential fields are proportional to the current density distribution over the antenna. Thus, if the current over the antenna (electric and magnetic fields) and the antenna itself (surface over the antenna) self-scales with wavelength, then the radiated fields and hence the antenna behavior will be independent of frequency. From this principle, V.H. Rumsey [45] concluded that an antenna with a shape only defined by angles would be a frequency-independent antenna, since it would not have any characteristic size to be scaled with wavelength. Spiral, conical and conical spiral antennas are some examples of antennas that were designed attending this criteria.

2.3.2 - Self-complementary Antennas

A metallic planar structure is said to be self-complementary if its shape remains unchanged when the metallic and void parts are exchanged. It is shown in [49],[52],[53]

that the input impedance of a metallic structure and its complementary part are related to the characteristic impedance of the medium by

$$Z_S \cdot Z_c = \frac{Z_0^2}{4} \tag{2.57}$$

which leads to the following impedance for a self-complementary antenna (Z_s=Z_c=Z_{sc})

$$Z_{sc} = Z_0 / 2 = 60\pi \tag{2.58}$$

It follows from equation (2.58) that a self-complementary antenna has an input impedance which is independent of frequency. Such an important result is taken into account in the design of some frequency-independent antennas such as the planar logarithmic spiral. It is important to remark though, that equation (2.58) is neither a necessary condition nor a sufficient one for an antenna to be frequency independent. It only implies frequency independence from the input impedance point of view, but it does not guarantee, for instance, a frequency independent pattern. Furthermore, several frequency-independent antennas have been developed which are not self-complementary [39],[42],[46]. Therefore, it can be concluded that self-complementarity is a desirable although not necessary feature to take into account when designing frequency-independent antennas.

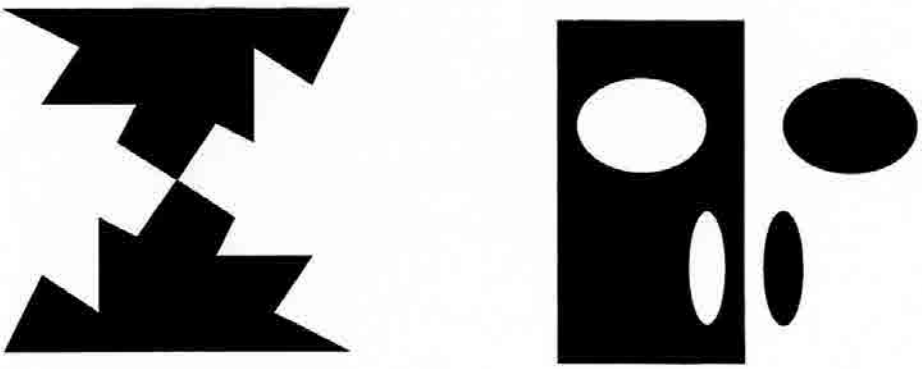

Fig. 2.22 Some self-complementary shapes.

2.3.3 - Cones and Spirals

2.3.3.1 - The Biconical Antenna

The conical dipole is maybe the simplest ideal structure which follows Rumsey's principle. It is a structure which is only characterized by the apex angles of the two cones that compose the antenna shape [45],[52],[67],[68]. It can be easily shown [45],[52] that the biconical structure behaves as an ideal spherical wave guide with characteristic impedance

$$Z_{cone} = \frac{Z_0}{2\pi} \cdot \ln\left(\frac{\tan\theta_1}{\tan\theta_2}\right) \tag{2.59}$$

being θ_1 and θ_2 the two apex angles of the cones as shown in Fig. 2.23. When infinite, the input impedance of such structure is equal to its characteristic impedance given by equation (2.59), which is pure resistive and independent of frequency.

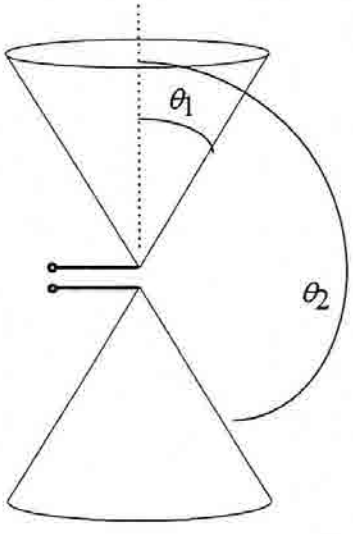

Fig. 2.23 The biconical antenna.

Such a theoretical model only applies strictly to the infinite shape. Of course, any feasible implementation of a biconical antenna would necessarily require a truncation of the infinite structure. Here, a tough problem arises since the truncated version of the infinite shape is no longer truly self-scaleable; it has a characteristic size (the height of the cones)

which does not scale with wavelength. The result is that a real biconical antenna does not have a frequency independent behavior but a broadband behavior instead. That is, it has a large bandwidth with respect to a dipole or monopole but a narrow bandwidth compared with frequency-independent antennas.

The truncation effect plays a key role in the development of frequency-independent antennas. The point is that the Rumsey principle alone is not practical since a shape only defined by angles is necessarily an infinite shape, and any truncation of such a shape will introduce a characteristic size on the antenna which is not scaleable with wavelength. However, such a problem can be overcome if the antenna structure provides a way of reducing the current over the antenna when it travels away from the feeder. That is, if the antenna current is small enough at a certain distance from the feeding point, the remaining antenna structure does not support any current with a significant contribution on the overall performance and thus, it becomes effectively disconnected. In this case, the antenna structure can be truncated at such a point without significantly perturbing its behavior. This states the so called *truncation principle* [39],[45] and must be taken into account when designing frequency-independent antennas. Unfortunately, the biconical antenna does not hold such a principle. Since it is a particular case of loss-less transmission line, the current is kept constant with distance instead of decreasing when traveling away from the feeding point (the apex). Therefore, when the current reaches the truncated end of the antenna it becomes reflected in a similar way a wave is reflected from an open circuit in an ideal transmission line, resulting in a frequency dependent standing wave over the antenna structure. Fortunately, some other self-scaleable structures hold the truncation principle and effectively behave as frequency-independent antennas.

2.3.3.2 - Spiral and conical spiral antennas

The shape of a logarithmic spiral can be described in polar coordinates (ρ,φ,z) by the following equation

$$\rho(\varphi) = e^{a\varphi} \tag{2.60}$$

where a is an expansion factor which controls how fast the spiral is enlarged at each turn. Such a shape is invariant when scaled by an arbitrary scale factor b. That is, if the radius is scaled such that $\rho'=\rho \cdot b$, then by defining a rotation angle φ_0 as

$$\varphi_0 = \ln\left(\frac{b}{a}\right) \tag{2.61}$$

then the spiral equation can be written as

$$\rho'(\varphi) = b \cdot e^{a\varphi} = e^{a(\varphi+\varphi_0)} = \rho(\varphi+\varphi_0) \tag{2.62}$$

which means that the scaling transformation is equivalent to a rotation by an angle φ_0. Therefore, it can be concluded that an antenna which had an spiral shape would be frequency independent except for a rotation of the radiated fields, which is not a major drawback. Actually, spiral antennas [40],[41],[44] are usually designed with a balanced two-armed shape which is also made self-complementary to enhance its frequency independent behavior (see Fig. 2.24). Also, practical spiral antennas are obviously truncated, being the largest and the smallest size in the structure what determine the longest and shortest operating wavelength and thus the bandwidth of the antenna.

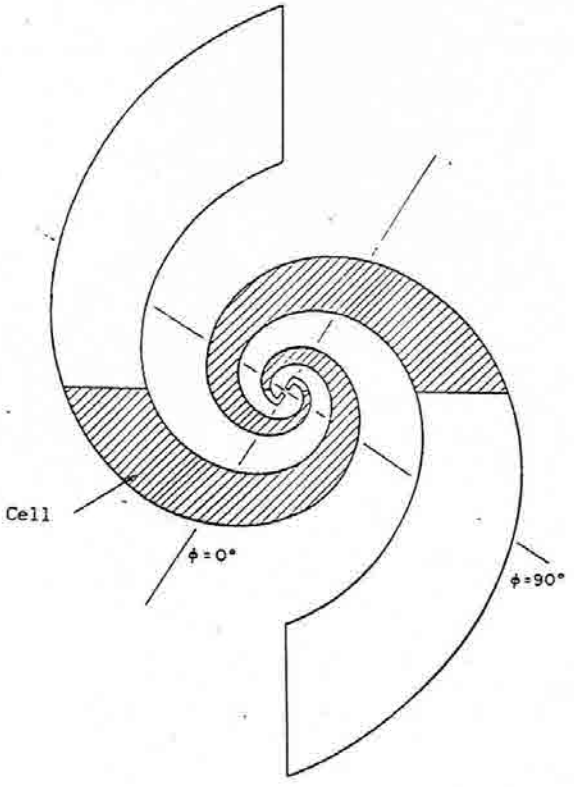

Fig. 2.24 The logarithmic spiral antenna.

Contrary to what happened to the conical structure, the spiral antenna holds the truncation principle, i.e., the current is decreased when traveling away from the feeding point (the center of the spiral) mainly due to the curvature of the structure [45]. It is said that an *active region* is formed on the antenna surface, which is the region where most of the current concentrates and mainly contributes to radiation. Such an active region is enlarged or reduced depending on the operating frequency but it keeps a similar shape and size with respect to wavelength, performing thus a wide-band behavior.

Conical spiral antennas are basically a combination of the conical and spiral shapes. They mainly consist on an spiral shape that wraps around a cone. It can be geometrically described by the equation

$$r = e^{a\phi \sin\theta_0} \tag{2.63}$$

which is also a shape only defined by angles (see Fig. 2.25). The main difference with respect to the planar spiral case is found on the radiation pattern. The antenna enhances radiation towards the nose of the cone and lowers radiation on the opposite direction. Such a behavior can be explained through a description of an electromagnetic wave traveling along the structure, inward toward the feeding apex [45].

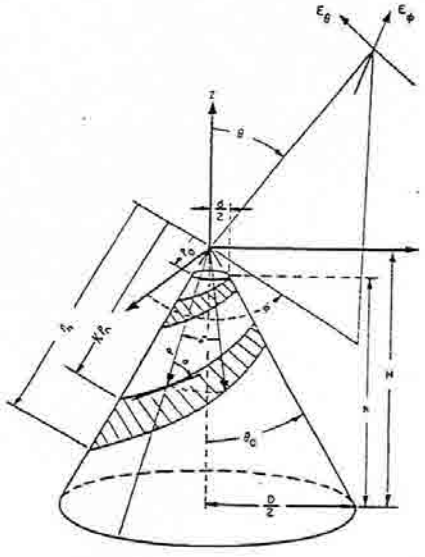

Fig. 2.25 The conical spiral antenna.

2.3.4 - Log-periodic antennas and antenna arrays

2.3.4.1 - Log-periodic planar structures

A structure is said to be log-periodic when it is composed by an infinite succession of cells which only differ by a constant scale factor τ. Figure 2.26 shows a general form of a log-periodic structure, where the lengths L_n and d_n hold the relation

$$L_n = \tau \cdot L_{n-1} \qquad d_n = \tau \cdot d_{n-1} \tag{2.64}$$

A log-periodic structure self-scales only when an integer power of the characteristic scale factor τ is applied in the scaling transformation. Strictly speaking thus, an antenna which

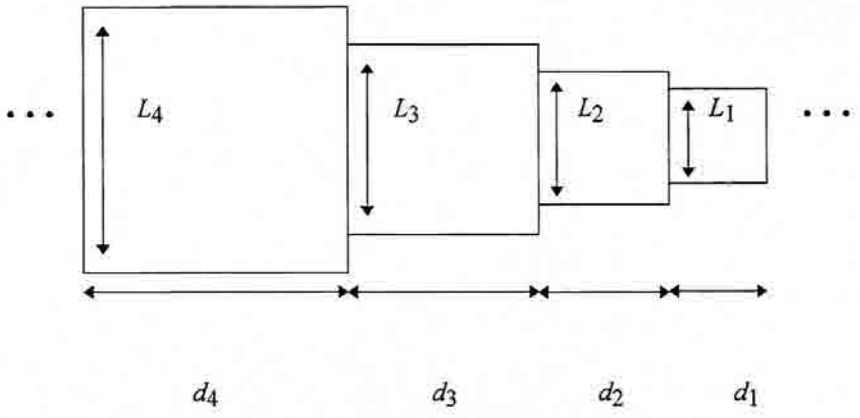

Fig. 2.26 General form of a log-periodic structure.

had a log-periodic shape would display a log-periodic behavior rather than a frequency independent behavior, i.e., the basic features (input impedance, radiation patterns) would be repeated at frequencies f_0 , f_1 , f_2,....f_n such that

$$f_n = f_0 \cdot \tau^n \tag{2.65}$$

which are a set of uniformly spaced frequencies in the logarithmic domain. If a log-periodic structure shows only small variations on its main features within a log-period, then the antenna becomes approximately frequency independent.

The form of the first successful log-periodic antennas is shown in Fig. 2.27. It basically consisted on two metallic circular sectors with some teeth log-periodically sized and distributed in the radial direction [39],[48],[45]. The antenna featured a 10:1 bandwidth with best results achieved with the self-complementary shape [45]. The radiated electromagnetic fields were linearly polarized in the direction of the teeth rather than in the radial direction, which suggests that the frequency-independent behavior depends on a highly selective resonance of the transverse component of the current [45].

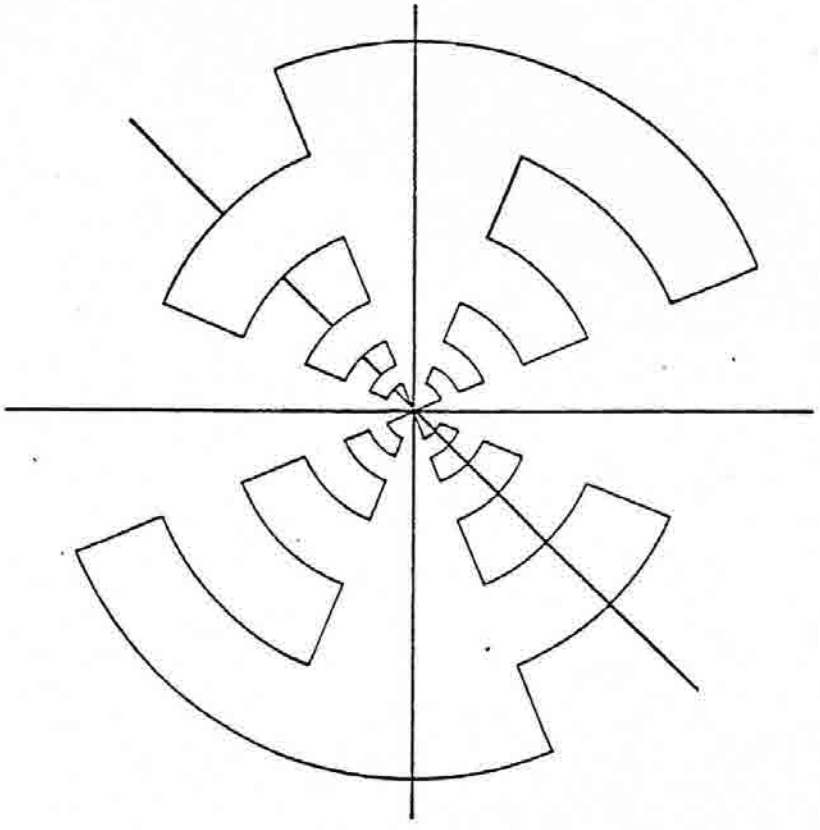

Fig. 2.27 The form of the first log-periodic antenna.

The pattern of the antenna presented a two-lobe shape which was not suitable for applications where directivity were a must. In order to enhance radiation in a particular direction, the two sides of the metallic shape were inclined and measured at several Ψ angles (see Fig. 2.28) [48],[45]. It resulted that the antenna displayed a directional pattern indeed, although the direction of radiation was just the opposite than the expected one [48]. The antenna again radiated toward the feeding point (the apex of the circular sector) which again suggested a wave traveling inward through the structure. Best results where achieved with inclination angles $60^{\circ} > \Psi > 30^{\circ}$.

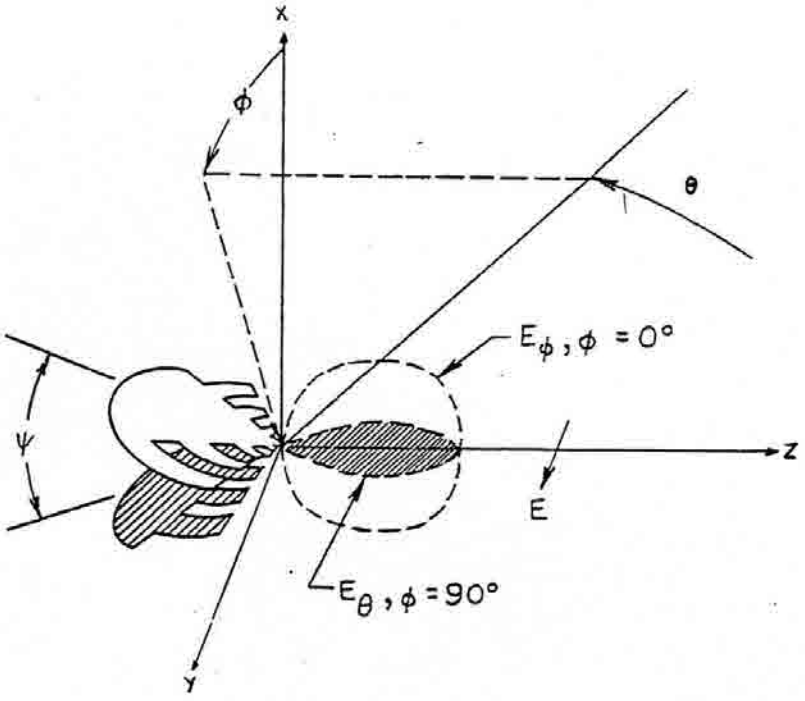

Fig. 2.28 The inclined version of the log-periodic antenna of Fig. 2.27

2.3.4.2 - Log-periodic arrays of dipoles

The invention of the log-periodic dipole array (LPDA) [39],[42],[45],[46],[48] was the next natural step after the development of the planar and inclined structures just described. Its shape can be seen as the limit case of the log-periodic sheet structure when the angle of the circular sectors is made equal to zero, the teeth are made straight and the inclination angle Ψ is taken to be Ψ=0° . Again, the array is characterized by an scale factor τ (see Fig. 2.29) which relates the lengths (l_n) and radius (a_n) of the dipoles and their distance from the apex (x_n) and relative spacing (d_n) as described in (2.64). That is,

$$\tau = \frac{l_n}{l_{n-1}} = \frac{a_n}{a_{n-1}} = \frac{x_n}{x_{n-1}} = \frac{d_n}{d_{n-1}} \tag{2.66}$$

Also, usually a normalized spacing between elements σ is defined as

$$\frac{d_n}{2l_n} = \sigma \tag{2.67}$$

which together with the scale factor τ, fully characterizes the LPDA.

The array is usually fed by a transmission line with the dipole terminals log-periodically distributed along the line. These connections are switched at each dipole with respect the previous one to provide an extra 180° progressive phase shift. Again, the antenna radiates in the backward direction toward the apex similarly to the inclined log-periodic and conical spiral antennas.

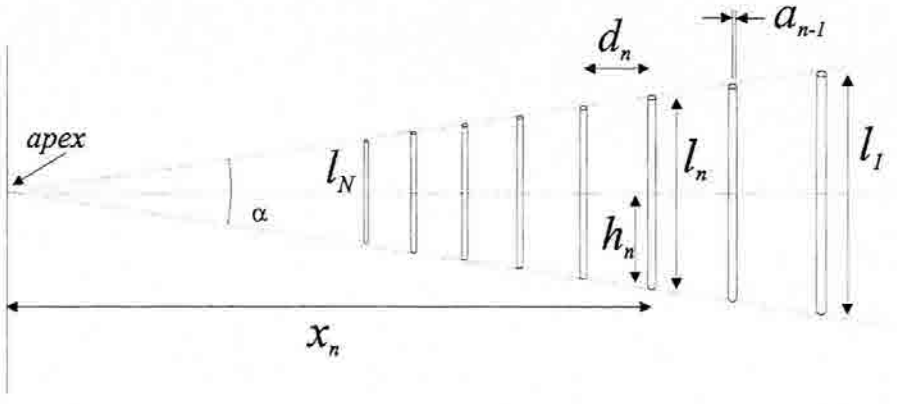

Fig. 2.29 The log-periodic dipole array.

2.3.4.2.1 Radiation mechanism and current distribution

The radiation mechanism of the array can be interpreted in the following way. The waves generated at the source start traveling along the transmission line at the apex of the array. If the first elements are short with respect to wavelength, they do not contribute significantly to radiation due to their size. Also, radiation is minimized because adjacent small dipoles are very close and their currents have opposite signs due to the phase reversal on the feeding network. Therefore, such dipoles mainly act as reactive elements and do not withdraw a significant amount of power from the traveling wave, which continues its way toward the larger dipoles. Where the traveling wave finds a set of dipoles which have a length comparable its wavelength, the electromagnetic power is removed from the line while being radiated into space. In such region within the array, the progressive phase and spacing between elements is such that radiation is enhanced backwards in a similar way as described in an endfire array (see Section 2.2.6). Since most of the power is removed in this region, the traveling wave becomes extinguished and the longer elements further away from the feeder become effectively disconnected. This region where most of the radiation takes place is called the active region, similarly to the active region of the spiral antenna. In practice, the infinite succession of dipoles is truncated as usual, and the bandwidth of the antenna becomes limited to the spectral band where the active region remains basically unaffected. Roughly speaking, the longest and the shortest dipoles determine the edges of

the pass-band of the antenna, which can be theoretically enlarged as much as desired by properly choosing their length.

The first to properly describe the behavior of the log-periodic dipole array was R.L. Carrel in [46]. He modeled the array as two N-port networks connected in parallel (see Fig. 2.30). The first network is the transmission line with its N connections log-periodically distributed, while the second one is the equivalent network formed by the N dipoles of the array. Both networks can be characterized by means of their admittance matrix $[Y_F]$ and impedance matrix $[Z_A]$ respectively.

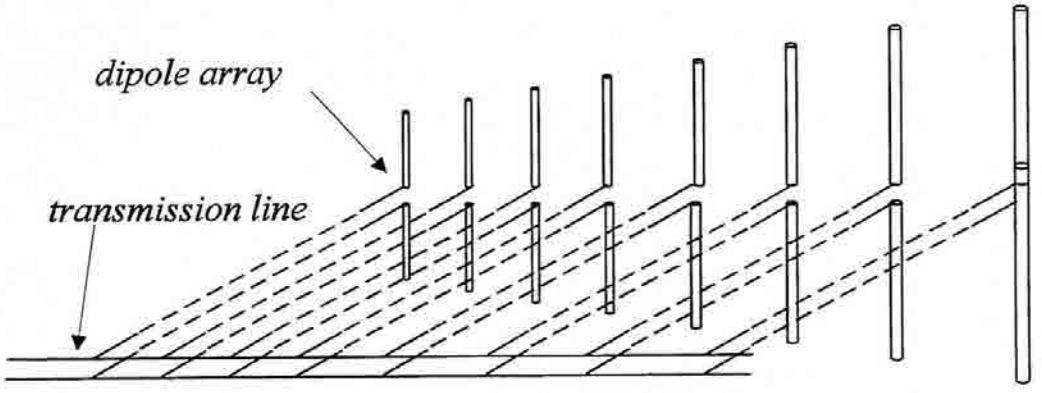

Fig. 2.30 The log-periodic array modeled as two N-port networks connected in parallel.

The transmission line admittance matrix $[Y_F]$ can be easily derived by means of basic microwave network theory and it is given by [46],[48],[54]

$$[Y_T]=\begin{bmatrix} (Y_T - jY_0\cot\beta d_1) & -jY_0\csc\beta d_1 & 0 & \cdots & 0 \\ -jY_0\csc\beta d_1 & -jY_0(\cot\beta d_1+\cot\beta d_2) & -jY_0\csc\beta d_2 & \cdots & 0 \\ 0 & -jY_0\csc\beta d_2 & -jY_0(\cot\beta d_2+\cot\beta d_3) & \cdots & 0 \\ \cdots & \cdots & \cdots & \cdots & \cdots \\ 0 & 0 & 0 & -jY_0\csc\beta d_{N-1} & -jY_0\cot\beta d_{N-1} \end{bmatrix} \tag{2.68}$$

where again d_n is the distance between adjacent dipoles, Y_T is the terminal load at the end of the line and Y_0 and β are its characteristic admittance and propagation constant respectively. The impedance matrix $[Z_A]$ of the dipole network can be computed by the method of moments [81]-[85] by identifying each element of the matrix either as a self-impedance (diagonal elements) or as a mutual impedance between each pair of dipoles (off-diagonal elements). Carrel used a Galerkin [48],[52],[53],[85] approach to the moments method

assuming a sinusoidal current distribution over the elements [46],[48]. Also, he computed the self-impedance terms from the mutual impedance relation assuming an equivalent separation d between elements of $d = \sqrt{2a}$, being a the radius of the corresponding dipole.

Once both matrices are determined, the amplitude of the sinusoidal current distribution can be computed as follows [46],[48]

$$[I_A] = [[U] + [Y_F][Z_A]]^{-1} \cdot [I] \tag{2.69}$$

where $[I_A]$ is an N-element vector containing the current amplitudes at each dipole, $[U]$ is the identity matrix, and $[I]$ is a an N-element vector containing the current amplitudes of the current sources connected at each terminal of the transmission line. Usually the array is only fed at the first terminal (at the apex) as discussed before, therefore, if a normalized current source is taken, $[I]$ becomes

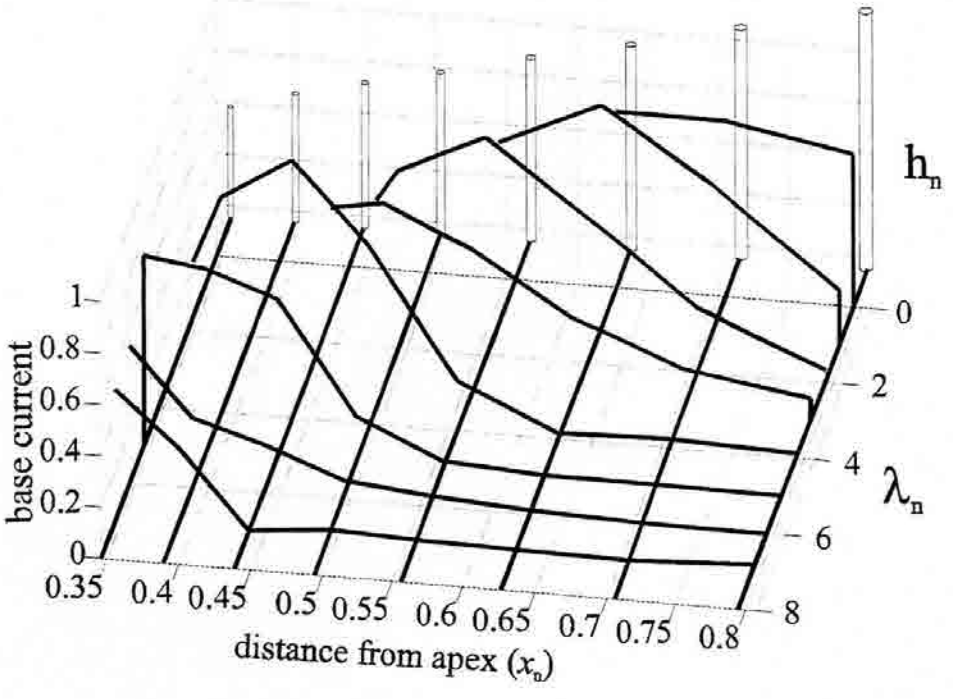

Fig. 2.31 Current distribution at several wavelengths over a log-periodic dipole array.

$$[I] = \begin{bmatrix} 1 \\ 0 \\ 0 \\ \vdots \\ 0 \end{bmatrix} \tag{2.70}$$

Figure 2.31 reproduces the analysis of Carrel [93], taking an equivalent radius a_e of [84]

$$a_e = a\left(1 - 0.40976a/H\right) \tag{2.71}$$

being a the dipole radius and H its length, for computing the self-impedance between dipoles, as suggested in [84]. The analyzed LPDA has eight elements (N=8), an scale factor τ=0.888, and a normalized spacing of σ=0.089 between elements. The array is fed through a Z_o=100Ω transmission line, terminated with a short-circuit at $\lambda_1/2$ of the longest dipole. The dipoles have a constant size (H) to radius (a) ratio of H/a=250.

The current distribution over the array (Fig. 2.31) is plotted for eight different wavelengths. In particular, the first resonant frequency for each dipole ($\lambda_n \approx 4 \cdot h_n = 2 \cdot l_n$) has been considered. It becomes clearly apparent that an active region is formed which only includes some elements of the array. Such an active region is shifted toward the longer elements when the wavelength is increased, and its shape is proportionally enlarged such that a constant size to wavelength ratio is kept. Such a behavior plays an essential role for the frequency-independent operation of the array.

2.3.4.2.2 Input Impedance and Radiation Patterns

The frequency independent behavior of an LPDA is demonstrated by means of the computed input reflection coefficient and radiation patterns. Figures 2.32 and 2.33 show both features at each computed wavelength. It can be seen that the antenna is well matched at the center frequencies, which means that almost all the power of the transmission line traveling wave is withdrawn and radiated by the dipoles; that is, the traveling wave is almost fully attenuated before reaching the short-circuit at the end of the line. Also, the patterns hold a notable degree of similarity among bands, with only some significant deviations from the common patterns at the end of the band.

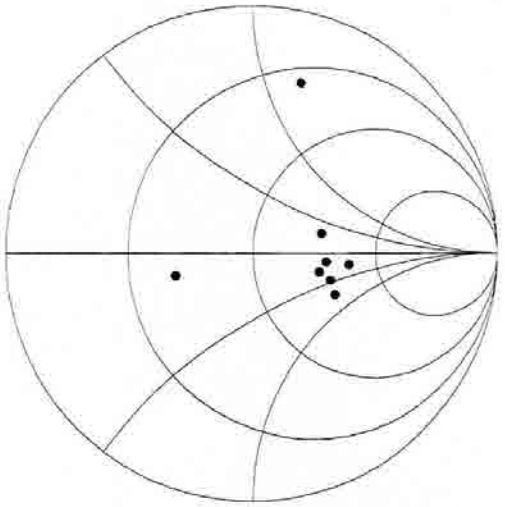

Fig. 2.32 Input reflection coefficient of the LPDA at the eight wavelengths.

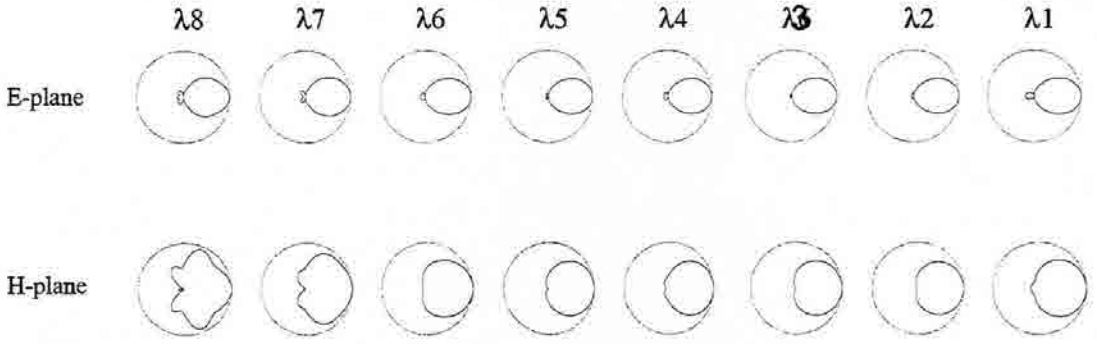

Fig. 2.33 E-plane (ϕ=0°) and H-Plane (Θ=90°) patterns of the LPDA (linear scale).

2.4 - Why Fractal Antennas ?

Once the main fractal characteristics have been introduced and the most common antenna features have been outlined, the reason for investigating fractal antennas should become apparent. Actually, such a reason is twofold. First of all, fractals have no characteristic size. They have an infinite range of scales within its structure, being composed of an infinite number of clusters which are equal to the whole shape but at a smaller scale. It has just been shown that characteristic sizes have to be avoided to design a frequency-independent antenna or at least, the antenna structure has to include many characteristic sizes to allow a multi-wavelength operation. Thus, it becomes presumable that fractal shapes, having a geometrical form which is self-similar and including multiple copies of themselves within their structure at several scales, are good candidates for becoming frequency independent (or at least multiwavelength) antennas. Section 2.4.1 deals with this particular issue from a theoretical point of view; the scaling properties of fractal shapes and their recursive generation algorithms are used to explore the potentiality of a multiwavelength operation.

On the other hand, fractals are highly convoluted, irregular shapes. As a matter of fact, they are the most irregular shapes described up to now. It is well known that sharp edges, corners and discontinuities enhance radiation from electric systems. Thus, it seems logical to expect that curves and surfaces which have discontinuities everywhere, that have a characteristic highly uneven shape (which is fundamentally different from that of classical Euclidean shapes) should become efficient radiators. This particular issue is introduced also in Section 2.4.2.

Finally, the idea of relating fractals and electromagnetics is not new. Several works [14]-[38] have already explored some interesting properties of fractal bodies when interacting with electromagnetic waves. The main results regarding this issue are overviewed in Section 2.4.3.

2.4.1 - Frequency Scaling Properties of Fractal Shapes

2.4.1.1 - The IFS as a convolution operator

An IFS process can be described in an alternative way by means of delta functions and convolution operators. First of all, we have to translate the set theory notation to the

function theory notation. That is, a subset of the plane A can be assigned to an index function $G(x,y)$ as follows

$$G(x,y)=\begin{cases}1 & \text{if } (x,y)\in A\\ 0 & \text{if } (x,y)\notin A\end{cases} \tag{2.72}$$

Then, a translation of A to a point (x_0,y_0) can be described as a convolution transformation in the following way

$$G(x-x_0,y-y_0)=G(x,y)*\delta(x-x_0,y-y_0) \tag{2.73}$$

A Hutchinson operator composed only by similarity transformations will be noted as

$$W[G(x,y)]=\sum_{i=1}^{N}G(r_i x,r_i y)*\delta(x-x_i,y-y_i) \tag{2.74}$$

where N is the number of similarity transformations of the operator and r_i is the reduction factor of each transformation. Once the Hutchinson operator has been defined as a linear combination of convolution operations, an IFS can be readily understood as a sequential procedure were the operator in (2.74) is applied iteratively to the function $G(x,y)$.

2.4.1.2 - GIFS and scaling properties of fractal attractors

Let's take an IFS where all the contractions reduce the input subset by the same scale factor r. Then one can separate the contraction and translation parts of (2.74) such that

$$W[G(x,y)]=G(rx,ry)*\sum_{i=1}^{N}\delta(x-x_i,y-y_i) \tag{2.75}$$

and write the Hutchinson operator in a more compact way,

$$W[G(x,y)]=G(rx,ry)*IF(x,y) \tag{2.76}$$

where the function $IF(x,y)$ has been properly defined as

$$IF(x,y) \equiv \sum_{i=1}^{N} \delta(x - x_i, y - y_i) \tag{2.77}$$

The function *IF(x,y)* would be the equivalent of the iterator in fractal terminology, and *G(x,y)* would be the equivalent of the generator. Now, the IFS can be described in a more compact way by a series of convolutions as

$$G_n(x,y) = G(r^n x, r^n y) * IF(r^{n-1}x, r^{n-1}y) * \cdots * IF(rx,ry) = G(r^n x, r^n y) \underset{m=0}{\overset{n-1}{\mathop{\Large *}}} IF(r^m x, r^m y) \tag{2.78}$$

where $*$ indicates the convolution operator. Now, if n is a large enough number, $G(r^n x, r^n y)$ tends to collapse into a single point if the original subset A is finite. Since the attractor of the IFS $G_\infty(x,y)$ is the same irrespective of the shape of the generator $G(x,y)$ due to the invariance property stated in (2.9), one can take a delta function as a generator (i.e. a point-like generator) and simply describe the IFS as

$$G_n(x,y) = \underset{m=0}{\overset{n-1}{\mathop{\Large *}}} IF(r^m x, r^m y) \tag{2.79}$$

Then, the attractor function will be described by

$$G_\infty(x,y) = \underset{m=0}{\overset{\infty}{\mathop{\Large *}}} IF(r^m x, r^m y) \tag{2.80}$$

which is not strictly speaking a self-scaleable function since

$$G_\infty(sx,sy) = \underset{m=0}{\overset{\infty}{\mathop{\Large *}}} IF(sr^m x, sr^m y) \neq G_\infty(x,y) \tag{2.81}$$

which is due to the finite size of the attractor. However, we can generalize the concept of IFS by defining a Generalized Iterated Function System (GIFS) in such a way that

$$G_n(x,y) = \sum_{m=-(n-1)}^{n-1} IF(r^m x, r^m y) \tag{2.82}$$

That is, not only smaller copies of the whole shape are added at each iteration, but also a larger copy which is the union of N objects obtained from the previous iteration is constructed. Then, the attractor will have an infinite size and will be defined by the equation

$$G_\infty(x,y) = \sum_{m=-\infty}^{\infty} IF(r^m x, r^m y) \tag{2.83}$$

This attractor of the newly defined GIFS is self-scaleable by its characteristic scale factor r and any power of it r^p, that is

$$G_\infty(r^p x, r^p y) = \sum_{m=-\infty}^{\infty} IF(r^{m+p} x, r^{m+p} y) = \{q=m+p\} = \sum_{q=-\infty}^{\infty} IF(r^q x, r^q y) = G_\infty(x,y) \tag{2.84}$$

Therefore, if one takes a set of log-periodically spaced wavelengths $\lambda_n = r^n \cdot \lambda_0$ and thinks of $G_\infty(x,y)$ as a current density distribution over a fractal antenna of shape A_∞, one would conclude from (2.84) that such an antenna would have a multiband behavior with the bands log-periodically spaced by a factor r. Of course, an infinite structure is assumed which is not feasible for a real antenna. However, such a limitation is also found in shapes only defined by angles as for instance the spiral antenna, but a frequency independent behavior is still supported by those antennas because they hold the truncation principle. Similarly, it can be stated that a practical (finite-size) fractal antenna will have a multiband operation behavior provided that the truncation principle is observed.

2.4.1.3 - IFS and Maxwell Equations

It was shown in Section 2.3.1 that the self-scaling principle for frequency-independent antennas can be directly derived from Maxwell equations. The scaling transformation described in (2.52) can be seen as a particular case of the affine linear transformations used to formally state the IFSs (Section 2.1.3.1). Therefore, it appears natural to look for a similar reasoning to explore the frequency dependence properties of

IFS fractal attractors. First of all, let us generalize a contraction transformation (plus translation) $w_i(x,y,z)$ to a three dimensional case, that is

$$\begin{pmatrix} x' \\ y' \\ z' \end{pmatrix} = \begin{pmatrix} r & 0 & 0 \\ 0 & r & 0 \\ 0 & 0 & r \end{pmatrix} \begin{pmatrix} x \\ y \\ z \end{pmatrix} + \begin{pmatrix} x_o \\ y_o \\ z_o \end{pmatrix} \tag{2.85}$$

Now, the curl operators in both domains applied to an arbitrary vector function $\vec{F}(x',y',z')$ are again related by

$$\nabla' \times \vec{F}(x',y',z') = \frac{1}{r} \cdot \nabla \times \vec{F}(x',y',z') \tag{2.86}$$

which shows that the curl operator is independent of a translation transformation. This leads to the Maxwell Equations in the transformed domain $\mathbf{R}^3$,

$$\begin{aligned} \nabla' \times \vec{E}(x',y',z') &= -j\left(\frac{\omega}{r}\right)\mu \vec{H}(x',y',z') \\ \nabla' \times \vec{H}(x',y',z') &= j\left(\frac{\omega}{r}\right)\varepsilon \vec{E}(x',y',z') \end{aligned} \tag{2.87}$$

As noted in (2.5) a Hutchinson operator *W[A]* can be written as a composition of N transformations like that in (2.85). Similarly, if *W[A]* is applied to a vector function $\vec{F}(x',y',z')$, a linear combination of N vector functions each one corresponding to a transformation in *W[A]* will be obtained, i.e.,

$$\vec{F}_T(x',y',z') \equiv W\left[\vec{F}(x,y,z)\right] = \sum_{i=1}^{N} \vec{F}_i(x',y',z') \tag{2.88}$$

where the subscript T indicates the transformed vector function and

$$\vec{F}_i(x',y',z') = w_i\left[\vec{F}(x,y,z)\right] \tag{2.89}$$

Now, since Maxwell Equations are linear, if each function of the linear combination in (2.88) is one of their particular solutions, then the transformed function $\vec{F}_T(x',y',z')$ will

be also a solution. In particular, if all the transformations are contractions by the same factor r, then the linear combination $\vec{F}_T(x',y',z')$ will be also a solution of the linear equations (2.87) in the R3'domain. On the other hand, the fractal attractor A_∞ of an IFS is invariant with respect to its Hutchinson operator as stated in (2.9). Thus, one can define an index vector function $\vec{G}_T(A_\infty)$ over the attractor, similarly to the scalar index function in (2.72), and such an index vector function will be also invariant and thus self-similar, i.e.,

$$\vec{G}_T(A_\infty) = W\left[\vec{G}_T(A_\infty)\right] \tag{2.90}$$

Such an index function could be interpreted as a uniform current density distribution over a fractal antenna of shape A_∞. The invariance property held by such current implies that the fields over the antenna would simultaneously attain Maxwell equations at frequencies f and f/r; therefore this automatically implies a log-periodic behavior since the same behavior would be held at any frequency f_n such that

$$f_n = \frac{f}{r^n} \qquad n \in \{0,1,2,\cdots\} \tag{2.91}$$

It is important to stress that a particular current distribution (the uniform distribution) has been assumed to conclude a log-periodic behavior of the antenna. However, any other distribution holding the invariance property (2.90) (i.e. any fractal current distribution) would also lead to a log-periodic behavior. What it is not still obvious is that a fractal metallic structure A_∞ has necessarily to support a fractal current distribution. The problem here is that the antenna structure is actually a boundary condition for the electric field, and Maxwell Equations do not explicitly deal with boundary conditions. However, a similar assumption has been always made when deriving the frequency independent behavior of self-scalable antennas, and such an assumption has been proven to be true in many cases (but not always [48]). Thus, it is not unreasonable to expect a similar behavior from fractal antennas and consequently, they should be considered as good candidates for multifrequency operation.

Finally, it should be noted that the self-similarity concept exploited in this section is quite different than the self-scaleability property of the previous one. In Section 2.4.1.2, the GIFSs algorithms were introduced to describe fractal self-scalable infinite structures. On the contrary, an infinite extent structure has not been assumed here and an invariance property with respect to a composition of contractions rather than a scaling transformation

has been used to derive the log-periodic behavior. Thus, self-scaling is not necessarily the only way of achieving a multifrequency response; self-similarity can provide it as well. The key point here is to take into account that the classical Hutchinson operator is always composed by contractions ($r<1$) which means that the log-periodic behavior will be held in only one direction, i.e. for the upper log-periods towards the larger frequencies, or for the lower log-periods towards the shorter wavelengths in the λ domain. Since the fractal structure has not an infinite extent, arbitrarily large wavelengths might not necessarily hold the same behavior as the smaller ones that better fit the antenna size.

2.4.2 - Small Fractal Antennas

Some fractal bodies have highly uneven shapes which might result specially suitable for radiating. The Koch curve, for instance, is an example of an specially irregular one. If we could made an antenna with its shape (for instance a dipole or a monopole) the antenna would display an infinite set of sudden bends and sharp corners. The velocity vector associated to the current flowing along the curve would experiment abrupt changes in direction in such bends, which means that the electrical charges would be highly accelerated. Actually, the curve has no defined derivative anywhere, which means that such a sudden acceleration would be held everywhere within the curve. Since the radiated electric field is proportional to the volumetric integral of the acceleration within the antenna (equation (2.32)), it is not clear that such an integral would be bounded when applied to a fractal contour; at least, one could reasonably expect an enhancement of radiation from such an antenna.

The topic is specially interesting when considering small antennas. As shown in Section 2.2.4, small antennas have a small radiation resistance, which decreases their radiation efficiency. Also, the ratio between stored (reactive) and radiated energy, i.e. the quality factor Q, is high, which also means a narrowband behavior. Thus, the idea of having an small but highly efficient and broadband antenna appears very attractive. Nevertheless, a theoretical fundamental limit has been established [58]-[64] which seems to discourage any improvement beyond such limit. However, it is arguable that such fundamental limit also applies for ideal fractal shapes since it was established with classical Euclidean geometry in mind, that holds common mathematical properties that are not always valid for fractal objects.

For instance, let us go back again to the Koch curve dipole example. The vector potential equation (2.25) for a linear current along an arbitrary one-dimensional wire reduces to

$$\vec{A}(\vec{r},\vec{k}) = \frac{\mu}{4\pi}\int_C \vec{I}(l')\frac{e^{-jkR}}{R}dl' \tag{2.92}$$

which is a line integral with respect to the arch length, where C is the curve path defining the wire antenna shape and $I(l)$ is the linear current flowing along it. If C is the Koch or a similar fractal curve, can it be assumed that the integral along a finite size but infinite length curve is going to be bounded ? . Actually, line integrals with respect to the arch length are defined for rectifiable (finite length) curves [110],[111] and the Koch curve is non-rectifiable. It could be argued that the exponential phasor term is also weighting the integral and might introduce some cancellations within the integral in case of a sign reversal due to proper phase retardation. In fact, the radiation mechanism is also understood as a process where, a system which is comparable in size to wavelength, introduces a sufficient phase retardation within the several parts of the system to allow an in-phase radiation contribution from them [55]. Therefore, an arbitrarily long (but not tall) Koch curve could fit any long wavelength which, contrasting to less convoluted non-fractal shapes, could provide the necessary phase retardation in an otherwise reduced space to constructively contribute to the radiation mechanism.

On the other hand, it has been shown in (2.26) that equation (2.92) can be reduced to a Fourier transform when evaluated at large distances from the source (i.e. in the far field). Such a Fourier integral can be also interpreted as a linear combination of an infinite set of plane waves, each one weighted by its own amplitude coefficient derived from the current distribution. Nevertheless, the Fourier transform has been proved to converge for piecewise continuous functions with a piecewise continuous derivative [112]. Again, the Koch curve is continuous but does not have a piecewise continuous derivative and consequently, it has not been proved that the implicit Fourier integral in (2.92) converges for this particular case.

Similarly, the derivation of the fundamental limit for an small antenna is based on the assumption that any field distribution around the antenna (in particular any current over the antenna) can be written as a linear combination of orthogonal spherical modes [58]-[59]. For an small antenna, the larger modes are said to be negligible because their argument kr (being r the largest distance from any part of the antenna to the origin) is very small and their real part becomes highly reduced. Consequently, only fundamental TE_{01} and TM_{01} modes are considered when deriving (2.45). Again, such an assumption should be reexamined when dealing with 'pathological', nowhere differentiable curves. The linear combination of modes does not need to converge, which might suggest that the fundamental

limit could not hold for a fractal curve and an arbitrarily short but electrically long antenna could be made from a fractal shape.

One could argue that an ideal fractal shape is unfeasible precisely due to its infinitely detailed structure and, in case of wired structures, due to the infinite length involved in their construction. Certainly, this would establish a technological practical limit; nevertheless a technological limit is a rather different concept than a fundamental limitation. In particular, the ideal fractal shape can be understood as a limit object obtained from a series of non ideal objects, which progressively approach the ideal fractal shape at each iteration of the recursive generating algorithm (the IFS described in 2.1.3). That is, the ideal fractal shape can be approached to an arbitrarily degree of similarity (i.e. with an arbitrarily small Hausdorff distance from the ideal fractal set [2]) with a non-ideal, non-infinite and maybe practical and technologically feasible shape. If the ideal fractal antenna had no limit on its Q factor, there should be a non-ideal and maybe technologically feasible shape which would go beyond the classical limit established for Euclidean shape antennas. In other words, its Q factor might be made arbitrarily small by choosing the suitable truncated non-ideal object to properly design the antenna shape.

As a matter of fact, Nathan Cohen has recently suggested in [100]-[103] that some fractal small dipoles and loops based on the Minkowski fractal shape can have a drive resistance larger than the expected one for their corresponding Euclidean countermates. His suggestions are based on numerical experiments carried out by means of the NEC version of the wire Method of Moments algorithm [71]. His results showed a shift on the resonant frequencies to larger wavelengths when increasing the length (not the size) of such loops and fractal dipoles. A further work in such a direction will be carried out in Chapter 6 through numerical and experimental results.

2.4.3 - Fractals and Electromagnetics

2.4.3.1 - Fractal Electrodynamics

The term fractal electrodynamics was first introduced by D.L. Jaggard about a decade ago [14]-[31] . Such a neologism was coined to describe a novel branch of science relating fractals and electromagnetics. The aim was to investigate whether the main properties of fractal bodies (such as the fractal dimension) could be derived from their interaction with electromagnetic waves. That is, wavelength could be taken as an electromagnetic yardstick to explore and measure the geometry of fractal bodies. Other several authors have significantly contributed to fractal electrodynamics [14]-[38], both

from fundamental [13],[32]-[34] and applied [35]-[38] points of view; here some of the main topics regarding this field will be outlined. Also, some of first works exploring the fractal design of radiating systems will be outlined [87]-[106],[16].

2.4.3.2 - Scattering from fractal targets

The main interactions between electromagnetic waves and fractal bodies currently investigated are scattering, reflection, transmission and diffraction. Scattering appears an especially interesting topic for several reasons. First of all, an important branch of geoscience research is carried out through modern satellite remote sensing techniques, which require proper models for scattering from rough surfaces and terrains. Fractional Brownian motion has been shown to be an accurate model for many natural landscapes and forms [1],[5] such as mountains, coastlines, clouds, river or lakes. Thus, it becomes apparent that a scattering model for fractal rough surfaces [21]-[23] should conveniently fit the requirements for such models. Similarly, the intrinsic fractal properties of natural forms could be used in pattern recognition and classification of synthetic aperture radar images [37]-[38]. Other interesting works relating remote sensing and fractals are those that model turbulence as a fractal phenomena and study the propagation of electromagnetic waves through such a chaotic media [17]-[19].

Second of all, scattering is also important when dealing with antennas. Actually, an antenna can be modeled as an scatterer, placed close to a source, that properly perturbs its fields to efficiently radiate in the desired directions. Again, Dwight L. Jaggard et al. described the scattering properties of a circular Cantor target [25],[26]. Their work revealed some interesting features of the radiated fields: the same kind of similarities found between different construction stages of the fractal target were also found in the scattered fields. That is, when the number of iterations was increased, the fractal structure appeared basically the same while displaying some finer details at smaller scales. Similarly, the radial pattern of the scattered fields showed basically the same envelope at each growing stage, but the degree of detail (i.e. the lobe structure) was increased also at each iteration. The most important conclusion that could be derived from that work is that electromagnetic waves acquire some fractal properties when interacting with fractal objects. Since fractal features are quite different from those of classical Euclidean shapes, one could expect novel applications in electromagnetic systems not already developed by means of classical geometry.

2.4.3.3 - Fractals and Optics

Linking with the Cantor target diffraction experiment, the diffraction of fractally serrated apertures has been also investigated [29],[30]. Diffraction was obtained at optical wavelengths from computer generated apertures. Again, some fractal properties were found to determine the features of diffracted fields, i.e., the Fourier transform of the fields over the illuminated aperture surface. Mainly, the angular dependence of the far field pattern was found to decrease when increasing the fractal dimension D ($1<D<2$) of the aperture's fractal perimeter. Such results are to find some application in optical pattern recognition schemes and image quality determination [29],[30].

Thin film layer structures are also of great interest in optical systems. The most selective compact optical filters are made by stacking several dielectric layers of different refraction indexes on both sides of a half-wavelength spacer. This way, an optical cavity is formed, (i.e. a Fabry Perot resonator) with both multilayer structures operating as reflecting mirrors at both ends of the cavity. Many of the microwave filter designing techniques can be also used in optics to develop optical filters of arbitrary characteristic spectral responses (i.e. Butterworth, Chebyschev, elliptic...). The main idea behind such designs is to modify the index of refraction of the layers the same way one modifies the characteristic impedance of the transmission lines in microwave band-pass cascading filter.

The filtering properties of a fractal distribution of layers based on the Cantor set (D.L. Jaggard and X. Sun [27],[28]) have been already investigated. Again, some interesting conclusions can be derived from that work. First of all, the similarity fractal properties found on the structure are also found in their reflection or transmission response. That is, an increase in the number of iterations of the fractal layer construction provided a finer degree of detail to the structure, which was also found in the reflection and transmission responses; such responses kept basically the same envelope at each growing stage although they displayed an increasing number of finer lobes. This result is comparable to that of the scattering from the circular Cantor target described previously. Therefore, it suggests that electromagnetic waves tend to become imprinted with fractal properties when interacting with fractal bodies, and that happens for remarkably different structures and kinds of interactions. Second of all, not only the similarity properties but also some of the main fractal characteristics such as fractal dimension can be retrieved from the response of the structure. This suggests that simple electromagnetic probing of fractal shapes could be used for scatter identification and classification. That might be a significant result if again, one takes into account that many natural forms are basically fractal and that remote sensing

techniques in geoscience relay on interactions of electromagnetic waves with such bodies to derive their features.

Finally a clever, efficient computational technique was also developed in the Cantor multilayer work. The developed algorithm allowed an iterative procedure to calculate the structure response, analogous to the iterative procedure for generating the structure itself. Basically, the algorithm required the same number N of computing stages as that of the fractal construction ones. If one takes into account that the number of layers grows exponentially as $3N$, the huge saving in computational time with respect to classical matrix cascading techniques, becomes especially interesting . If a similar result were generalized for a general self-similar fractal structures, it would become a major advance for analyzing otherwise rather complex and time-consuming fractal shapes.

2.4.3.4 - Early investigations in fractal arrays

Array theory is a rather broad discipline which far exceeds the scope of antenna theory. Arrays are used not only in antennas but also in several branches of mathematics, physics and engineering, namely, clustering in chemical aggregates, in crystalline lattice structures or even in galaxies spatial arrangements. Also, array theory is tightly linked to discrete signal processing as discussed previously [107],[108]. Some work has been carried out on fractal arrays although not always taking into account their specific properties when considering antenna systems. Here, some of them are briefly introduced.

One of the earliest works relating fractals and arrays came out in 1986 [16]. The aim was to investigate the side lobe ratio (SLR) of random fractal arrays compared to classical random ones. Such random classical arrays display a better tolerance to element position errors than their deterministic counterparts, although they present the inconvenient feature of large secondary lobes. The random fractal array element distribution was generated by taking a classical random array as the initiator, and a periodic deterministic one as the generator. The most important result from that work was the SLR improvement achieved with the fractal array.

C. Allain and M. Cloitre [106] analyzed in 1987 some of the spatial spectrum properties of a general family of self-similar arrays. They used an iterative convolution scheme, analogous to the one described in Section 2.4.1, to generate the array structure and derive its spatial spectrum (the power array factor in antenna terminology). Mainly, they derived their asymptotic behavior for infinitely large arrays and described a recursive

notation for the spatial spectrum. Also, they established some similarity relations among the several construction stages for the recursively generated spectrum.

A similar convolution scheme had been also previously described in 1986 [13] by A. Lakhtakia et al when investigating the fractal properties of the spatial spectrum of Sierpinski arrays. It was established in such work that the fractal dimension (actually the similarity dimension) could be again derived from the array factor. The authors suggested that this feature might be exploited in pattern recognition and identification as well. A year later, the same authors [105] considered an ideal array of dipoles arranged spatially over a Sierpinski gasket grid, and analyzed its time dependent radiation. The main conclusion was that the bifractal array (the term bifractal rather than two-dimensional was used to clearly distinguish the spatial arrangement over a plane from the fractional dimensional properties of the structure) displayed a bifractal spatial spectrum and a unifractal (i.e., one variable dependent) time response as well.

Another significant work regarding the fractal design of antenna arrays was carried out by C. Goutelard in 1992 [104]. He described some fractal distributions for an antenna array, mainly based on a generalization of the Cantor structure, and investigated the relationship between the fractal dimension and the SLR and main lobe width of the array. It was concluded in that work that the SLR was dependent upon the fractal dimension D as

$$SLR = M \cdot D \cdot 10\log(\delta) \tag{2.93}$$

being d the characteristic scale factor among the M stages of the Cantor array construction. Such a relation was derived from the ratio between the maximum field intensity in the main lobe direction, and the power-law envelope of the array factor in other directions. Although this approach appears basically correct for directions at large angular distances from the main lobe, it is not accurate for some specially lacunar arrays as it is shown in next chapter of this thesis. Actually, it will be shown that the SLR can dangerously become arbitrarily small if a maximum lacunarity criteria is not taken into account.

2.4.4 - Concluding remarks

Maybe the most important conclusion one can take from the current work in fractal electrodynamics is that fractal bodies do provide fractal properties to scattered, diffracted or reflected electromagnetic fields. Furthermore, some work in general theory of arrays have demonstrated that some of those properties appear especially attractive for antenna systems,

namely, high side-lobe ratios and pattern self-similarities. Given the previous work in frequency-independent antennas, it appears natural to extend such work to fractal shapes to exploit their multiscale nature. Fractal geometry can provide the proper framework for such a purpose, introducing a huge and rich new set of shapes to explore in the design of multifrequency antennas.

In this thesis, the multifrequency properties of fractal antenna systems will be explored. First of all, the performance of fractal arrays and array factors will be investigated. Although maybe sometimes too ideal or simple, array theory provides a compact analytical way of exploring the feasibility of multi-frequency operation. This approach will be used in Chapter 3 where arrays and array factors will be theoretically investigated. On the other hand, experimental research in array systems is rather expensive and has little motivation when lacking of a particular application behind. Furthermore, any practical multifrequency array system would require multifrequency elements, i.e. multifrequency antennas, to operate correctly. Thus, it appears clear that fractal antennas rather than arrays should be experimentally investigated. Such an approach will be held in Chapter 4 and subsequents. Also, we should not forget the interesting numerical results from N.Cohen regarding small fractal antennas, which gives an additional motivation for experimental research in fractal antennas.

3. Fractal Arrays and Array Factors

Array factors are highly dependent on the operating wavelength. As described in the previous chapter, an increase in the operating frequency is translated into an expansion of the visible range, which means that grating lobes will appear in the radiation pattern at high enough frequencies. This is a strong inconvenient because, although many different techniques allow us to synthesize array factors with a desired directivity or side-lobe ratio (SLR), the design is strongly frequency dependent. Most of these techniques assume a uniform spacing between elements, which becomes the main bandwidth limiting factor. In this chapter two novel techniques are introduced. In the first one a fractal distribution of the array elements is suggested, while in the second one the multiband features are achieved by fractally shapping the array factors.

3.1 - Fractal Arrays

In this section we will analyze a fractal, non-uniform spacing for the element distribution of an antenna array. An ideal current feeding system to each array element is assumed as usual in array theory. The structure is based on the Cantor set, one of the simplest fractal structures. Although other fractal structures could be used for designing arrays, this particular one has been chosen for the analysis because it provides a simple, well known fractal set of discrete points that can describe a linear array.

3.1.1 - Multiband properties of the ideal Cantor array

One of the main features of the Cantor set (also named Cantor dust) is its self-similar shape. It contains an infinite number of sub-structures or sub-clusters at different scales, which are all identical to the whole set. Thus, if one built an array by placing the

elements at the points of the Cantor set (Fig.3.1), one could expect these smaller sub-structures to radiate at shorter wavelengths in the same way the whole structure radiates at longer wavelengths.

A bandlimited [14] version of the fractal structure can be constructed iterating several convolutions which leads to an analytical expression for the array factor, providing a compact way of deriving the properties of the resulting array. Such a procedure is a particular case of the IFS and GIFS processes described in Section 2.4.1.2. The procedure starts by taking two delta functions, spaced a distance d in the z axis, as the basic structure (usually known as generator in fractal terminology). Then, the generator is scaled by a factor of three to obtain another structure composed by two delta functions spaced $d/3$. If we apply the convolution operator to these two structures, we will have a set of four delta functions located at the points of a Cantor Set constructed with only two iterations. It can be seen that this convolution could be extended to an infinite number of terms to obtain the complete set. That is, if we call $f(z)$ the two delta function generator, the whole Cantor set $c(z)$ can be written as

$$c(z) = \ldots f(z) * f(3 \cdot z) * f(9 \cdot z) \ldots * f(3^n \cdot z) \ldots \tag{3.1}$$

It should be noticed that this procedure can be carried out with a different generator (with an arbitrary number of delta functions) and with a different scaling factor δ instead of δ=3. In this case, we could define a generalized Cantor structure (hereafter Cantor array) as follows

$$c(z) = \overset{\infty}{\underset{n=-\infty}{X}} \left\{ f(z \cdot \delta^n) \right\} \tag{3.2}$$

where X symbolizes the convolution operator. Here, the IFS generating algorithm has been generalized to a GIFS algorithm (see Section 2.4.1.2) to allow growth to both smaller and larger scales, which is accomplish by letting both positive and negative powers of the scaling factor δ. Now, the array factor corresponding to $c(z)$ can be written in terms of the Fourier transform of the generator $F(\Psi)$ as

$$C(\Psi) = \ldots \delta^2 \cdot F\left(\delta^2 \Psi\right) \cdot \delta \cdot F(\delta \Psi) \cdot F(\Psi) \cdot \frac{F(\Psi/\delta)}{\delta} \cdot \frac{F\left(\Psi/\delta^2\right)}{\delta^2} \ldots = \prod_{n=-\infty}^{\infty} F\left(\Psi/\delta^n\right) \tag{3.3}$$

where Ψ is defined as usual in array theory as $\Psi=kd\cdot\cos\theta+\beta$, being d the spacing of the generator array, θ the angle between the direction of propagation and the axis of the array, and β the progressive phase-shift of the generator array. Now, a frequency change by a factor of r implies a proportional scaling of both the Ψ parameter and the array factor $C(\Psi)$. That is, $C(\Psi)$ becomes

$$C(r\Psi)=\ldots F(r\delta\Psi)\cdot F(r\Psi)\cdot F(r\Psi/\delta)\cdot F(r\Psi/\delta^2)\ldots\cdot F(r\Psi/\delta^n)=\prod_{n=-\infty}^{\infty}F(r\Psi/\delta^n) \tag{3.4}$$

If one takes the frequency shift r to be δ^p then the array factor becomes

$$C(\delta^p\Psi)=\prod_{n=-\infty}^{\infty}F(\delta^p\Psi/\delta^n)=\prod_{n=-\infty}^{\infty}F(\Psi/\delta^{n-p})=\prod_{m=-\infty}^{\infty}F(\Psi/\delta^m)=C(\Psi) \tag{3.5}$$

which implies that the array factor generated by the Cantor structure is a log-periodic (LP) function with a log-period δ. That is, in logarithmic scale

$$C_{\log}(\log(\Psi))=C_{\log}(\log(\Psi)+p\cdot\log(\delta)) \tag{3.6}$$

being p an integer. The main conclusion derived from (3.6) is that the infinite Cantor array would have the same array factor at an infinite number of bands, which is a remarkable property not shared by common uniformly spaced arrays. Before going any further in our conclusions, we should point out some important facts. Firstly, that this would be a

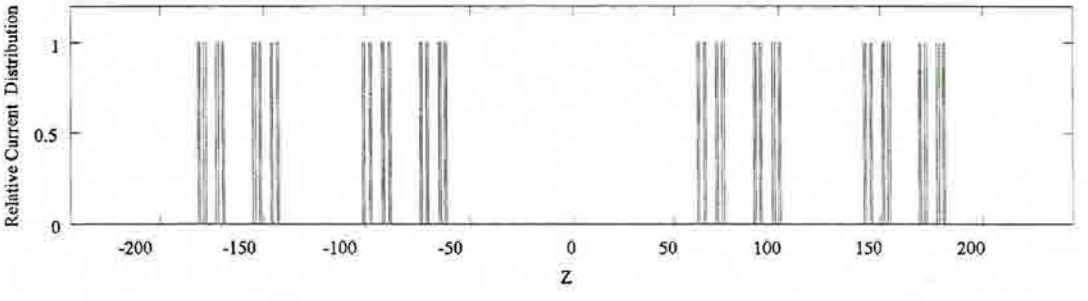

Fig. 3.1. Cantor Array based on the classical Cantor Set. The array has 128 elements and it is constructed from a two element generator and a log-period δ=3.

multiband system, not a frequency-independent system, since Equation (3.6) only implies that the behavior will be the same at several bands spaced by a factor of δ, but it does not imply a uniform behavior within each band. Secondly, this property would apply only to the infinite array. Any implementation of such an array would necessarily limit its number of elements, which will affect the multifrequency behavior of the system. Thirdly, the log-periodicity applies only to the array factor, not to the antenna pattern.

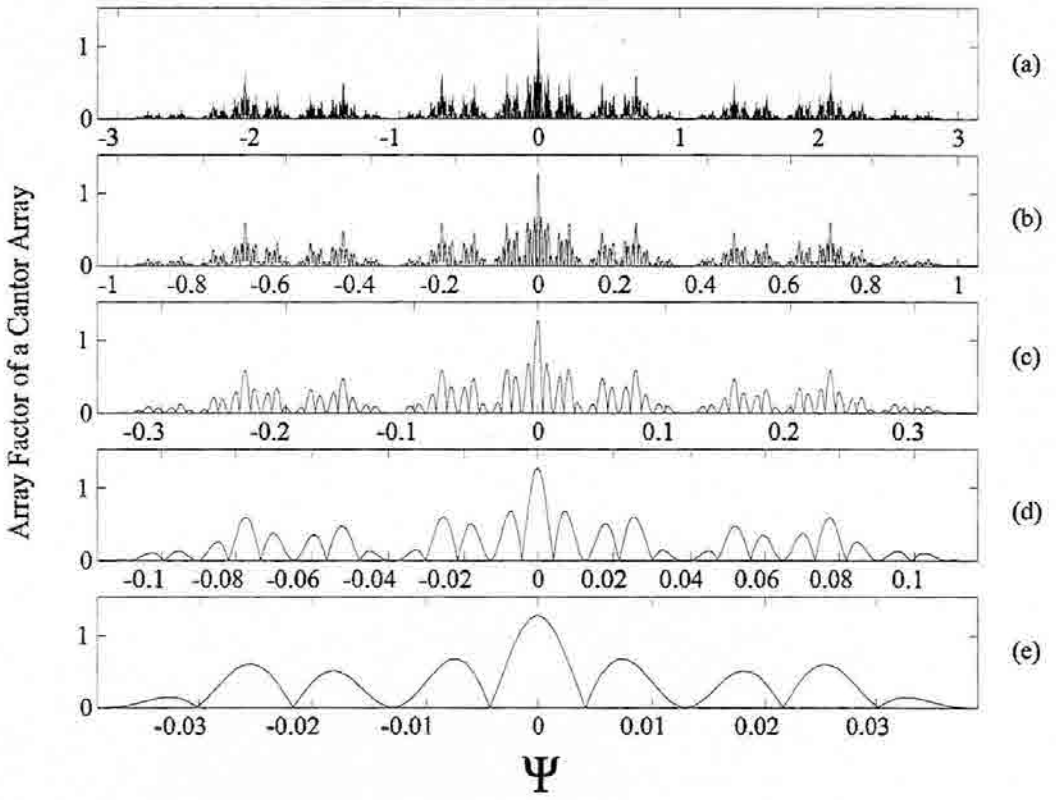

Fig. 3.2 Array factor for the Cantor array on Fig.3.1. The array factor is plotted for five operating wavelengths: $\lambda_0=d/2$ (a); $\lambda_1=3\lambda_0$ (b); $\lambda_1=9\lambda_0$ (c); $\lambda_1=27\lambda_0$ (d); $\lambda_1=81\lambda_0$ (e). It can be noticed the similar lobe structure of the patterns at those frequencies.

In order to analyze the truncation effect, the array factor for a Cantor array generated with only 7 iterations (2^7=128 elements) has been computed for several wavelengths. The array is shown in Fig. 3.1 and the corresponding array factors Fig. 3.2. The patterns on Fig. 3.2 present some interesting features. They look similar in the sense that they show an alike distribution of the main secondary lobes, and that the SLR is kept almost constant through the whole set of bands. Nevertheless, the patterns also show some undesirable characteristics. First of all, the similarity properties are held only for a finite number of bands due to truncation. Second, the patterns present very high secondary lobes.

And third, the width of the main lobe increases as the frequency is reduced, increasing at each band shift by a factor equal to the log-period of the array (in this particular Cantor structure by a factor δ=3), as a consequence of the corresponding reduction of the visible range.

3.1.2 - Uniform generators and SLR protection

The problem of the high secondary lobes of the pattern is related to the lacunarity of the fractal array (Fig. 3.3 and Fig. 3.4) A fractal structure is said to present high lacunarity when it has large gaps between the different fractal substructures [1],[8]. In terms of the array of Fig. 3.1 the gaps between sub-arrays are too large compared to the smallest operating wavelength, which has been chosen to match twice the distance between two elements of the smallest sub-structure. To illustrate this fact, the array factors in Fig. 3.4 correspond to another particular case of the generalized Cantor set. It is based on a

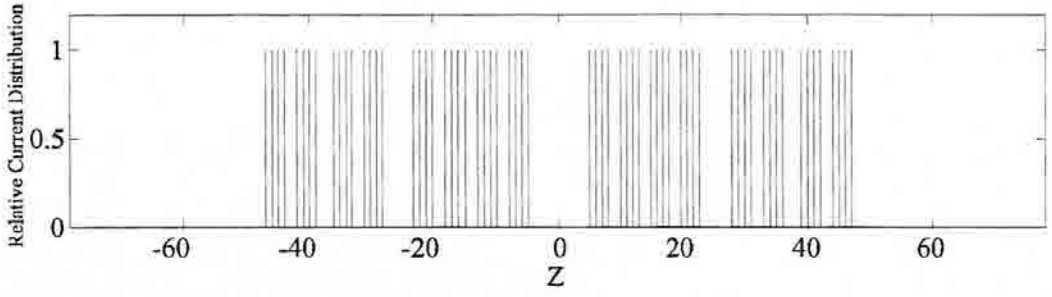

Fig. 3.3 Cantor Array for δ=2.2, N=2, M=7. Notice the lower lacunarity with respect the classical Cantor array (δ=3, N=2).

two-element generator as the array of Fig. 3.1, but has a log-period of δ=2.2 instead of δ=3. The array generated this way is shown in Fig. 3.3, where one notices a gap reduction between sub-structures, i.e., a lower lacunarity. The corresponding patterns show a smoother shape and lower side-lobes than in the previous example, yet keeping the same interesting similarity properties at frequencies spaced 2.2^n.

In order to analyze the effect of the lacunarity and the log-period in the pattern conformation, we are going to particularize our analysis to the simplest case, i.e., Cantor arrays constructed from an N-element uniform linear array generator. Such arrays are constructed by means of a generator $f(z)$ such as

$$f(z)=\sum_{n=1}^{N}\delta(z-nd+\frac{N-1}{2}d) \tag{3.7}$$

Therefore, according to Equation (3.3), the normalized array factor for a Cantor array generated after M iterations with the above generator can be written as

$$C(\Psi)=\prod_{n=0}^{M-1}\frac{\sin\left(N\frac{\Psi}{2}\delta^n\right)}{N\sin\left(\frac{\Psi}{2}\delta^n\right)} \tag{3.8}$$

where N is the number of elements of the generator in (3.7) and δ is the log-period. The ratio δ/N is strongly related to the lacunarity of the fractal structure: the larger the ratio, the larger the gaps among subarrays. Also, this ratio can be related to the fractal dimension D, which can be calculated as [1],[2]

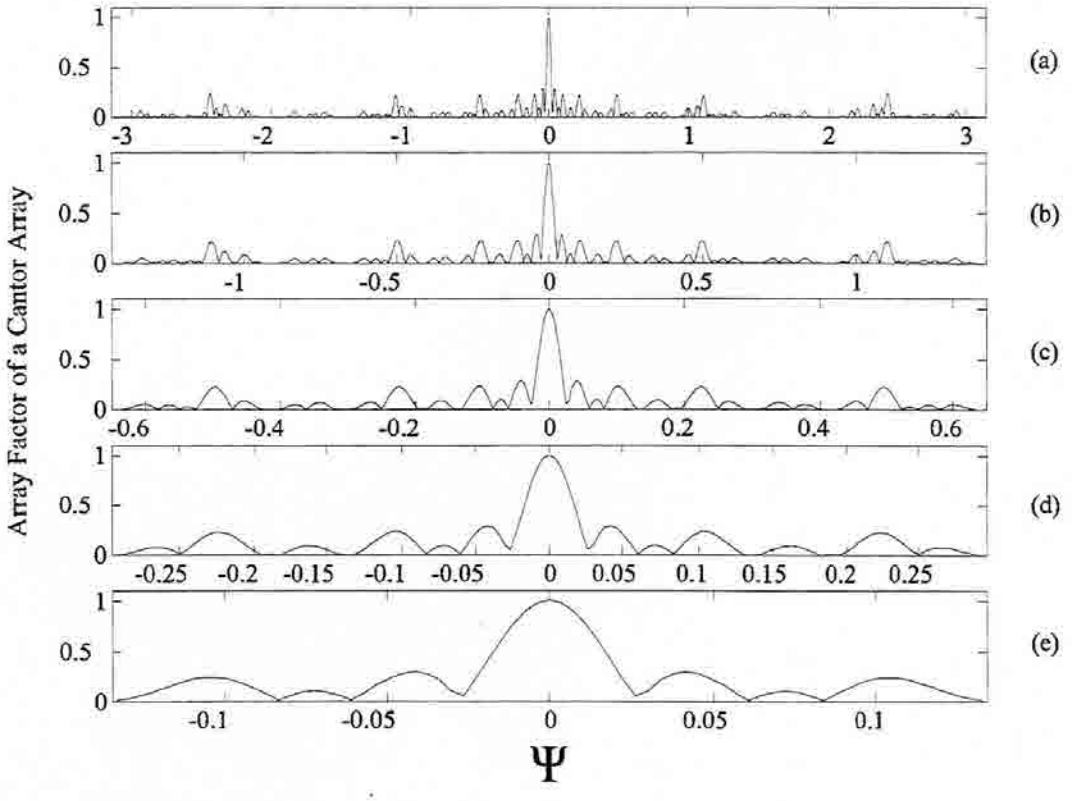

Fig. 3.4 Array factor for the Cantor array on Fig.3.3. The array factor is plotted for five operating wavelengths: $\lambda_0=d/2$ (a); $\lambda_1=2.2\lambda_0$ (b); $\lambda_2=2.2^2\lambda_0$ (c); $\lambda_3=2.2^3\lambda_0$ (d); $\lambda_4=2.2^4\lambda_0$ (e). It can be noticed the similar lobe structure of the patterns at those frequencies, and the larger SLR with respect to the classical array due to a lower lacunarity

$$D = \frac{\log(N)}{\log(\delta)} \tag{3.9}$$

For instance, Equation (3.9) gives us a fractal dimension of D=0.63 and D=0.79 for the cases presented in figures 3.1 through 3.4. In general, these two examples suggest that a low lacunarity (small δ/N) and large fractal dimension ($D\rightarrow 1$) are required for enlarging the SLR.

3.1.2.1 - The classical uniformly spaced uniform amplitude array

The classical uniform amplitude array with a uniform element spacing can be seen as a particular case of the Cantor array and is described here for the sake of completeness. The case under study is now δ=N. Again, by taking the general expression in (3.8), we get

$$C(\Psi) = \frac{\sin\left(N\frac{\Psi}{2}\right)}{N\sin\left(\frac{\Psi}{2}\right)}\cdot\frac{\sin\left(N^2\frac{\Psi}{2}\right)}{N\sin\left(N\frac{\Psi}{2}\right)}\cdots\frac{\sin\left(N^M\frac{\Psi}{2}\right)}{N\sin\left(N^{M-1}\frac{\Psi}{2}\right)} = \frac{\sin\left(N^M\frac{\Psi}{2}\right)}{N^M\sin\left(\frac{\Psi}{2}\right)} \tag{3.10}$$

which is the array factor for a uniform distribution of N^M elements. The construction of this uniform array as a convolution of M uniform distributions at different scales can be seen again as a particular case of the GIFS process described previously. The scaling parameter is such that at each iteration, the separation between subarrays is equal to the spacing between two elements of those subarrays. In this particular case, the array is no longer fractal and loses some of their related properties, such as the self-similarity property. The uniform amplitude, uniformly spaced array has a SLR around 13dB, regardless the value of the parameters N and M.

3.1.2.2 - Optimum Lacunarity for SLR protection

We are now ready to analyze the relationship between the lacunarity of the fractal structure and the SLR of the patterns for a more general case. As we pointed out in (3.3), the Cantor array factors can be understood as a product of M sub-patterns at different scales. Each time we convolve the structure with the next wider sub-array, the pattern is multiplied with a compressed version of the generator's array factor. If δ is made large enough, the compression will be such that many grating lobes of the larger sub-arrays will appear within the visible range. The limit case, as shown in Fig. 3.5, is given by the condition δ=N, i.e.,

the uniformly spaced array just discussed. For this particular case the main grating lobe of a sub-array is placed (in the Ψ domain) at the first null of the previous sub-array in the iteration and thus becomes canceled. As a matter of fact, Equation (3.10) demonstrates that the product of these two sinc functions results in a narrower sinc function as well and thus the SLR is kept around 13 dB.

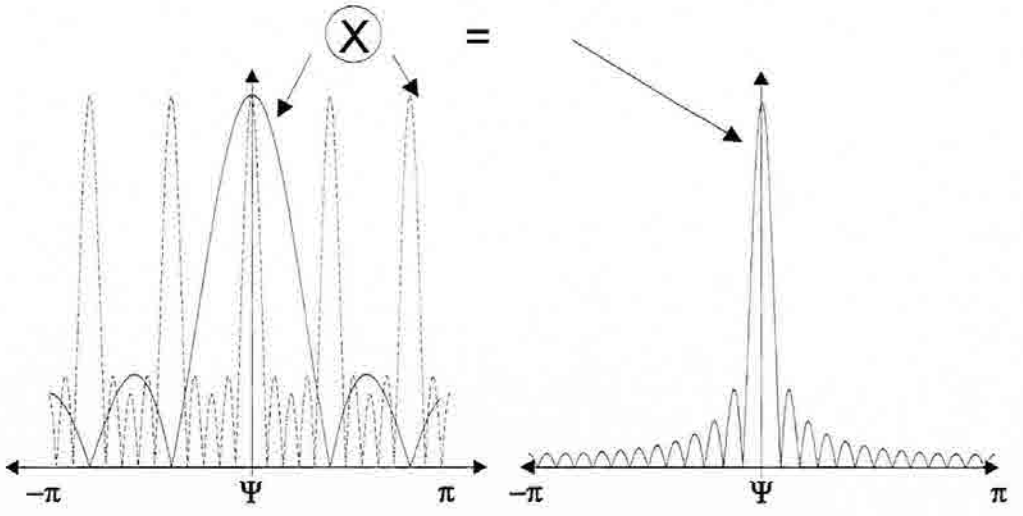

Fig. 3.5 When δ=N, the Cantor array reduces to the uniformly spaced and weighted array. The main grating lobe of the subarray falls at the first null of the larger array. The result is again the typical sinc pattern of the uniform amplitude array.

The SLR degradation becomes specially important when the δ/N ratio is made larger than unity. The grating lobes appear within the main lobe of the previous array factor of the iteration and, if such lobes fall near the maximum of this previous array factor, they will be greatly enhanced. Figure 3.6 illustrates this fact. The log-period was chosen to be 12 while the number of generating elements was 5 (i.e. δ/N=12/5=2.4). The array presents a highly lacunar distribution and consequently large secondary lobes. Such a phenomena was not taken into account in [104] where only the power-law envelope of the pattern was considered (which is valid for the lobes far away from the main lobe).

We can establish an upper bound to safely design fractal Cantor arrays without increasing the side-lobe level above the one of uniform generator. By choosing a ratio $\delta/N\approx$1.2 (Fig 3.7) we place the first grating lobe at a Ψ point within the main lobe such that, when weighted by the amplitude of this main lobe, it becomes reduced to the level of the first secondary lobe (i.e., around 13 dB). Therefore, we could state that Cantor arrays should be designed with a lacunarity ratio such that

$$\frac{\delta}{N} < 1.2 \tag{3.11}$$

The array in Fig. 3.3 and its corresponding array factors in Fig. 3.4 are a particular case of an array designed by following such a criteria. We should notice that the safe lacunarity ratio just established only strictly guarantees SLR>13dB for large values of N (for low values the digital sinc function deviates from the classical sinc function and has a

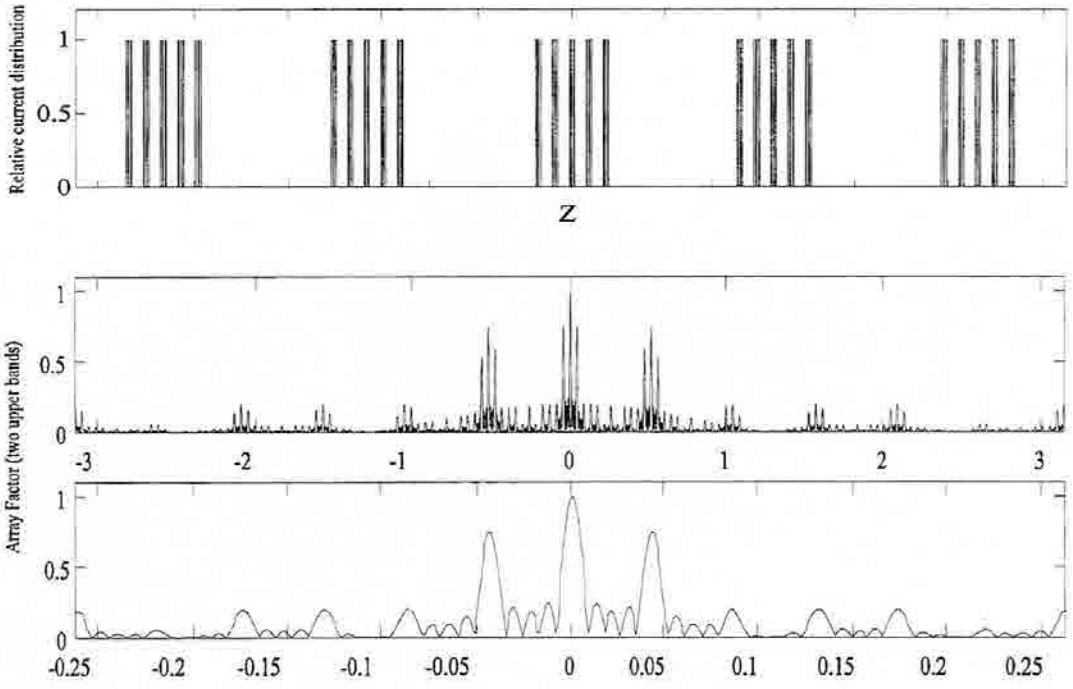

Fig. 3.6 Highly lacunar array with large secondary lobes (δ=12, N=5, M=3). The array factor is plotted at the upper two bands to show its similarity properties.

SLR smaller than the asymptotic 13.46 dB). In fact the limit lacunarity ratio which prevents a SLR deterioration depends on the number of elements of the generator as shown in *Table 3.1* . However, for N>2 such a dependence becomes less significant and Equation (3.11) can be taken as a rule of thumb when designing Cantor arrays.

N	2	3	4	5	6	7	8	9	10
δ/N	1.112	1.194	1.207	1.214	1.217	1.219	1.221	1.222	1.222

Table 3.1.- Lacunarity ratio for SLR=13dB as a function of the number of elements in the generator (N).

An interesting feature of Cantor arrays are their narrow main lobe with respect to classical uniform arrays of the same number of elements. The main lobe width (full width at half maximum) and directivity of the generalized Cantor array are plotted in Fig. 3.8 for the broadside case. The same parameters for a classical uniform array (with the same overall number of elements) are plotted for comparison as well. The Cantor arrays have been designed by following the lacunarity ratio criteria such that their SLR is kept at 13.46 dB (the asymptotic SLR of the uniform array). Both features are plotted as a function of the number of elements in the generator (N) for several iteration numbers (M), such that the number of elements within the array are the same for both kinds of arrays (i.e., N^M).

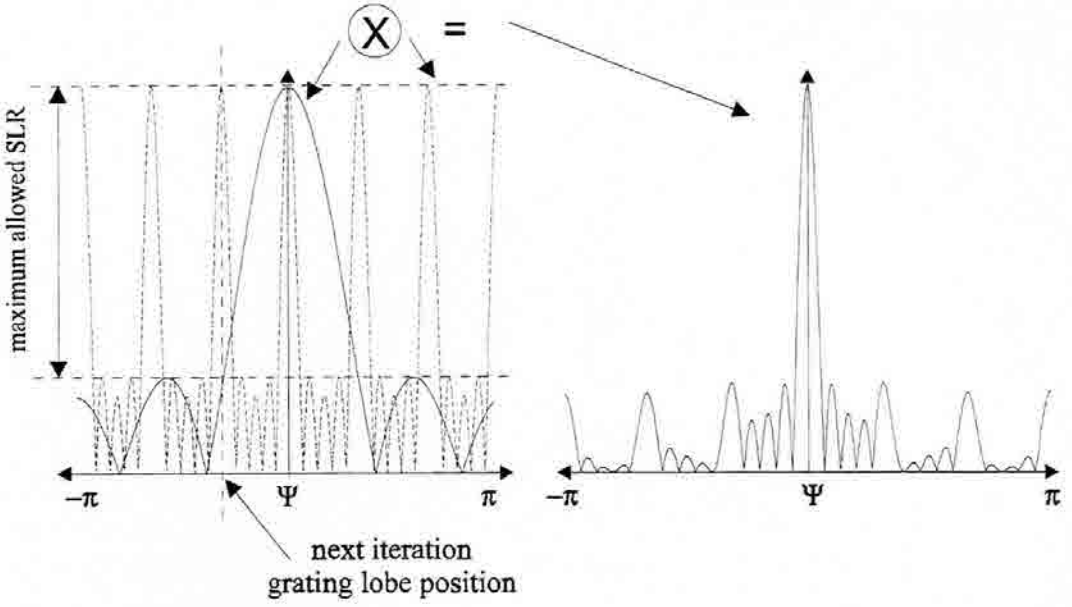

Fig. 3.7 Safe lacunarity for SLR control. The first grating lobe falls where the main lobe has the same level as the first secondary lobe.

Even though the directivity is basically the same for both kind of arrays, the main-lobe of the Cantor arrays is significantly narrower. This is mainly due to the larger extension of the Cantor arrays with respect to classical uniform arrays. Although both arrays have exactly the same number of elements and a uniform current distribution, the larger log-period of Cantor arrays makes their whole shape longer than uniform arrays. On the other hand, Cantor arrays present some larger gaps within its structure which enhances the number of significant side-lobes; however, such lobes never exceed the level of those of the classical uniform array due to the safe lacunarity ratio criteria that has been applied. Such an increase in the number of significant side-lobes explains also why the directivity is not

improved with respect the uniform array: the narrowing of the main-lobe is compensated by the power density spreading in the side-lobe directions.

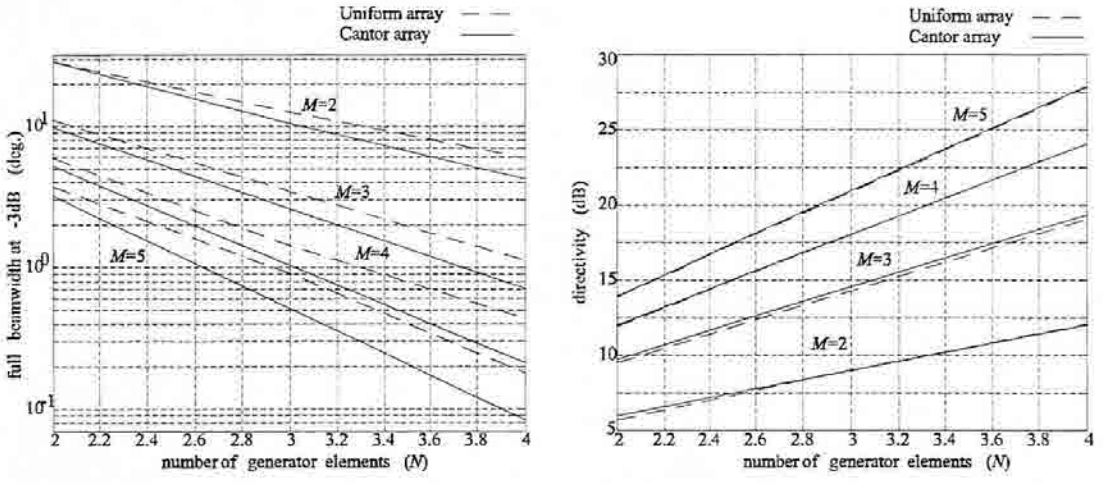

Fig. 3.8 Main beam width (half width at half maximum) and directivity (right) for the generalized Cantor array compared to a classical uniform array. Both arrays are broadside and have a minimum spacing of $d=\lambda/2$ between the closest elements.

3.1.3 - Non uniform generators for a further SLR protection

The development in Section 3.1.2 was based on a uniform amplitude generator. Although this might be the optimal choice for directivity considerations, other shapes could be essayed to improve the SLR. For instance, instead of convolving M uniform distributions of different scales, M triangular distributions could be used. Since a triangular distribution $t(z)$ can be written as the convolution of two identical uniform distributions $u(z)$, a triangular Cantor array $tc(z)$ could be generated as follows

$$tc(z)=\sum_{n=0}^{M-1} t(z\cdot\delta^n)=\sum_{n=0}^{M-1}\left\{u(z\cdot\delta^n)*u(z\cdot\delta^n)\right\} \tag{3.12}$$

The corresponding array factor $TC(\Psi)$ can be written now as

$$TC(\Psi)=\prod_{n=0}^{M} T(\Psi/\delta^n)=\prod_{n=0}^{M}\left(U(\Psi/\delta^n)\right)^2=\left(\prod_{n=0}^{M} U(\Psi/\delta^n)\right)^2 \tag{3.13}$$

which implies that the SLR has been doubled with respect to the uniform Cantor set $C(\Psi)$. Equation (3.13) also implies that the triangular Cantor array is equivalent to the convolution

of two equal uniform Cantor Arrays, an alternative procedure for its construction algorithm. The shape and the pattern of this triangular Cantor array are shown in Fig. 3.9.

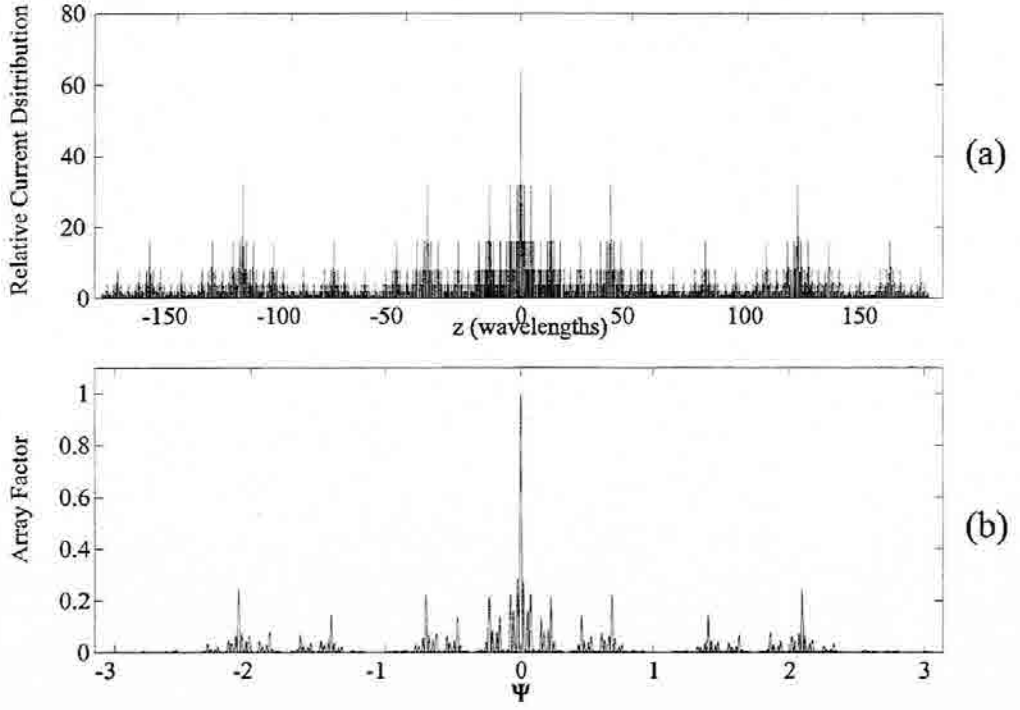

Fig. 3.9 Triangular Cantor (M=6, δ=3, N=2) array (a) and its array factor(b). The SLR has been doubled with respect the uniform case (Fig. 3.2).

Although this construction scheme may be useful for SLR improvement, it introduces the inconvenience of non-uniform amplitude distribution of the elements. This problem could be solved by substituting the triangular generator by a Cantor generator that would approach the same basic pattern as it will be shown in Section 3.1.5.

3.1.4 - The Cantor Fishbone Antenna

A practical design for a Cantor array is explored in this section. A transmission line is chosen to feed an array of short dipoles spatially arranged in a Cantor array configuration. The transmission line feeding scheme is suggested because it provides a simpler mechanism than feeding each element individually. Also, the traveling wave along the transmission line

provides a progressive phase shift to the array elements that might enforce endfire radiation. Actually, such an scheme is the same as that of the classical fishbone antenna [51]. The fishbone antenna is composed by an array of identical linear dipoles, uniformly distributed along a terminated transmission line. The matched load at the end of the transmission line prevents reflection of the traveling wave, such that the convenient progressive phase among elements is not distorted by a stationary wave configuration. Such a load makes the whole antenna highly inefficient and the antenna is seldom used for transmitting purposes. However, it has been shown to be very effective as a receiving antenna in discriminating against noise [51].

The array dipoles are placed at the points of a Cantor set, constructed after 5 iterations (M=5) from a two-element generator (N=2). In order to prevent a high side lobes a log-period δ=2.4 has been chosen following the criteria established in (3.11). The dipoles are short at all wavelengths such that their radiation pattern is kept constant through the bands. This makes the whole antenna highly inefficient for transmitting purposes as just discussed, but is the only way of keeping a constant element pattern through the five bands (waiting for the development of fractal multiband antennas which is the topic of next chapters). Bands are chosen as usual such that the minimum spacing between elements is a half of the shortest wavelength.

A Method of Moments algorithm has been used to numerically simulate the Cantor fishbone antenna. The algorithm is basically the same as the one used in Section 2.3.4.2 to reproduce Carrel's analysis of the log-periodic dipole array [46],[93]. That is, the transmission line and the array of dipoles are considered as two multiport networks which are connected in parallel. A sinusoidal current distribution is assumed for the short dipoles to compute the mutual impedance matrix of the array, while the admittance matrix of the feeding network (the transmission line) is basically that of Equation (2.68).

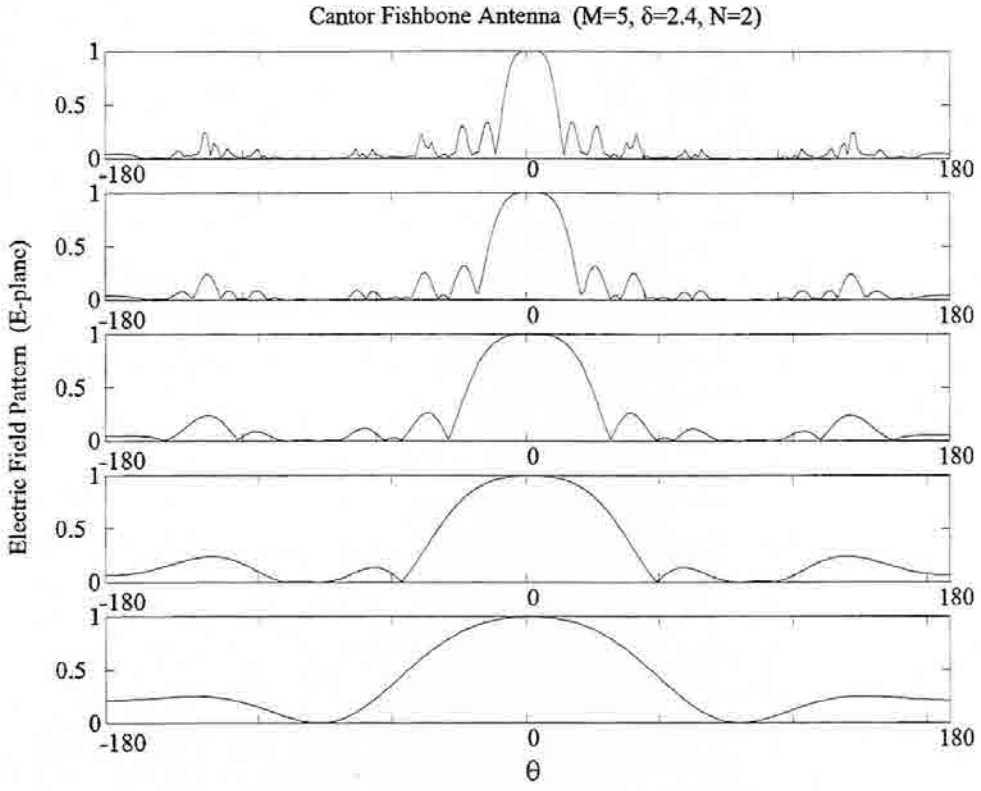

Fig. 3.10 E-plane patterns of a Cantor Fishbone array at the five operating bands.

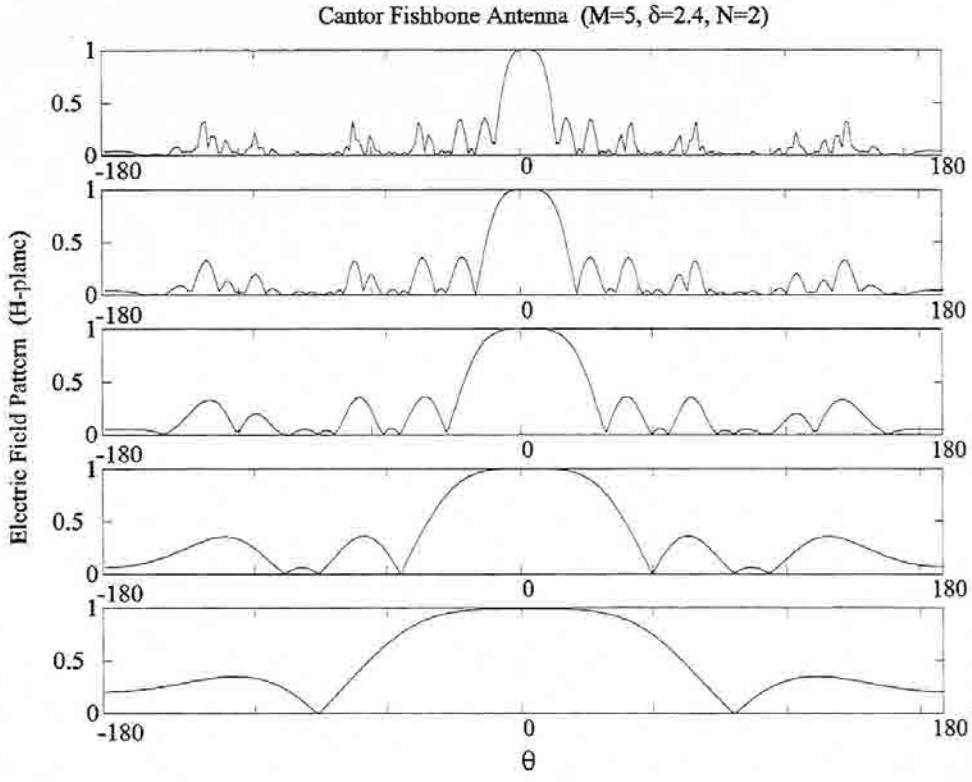

Fig. 3.11 H- plane patterns of a Cantor Fishbone array at the five operating bands.

The resulting patterns at the five bands are plotted in figures 3.10 and 3.11 (*E* and *H* planes). It is interesting to notice that the lobe structure is basically the one described in Fig. 3.4, although radiation is directed to the endfire direction due to the progressive phase introduced by the transmission line. Mainly the lobe structure is kept similar through the bands in the same way it has been described for the ideal Cantor array. On the other hand, the main-lobe widens at larger wavelengths, which is an inconvenient feature that could be expected from the analysis of previous sections. Nevertheless, it should be noticed that the main lobe widening is not as large as one could think at first glance (i.e. a δ=2.4 factor): the non-linear transformation from the Ψ domain to the polar θ domain tends to expand further the narrow lobes than the wider in such a way that roughly only 1.6 lobe widening factor within bands is obtained.

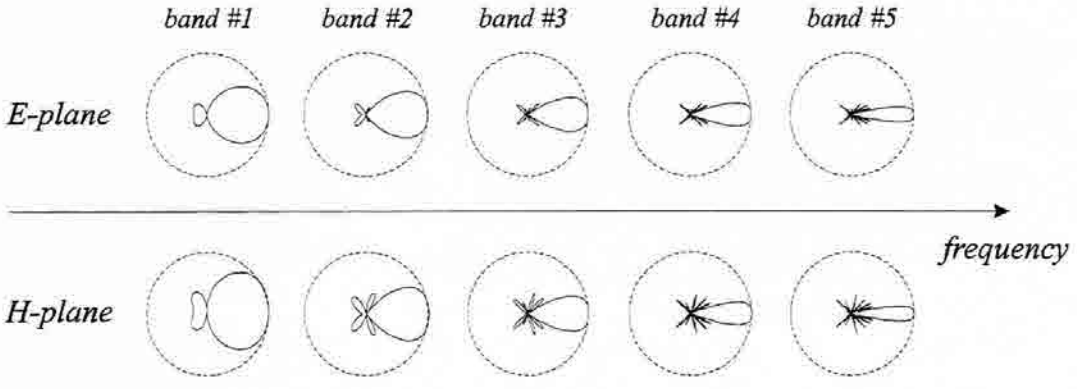

Fig. 3.12 Cantor Fishbone array patterns at five operating bands (M=5, δ=2.4, N=2).

It is also remarkable that, although the smaller spacing between elements is d=λ/2, radiation takes place in only one of the two endfire directions (i.e. θ=0^0). Such a behavior is mainly due to the progressive phase introduced by the wave propagating along the transmission line, and the non-uniform spacing among elements. This can be readily derived from the array factor of a four-element fishbone Cantor array (with characteristic parameters M=2, N=2, δ=2.4) that can be written as

$$AF(\theta)=\frac{1}{4}\left(e^{jk_z d_1+\beta_1}+e^{jk_z d_2+\beta_2}+e^{jk_z d_3+\beta_3}+e^{jk_z d_4+\beta_4}\right) \tag{3.14}$$

being d_i the distance of any of the four elements from the origin and β_i the progressive phase introduced by the transmission line, i.e., $\beta_i \approx -kd_i$. A uniform amplitude distribution

has been assumed since the dipoles do not significantly perturb the wave traveling along the line due to its short length. If the center of the array is placed at the origin, the distances become d_1=-0.85λ, d_2=-0.35λ, d_3=0.35λ, d_4=0.85λ, which leads to

$$AF(\theta)=\frac{1}{2}\left[\cos\left(0.7\pi(\cos\theta-1)\right)+\cos\left(1.7\pi(\cos\theta-1)\right)\right] \tag{3.15}$$

that can be approximated as

$$AF(\theta)\approx\frac{1}{2}\left[\cos\left(\frac{3\pi}{4}(\cos\theta-1)\right)+\cos\left(\frac{7\pi}{4}\pi(\cos\theta-1)\right)\right]\approx\begin{cases}1 & \theta=0\\ 0 & \theta=\pi\\ 0 & \theta=\pi/2\end{cases} \tag{3.16}$$

thus, it becomes apparent that the log-period δ=2.4 is shown to be useful in both providing a safe SLR level and a directional endfire pattern.

3.1.5 - Low Side-Lobe Arrays Based on the Cantor Set

The convolution GIFS algorithm we have been introduced for generating the Cantor array can be further extended to non self-similar shapes. It has been shown that classical uniform arrays can be constructed with the same algorithm when δ=N. Similarly, other positive real numbers for δ<2 could be taken as the characteristic scale factor, in particular any value within the range 1<δ<2 (the case δ<0.5 is the same as δ>2). It is shown here that the array loses its self-similarity properties (and its multiband behavior) in such cases, however, they still appear useful for designing single-band, low side-lobe arrays.

3.1.5.1 - The binomial array as a particular case of the Cantor array.

The particular case δ=1 represents the convolution of M equal distributions. In this case, (3.18) can be rewritten as

$$C(\Psi)=\left(\frac{\sin\left(N\frac{\Psi}{2}\right)}{N\sin\left(\frac{\Psi}{2}\right)}\right)^{M} \tag{3.17}$$

The binomial distribution can be obtained thus, by taking a generator with only two elements, i.e., N=2 and a log-period δ=1. A larger number of elements in the generator will implement a triangular distribution for M=2 and a distribution that tends to a Gaussian shape for increasing values of M (central limit theorem). In this later case (N>2), the SLR in dB decreases linearly with the number of iterations, which is a convenient method for designing low-side lobe arrays. Nevertheless, this method has a great inconvenient: the dynamic range of the element amplitudes within the array is so large that small errors in the feeding network change the weight of smallest elements, distorting the final pattern. However, a low side-lobe, equal amplitude array can be obtained by slightly deviating the log-period δ from unity.

3.1.5.2 - Uniform amplitude, nonuniformly-spaced arrays for near-binomial pattern design

The log-period δ can be chosen in general to be any real number. Some values for such a log-period have been shown to be specially interesting. For instance, we can generate a pattern without any side-lobe based on the binomial distribution we described before (δ=1). Now let us take a generator with two elements and chose a log-period close to 1, for example δ=1.1. We can expect this pattern to look very similar to the binomial pattern since the expression for the array factor (3.18) will be almost the same. Nevertheless, there is a fundamental difference between the shape of this array and the binomial one. In the δ=1.1 case none of the elements of the M convolving subarrays overlap, thus having a final array with a uniform-amplitude distribution over 2^M non-uniformly spaced elements. The array factor of this array is plotted in Fig. 3.14 , and the array structure in Fig. 3.13.

The main feature of this array is that, although the pattern is very close to the binomial one, the amplitude distribution of the elements is uniform, which greatly simplifies the feeding network. Furthermore, since the total number of elements is a power of two, such a feeding network could be conveniently implemented by successive cascading of symmetrical power dividers. A uniform current amplitude distribution through all the array elements can be obtained by means of a combination of $\lambda/4$ and $\lambda/2$ transmission lines, regardless of mutual coupling effects [51]. Also, it becomes apparent that this scheme could be repeated to generate very close patterns to any of the family described in (3.17), but with uniform distributions of elements. In particular, a large SLR self-similar triangular Cantor array pattern could be synthesized by replacing the initial triangular generator by an approximate array with a uniform current distribution.

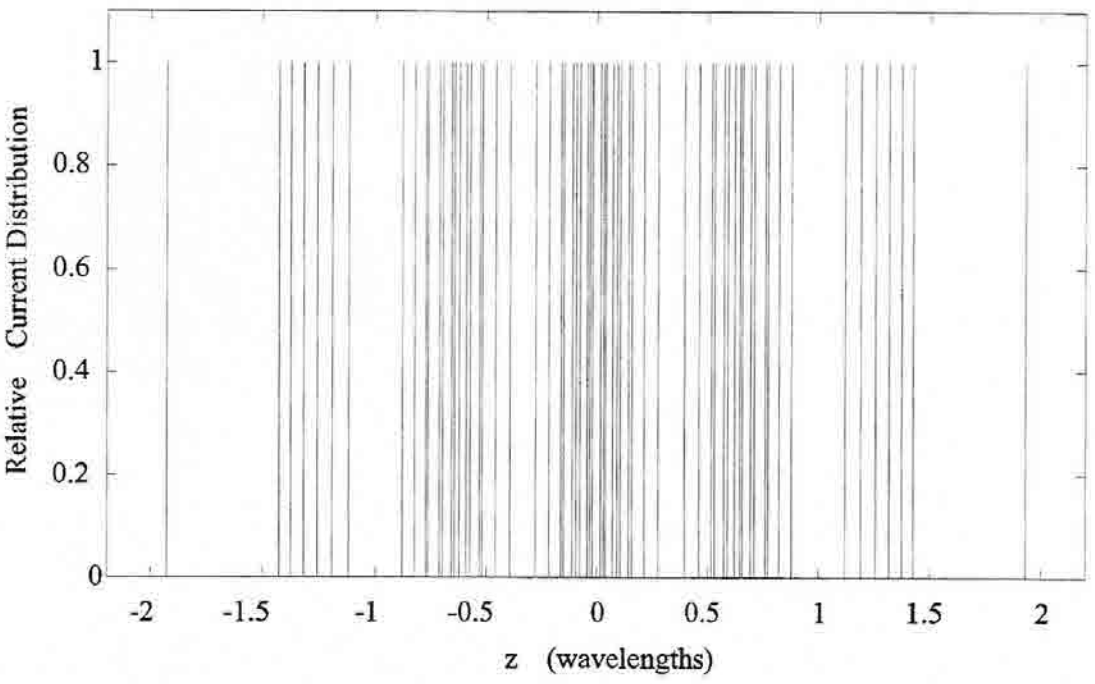

Fig. 3.13 Array element distribution for nearly binomial pattern conformation. It has been generated

The graphs in Fig. 3.15 can give us an insight of the main features of the Cantor array just described. They show SLR, spacing between the two closest elements in the array, and directivity versus log-period (δ) for a Cantor Array constructed with a two-element generator (N=2) of equal amplitude. In these graphs, δ=1 corresponds to the binomial array of 2^M elements, δ=2 to the uniform array of 2^M elements, and δ=3 to the classical Cantor set array of 2^M elements. In Fig. 3.15(a) we can see that secondary lobes start to raise above -30dB when the log-period is made larger than δ=1.2. Thus, the criteria of choosing a log-period δ<1.2 could be established for designing near-binomial array factors with very low side-lobe levels. However, by looking at Fig. 3.15(b) we can realize that such an array would have some elements within a minimum spacing below 0.15λ and that can be a design limiting factor. Thus, the designer could choose the proper log-period which satisfies the SLR requirements (Fig. 3.15(a)) keeping a feasible spacing between elements (Fig. 3.15 (b)).

The minimum spacing between elements converges to 0.5λ when the log-period is made larger than two (δ>N), a most logical result if we take into account that in these cases the convolving sub-arrays never overlap and the minimum spacing is always the distance between elements of the smallest sub-array. Also, at some specific points the minimum distance between elements becomes zero; at these points, some elements of the convolving arrays overlap into a single element with a larger weight. And this is precisely what we try to avoid: a non-uniform amplitude distribution between elements. Hence, Fig. 3.15(b) can also be used in the design process to identify those undesireable log-periods which imply a non-uniform amplitude distribution of the array elements.

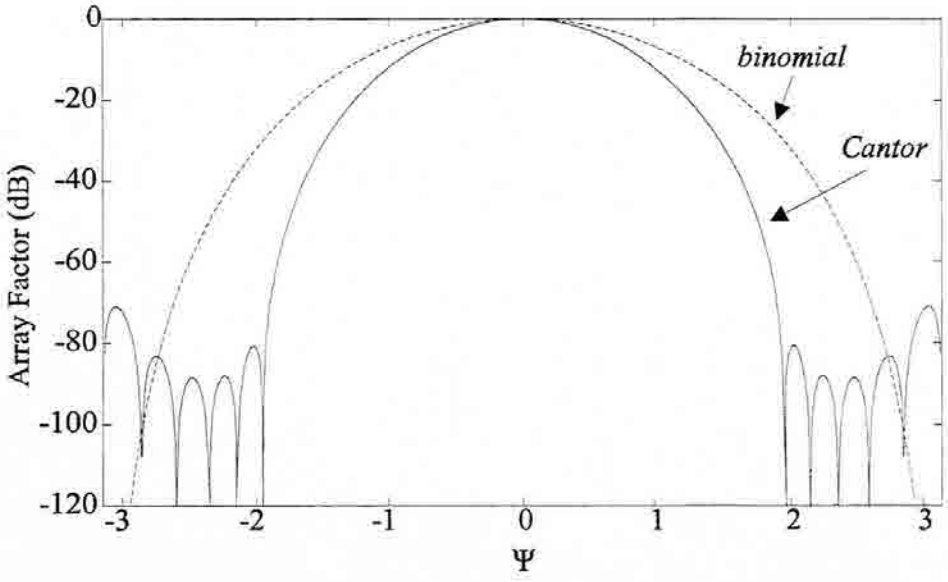

Fig. 3.14 Array Factor of a nearly binomial array with a uniform amplitude current distribution.

Another interesting feature of the array factor, the directivity, is shown in Fig. 3.15(c). It is remarkable that the directivity increases with the log-period until it reaches the maximum value for δ=2: the log-period corresponding to a uniform distribution, as we discussed before. As usual, the price we pay for a large directivity is a poor SLR. On the other side, it can be seen that the directivity can be improved by increasing the number of iterations (M) we use to construct the array, parameter that has a low effect on the SLR degradation, which mainly depends on the log-period. Thus, we can design an array with a desired SLR by choosing the proper log-period (δ) and increase the directivity by adding more elements to the array by iterating the generating process a larger number of times.

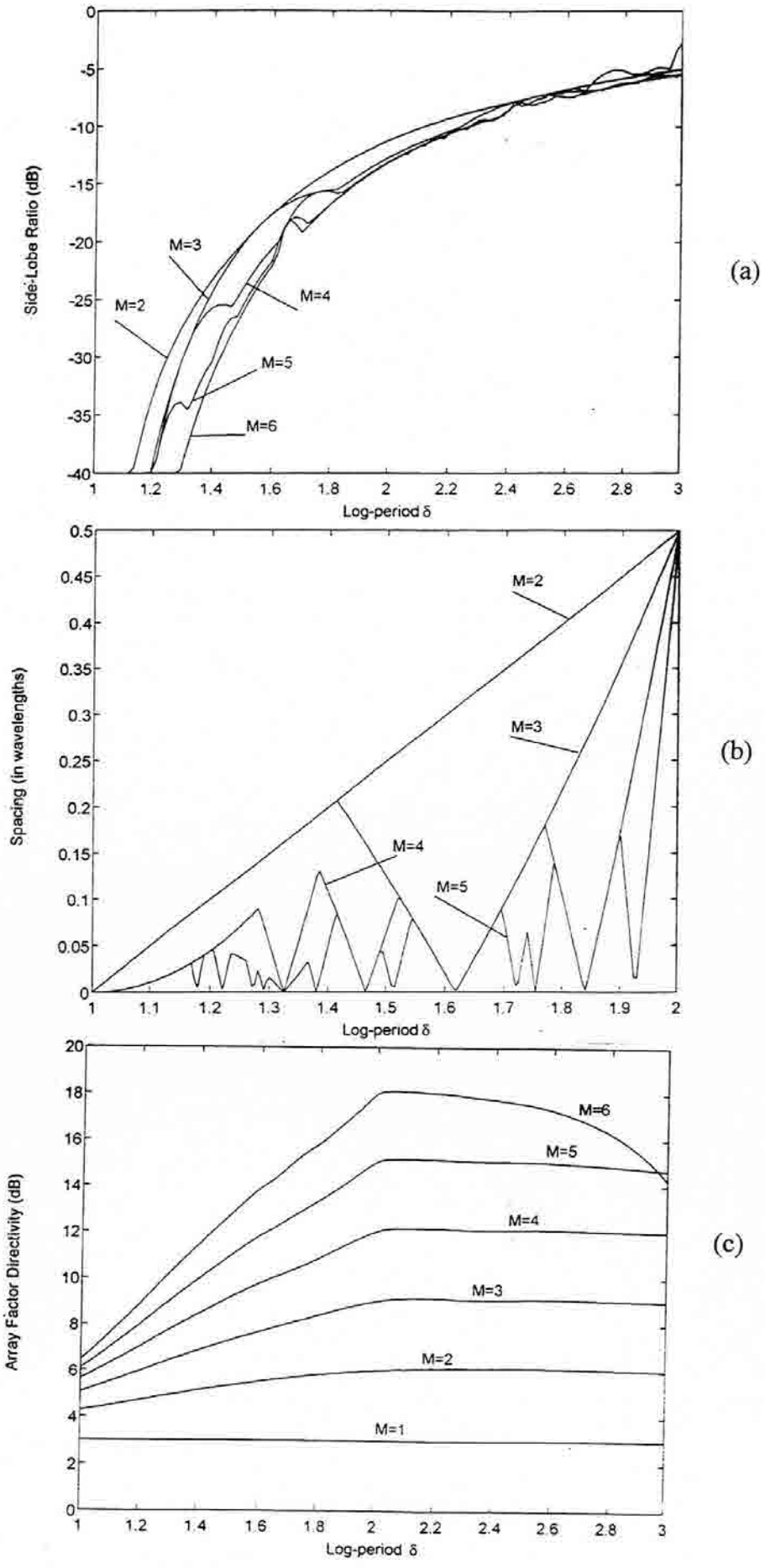

Fig. 3.15. SLR (a), minimum spacing between elements (b) and directivity (c) for Cantor set based arrays. All features are plotted for several iteration numbers as a function of the log-period δ.

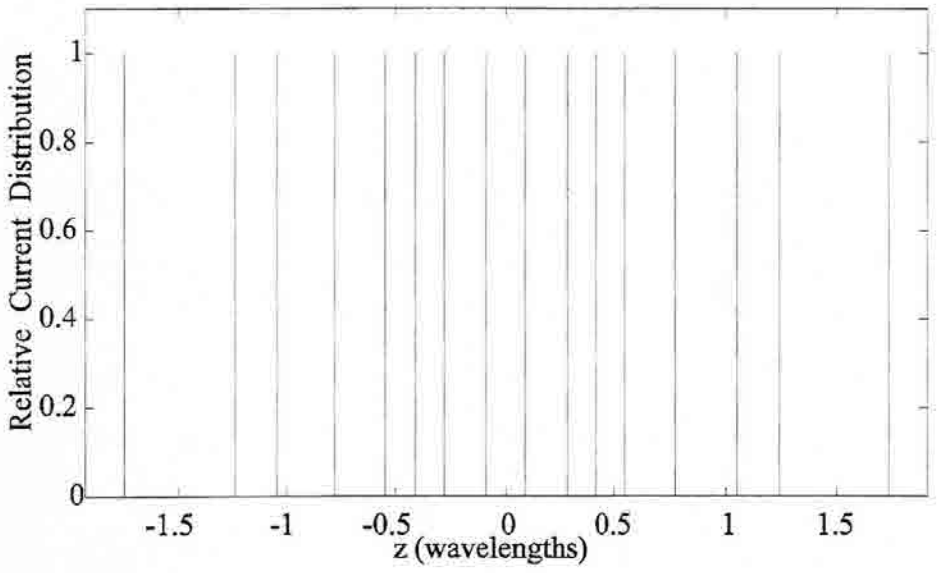

Fig. 3.16 Design of a uniform amplitude low side-lobe (M=4, N=2, δ=1.385, SLR=25dB) array.

To illustrate the fractal design, figures 3.16 through 3.18 show a design example using the graphs in Fig. 3.15 . A SLR larger than 25 dB suggest a selection of a log-period δ<1.5 according to Fig. 3.15(a). Then, by looking at Fig. 3.15(b) we can see that the largest

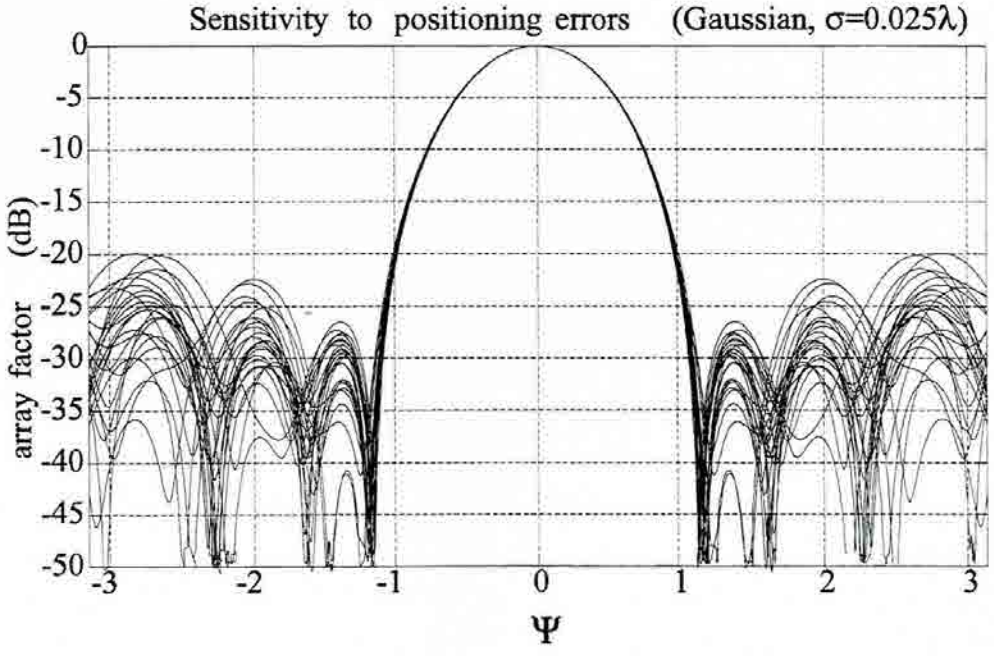

Fig. 3.17 Sensitivity to positioning errors (Gaussian error, σ=0.025λ).

minimum spacing between elements has a maximum for M=4 at a log-period δ=1.385. With these two parameters the array is fully characterized. The resulting array is plotted in Fig. 3.16. The graphs in figures Fig.3.17 and Fig.3.18 show a sensitivity analysis of the resulting pattern with respect to slight variations on the element position and weight. It can be seen that the design keeps its main features for reasonable deviations from the nominal value.

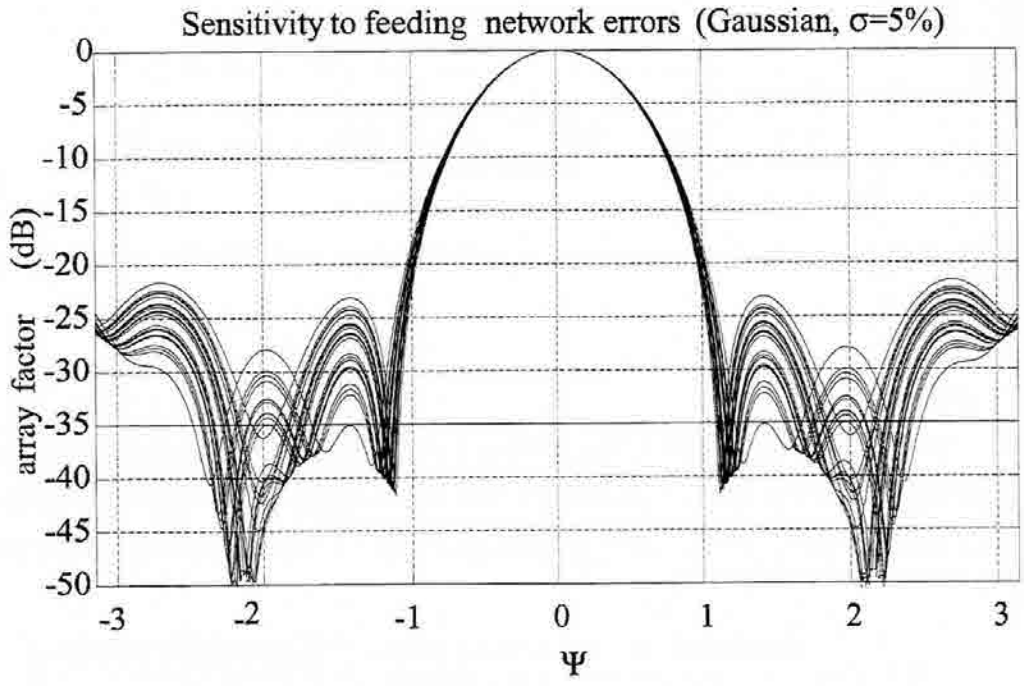

Fig. 3.18 Sensitivity to feed network errors (Gaussian error, standard deviation 5%).

3.2 - Fractal Array Factors

In the previous section a fractal analysis and design of several array factors has been developed. Fractal element distributions have shown to be useful for designing low side-lobe array factors with a uniform amplitude distribution of elements. On the other hand, these fractal arrays have shown some interesting similarity properties at several wavelengths. However, these similarity properties do not satisfy some requirements one would desire for a truly multifrequency array: the directivity and the main-lobe width are not held constant at each band. In general, one would like to have an array factor which had the same shape at different scales to keep the same radiating parameters at several wavelengths. This leads to the approach presented in this section: the design of fractal array factors.

3.2.1 - Multiband behavior of Koch array factors

The patterns designed in this section are based on the family of self-similar Koch curves [1],[4],[8]. The pattern construction algorithm is quite similar to that of such curves, but they are modified to provide a functional form. The shape and the principle of work of this kind of array factors is summarized in Fig. 3.19.

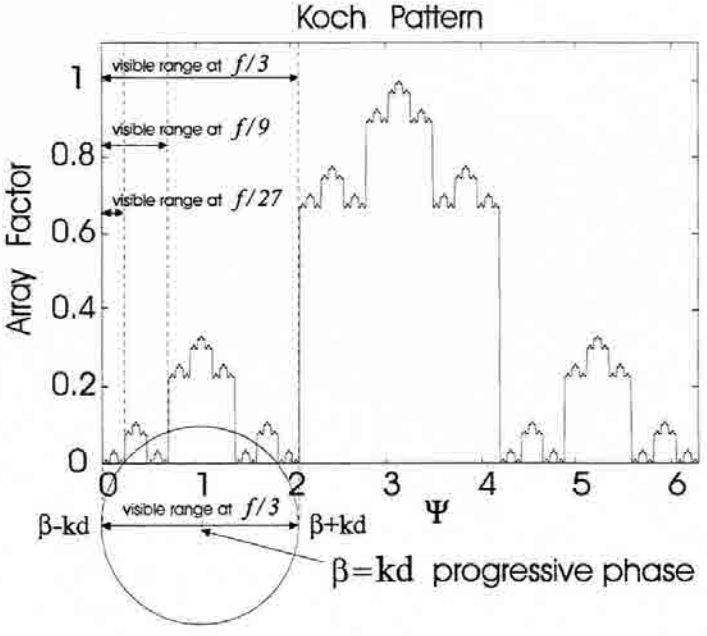

Fig. 3.19 The Koch array factor. The curve keeps its similarity properties at 6 different scales (6 iterations, M=6). By adding a progressive phase β=kd the visible range is always centered at a secondary lobe that has the same shape as the total pattern. The frequency change by a factor δ=1/3 reduces the visible range around this similar sub-pattern.

The main feature of this pattern is that each lobe of the curve is a scaled-down copy of the whole pattern. When the array radiates at a longer wavelength, the visible range is reduced and only a fraction of the whole array factor appears in the radiation pattern. Thus, if we were able to design an array with an array factor like that on Fig. 3.19, and if we could reduce the visible range around one of the secondary lobes, the resulting visible pattern would be the same as the original one. The visible range can be centered to any arbitrary point of the Ψ domain by adding a progressive phase β, as stated in (2.49). It can be seen that if we take such a progressive phase to be

$$\beta = kd \tag{3.18}$$

the visible range will cover the interval $\{0, 2kd\}$ at any frequency. Hence, for the particular case of Fig. 3.19 , a frequency reduction by a factor of $(1/3)^n$ would reduce the visible range around a secondary lobe which has the same shape as the whole pattern. In other words, we would have an array factor with the same radiation parameters for a set of bands spaced a factor of 1/3. It is also interesting to point out that, although the progressive phase in (3.18) is usually intended for endfire arrays, the Koch patterns are here designed to radiate in the broadside direction.

It should be noticed that, although the arrays just described would have a similar radiation pattern at several bands, the pattern magnitude is reduced when the operating wavelength is increased. That means that for the same current distribution, the electric field intensity is reduced at lower bands, or in other words, neither the radiation resistance nor the radiation efficiency are held constant through the bands. This is an intrinsic constraint of such an array design which should be faced in the physical implementation of the array.

3.2.2 - Analysis of the array element distribution

Once the fractal array factor has been defined to have a multiband behavior, its relative current distribution among elements should be derived. Such a distribution can be numerically derived by taking the Inverse Fourier Transform of the Koch array factor. The result, shown in Fig. 3.20 in a semilogarithmic scale, indicates that the magnitude of the relative current distribution has a $1/|z|$ shape, which is a self-affine function as shown in Section 3.2.4.

Another important issue concerning the computed array structure is that it is defined for 3^6=729 points or elements. This quantity comes from the design of the Koch curve itself, which needs a minimum of N points to achieve the desired degree of detail

$$N = (log - period)^{iterations} \equiv \delta^M \tag{3.19}$$

The number M of iterations we use to construct the curve determines the number of times the curve will look similar under a δ factor scaling transformation. In other words, M is the number of bands or log-periods in which the array will have a similar pattern. Hence, there is a trade-off between the size of the array and the number of operating bands. Of course, here arises what can be an intrinsic inconvenient of these arrays: the number of elements grows exponentially with the number of log-periodic bands. Thus, a method to reduce this number should be essayed before going any further.

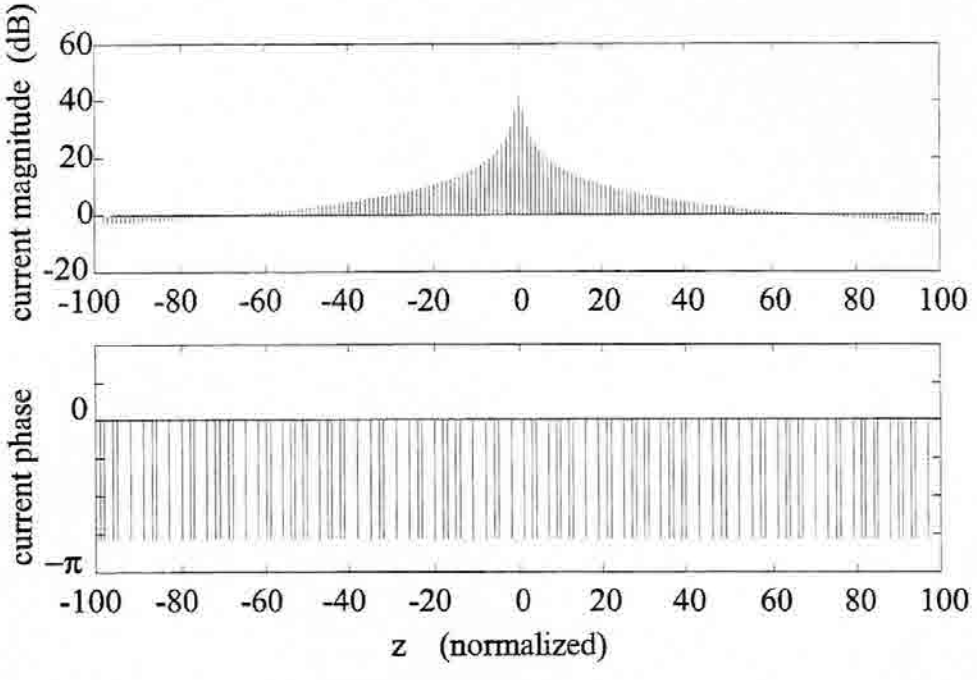

Fig. 3.20 Magnitude and phase of the array elements that conform the Koch pattern on Fig 3.19. The current magnitude has a hyperbolic like shape.

3.2.2.1 - Reducing the number of elements: array truncation

All different Koch patterns that have been analyzed [87](see some Fig. 3.28) have the common characteristic of concentrating the most important current contribution around the central element. Also, all relative current distributions have shown to decay near the tips of

the array. Hence, one could think that the number of elements could be reduced by merely truncating the array at its tips thus keeping only the central part. Figure 3.21 shows the result of truncating the array of Fig. 3.20 from 729 elements to only the first 84 around the maximum.

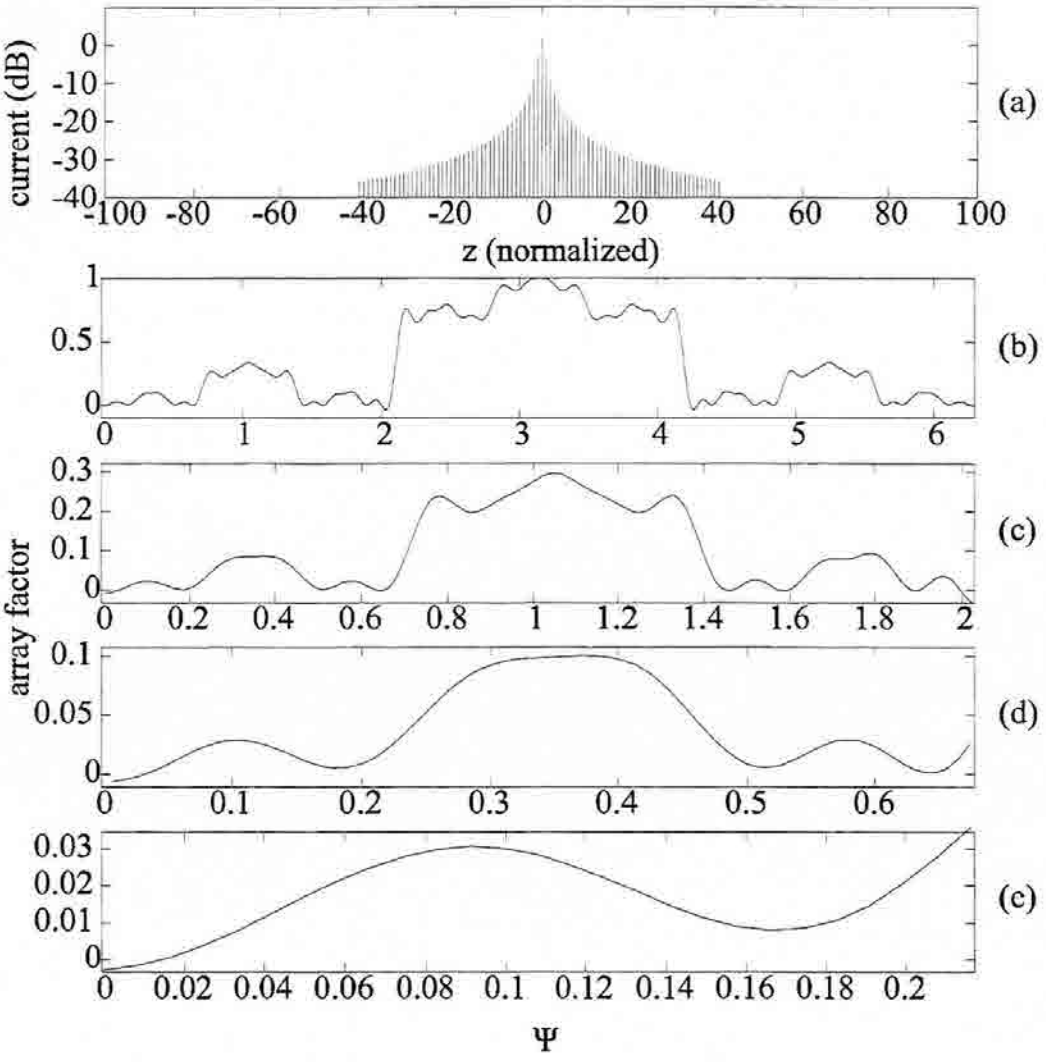

Fig. 3.21 Truncation of the Koch array to the central 84 elements (a). The resulting patterns only keep similarity properties up to four bands at wavelengths $\lambda_0=d/2$ (b); $\lambda_1=3\lambda_0$ (c); $\lambda_2=9\lambda_0$ (d) and $\lambda_3=27\lambda_0$ (e).

It is clear that the truncation in the spatial domain has low-pass filtered the patterns reducing their degree of detail. As a result, the pattern looks only similar at four different scales (four different bands), which is understandable if we take into account that (3.19) implies that the curve for only 4 bands could be defined with $3^4=81$ elements. A deeper

analysis of the Koch array structure will help in both understanding its behavior and reducing the number of elements.

3.2.2.2 - Analysis of the array element distribution for Koch-pattern conformation

A key point for understanding the array current distribution derived from the fractal patterns is the Koch-pattern construction algorithm itself (see Fig. 3.22) . Let us take a periodic pulse train in the spatial-frequency domain Ψ and scale its width by a factor δ and its amplitude by a factor of $\alpha\delta$. After iterating this scheme M times, the M resulting patterns are then added, obtaining a Koch pattern like that on Fig. 3.19 . In particular, for the pattern on Fig. 3.19, a rectangular pulse, a log-period δ=3, and an amplitude factor α=1 was chosen for generating the pattern with M=6 iterations.

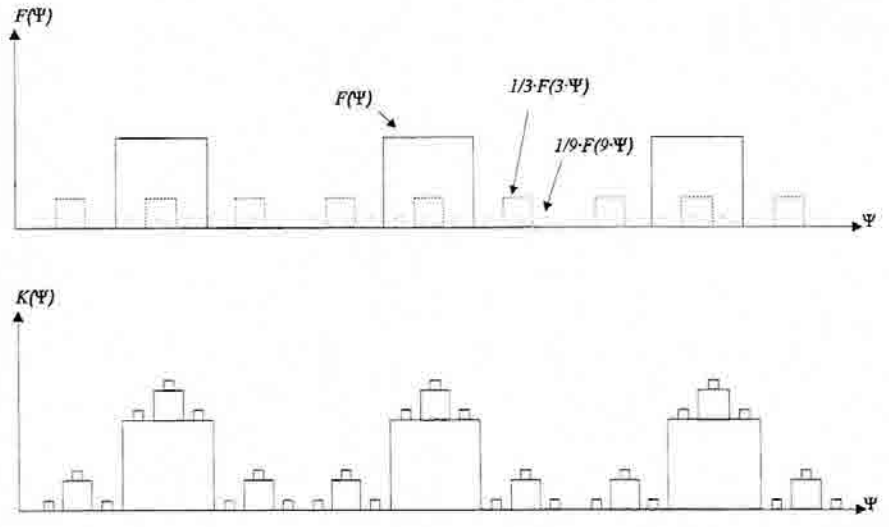

Fig. 3.22 The Koch patterns can be constructed by adding several pulse trains at M different scales.

The analytical expression for each generating pulse train can be written as

$$F(\Psi) * \sum_{n=-\infty}^{\infty} \delta(\Psi - n\Psi_T) \tag{3.20}$$

where $F(\Psi)$ is the single pulse function, which in general could be taken to have any arbitrary window shape, and Ψ_T is the period of the pulse train. From (3.20), the analytical expression for the Koch pattern $K(\Psi)$ after adding the M scaled pulse trains is

$$K(\Psi)=\sum_{p=0}^{M-1}F(\delta^p\Psi)*\left\{\frac{1}{\alpha^p\delta^p}\sum_{n=-\infty}^{\infty}\delta(\Psi-n\frac{\Psi_T}{\delta^p})\right\} \tag{3.21}$$

Again, for the Koch-pattern on Fig. 3.19, the reduction factor was chosen to be α=1, i.e., no extra reduction or magnification was applied. Several combinations of α,δ and M are essayed in the arrays of Fig. 3.28. A rectangular generating pulse is chosen on the first three examples, and a Blackman window on the last one. Once an expression for the Koch pattern has been derived, an expression for the Koch array element distribution *k(z)* can be easily found by taking the Inverse Fourier Transform of (3.21).

$$k(z)=\frac{1}{\Psi_T}\sum_{p=0}^{M-1}\frac{1}{\delta^p}f\left(\frac{z}{\delta^p}\right)\cdot\left\{\frac{1}{\alpha^p}\sum_{n=-\infty}^{\infty}\delta(z-n\cdot d\cdot\delta^p)\right\} \tag{3.22}$$

The train of delta functions in (3.22) samples the current distribution at the discrete set of points $z=n\cdot d\cdot\delta^p$ where the array elements are located. Hence, taking into account that

$$\Psi_T=kd=\frac{2\pi d}{\lambda} \tag{3.23}$$

one can write

$$k(z)=\frac{\lambda}{2\pi d}\sum_{p=0}^{M-1}\left\{\left(\frac{1}{\alpha\delta}\right)^p\cdot\sum_{n=-\infty}^{\infty}f(nd)\cdot\delta(z-n\cdot d\cdot\delta^p)\right\} \tag{3.24}$$

which gives an insight into the shape of the resulting array: the Koch array is a superposition of M arrays that have the same element distribution but a wider spacing between elements, depending on the iteration stage to which they belong (Fig. 3.23). That is, the elements are uniformly spaced within the same array, but the spacing changes at each sub-array by a factor δ^p. When the arrays are added, some elements might fall at the same position as other elements from the other arrays; in such a case the result is a single element whose weight is the sum of the weights of all the elements that would fall at that point. In particular, it can be seen that all the arrays have a common element at

$$z=n\cdot d\cdot\delta^{M-1} \tag{3.25}$$

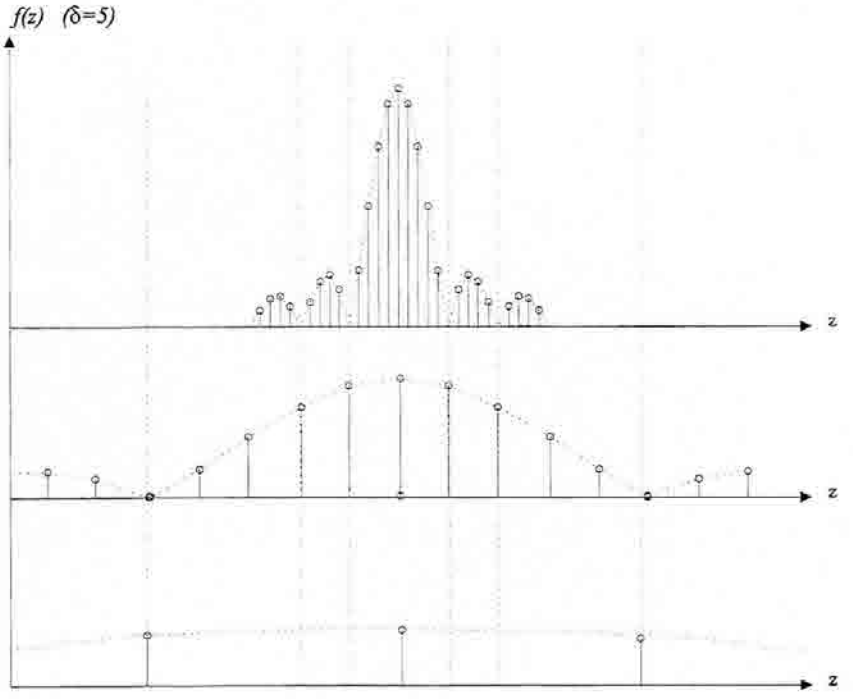

Fig. 3.23 Construction of a Koch array as the superposition of M arrays of equal shape but different scales.

Equation (3.24) can give us an insight on the power-law shape of the current distribution that generates the Koch pattern in Fig. 3.19. For this particular case, the squared pulse generator has an inverse transform

$$f(z)=\frac{\sin\left(\frac{\pi}{d\cdot\delta}z\right)}{\pi z} \tag{3.26}$$

which give us the shape of all the M sub-arrays that conform the Koch array. The weight of each element can be easily found by sampling (3.26) at $z=m\cdot d$. It can be seen that for the case we have been studying (δ=3)

$$|f(md)|=\left|\frac{\sin\left(\frac{\pi}{3}m\right)}{\pi md}\right|=\begin{cases}\left|\frac{\sqrt{3}}{2\pi d}\right|\cdot\frac{1}{|m|} & m\neq 3^w \\ 0 & m=3^w\end{cases} \tag{3.27}$$

which is, in absolute value, a power-law (hyperbolic) function of the index element m. Another important property can be seen if we realize that (3.27) is null for those m such that

$$m = \delta^W \tag{3.28}$$

being W an integer. From this property, we can conclude that all the sub-arrays contribute on the weight of the central element, but that they do not overlap at any other point since the nulls of each array is filled by an element of an array corresponding to the next iteration stages. Therefore, the global array obtained after M iterations can be seen as an array composed by interleaving the elements of M-equal arrays at M-different scales. The result for the particular case δ=3 and a squared pulse generator, is an equally spaced array with a hyperbolic distribution of the element- current magnitudes (Fig. 3.24).

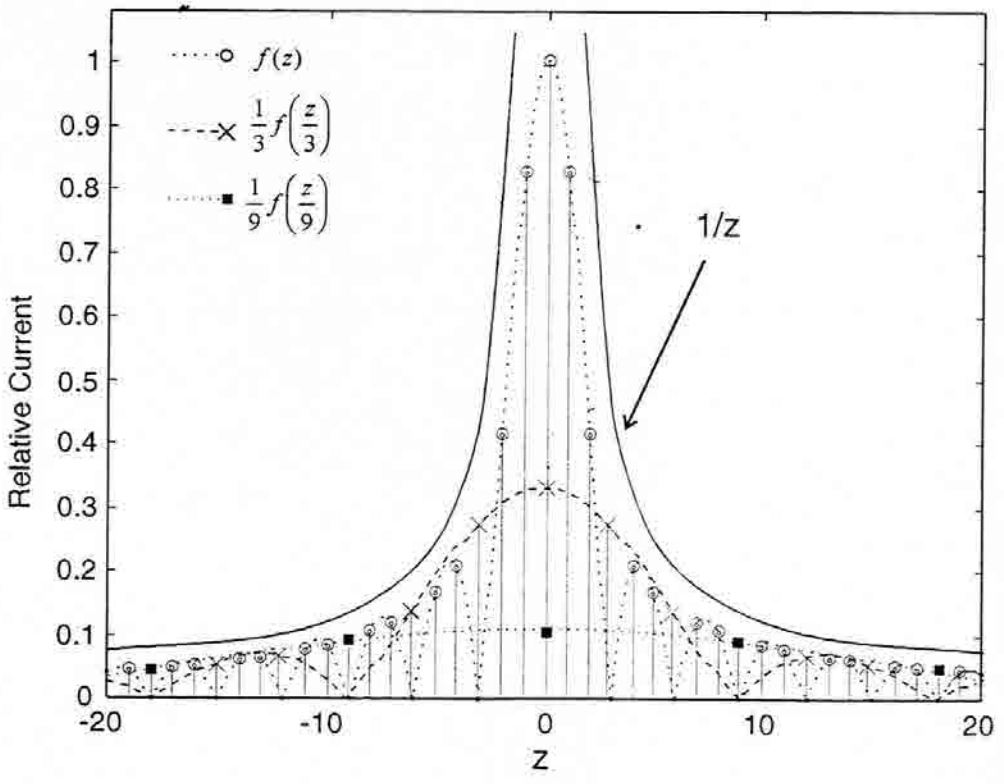

Fig. 3.24 Construction of the Koch array with δ=3. M hyperbolic arrays at M different scales are superimposed. The resulting hyperbolic pattern can be seen as an spatial interleaving of the different array elements.

Two important conclusions can be derived from the analysis of the generalized Koch array *k(z)* and the particular case we have just studied. First, the shape of the *M*-superimposed sub-arrays depends on the shape of the pulse generator. Second, the superposition of the sub-arrays might result in the confluence of many elements in a single location or might result into an interleaving of the elements. As we show in the following subsection, both conclusions will help in the reduction of the number of elements of the Koch array.

3.2.3 - The Blackman-Koch array factor

Since the array current distribution is basically a superposition of the inverse transforms of the pulse generator, we should choose a pulse generator with a low side-lobe level transform to allow a better truncation of the Koch arrays just shown. The Blackman window is characterized for having low side-lobes in the transformed domain [108]. Therefore, one could chose a train of Blackman pulses to generate the Koch patterns instead of the rectangular ones. The results of applying such a technique are shown in Fig. 3.25 through Fig. 3.27.

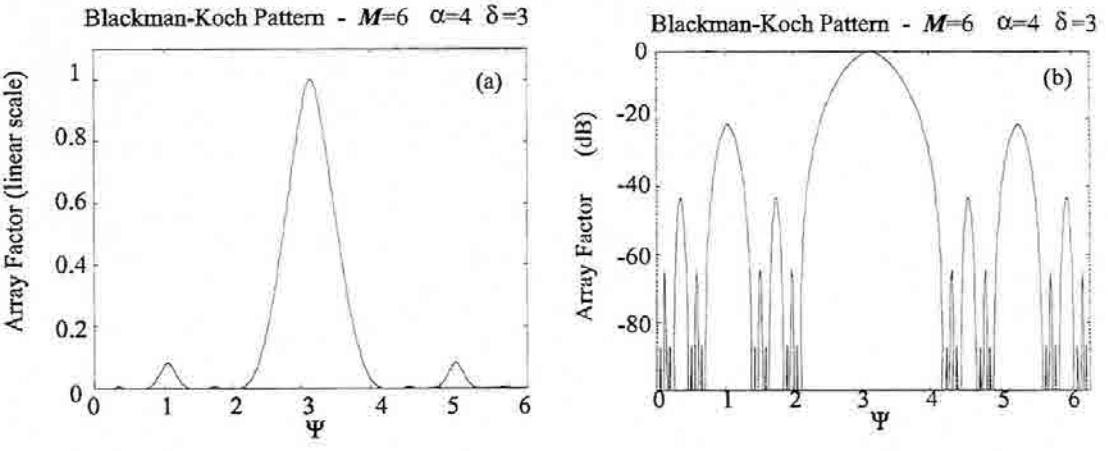

Fig. 3.25 The Blackman-Koch pattern. The main construction parameters are M=6, δ=3 and α=4. The reduction factor α=4 has been chosen here to improve the SLR with respect to the previous case on Fig.3.19.

It can be noticed that the pattern results in a smoother shape that keeps the same similarity properties of the Koch array factor of Fig. 3.19 (see Fig. 3.25). The main advantage of this pattern is that the array relative current distribution has lower side-lobes and a better confinement around the central elements (Fig. 3.26(a)). Thus, it seems that the

array simplification will be much easier in this case. The logarithmic plot of the current distribution reveals some important isolated current peaks well beyond the center of the array. One should expect a significant contribution of these isolated elements to the global-pattern conformation. Thus, instead of just truncating the tips of the array, a threshold level can be set to discern which elements are important in the pattern synthesis and which are not. The result is the simplified array of Fig. 3.26(b) . It can be seen (Fig. 3.27) that, although the array has been simplified to only 75 elements (as opposed to 729), it keeps its self-similar behavior at five bands through a whole 81:1 frequency range, with a lower degree of pattern distortion with respect to the rectangular pulse case.

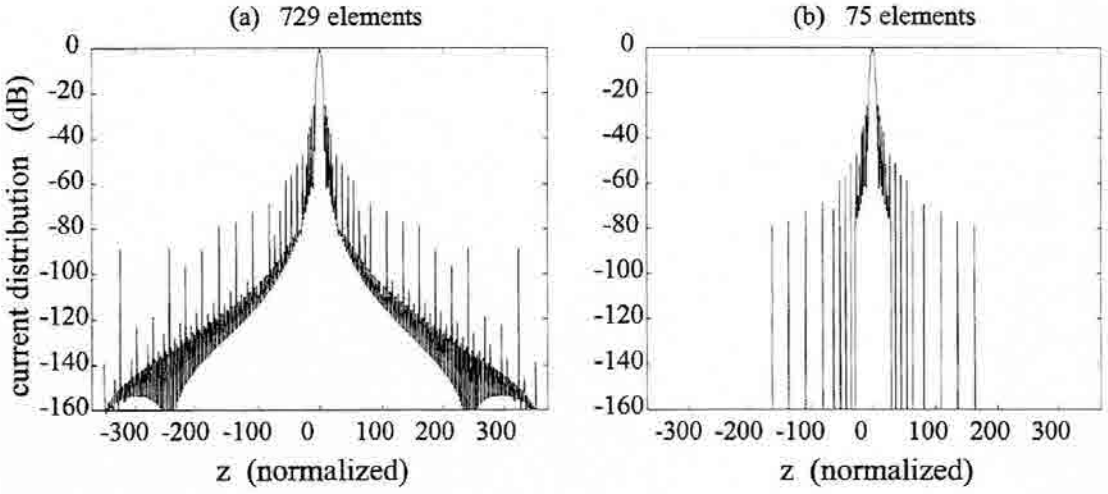

Fig. 3.26 The Blackman-Koch array: current distribution, logarithmic scale (a). Current distribution after truncation to 75 elements (b).

The resulting array is no longer a uniformly-spaced array since the main 75 current elements are not placed together near the midpoint of the array. Thus, some elements are placed further from the origin than in the truncation scheme which means that faster variations will appear in the dual domain (the pattern domain). This explains why this scheme can better keep the multiband behavior in a larger number of bands than the truncation scheme: the further the elements are placed form the origin, the finer will be the resulting lobe structure which will allow the pattern to keep the same shape for a further reduction of the visible range.

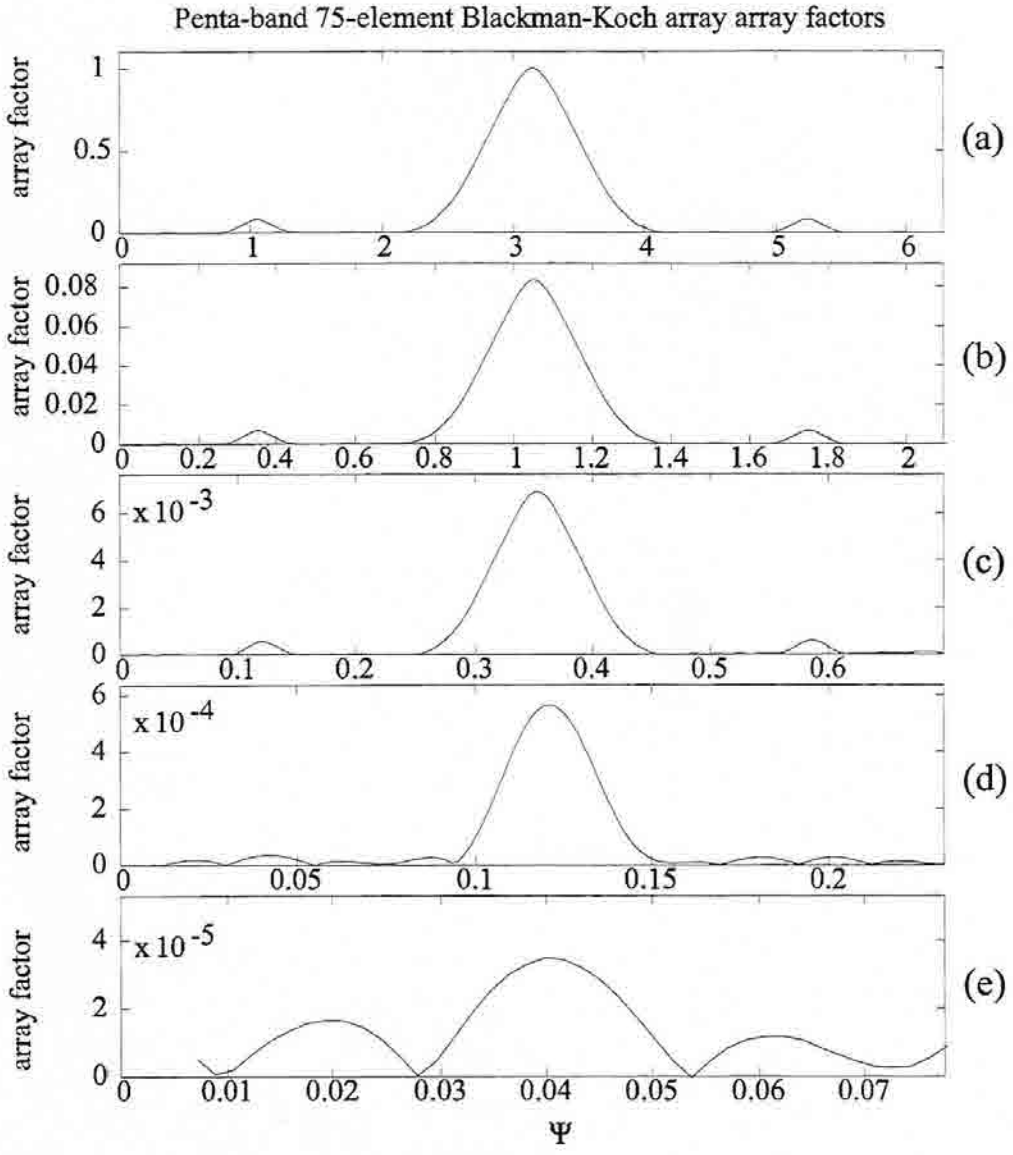

Fig. 3.27 Resulting Blackman-Koch patterns after truncation to only 75 elements. The array factor is plotted for λ_0=d/2 (a); λ_1 =3λ_0 (b); λ_2=9λ_0 (c) ; λ_3 =27λ_0 (d) and λ_3 =81λ_0 (e). Notice the low degree of pattern distortion (5 bands) as opposed to the patterns on Fig.3.24 (4 bands).

3.2.4 - Self-similarity and self-affinity in spatial and spectral domains

The goal now is to gain an insight into the array properties that make its pattern self-similar. A structure is said to be self-similar if its shape and size remain constant under a change of scale, while it is said to be self-affine if the structure keeps only its shape, but not necessarily the same aspect ratio, after the scaling process. If we use those definitions to characterize mathematical functions, we could state that a function is self-affine if

$$f(z) = \delta^{\beta} \cdot f\left(z/\delta\right) \tag{3.29}$$

where δ is the scale factor and β is a real number. If β=0, then the scaled function is equal to the original one, having thus, a self-similar function. The infinite Koch patterns designed in Section 3.2.1 show a 1/3 reduction on the amplitude when expanded by a factor of 3. Hence, they can be seen as particular cases of (3.29) for δ=3 and β=1. It can be easily seen that a function that held property (3.29) would have a Fourier transform $F(\Psi)$ such that

$$F(\Psi) = \delta^{\beta+1} \cdot F(\delta \cdot \Psi) = \delta'^{\beta} \cdot F\left(\Psi/\delta'\right) \tag{3.30}$$

which has been conveniently reduced to (3.29) by properly defining the parameters $\delta' \equiv \delta^{-1}$ and $\beta' \equiv -(\beta+1)$. That is, the spectrum of a self-affine function as defined in (3.29), is also a self-affine function. Examples of functions satisfying (3.29) can be easily found in power law functions since

$$\left.\begin{aligned} f(z) &= z^{\nu} \\ f\left(z/\delta\right) &= \frac{1}{\delta^{\nu}} \cdot z^{\nu} = \frac{1}{\delta^{\nu}} \cdot f(z) \end{aligned}\right\} \Rightarrow \beta = \nu \tag{3.31}$$

$$\left.\begin{aligned} f(z) &= \frac{1}{z^{\nu}} \\ f\left(z/\delta\right) &= \delta^{\nu} \cdot \frac{1}{z^{\nu}} = \delta^{\nu} \cdot f(z) \end{aligned}\right\} \Rightarrow \beta = -\nu \tag{3.32}$$

We saw in Section 3.2.2 that the Koch pattern had a power-law (hyperbolic) shape for the magnitude of the current distribution. In that case properties (3.29) and (3.30) do not strictly apply because the fractal pattern is truncated and repeated periodically, resulting in a sampled version of a hyperbolic function. However, most of the analyzed fractal patterns seem to be generated by structures that result from interleaving power-law self-affine functions. Fig. 3.28 shows several configuration of Koch patterns and their corresponding array distributions in a log-log scale. Again, δ is the log-period or band ratio, M is the number of iterations (and the number of bands), and α is the amplitude weight factor that adds an extra degree of freedom in the pattern design as discussed previously. Only the half right-side of the array current distribution is displayed since it is symmetrical around its central element. The linear shape of the current distributions suggest such an interleaving of power-law sub-arrays, which provides their self-scaling properties and thus their multiband

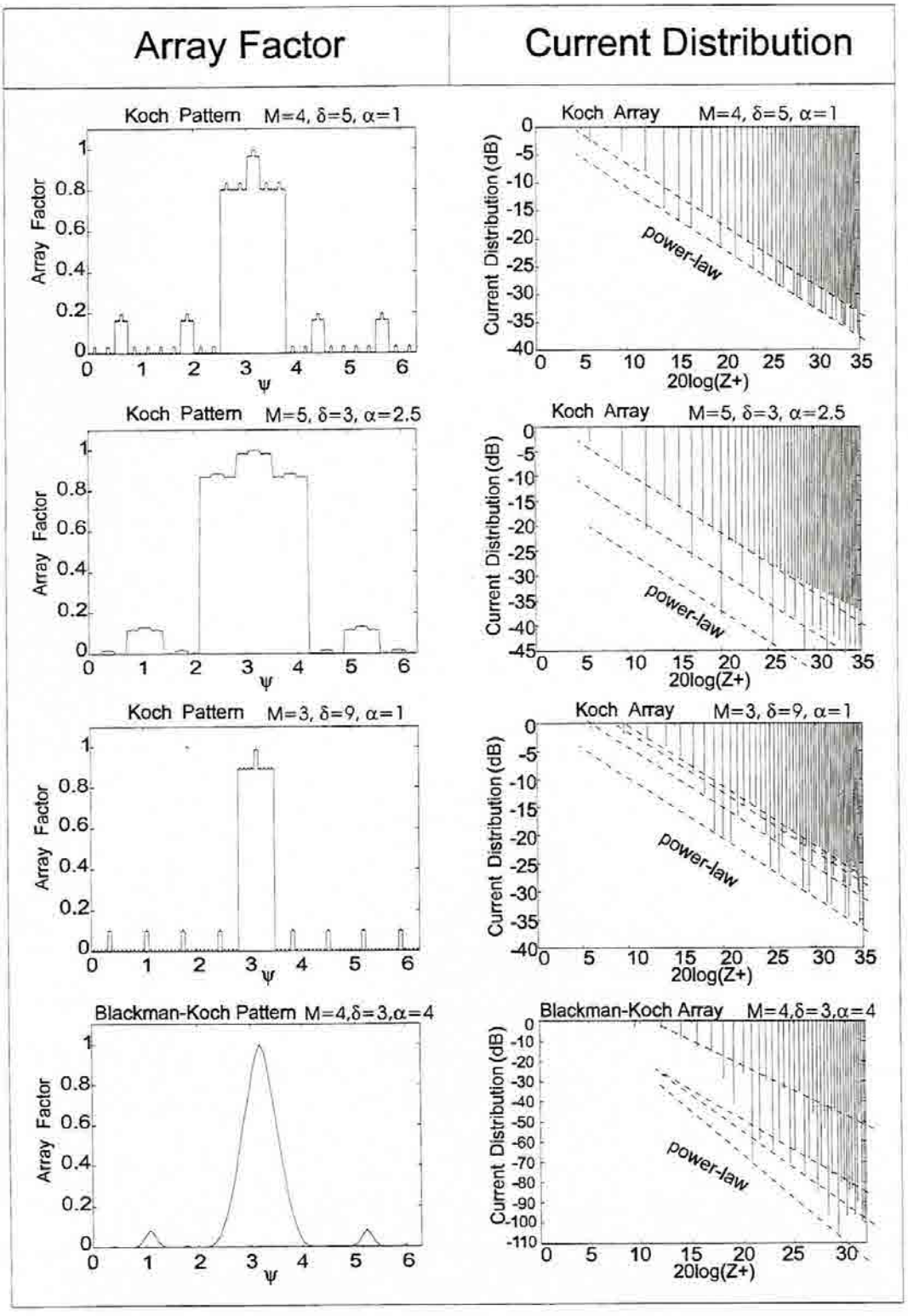

Fig. 3.28 Koch patterns are conformed with arrays constructed by interleaving hyperbolic distributions.

behavior. We should stress that feature is quite different from current frequency-independent antennas or arrays. Such antennas are based on an active region of the antenna that changes its size with frequency. On the contrary, the fractal arrays introduced here assume a current distribution that does not change with frequency but have a scale-independent shape.

3.2.5 - The Weierstrass array

Weierstrass functions are among the best known, non-differentiable fractal functions [14],[136]. The classical bandlimited Weierstrass function $w(z)$ is given by [14]

$$w(z) = w_0 \sum_{n=N_1}^{N_2} \delta^{(D-2)n} \cos\left(2\pi k_0 \delta^n z + \theta_n\right) \tag{3.33}$$

being δ an scale factor (δ>1), $k_0\delta^{N_1}$ the fundamental spatial frequency, w_o and arbitrary constant, D the fractal dimension of the function (1<D<2) and θ_n the phase of the spatial harmonic (which is usually taken as a random distribution on [0,2π]). When an infinite number of harmonics is taken ($N_1 \to -\infty$, $N_2 \to \infty$) all of them with a null phase, $w(z)$ becomes a self-affine function which holds (3.29) with β=2-D. Hence, it has also a self-affine Fourier transform. Its power spectral density function is of the form

$$P(\Psi) = P_0 \sum_{n=N_1}^{N_2} \delta^{2(D-2)n} \left[\delta\left(\Psi - k_0\delta^n\right) + \delta\left(\Psi + k_0\delta^n\right)\right] \tag{3.34}$$

which is quite similar to the power-law arrays described for the Koch array factors. In general, (3.33) could be extended to other bounded periodic even functions $g(z)$ such as a generalized Weierstrass function $W(z)$ could be defined as [136]

$$W(z) = W_0 \sum_{n=1}^{\infty} \delta^{(D-2)n} g\left(\delta^n z\right) \tag{3.35}$$

It is apparent that such generalized Weierstrass function could be used for synthesizing fractal arrays and patterns with self-similarity properties as well. As a matter of fact, X. Liang *et al.* [136] have recently described some scaling properties of a circular array based on (3.35). Such an array is actually an array of concentric ring arrays of radius

$$a_n = a_0 \delta^n \tag{3.36}$$

with a power-law function relating the relative current amplitude I_n among the concentric arrays

$$I_n = I_0 \delta^{(D-2)n} \tag{3.37}$$

All rings are densely composed by a large number M of equally spaced elements lying on the xy plane. By defining Ψ as

$$\Psi \equiv k a_0 \sin\theta \tag{3.38}$$

the overall array factor $W(\Psi)$ can be written as [136],[79]

$$W(\Psi) = \sum_{n=1}^{N} I_0 \delta^{(D-2)n} \cdot J_0\left(\Psi \delta^n\right) \tag{3.39}$$

being J_0 the Bessel function of the first kind and zero-order. The array factor is thus a particular case of self-similar Weierstrass function, provided that J_0 is almost periodic for large arguments.

The similarity properties of the array factor $W(\Psi)$ are shown in Fig. 3.29. It displays the array factor of a concentric ten-ring array having a fractal dimension D=1.9, and a characteristic scale factor δ=2.34. The array factor is plotted at five operating bands logarithmically spaced by δ. While a scale factor of 10 is used in [136] to compare two scaled array factors, the characteristic factor δ is taken here because the agreement among patterns is better at frequencies such that $f_n = f_0 \delta^n$.

The alike behavior among bands becomes clear in the plot. However, it should be noticed that the vertical scale used in Fig. 3.29 changes from band to band. Such a scaling becomes necessary to get the perfect agreement among bands. This fact becomes clearer when looking at a horizontal logarithmic plot of the half right side of the array factor (Fig. 3.30).

The array factor has a log-periodic distribution of lobes which makes possible the similarity among bands when the visible range is compressed around the origin. However, it is apparent that a constant field level should be subtracted from the pattern (which is what is has been actually done in Fig. 3.29) to keep similarity. Actually, such a kind of behavior is the same one obtains if the visible range is contracted by a factor of δ around the main-lobe in any of the Koch patterns described in sections 3.2.1 through 3.2.3. Obviously, neither the directivity nor the SLR would be kept constant in this case. A possible solution to this problem would be controlling the current amplitude of the central element of the array. By subtracting the proper amount of current amplitude to such a central element, the DC field level could be adjusted in the pattern domain to achieve the desired behavior through the bands. In the case of arrays with no central element, which is actually the case of the concentric ring array, an additional central element with an adjustable negative current amplitude level would be required.

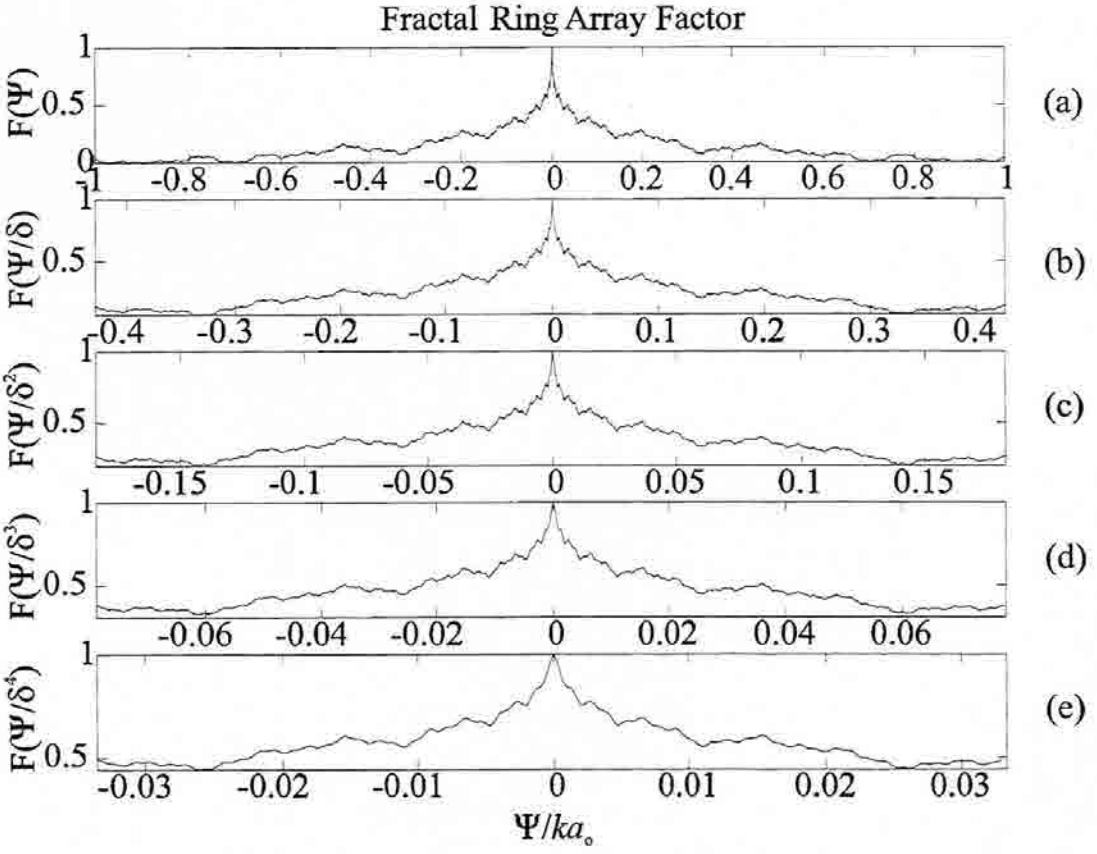

Fig. 3.29 Weierstrass array factor from a fractal concentric ring array (D=2, δ=2.34, M=10). The patterns correspond to the five upper bands λ_0=d/2 (a); $\lambda_1 = \delta\lambda_0$ (c); $\lambda_2 = \delta^2\lambda_0$ (c); $\lambda_3 = \delta^3\lambda_0$ (d) and $\lambda_4 = \delta^4\lambda_0$ (e). Notice the variation on the vertical axis scale.

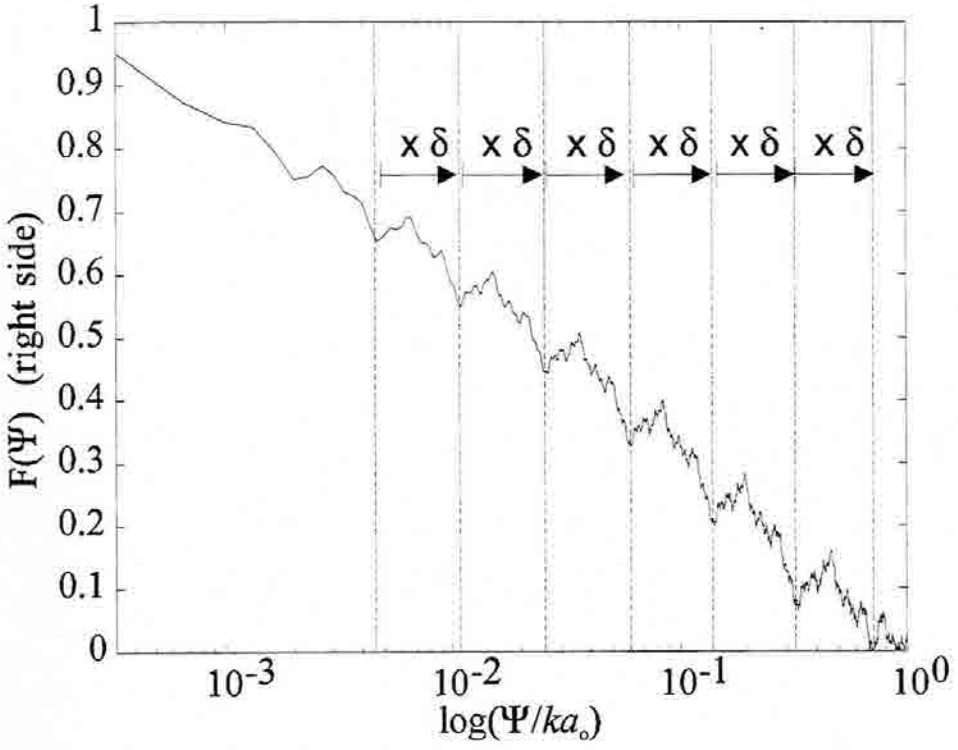

Fig. 3.30. Logarithmic plot of the half right side of the array factor of Fig. 3.29(a). Notice the similarity among lobes which, however, are located at different levels (self-affinity).

3.3 - Conclusions

A novel approach to the design of frequency independent radiating systems has been presented in this chapter. Fractal structures are used in the design because of their self-similarity properties. The effort has been focused in describing a technique to design low side-lobe and multiband arrays, which has always been difficult due to the sensitivity of most current design techniques to variations on the operating wavelength.

Two main approaches have been followed in sections 3.1 and 3.2 respectively: the placement of the array elements on a fractal set of points (the Cantor set), and the design of array factors with a fractal (Koch) shape. Although the Cantor arrays have shown to have similar patterns at several bands, some important properties such as main-lobe width and directivity are not held constant through the bands. On the other hand, such structures have shown to be useful to synthesize low side-lobe patterns with uniform amplitude current distribution arrays. Some design rules have been established for synthesizing uniform amplitude arrays with a nearly binomial shape taking into account minimum spacing among elements and directivity constraints.

The Koch array factors designed in Section 3.2 do keep the same directivity, lobe structure and SLR at each operating band. A Koch pattern designed by using a Blackman window generator can be conformed with seventy-five elements, resulting in an array factor that would operate at five bands, covering a total 81:1 frequency range. Such an array would present a multiband behavior rather than a frequency independent behavior and its radiation resistance is not held constant through the bands. The current distribution that would generate such a pattern can be seen as an interleaving of power-law arrays, which present some interesting self-similarity properties as well.

The similarity properties of Weierstrass array factors have been also discussed. The example of a fractal concentric circular array shows that such arrays can present a multiband pattern, provided that a proper amplitude correction on the central element of the array is done.

Any practical implementation of the fractal multiband arrays and array factors would require multiband antenna elements. This issue is covered in next chapters.

4. *On the Behavior of the Sierpinski Antenna*

Fractals have shown to display some interesting self-similarity properties which might provide multifrequency features to radiating systems. Some theoretical aspects upon this issue were investigated in Chapter 2, while a first design approach to multiband fractal antenna arrays has been introduced in Chapter 3. The present and next chapters deal with the design of fractal antennas. Both experimental and numerical results are presented to describe the operation of some fractal antenna prototypes.

4.1 - Multiband features of the Sierpinski monopole

The triangular Sierpinski gasket was chosen as the first candidate to explore the multiband properties of fractal antennas. Several reasons led to that choice. First of all, its behavior can be readily compared to the well known [67]-[69] triangular (bow-tie) antenna. Second of all, its overall triangular shape provides a convenient way of feeding the antenna structure through one of its apex. Given the self-similarity property of its shape, one could expect electromagnetic waves traveling from the apex to the tips becoming radiated by the smaller subgaskets when the wavelength properly matches any gasket size. One could assume that for a particular wavelength, smallest details (i.e., the small fractal iterations) could not be resolved by such waves and thus not significantly contribute to the overall performance of the antenna. Analogously, if the traveling waves become efficiently radiated in some part of the antenna, the rest of it could become effectively disconnected such that the larger scale would not contribute much to the radiation process either. This way, only a finite range of scales would intervene in the antenna behavior. Since such a range is available at several sizes within the antenna structure, a similar performance among the wavelengths matching such sizes should be obtained, yielding this way, a multifrequency operation.

4.1.1 - Input impedance and return-loss

Several prototypes of Sierpinski monopoles were constructed and tested [89],[93],[95],[96] the first of them being a four-iteration structure (Fig.4.1) of thin triangular copper plate properly welded together to conform the antenna shape [93]. The standard printed circuit technique has been shown to be the easiest and most reliable method for constructing the antenna. Applying such a technique, a five-iteration gasket was single-side printed on a standard microwave Cuclad 250 GT substrate (dielectric permitivity ε_r=2.5, thickness h=1.588 mm) to provide a stiff support to the thin copper antenna shape.

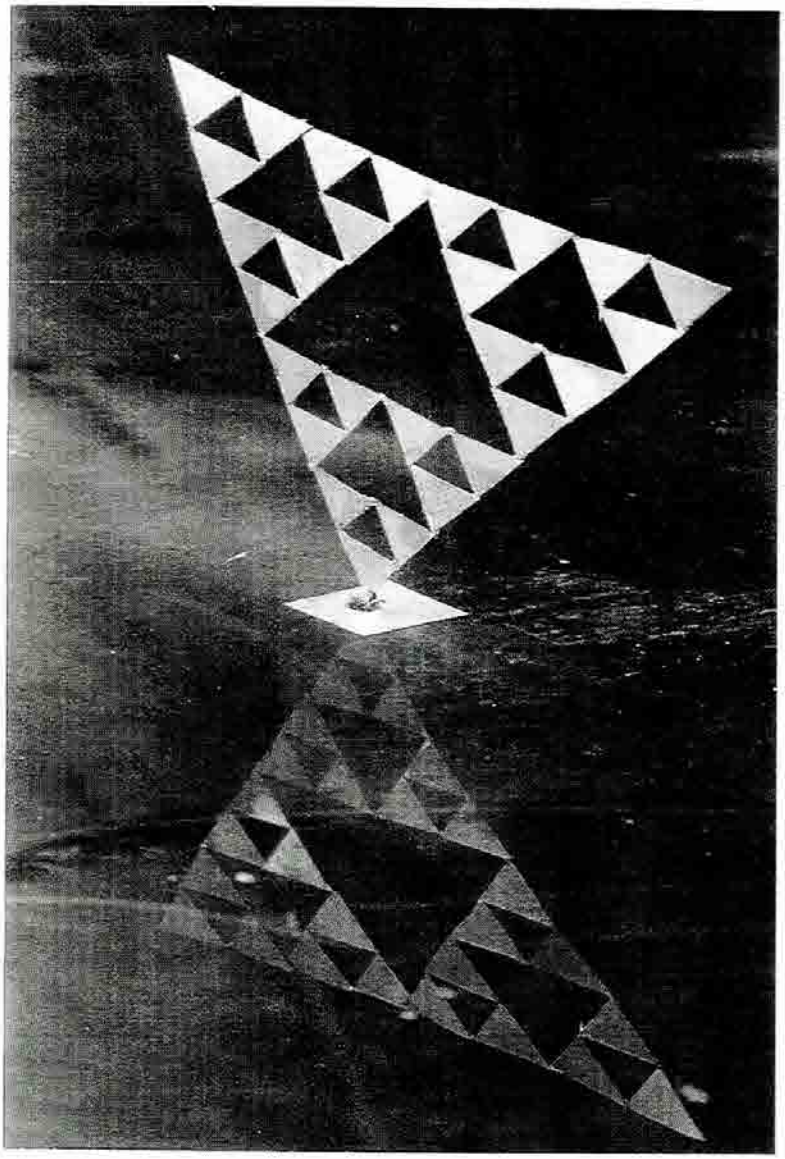

Fig. 4.1 The prehistory of fractal antennas: the Sierpinski monopole first prototype.

The printed structure was mounted over a 80 x 80 cm^2 aluminum ground plane and fed through a 50Ω coaxial probe. The monopole configuration was chosen because it provides a simple way of feeding the antenna and avoids using a balun transformer. Since the main goal was investigating the input impedance behavior through a very large frequency range, a broadband balun would had been necessary for a dipole configuration. Although some schemes have been already described for designing broadband baluns [45],[70], a proper deembeding algorithm should be applied to subtract the balun effect from the measured input impedance and thus derive the true fractal antenna performance.

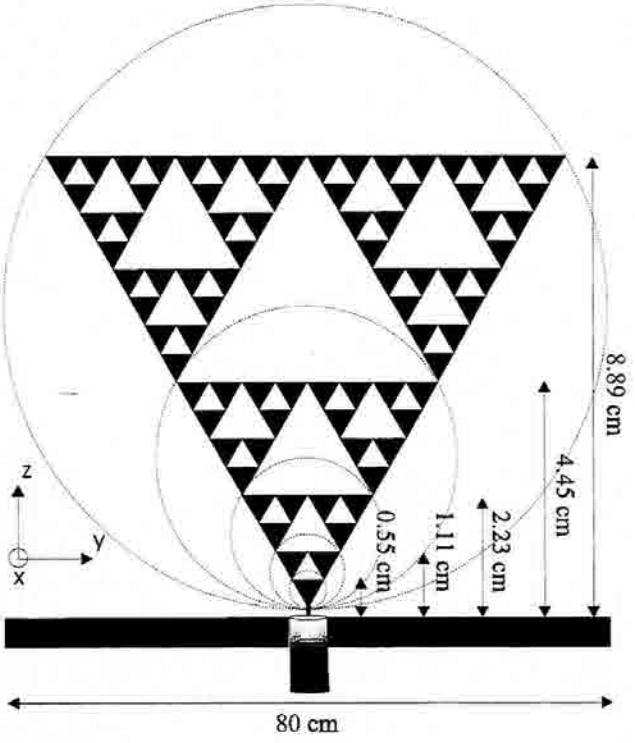

Fig. 4.2 The Sierpinski monopole (five iterations). Each subgasket (circled) is an scaled version of the whole fractal shape.

The 8.89 cm tall fractal monopole (Fig. 4.2) was measured in an HP-8510B network analyzer in the 0.05 GHz - 16 GHz frequency range. Also the antenna was numerically analyzed both using an FDTD algorithm [94],[113],[114] (see more details in Section 4.2.3) running on a Connection Machine (a CM-200 at the CEPBA[1] and a CM-5 at the CNCPST[2]),

[1] CEPBA is *Centre Europeu de Paral.lelisme de Barcelona.*

[2] CNCPST is *Centre National de Calcul Parallele en Sciences de la Terre* in Paris.

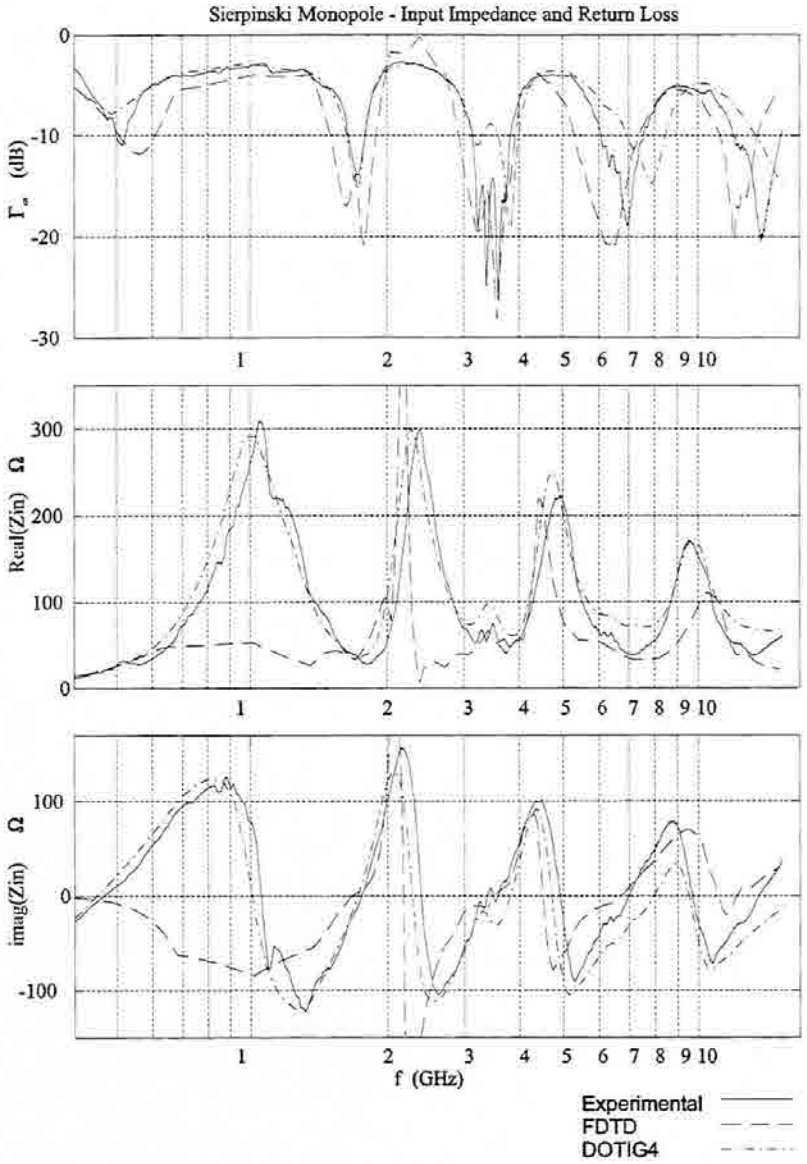

Fig. 4.3 Input reflection coefficient, Γin, relative to 50Ω(a), input resistance Rin(b) and input reactance Xin(c) of a five-iteration Sierpinski monopole.

and the DOTIG4[3] software package running on a Sun Sparc workstation. The input resistance R_{in} and reactance X_{in}, together with the magnitude of the input reflection coefficient Γ_{in} relative to 50Ω (also named the input return loss L_r) are plotted versus a logarithmic frequency scale in Fig. 4.3.

[3] The DOTIG4 simulation is a courtesy of Dr. Rafael Gomez from the University of Granada.

The multiband behavior of the fractal antenna is precisely stated in this plot. Five log-periodically spaced bands are clearly distinguished in all three parameters. Experimental and numerical results are in a good agreement and both yield to such a multiband behavior. To show the manifest agreement among experimental and numerical results a proper linear phase correction has been applied to the measured input reflection coefficient. Such a correction (which does not perturb the measured return-loss characteristic) is necessary due to the non-ideal point-like feeding source in the experimental setup.

While a point-like source can be theoretically placed at the antenna apex in the numerical simulations, the finite SMA-connector size can not be avoided in the real antenna. Nevertheless, the results show that the effect of the non-ideal terminal region can be simply modeled by a short piece of a 50Ω transmission line of length d, which only introduces a reference plane displacement on the measured input impedance. Such a length was empirically adjusted by shifting the input reflection coefficient reference plane as

$$\Gamma_{in}' = \Gamma_{in} e^{j4\pi fd/c} \tag{4.1}$$

until the best agreement was found.

The Sierpinski monopole is well matched (VSWR<2, L_r<9.5 dB) at five bands because the input resistance approaches 50Ω where the input reactance becomes negligible (odd resonances). The main features of regarding the band locations, width and spacing are described in *Table 4.1*.

n (band n^o)	f_n (GHz)	BW (%)	L_r (dB)	f_{n+1}/f_n	h_n/λ_n
1	0.52	7.15	10	3.50	0.153
2	1.74	9.04	14	2.02	0.258
3	3.51	20.5	24	1.98	0.261
4	6.95	22	19	2.00	0.257
5	13.89	25	20	-	0.255

Table 4.1. Main parameters of the measured Sierpinski monopole

The five bands frequencies (f_n) are picked up at the lowest input return-loss points (band number in column 1, frequencies in column 2). The third column describes the relative bandwidth at each band for VSWR<2; the fourth one the input return-loss; the fifth one represents the frequency ratio between adjacent bands, and the sixth one the ratio

between the height (h_n) of the five subgaskets (circled in dashed lines in Fig. 4.2) and the corresponding band wavelength (λ_n).

It is interesting to notice that the bands are log-periodically spaced by a factor of δ=2, which is exactly the characteristic scale factor that relates the several gasket sizes within the fractal shape. The number of bands is directly associated with the number of fractal iteration stages, which indicates that one could freely design the number of operating bands by properly choosing such a construction number. The antenna performance is kept similar through the bands, with a moderate bandwidth (~21%) at each one. From the band location and the height to wavelength ratio numbers, an empirical design equation for the Sierpinski monopole can be derived

$$f_n \approx 0.26\frac{c}{h}\delta^n \tag{4.2}$$

where c is the vacuum speed of light, h is the height of the largest gasket (i.e. the whole antenna) and δ is the log-period (δ≈2). The bands are slightly deviated from those reported in [89], where h/λ≈0.29. This is related to the thicker substrate (h=1.588 mm as opposed to h=0.127 mm) and its higher permitivity (ε_r=2.5 as opposed to ε_r=2.17), which makes the whole antenna structure appear slightly longer [65],[66].

A significant deviation from the log-periodic behavior can be stated at the first band. Neither the bandwidth and return-loss, nor the spacing with respect the next band is kept similar to the rest of the bands. Such a phenomena can be mostly related to the truncation effect; the largest gasket (the overall structure) lacks of larger fractal iterations breaking this way the symmetry with respect to the central bands. To get a deeper insight on the antenna behavior and the truncation effect, the antenna is compared in Section 4.2 to a classical Euclidean triangular antenna through numerical and experimental results.

4.1.2 - Radiation patterns

A truly multiband performance can not be solely stated from the antenna input impedance behavior; the agreement among bands has to be proved too. While in many antennas usually the bandwidth constrains come from the input impedance rather than from the radiation patterns, here the whole frequency range is very large (1:8) and the agreement among patterns can not be assumed. The antenna is about 4 wavelengths long at the highest bandwidth and one could expect many grating lobes appearing within the visible range,

similarly to what is found in common antennas (an example of the increase of the number of grating lobes with frequency for a common monopole has been already shown in Fig. 2.19, Section 2.2.2.2).

The full radiation patterns of the Sierpinski monopole, measured at the minimum VSWR frequency points, are shown in Fig. 4.4. It becomes apparent that their main features are kept similar through the bands: a two lobe structure with some tendency to enhance radiation in the x direction. Such a propensity could be expected if one takes into account that the antenna is planar and displaying the larger extension in the yz plane, orthogonal to the maximum direction. The antenna is basically linearly polarized in the θ direction, with an average

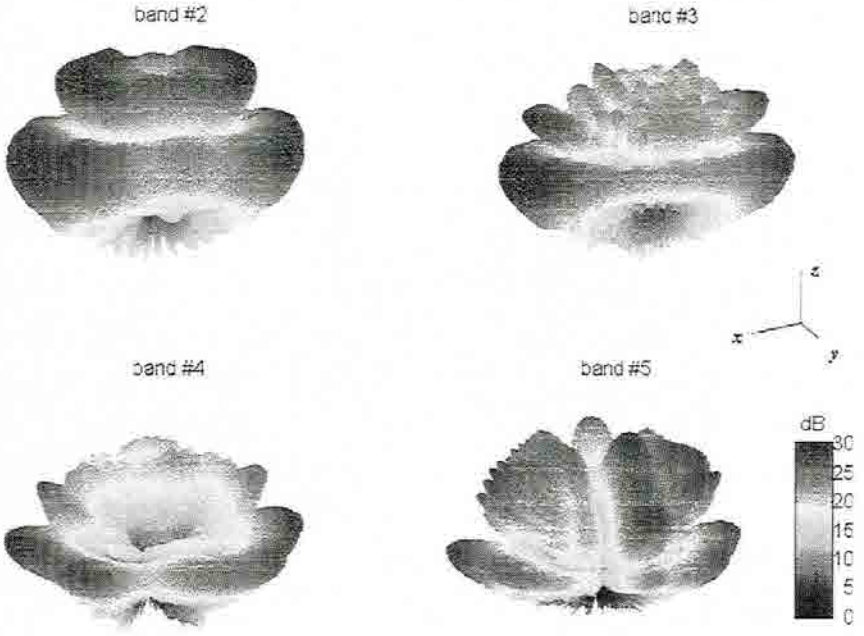

Fig. 4.4. Radiation patterns (E_θ component) of the Sierpinski monopole at the four upper bands. The patterns have been measured at VSWR minimums.

cross-polar ratio around 20 dB in the maximum direction. The valley between the main two lobes is kept approximately at 30° at all wavelengths. The patterns also display a minimum

along the longitudinal direction (z axis), which could have been anticipated from the antenna geometry as well.

Beyond the overall similarities the patterns exhibit some disagreements among bands too. Mainly, the lobe closest to the zenith tends to display a higher ripple for increasing frequencies. One could link such behavior to the non multiband performance of the finite ground plane; the currents flowing over it can become reflected at its edges resulting in a standing wave distribution which would have the most important contribution to radiation along the plane's orthogonal direction. Since the square plane is not self-scaleable, its size relative to wavelength is larger at the upper bands, resulting in a interference pattern with faster variations which might explain the pattern ripple at the upper bands. Also, the expected null in the z-axis direction is hidden by the contribution of the antisymmetrical mode of the ground plane to the overall radiated power [51] .

A more detailed view of the antenna frequency behavior is displayed in Fig. 4.5 and Fig. 4.6 .The main cuts (front-to back φ=0°, left-to-right φ=90° and azimuth θ=90°) are displayed for both the E_θ and E_φ components with a 30dB dynamic range. All cuts are normalized with respect to the absolute pattern maximum, and two cuts are shown for each band: the cut at the VSWR minimum and the cut at the band edge. It is interesting to notice that the multiband behavior appears even more clear near the band-edge, at frequencies 2, 4, 8 and 16 GHz. The E_φ component is almost negligible everywhere except for the φ=90° cut at the upper bands. Such an increase of the crosspolar component could be explained through the thickness of the antenna substrate (h=1.588mm) which becomes barely one tenth of a wavelength at the highest frequency. A surface wave similar to that of thick microstrip antennas [73],[116] can be trapped within the substrate and become radiated at the antenna's edges. Anyway, such a crosspolar component should be related to the antenna behavior rather than to a parasitic ground plane effect, since the shape of the pattern is kept constant through the bands for this component as well.

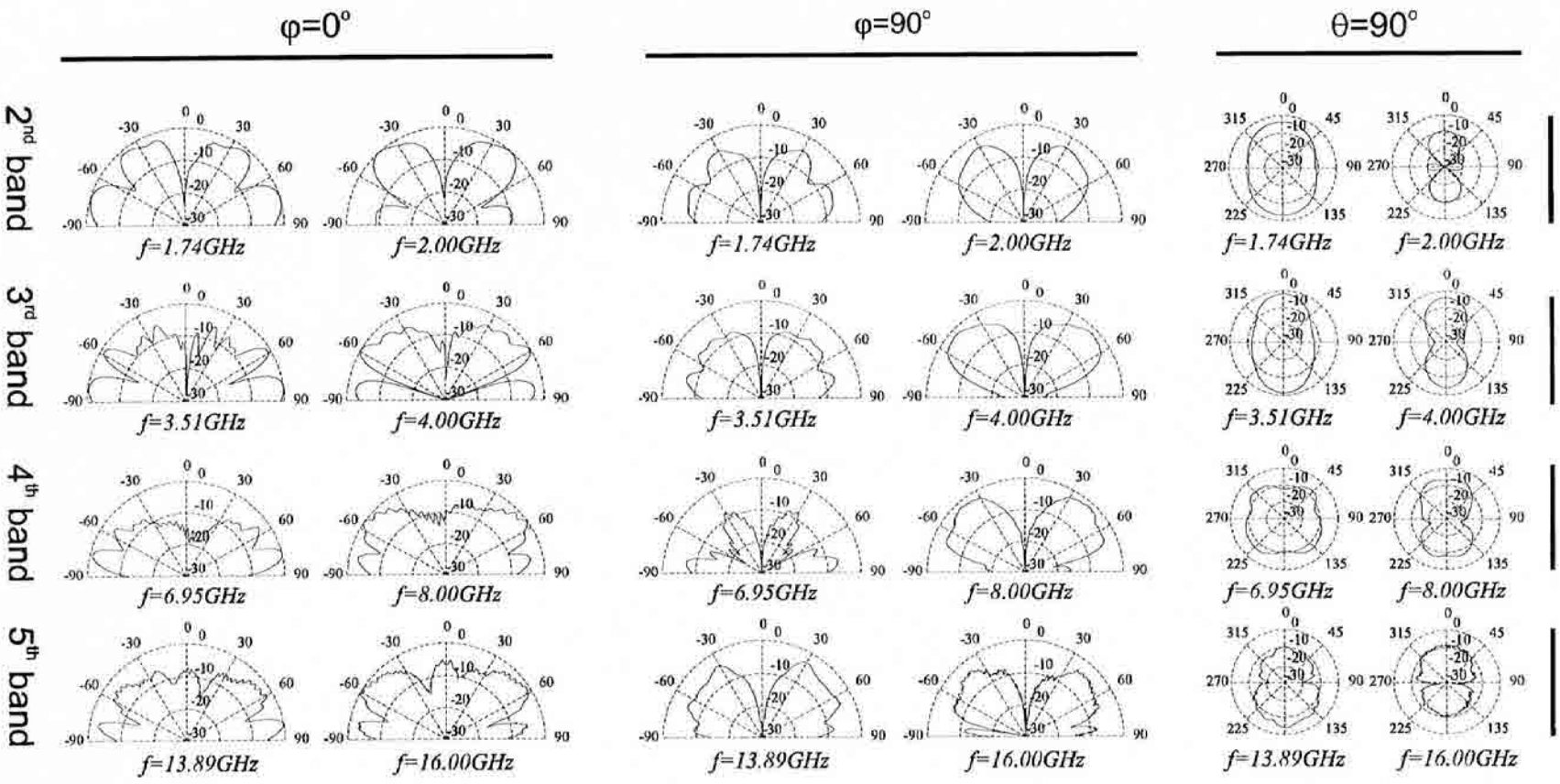

Fig. 4.5 Sierpinski monopole radiation pattern main cuts(E_θ component). Two cuts are displayed for each band, the first at the minimum VSWR points and the second at the upper band edge. The similarity among cuts is more clear at frequencies 2, 4, 8 and 16 GHz.

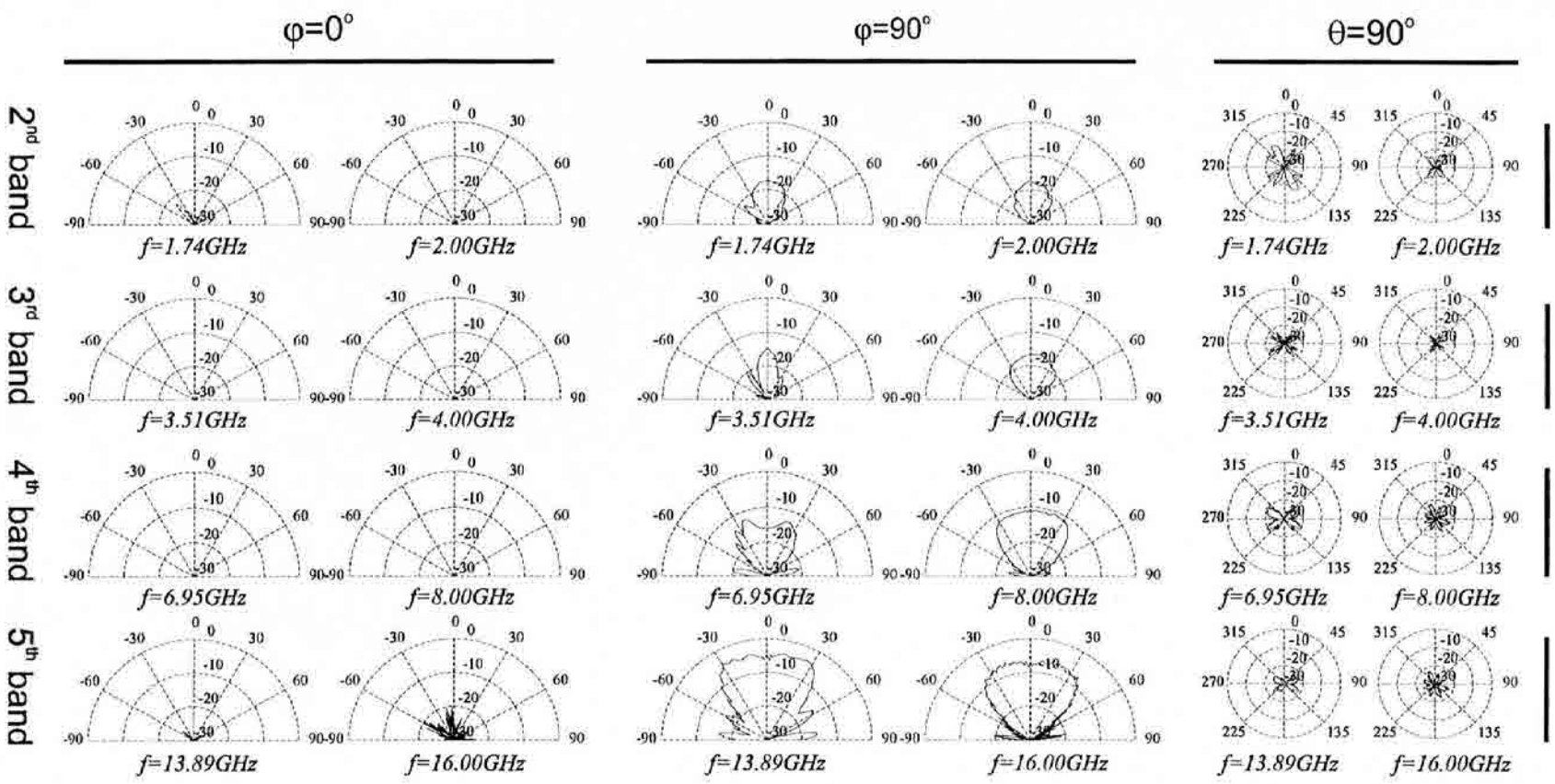

Fig. 4.6 Sierpinski monopole radiation pattern main cuts(E_φ component). Two cuts are displayed for each band, the first at the minimum VSWR points and the second at the upper band edge. This component is normalized with respect to the E_θ one. The antenna is basically linearly polarized, although an increase on the level of the crosspolar component is observed at the upper bands.

4.2 - Comparison with the Euclidean triangular antenna.

A deeper understanding on the antenna performance can be gained through the study of the Euclidean mate of the fractal Sierpinski antenna. The triangular (bow-tie) antenna was developed as a natural approach to the conical antenna. Featuring a convenient planar form, it was expected that the triangular shape presented a broadband behavior since it is ideally a shape only defined by angles. However, the results where discouraging since the truncation principle was not held, similarly to what happened to the conical model, and a frequency-independent behavior was not supported by the antenna. A thorough experimental study of the bow-tie antenna was carried out by Brown and Woodward in [67].

4.2.1 - Input impedance and Return-Loss

Five copper bow-ties of the same size (8.9 cm, 4.45 cm, 2.23 cm, 1.11 cm and 0.55 cm) as each one of the gaskets on the Sierpinski antenna (circled in dashed lines in Fig. 4.2), were measured to compare the results between the fractal and the Euclidean shape. The input return loss (L_r) of the six antennas are shown in Fig. 4.7 . While the fractal antenna features a log-periodic band distribution which follows the law in Equation (4.2), the measured bow-tie antennas have a harmonic (periodic) distribution of resonant frequencies which can be described by the following rule

$$f_n \approx (0.17 + 0.44n)\frac{c}{h} \tag{4.3}$$

being n the frequency number and h the height of the triangle. These results basically agree with those of Brown and Woodward [67] who measured, from a thinner bow-tie, a first match at $0.194c/h$ and a second one at $0.43c/h$ from the first (a broader frequency range is shown here since the results in [67] only showed the performance for the first two match frequencies).

The second match of the bow-tie antenna is always better than the first one (L_r>15dB as opposed to L_r =8dB), which might suggest that it can have a more significant effect on the Sierpinski behavior. Thus, if we assimilate each of the lowest subgaskets to a bow-tie, the Sierpinski bands could correspond to the second one of the triangular antennas. The frequency shift towards the origin experimented by the fractal antenna resonances with respect to the triangular ones can be related to the capacitive loading of the upper subgaskets. Such a capacitive loading becomes enhanced by the dielectric substrate bearing the fractal structure.

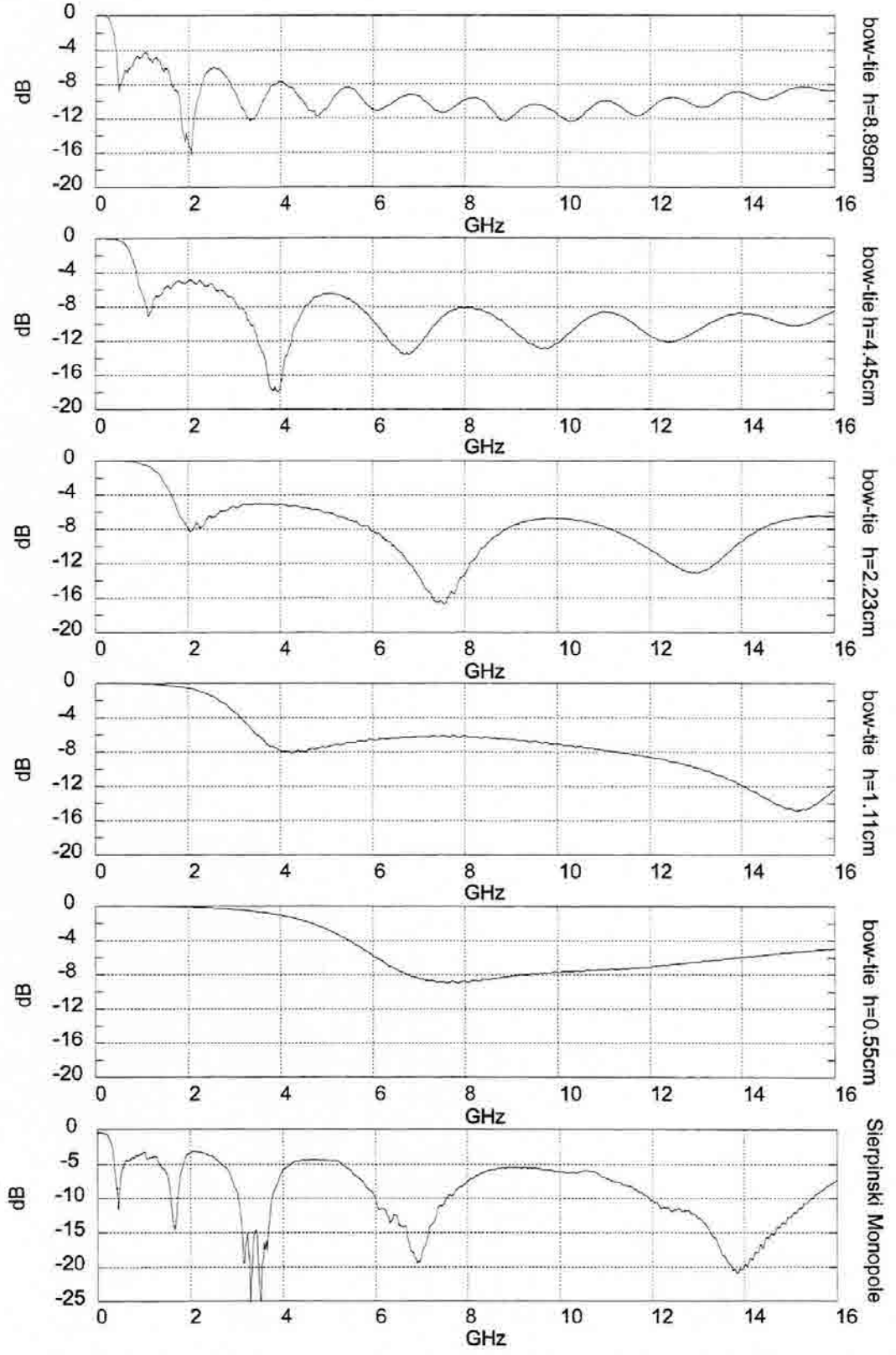

Fig. 4.7 Input return-loss (relative to 50Ω) of the five bow-ties scaled as each one of the five subgaskets on the Sierpinski monopole (from top to down 8.9cm, 4.45cm, 2.23cm, 1.11cm, 0.55cm).

The truncation effect appears clear now: the first Sierpinski band is located at the same position of the first bow-tie resonant frequency because the largest gasket lacks of larger iterations to follow the log-periodic rule. Being the antenna height less than one sixth of the operating wavelength, the holes within the fractal structure have a negligible contribution to radiation and the antenna behaves basically as if it were an Euclidean triangular one.

One could think that the triangular antenna also features a multiband behavior, with a periodic rather than log-periodic distribution of bands. However, each matched frequency on the bow-tie antenna corresponds to a higher order mode with a rather different current distribution. As it is shown in the next section, the radiation pattern is not held through the bands and a truly multiband behavior is therefore not supported by the antenna.

4.2.2 - Dipole radiation patterns

To properly distinguish the real influence of the Sierpinski structure on the antenna radiation patterns, a Sierpinski dipole was constructed and measured. The antenna was fed by means of a coaxial tapered balun similar to that described in [70] to balance and match the dipole through the whole 1-16 GHz frequency range (see Fig. 4.8). Both arms of the antenna were printed on the same substrate used in the monopole. The measurements where carried out in a roll over azimuth configuration with the balun mounted along the y an x axis alternatively to minimize the effect of both the rotation axis and the balun on the φ=0° and φ=90° patterns respectively. The same procedure was used to measure an equilateral bow-tie antenna the same size as the Sierpinski one.

The patterns of both the Sierpinski dipole and a bow-tie antenna of the same size (arm height 8.9 cm) can be compared in Fig. 4.9 through 4.11. Each row displays three patterns within each one of the four upper bands of the Sierpinski antenna. Only the most significant polarization component E_θ is shown. The cuts corresponding to the Sierpinski one are represented on the left half-side of the figure, while the same cuts corresponding to the bow-tie antenna are plotted on the right. Each one of the three figures displays a cut through the main planes (φ=0°, φ=90°, θ=90°) for both antennas. The θ=90° cut is less significant in this situation due to the roll over azimuth measurement scheme.

That is, the antenna is mounted on a vertical post (along the z direction) with the balun being orthogonally mounted parallel to XY plane; when measuring the azimuth cut, the post is rotated around the z-axis such that the antenna becomes necessarily hidden by the support for some angular range. Furthermore, the spurious radiation from the non-ideal balun (see the 3D full pattern measurements in Fig. 4.12) yields the most important contribution to radiation in this plane.

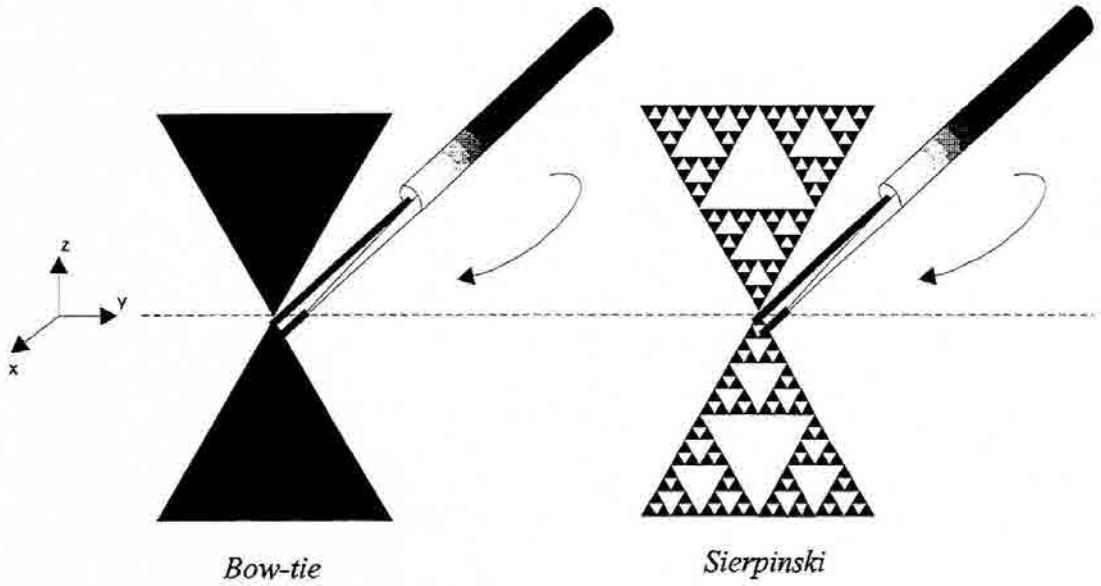

Fig. 4.8 Bow-tie and Sierpinski dipoles. The tapered balun was mounted alternatively along the x and y axis to measure the $\varphi=90^{o}$ and the $\varphi=0^{o}$ cuts respectively.

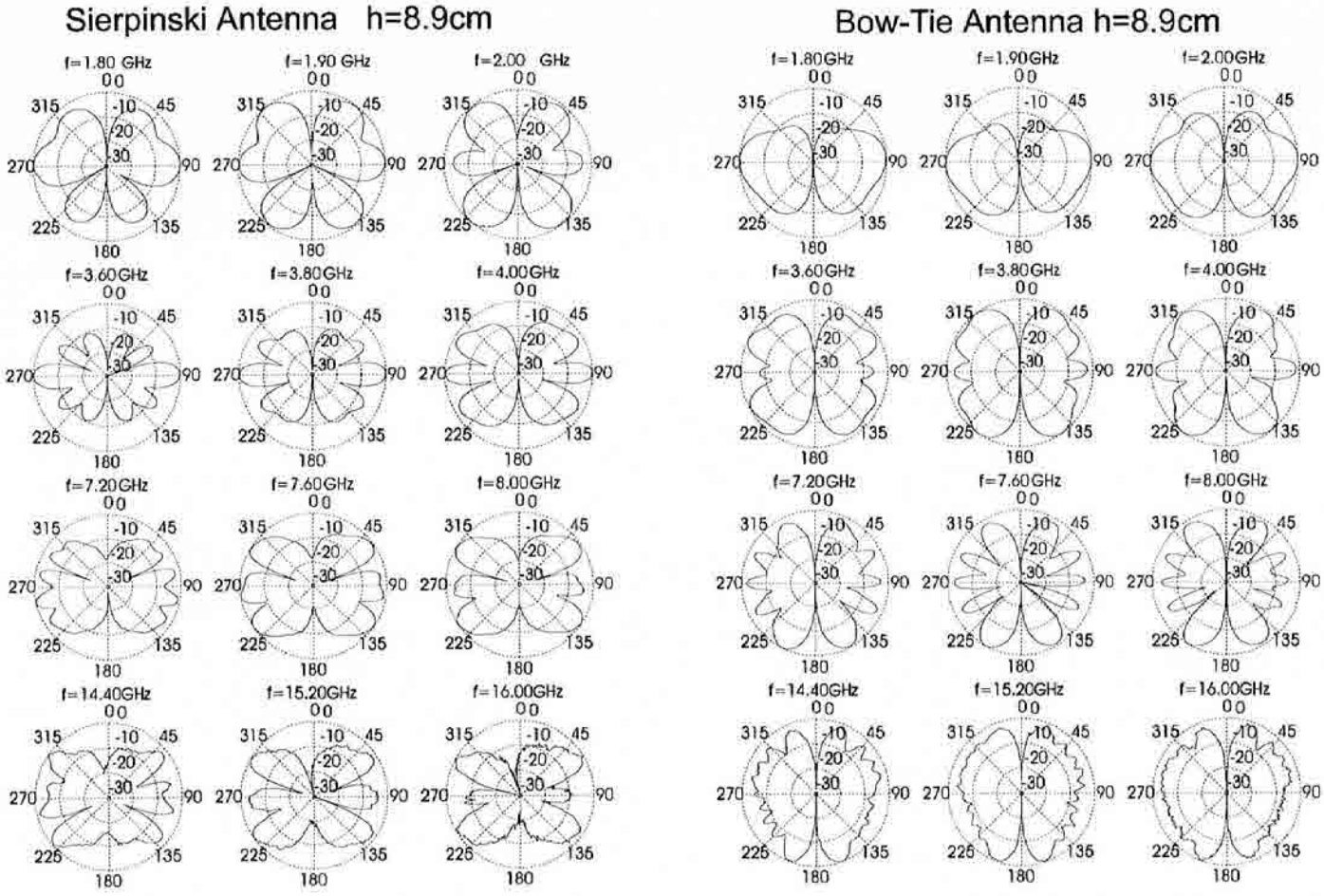

Fig. 4.9 Front to back cut (φ=0°) of both the Sierpinski monopole radiation pattern (left) and the bow-tie antenna (right). The patterns correspond to the Eq component. Each row displays three cuts within one band. Notice the similarity between rows (multiband behavior) as opposed to the differences among columns (not a frequency independent behavior) of the Sierpinski antenna.

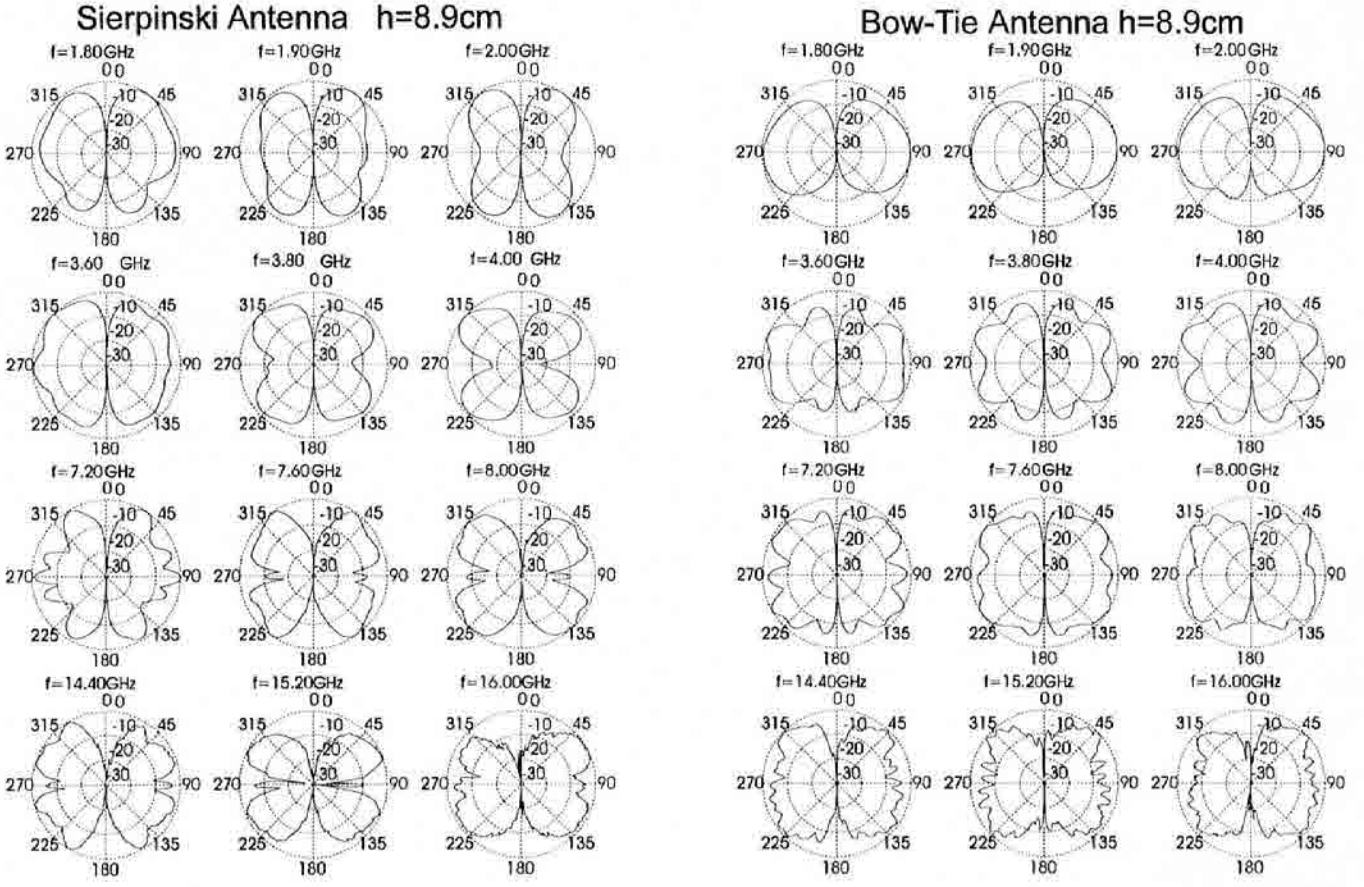

Fig. 4.10 *Left to right cut (φ=90^{o}) of both the Sierpinski monopole radiation pattern (left) and the bow-tie antenna (right). The patterns correspond to the Eq component. Each row displays three cuts within one band. Notice the similarity between rows (multiband behavior) as opposed to the differences among columns (not a frequency independent behavior) of the Sierpinski antenna*

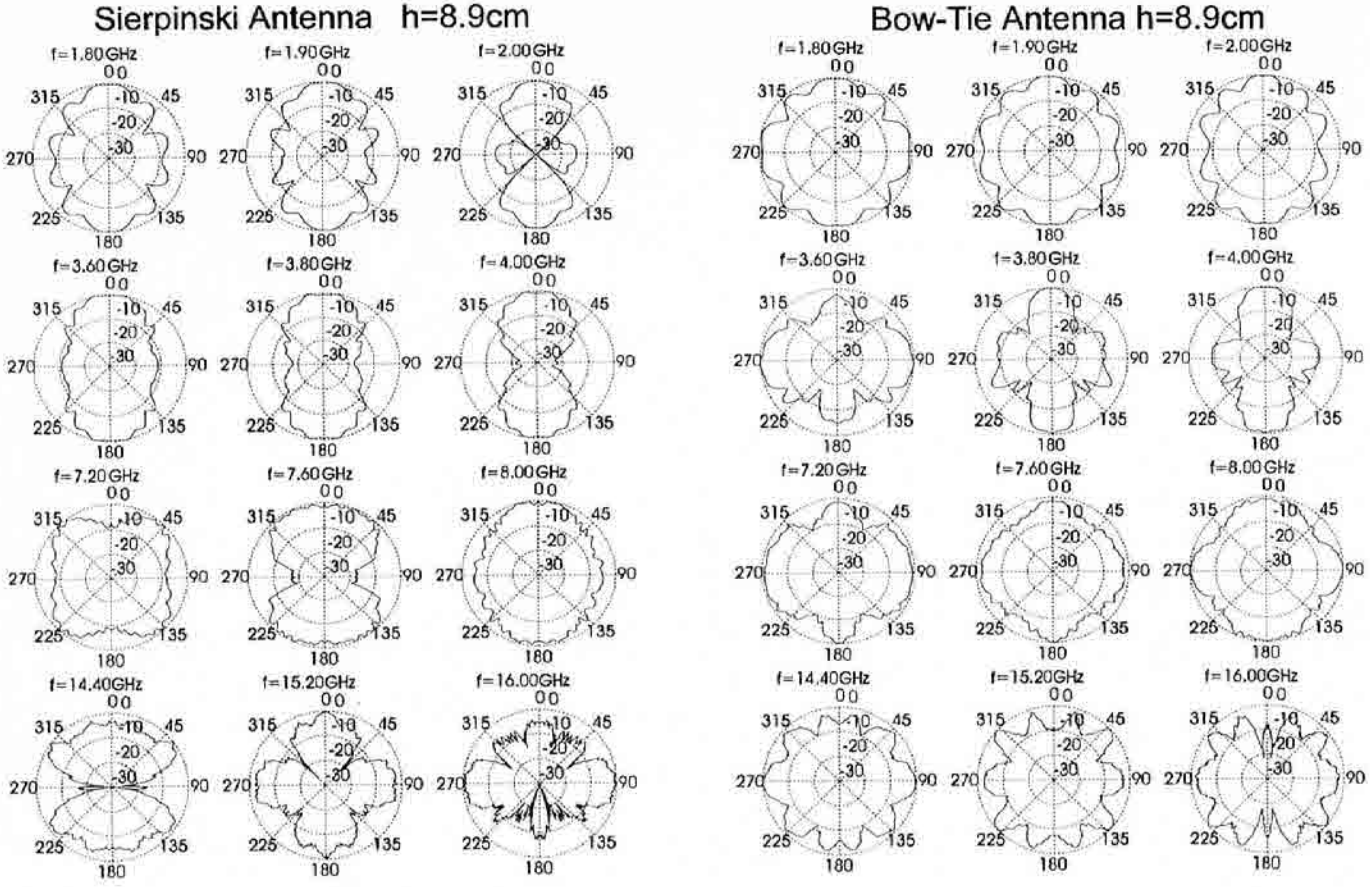

Fig. 4.11 Azimuth cut (θ=90°) of both the Sierpinski monopole radiation pattern (left) and the bow-tie antenna (right). The patterns correspond to the E_θ component. Each row displays three cuts within one band. The roll-over azimuth measurement scheme highly distorts the resulting pattern.

In general, the pattern similarities among bands (rows) appears clear for the Sierpinski antenna. Again, such similarities are specially remarkable at 2, 4, 8 and 16 GHz. These results are clearly different to those of the bow-tie antenna. Although the bow-tie antenna has many resonant frequencies, each one features a different pattern. The behavior is more similar to that of a single-band linear dipole in which increasing the operating frequency results in an increment on the number of grating lobes of the pattern. On the contrary, the Sierpinski antenna must be considered a multiband antenna owing to its coherent behavior through the bands. Nevertheless, it is not a frequency-independent antenna, since both the input return-loss and the radiation patterns yield significant variations within each log-period. A three-dimensional view of four patterns is plotted in Fig. 4.12 as well.

When comparing the dipole patterns to the monopole ones, the non-ideal performance of both the balun and the ground plane can be detected. The balun does not perfectly balance the current between both arms of the dipole, consequently the cuts over the planes orthogonal

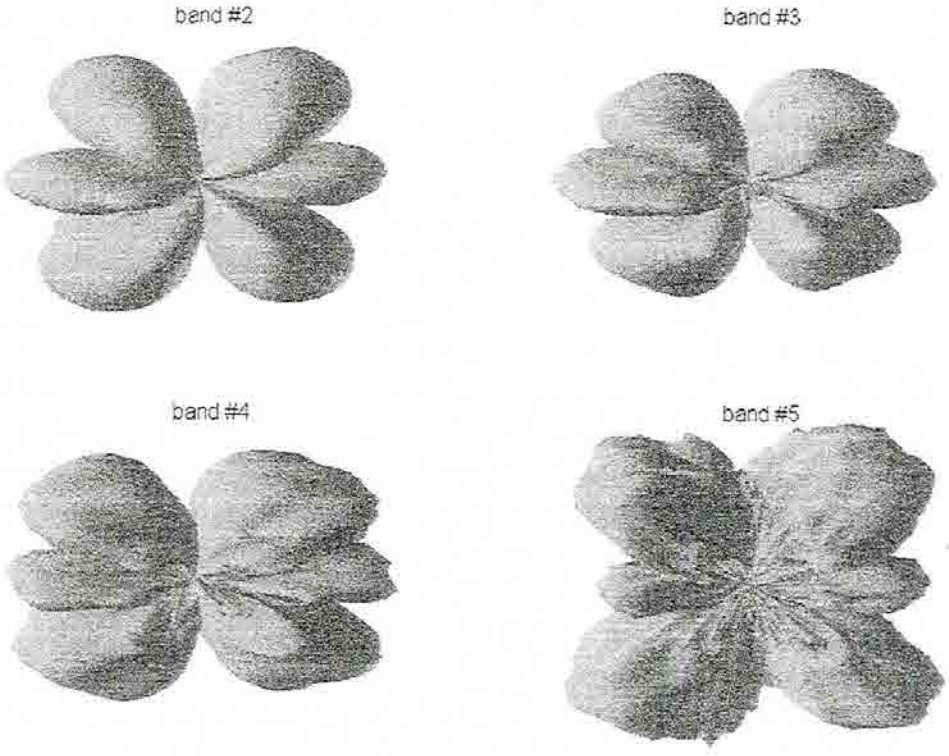

Fig. 4.12 Full patterns of the Sierpinski dipole at the four upper bands (φ=80° view).

to the XY plane display a slight asymmetry. Such an asymmetry enhances radiation towards the -z axis (see the φ=0° cut at 3.6 GHz and 7.2 GHz) and tends to hide some nulls of the pattern. However, the lobe structure becomes apparent and the similarity among bands appears clearly. Furthermore, the expected nulls along the z axis can be distinguished now, which supports the idea that the former ripple and lobes that appeared in the monopole were due to the ground plane.

Another interesting feature of the Sierpinski patterns is the characteristic three-lobe structure on the φ=0° cut. Such a pattern is comparable to that on the third matched frequency of the bow-tie antenna (f=3.34 GHz for the h=8.9 cm case); if we compare the third band frequencies (Eq. (4.2)) of the five bow-ties to those of the Sierpinski one (Eq. (4.3)), one can notice that those on each bow-tie are very close to a Sierpinski one. Hence, instead of relating each Sierpinski band to a bow-tie one, this suggests that the fractal antenna actually opeartes at each band in a combination of two modes corresponding to two bow-ties at different scales, the larger working on its third resonance and the smaller on its second one.

4.2.3 - Current Density distribution

In order to get a deeper physical insight on the behavior of the Sierpinski antenna, a Finite-Difference in the Time Domain algorithm (FDTD) was developed to calculate the current density distribution over the fractal surface. The FDTD method [94],[113],[114],[115] basically consists on sampling both time and space and solving Maxwell differential equations by approaching spatial and temporal derivatives by sample increments. This way one can calculate the evolution of electromagnetic waves, when interacting to an arbitrary object, for any point in time and space. This method is particularly suitable for analyzing transient effects. Also, it appears very convenient when analyzing an electromagnetic problem on a wide spectral range : a narrow pulse containing a wide spectrum of frequencies can be easily launched into the FDTD algorithm, then the spectral response over the whole frequency range can be easily derived by Fourier transforming the time domain response.

4.2.3.1 - The FDTD Sierpinski Antenna Analysis

The FDTD algorithm was written in a C* code and run on a Connection Machine CM-5 using a 32 x 256 x 256 cell space. That is, the (x,y,z) rectangular coordinate system was sampled such that six matrices (one for each of the three components of electric and magnetic fields) of the same size as the cell space contained all the electromagnetic

information at every discrete instant of time. The space samples became described by three indexes (i,j,k) being the space among such samples $(\Delta x,\Delta y,\Delta z)$ the so called Yee cell [113]. To simulate the Sierpinski antenna problem, the Yee cell dimensions were chosen to be Δx=0.463 mm, Δy=0.267 mm, Δz=0.463 mm [94]. Tipically, one has to pick a high enough sample rate such that any side of the Yee cell is smaller than $\lambda/10$, being λ the shortest considered wavelength. This criteria ensures a smooth variation of the fields from one cell to the other such that the finite difference becomes a good approach to the derivative of the differential equation governing the field evolution. Similarly, the time increment Δt is chosen to follow the Courant stability criteria [115], which states

$$v \cdot \Delta t \leq \left(\frac{1}{\Delta x^2} + \frac{1}{\Delta y^2} + \frac{1}{\Delta z^2} \right)^{-1/2} \tag{4.4}$$

being v the maximum phase propagation constant (the vacuum speed of light c in our case). Although (4.4) just establishes an upper bound for Δt, it is not convenient to pick an arbitrary small value. This would lead to a larger number of calculations to cover the same overall simulation time interval, and that might convey an increase of the cumulative numerical errors.

To minimize both memory space and computing time, the object symmetry was properly taken into account in the modeling process. Being the antenna placed on the YZ plane with the apex at the coordinate origin, the lower half-space (z-) does not need to be simulated if an electric wall is placed at the XY plane. Also, the even symmetry with respect to the XZ (left to right) and YZ (front to back) planes can be taken into account by placing there two magnetic walls. Electric walls can be conveniently introduced by forcing the tangential components of electric fields to vanish at the wall position. Analogously, magnetic walls are implemented by forcing the equality among the tangential electric field components from neighbor cells at both sizes of the wall. By following such a procedure, the simulation space becomes reduced to $1/8^{th}$ of the whole space, i.e., the space sector defined by the positive directions (x+,y+,z+).

Even though the use of electric and magnetic walls considerably reduces the size of the simulation space, it still remains infinite unless it is properly truncated at some point. This was achieved by placing second order Mur absorbing boundary conditions [114] at the three remaining walls, i.e., i=32, j=256 and k=256. The absorbing boundary conditions predict the value of electromagnetic fields at the outer limits of the simulation space such that the field boundary values inside it can be computed. Such a prediction must be accurate

to avoid residual numerical induced reflections of the waves reaching the space limit, which would interfere the true solutions of the problem [113]-[115].

Once the simulation space and the antenna structure were properly modeled, a voltage source (i.e., an electric field source) was placed at the antenna apex (i_o,j_o,k_o). When computing the antenna input impedance $Z_{in}(\omega)$, a short Gaussian pulse in the time domain was chosen to explore the whole frequency range. That is, the E_z component of the electric field was forced to be

$$E_z^n(i_0,j_0,k_0) = -\frac{1}{\Delta z} e^{-\alpha((n-\beta)\Delta t)^2} \tag{4.5}$$

where α and β defined the pulse time length and position. They were taken to be

$$\alpha = \left(\frac{4}{\beta \cdot \Delta t}\right)^2$$
$$\beta = 32 \tag{4.6}$$

with Δt=0.804 ps. Such values ensured an almost flat response through the whole frequency range covering the first five antenna bands (the -3dB cutoff frequency was placed at 22.3 GHz). While running the FDTD algorithm through N=4096 time increments, the input current was computed as the circulation of the magnetic field along a closed path around the feeding point (Ampère's law [52],[53]). Knowing the input voltage and current responses, the input impedance was computed applying the Fourier Transform (by means of an FFT algorithm) to both responses such that

$$Z_{in}(\omega) = \frac{V_{in}(\omega)}{I_{in}(\omega)} \tag{4.7}$$

The computed results displayed a good agreement with the experimental ones as shown in Fig. 4.3.

4.2.3.2 - Sierpinski Antenna Current Density Distributions

A sinusoidal signal at each of the four upper bands was used to excite the antenna and compute the current density distributions at each matched frequency. Figures 4.13 through 4.17 display the magnitude $|\vec{J}|$ of the overall current density vector, and the

magnitude and phase of both vertical (J_z) and horizontal (J_y) current density components (all magnitude plots are normalized with respect to its maximum and covering a 30 dB dynamic range). To calculate the current amplitude, the current density maximum at each point was detected at the first period after the transient interval. Analogously, the phase distribution was calculated by computing the time needed by each cell over the antenna structure to reach the current maximum from the first instant of the steady state period.

The right column of the plots in figures Fig. 4.13 through Fig. 4.17 present an expanded view of the region where most of the current is concentrated at each frequency. All of them are scaled by a factor of two, the scale factor existing among bands. The most interesting feature of such plots is noting that the current density distributions on the right column are very similar among them. That becomes specially apparent when one neglects the effect of the smaller holes at the lower bands. This is a reasonable approximation since such holes are small compared to the wavelength and the current density is lower at the regions where holes are placed.

The similarity among the patterns shown in the previous section can now be readily explained: at each band the current concentrates over a properly scaled substructure on the antenna which has the main contribution to the overall antenna performance. When frequency is increased, this region becomes smaller and the current does not reach the top of the antenna at the highest bands. This way, a large area of the structure becomes effectively disconnected. Such a phenomenon is equivalent to the active region found in the log-periodic arrays described in the early sixties by Carrel and Mayes [46],[48], that has been properly introduced in Section 2.3.4, Fig. 2.31. Now, an additional explanation on the behavior of the fractal antenna can be given. When an electromagnetic wave is fed through the tip of the antenna it starts to propagate over the structure towards the flat end of the gasket. When the wave finds a cluster comparable in size to its wavelength it becomes radiated; this way the power of the traveling wave is lost and no current reaches the end of the antenna. The structure has many discontinuities that enhance radiation and emphasizes such a process. If the wavelength is long, the small triangles of the shape contribute less to the overall radiation process such that the current can travel further over it. Then, a larger active region is formed (which will have a similar shape to that of a shorter wavelength) and a similar radiation pattern for such a lower band will be obtained.

Likewise, the current reconstruction also give some insight on the truncation effect outlined before. Although it is difficult to precisely establish the bounds of the active region, it is clear that it actually covers a wider area than the encircled clusters of Fig. 4.2 which, roughly speaking, are about $\lambda/4$ tall. Actually, such a large extent of the current in the z

direction (larger than one wavelength) could explain the similarity of the φ=0° pattern to that of a 1.5λ dipole [52]. Therefore, to properly model the antenna behavior at least an additional scale level should be taken into account. Hence, it becomes clear that the whole antenna is not large enough to support an equivalent active region at the lowest band; this way the active region becomes distorted and the antenna looses the self-similarity properties with respect the higher bands. This way, one could say that the antenna operates in a "bow-tie mode" rather than into a true Sierpinski multiband mode. The first resonant frequency is barely the same as the triangular antenna except for a slight shift towards the shorter wavelengths due to the extra self-inductance introduced by the holes of the gasket.

Finally, it is remarkable that the current similarity is held for both components of the current density as well as for the phase maps. Therefore, it can be naturally assumed that such an agreement is not a matter of chance, but it is due to a translation of the self-similarity geometrical properties of the fractal shape to its electromagnetic behavior.

For the sake of completeness, the current density distribution over the bow-tie antenna is also displayed in Fig. 4.18. The plots show the distribution at the first six match frequencies of the antenna. The main difference among these and the former Sierpinski antenna plots is that the bow-tie antenna does not operate through a self-scaleable active region. The current easily flows from the apex to the tips of the antenna traveling along the structure edges; the current distribution keeps always the same size (the antenna's size) and does not scale with wavelength making the whole antenna to remain single-band. It is interesting to notice that the current forms a sort of standing wave distribution, with faster variations at the higher frequencies.

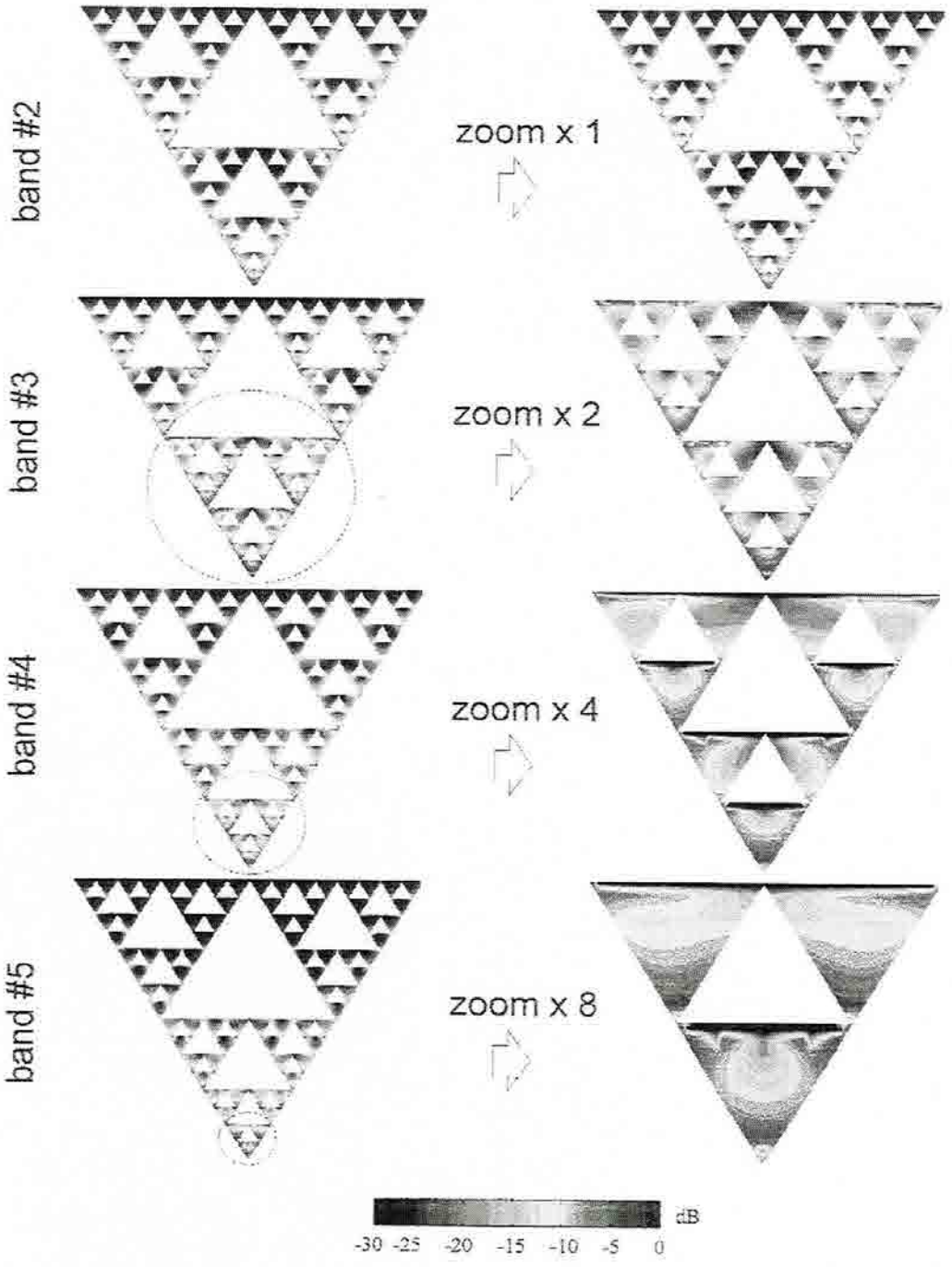

Fig. 4.13 Magnitude of the current density distribution over the Sierpinski antenna (FDTD). The right column displays a zoomed view of the active region at each band. Notice the similarity among regions when scaled by wavelength.

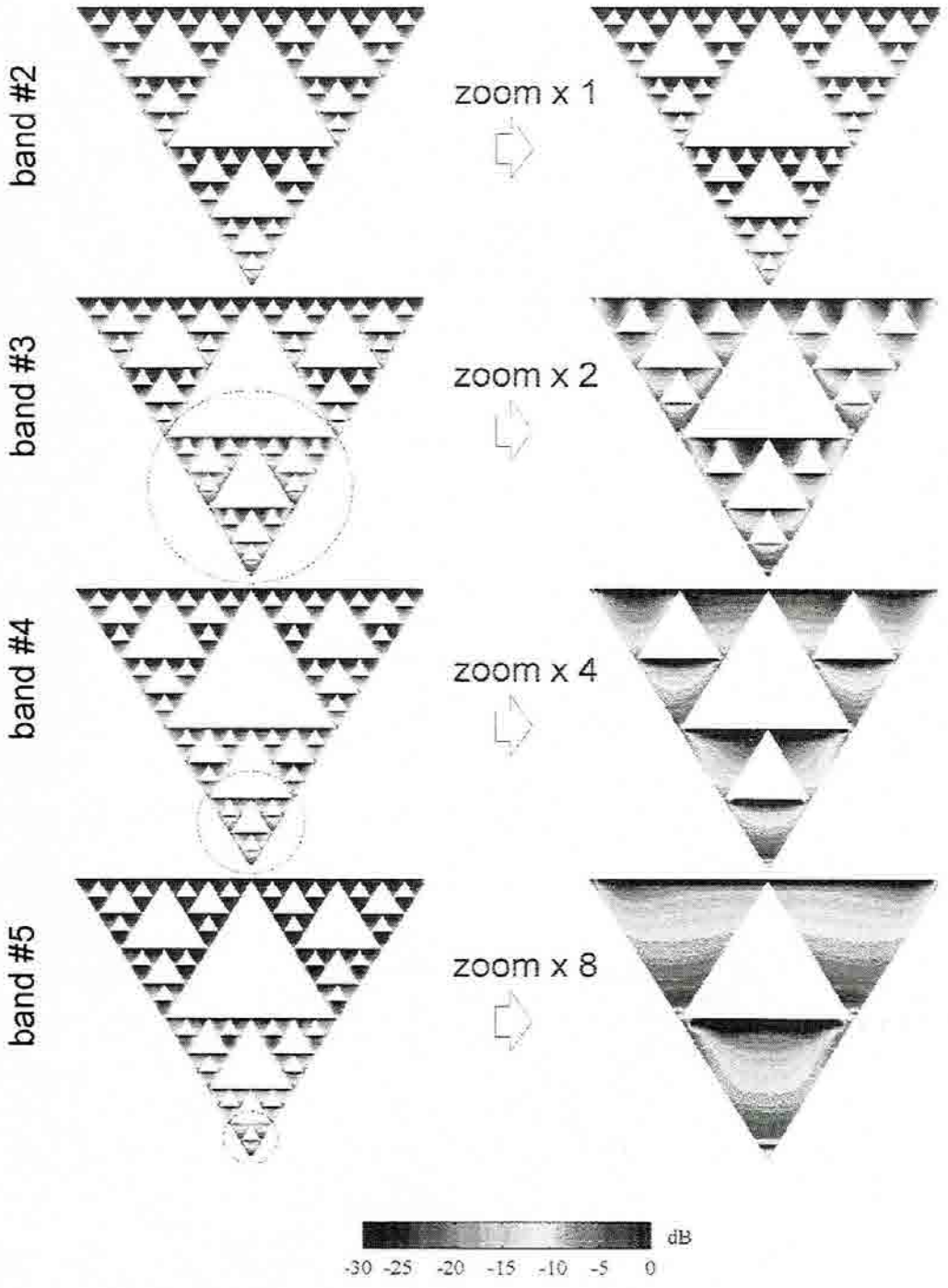

Fig. 4.14 Magnitude of the current density vertical component (J_z) over the Sierpinski antenna (FDTD). The right column displays a zoomed view of the active region at each band. Notice the similarity among regions when scaled by wavelength.

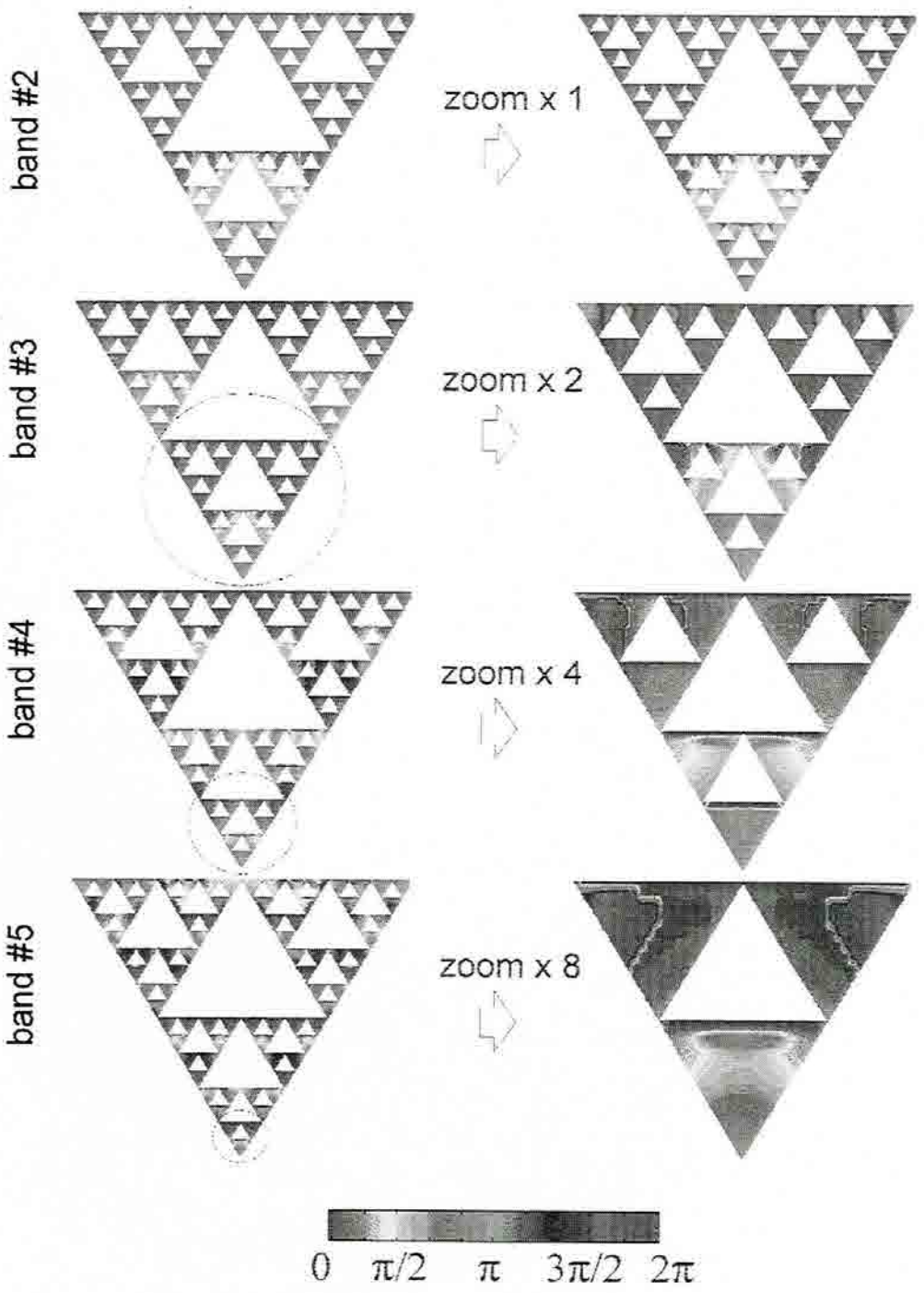

Fig. 4.15 Phase of the current density vertical component (J_z) over the Sierpinski antenna (FDTD). The right column displays a zoomed view of the active region at each band. Notice the similarity among regions when scaled by wavelength.

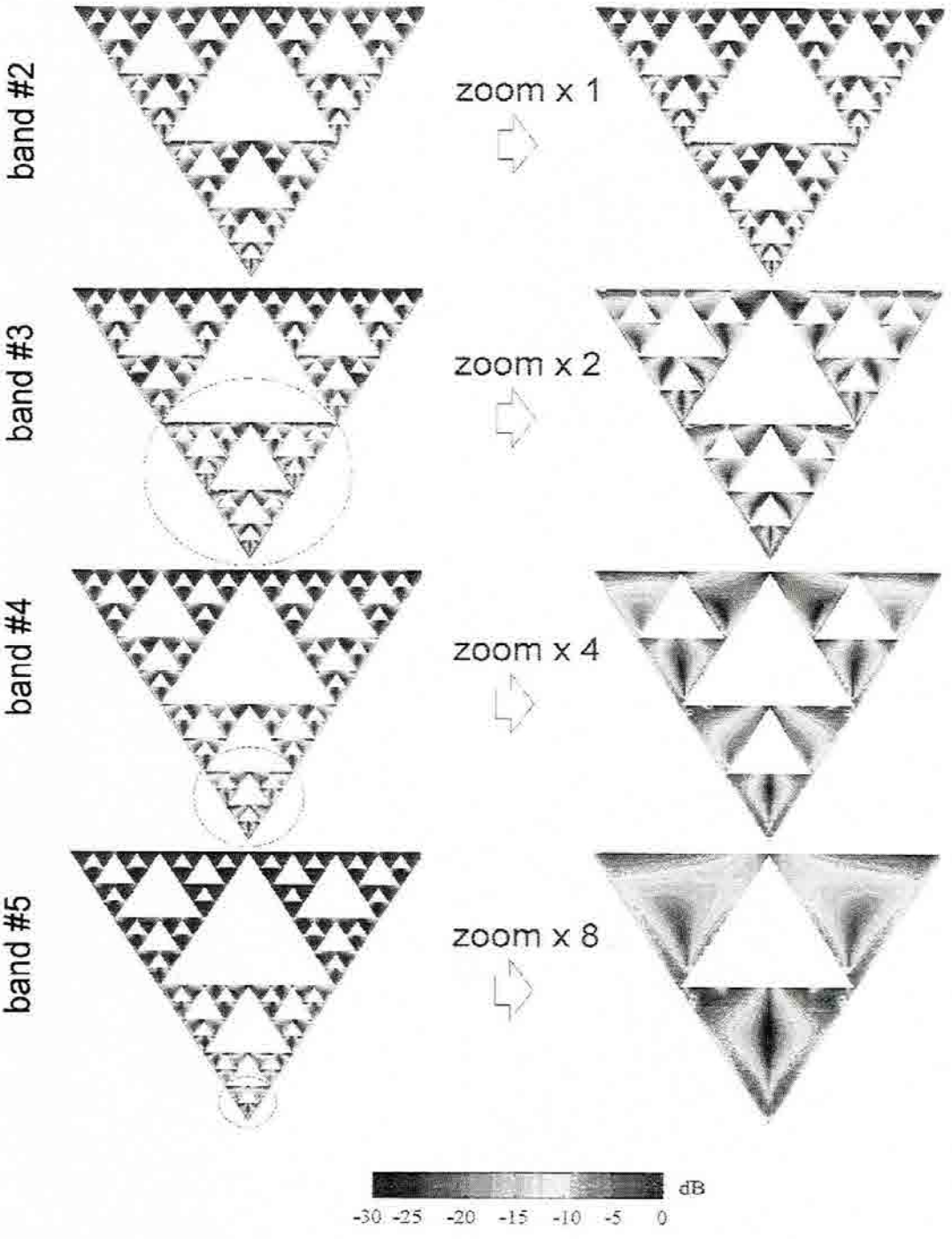

Fig. 4.16 Magnitude of the current density horizontal component (J_y) over the Sierpinski antenna (FDTD). The right column displays a zoomed view of the active region at each band. Notice the similarity among regions when scaled by wavelength.

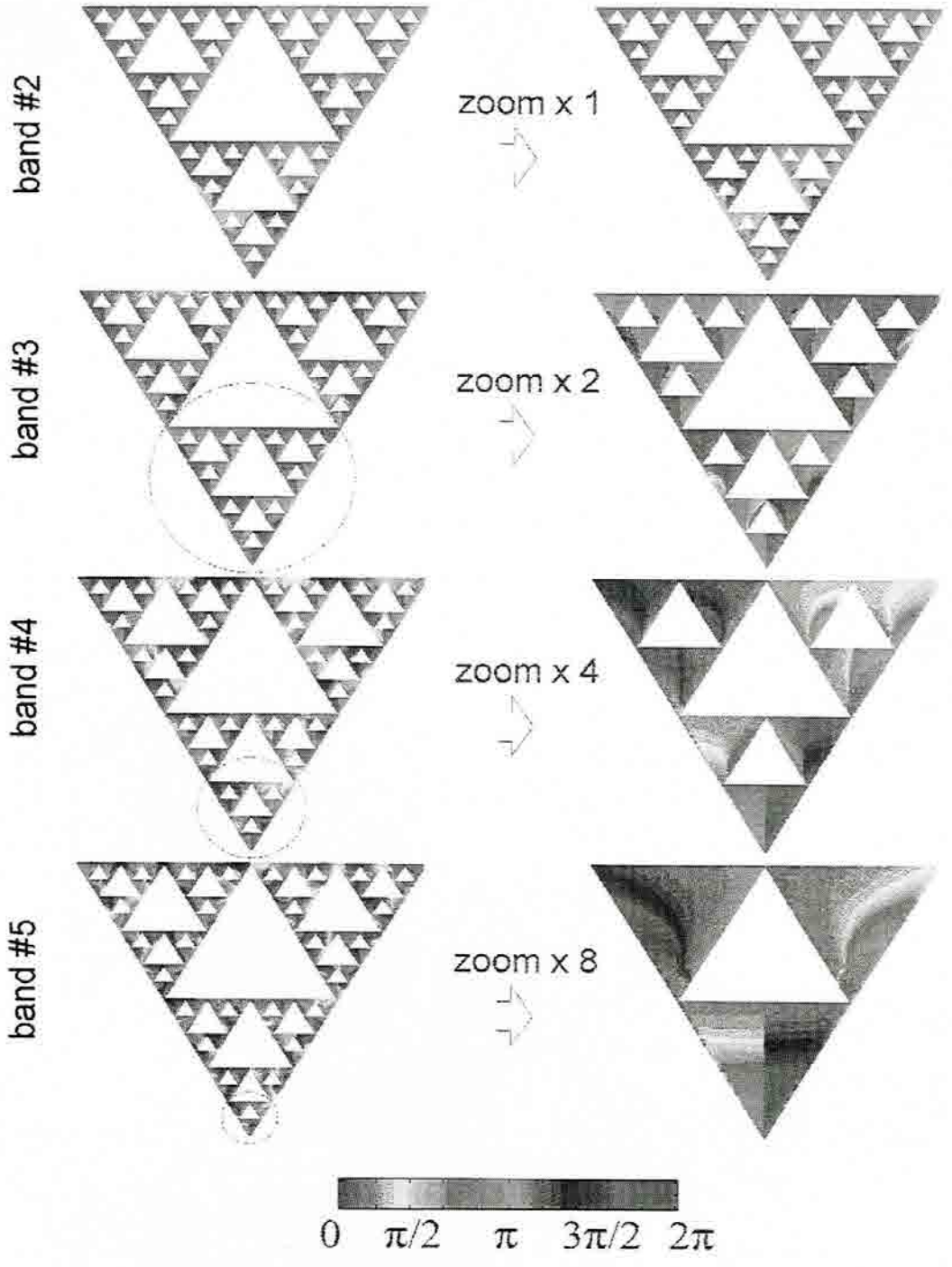

Fig. 4.17 Phase of the current density horizontal component (J_y) over the Sierpinski antenna (FDTD). The right column displays a zoomed view of the active region at each band. Notice the similarity among regions when scaled by wavelength.

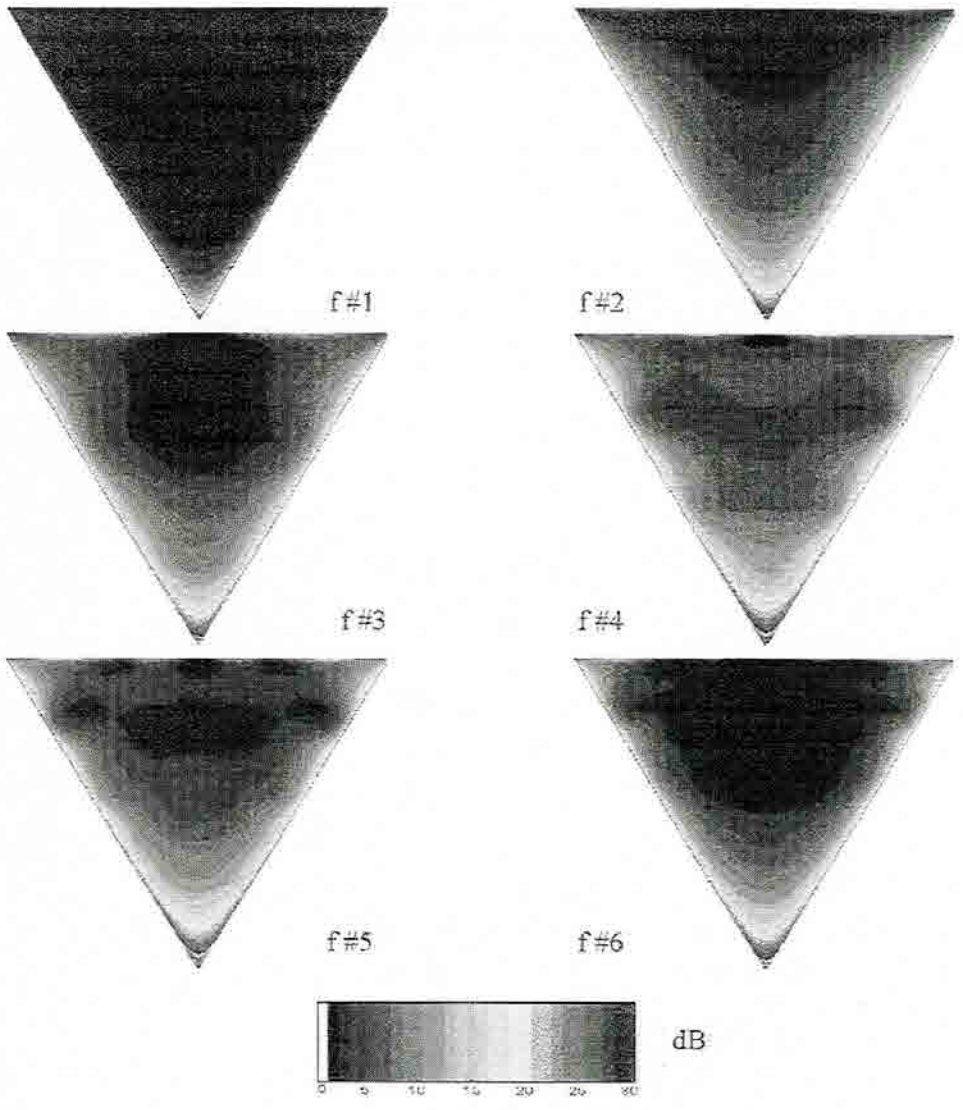

Fig. 4.18 The triangular (Bow-tie) antenna current density distributions (magnitude) at the first six matched frequencies. The current reaches the tips of the antenna at all bands.

4.3 - Wire Model of the Sierpinski Antenna

A common method for analyzing the interaction of electromagnetic waves with objects of arbitrary shape, consists on modeling the object by covering its surface with a wire mesh. This way, a surface current distribution is replaced by a set of linear current elements, which greatly simplifies the problem. The interaction of linear current elements in a three dimensional space has been extensively studied [81]-[84]. In particular, the wire Method of Moments (MoM) approach is based on a decomposition of the wire mesh current into a set of small straight segments supporting a known current distribution, that is,

$$\vec{J}(x,y,z)=\sum_{n=1}^{N}\vec{I}_n(x_n,y_n,z_n)=\sum_{n=1}^{N}I_n\cdot\vec{i}_0(x_n,y_n,z_n) \tag{4.8}$$

Given a common current distribution $i_0(x,y,z)$ to all elements, the problem of computing the unknown parameter $J(x,y,z)$ reduces to computing the set of coefficients I_n which weights the current on each small straight segment. In general, the current distribution $i_0(x,y,z)$ can have any arbitrary shape as long as the linear combination of the currents over all segments is able to reproduce the desired solution $J(x,y,z)$. A widespread technique consists on assuming a sinusoidal (triangular) current distribution over each segment; this way the approach can be physically interpreted as a decomposition of the object structure into a set of small dipoles. Then, the interaction of the several parts of the structure can be easily derived from the interaction of several dipole pairs, which is a considerably simpler problem than dealing with the whole shape at once.

To minimize computing errors, the length l of the dipoles is to be small compared to the wavelength, typically $l<\lambda/10$. Thereby, the electric field over the dipole can be assumed uniform and proportional to the voltage across the dipole terminals. The voltage V_n and currents I_n at each element is related to the voltage and currents at the remaining elements through an impedance matrix [Z] such that [V]=[Z][I], i.e.

$$\begin{bmatrix}V_1\\V_2\\\vdots\\V_N\end{bmatrix}=\begin{bmatrix}Z_{11}&\cdots&Z_{1N}\\&\ddots&\\\vdots&&\vdots\\Z_{N1}&\cdots&Z_{NN}\end{bmatrix}\begin{bmatrix}I_1\\I_2\\\vdots\\I_N\end{bmatrix} \tag{4.9}$$

where Z_{ij} can be physically interpreted as the mutual impedance between elements i and j and Z_{ii} as the self-impedance of the i^{th} dipole. A thorough discussion of a proper method for computing the self and mutual impedance between straight and skewed dipoles in any space position and orientation can be found in [81]-[83].

When the electromagnetic problem consists on evaluating an antenna performance, usually the input impedance and the radiation patterns are the desired unknown parameters which can be directly derived from the current distribution. Usually, antennas are fed through a single terminal, while the remaining small dipoles composing the structure are shorted. This way, the current distribution over the antenna when it is fed by a voltage source at the n^{th} terminal can be derived through

$$\begin{bmatrix} I_1 \\ I_2 \\ \vdots \\ I_N \end{bmatrix} = \begin{bmatrix} Y_{11} & \cdots & Y_{1N} \\ & \ddots & \\ \vdots & & \vdots \\ Y_{N1} & \cdots & Y_{NN} \end{bmatrix} \begin{bmatrix} 0 \\ V_n \\ \vdots \\ 0 \end{bmatrix} \tag{4.10}$$

where the admittance matrix [Y] is calculated as usual as $[Y]=[Z]^{-1}$. Also, the input impedance can be then computed as

$$Z_{in} = \frac{V_n}{I_n} \tag{4.11}$$

The wire Moment Method approach just described is just a particular case within a large set of Moment Method techniques. In general, any set of orthogonal functions can be used to describe electromagnetic fields either in time, space or spectral domain. Such functions can have either a finite or infinite extent, and have a linear, surface or volumetric shape. A complete description of the Moment Method can be found in [48],[52],[53],[85].

4.3.1 - Moments Method and Experimental Analysis

Being a simple but flexible algorithm, the wire Moments Method assuming sinusoidal current distributions over short linear elements has been used to model the Sierpinski antenna. Only the contour of the triangular elements of the antenna has been modeled. We know from fractal theory, that the shape of the initial set A_0 (also named as initiator) one uses to generate the fractal attractor is not significant, since the fractal solution

will naturally arise from the iterative construction itself. Thus, one should not expect a major deviation of the wire Sierpinski antenna behavior from the solid one.

Contrary to the FDTD algorithm, the MoM just outlined is not particularly suitable for analyzing wide spectral ranges. The mutual impedance matrix [Z] has to be evaluated and inverted for every particular wavelength to apply Equation (4.10) and derive the desired antenna parameters. Being this method highly computational time consuming, only the first two Sierpinski modes of a three-stage wire Sierpinski monopole are displayed here. Figure 4.19 displays measured and computed data for a 8.9cm tall, three-iteration wire

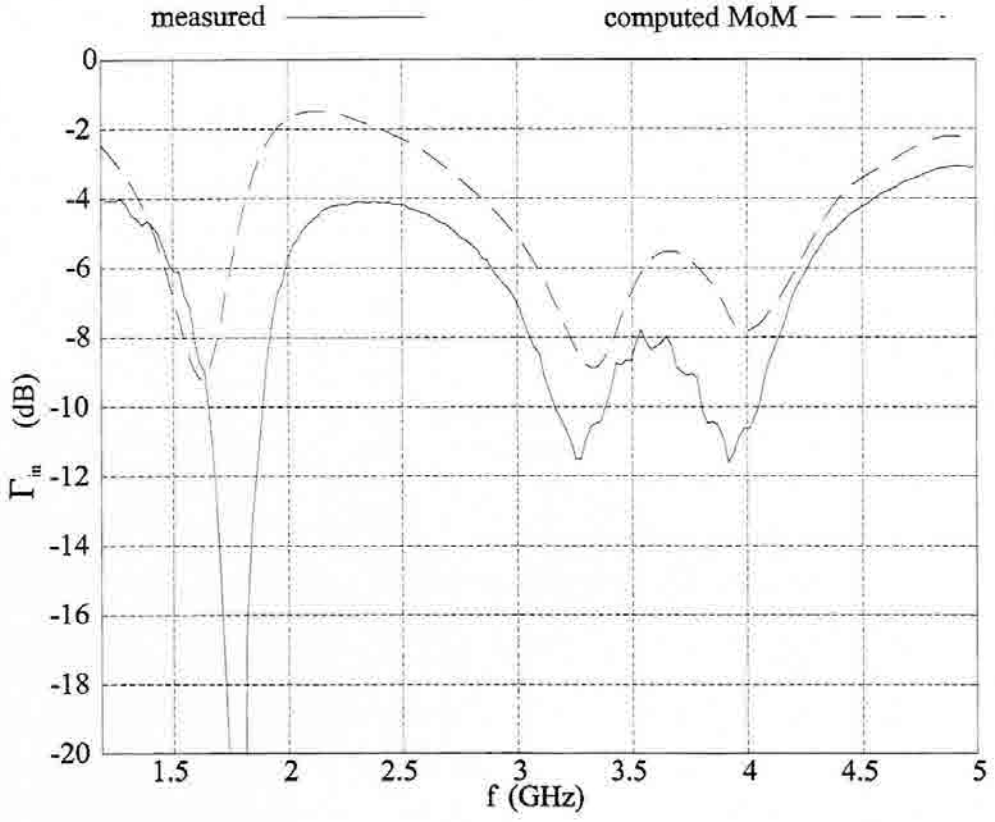

Fig. 4.19 The Wire Sierpinski monopole constructed after 3 iterations. Only the two Sierpinski modes are shown for comparison to the solid model.

Sierpinski monopole. A copper wire with a diameter of 0.4 mm was used to build the antenna structure.

Basically the antenna features two Sierpinski bands spaced by a factor δ=2. The bands are slightly shifted to the higher frequencies with respect to the solid model. Two main reasons should explain such a phenomena. First of all, the wire model is not backed by a dielectric support which tends to enlarge the antenna. Second of all, the finite fractal structure is rather different whether it is made up of solid or void triangular shapes; if one considers each triangle as a loop which inductively contributes to the input impedance, the wire model has a larger number of loops which makes the whole antenna appear slightly shorter.

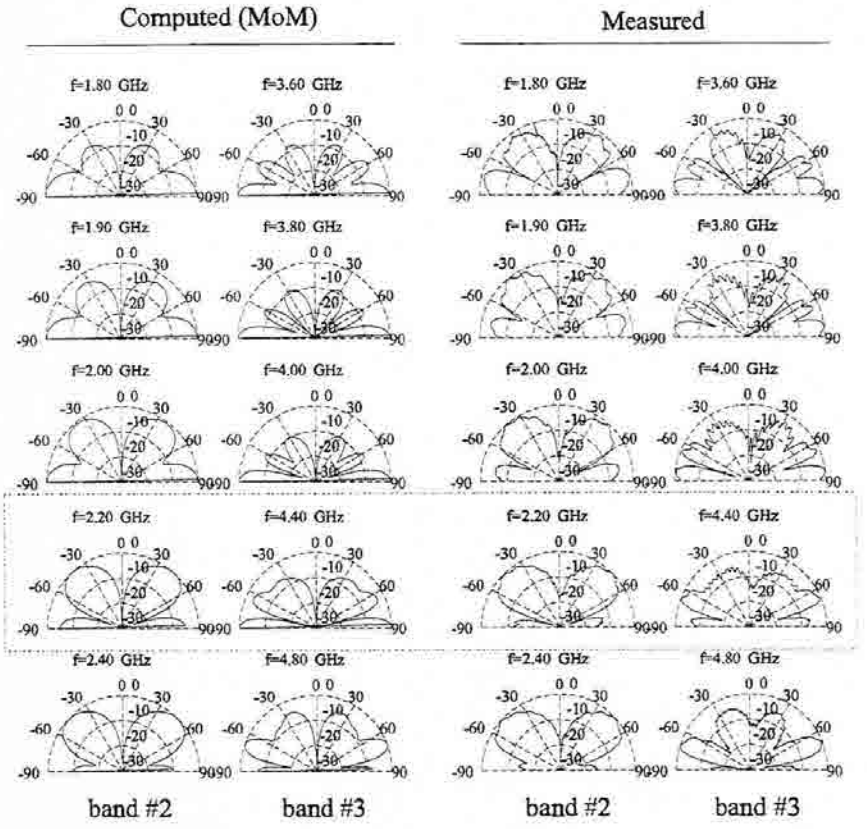

Fig. 4.20 Computed (MoM) and measured (right) φ=90° cut of a three-iteration wire Sierpinski monopole radiation pattern (E_θ). Only the two upper bands are shown.

Computed and measured radiation patterns are also shown in Fig. 4.20 through Fig. 4.22. The patterns are basically the same as those of the solid model, although again, they appear slightly shifted towards shorter wavelengths. The similarity among the two bands is more evident in the 2.1~2.3 GHz and 4.2~4.6 GHz frequency range. Below such ranges it seems like the number of lobes increases from one band to the next, such that the similarity

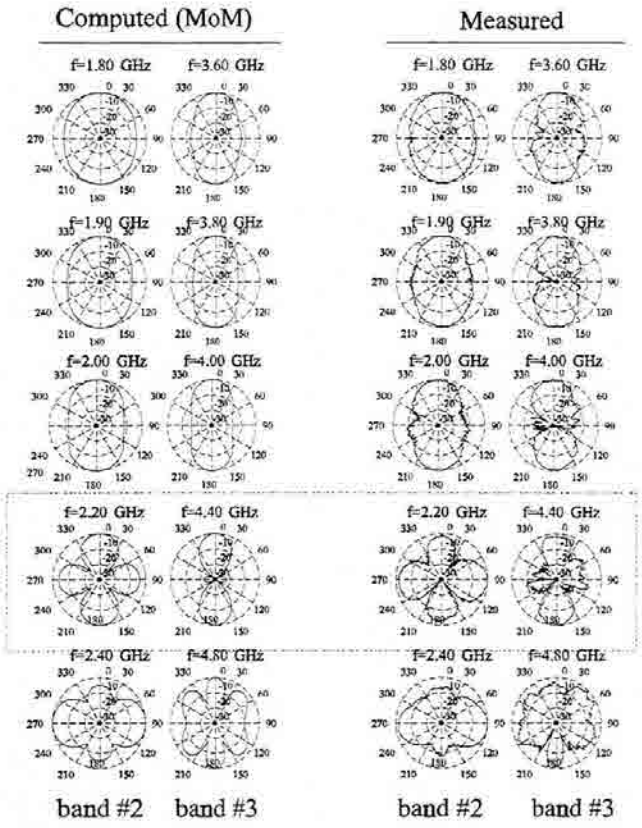

Fig. 4.21 Computed (MoM) and measured (right) φ=90° cut of a three-iteration wire Sierpinski monopole radiation pattern (E_θ). Only the two upper bands are shown.

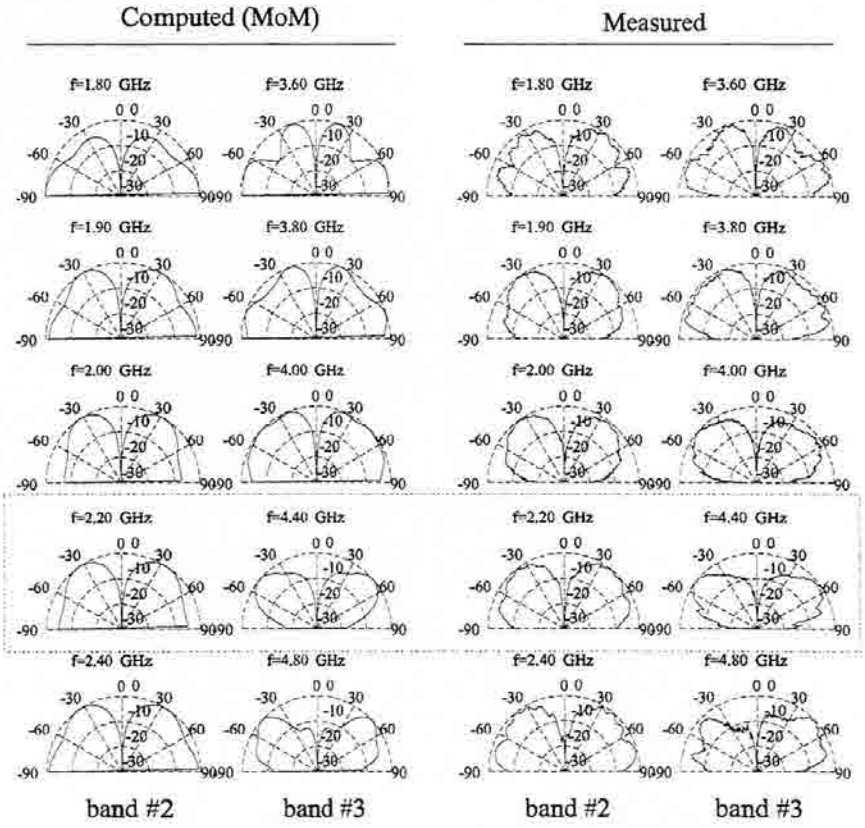

Fig. 4.22 Computed (MoM) and measured (right) φ=90° cut of a three-iteration wire Sierpinski monopole radiation pattern (E_θ) . Only the two upper bands are shown.

among bands is lost. This suggests that former disagreements among patterns found in the monopole and dipole solid models where not due to environmental measurement effects, i.e., the non ideal balun and ground plane, but due to a performance of the antenna itself.

4.3.2 - Iterative Transmission Line Network Model

The accuracy of a numerical analysis technique is usually directly related to its complexity. An accurate numerical model of an electromagnetic problem is often highly computer memory and time consuming. Sometimes, algorithms become highly specialized for a particular kind of structure and they are not flexible enough to essay many different set-ups. This way, the cost in time and resources of experimental work can become even lower than those of numerical analysis. From the engineering point of view, it is sometimes of more value having a simpler but less accurate model to support experimental work by predicting tendencies instead of precise behaviors.

Network models can be very useful when predicting the input impedance behavior of antennas. The LPDA has been successfully analyzed from a two-network model (see Section 2.3.4.2); similarly, the gross behavior of a dipole input impedance can be approximated from that of a lossy transmission line. Also, we know that not only the input impedance but the overall current distribution over a wire antenna can be approximated by that of a transmission line. Here, an iterative network model based on a combination of transmission lines is suggested for the Sierpinski antenna.

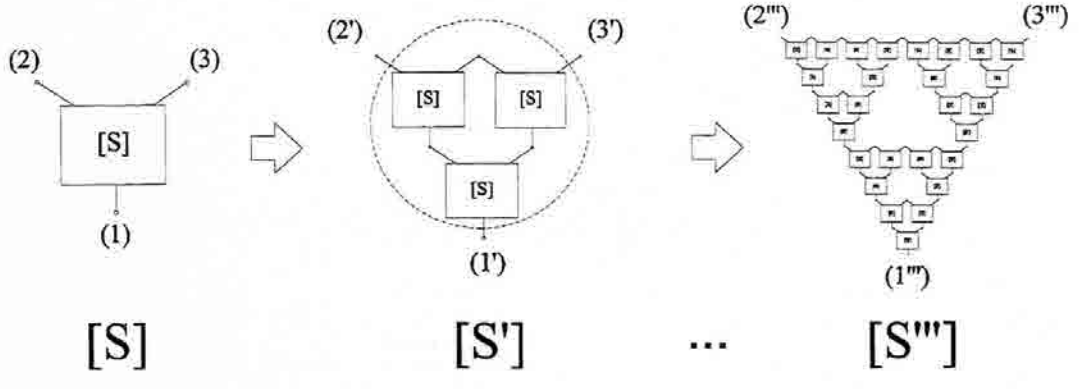

Fig. 4.23 Iterative model for a Sierpinski Network.

The FDTD analysis of the antenna suggests that most of the current density concentrates at the apex and borders of the triangular clusters. Therefore, it is not senseless to assume that most of the current flowing through any triangle come from the direct ohmic contact from its neighbors. This way, a general Sierpinski structure could be analyzed as shown in Fig. 4.23.

That is, such a Sierpinski network can be seen as an iterative nesting structure of three-port networks. It is interesting to notice that the whole information upon the network behavior can be subtracted from only two basic relations: the characteristic [S] matrix of the basic network (the *initiator* in fractal terminology), and the *generator* constitutive relations that link the [S] parameters of a particular stage of the fractal construction to the [S'] parameters of the next stage.

Regardless of the particular value of the [S] matrix of the triangular initiator, we know that due to the equilateral symmetry of the structure and its reciprocity, it has to be of the form

$$[S]=\begin{bmatrix} \alpha & \beta & \beta \\ \beta & \alpha & \beta \\ \beta & \beta & \alpha \end{bmatrix} \tag{4.12}$$

After some algebraic manipulation, it can be shown that the generator relates the [S'] parameters of the following stage with the [S] of the previous one as

$$\alpha' = \alpha + \frac{2\beta^2\left(\alpha+\frac{\beta^2}{1-\alpha}\right)}{1-(\alpha+\beta)\left(\alpha+\frac{\beta^2}{1-\alpha}\right)} \tag{4.13}$$

$$\beta' = \frac{\beta^2\left(\alpha+\frac{\beta}{1-\alpha}\right)}{1-(\alpha+\beta)\left(\alpha+\frac{\beta^2}{1-\alpha}\right)} \tag{4.14}$$

Although [S] parameters have been used here due to its widespread use in microwave systems, similar relationships could have been also derived for [Z], [Y] and other related circuit matrices. One of the most interesting features of the recursive relations

(4.13) and (4.14) is that they allow us to efficiently predict the antenna (network) behavior at any iteration stage without an increase of the model complexity. Such equations can be easily programmed even in a portable scientific calculator because it only requires a minimum memory capacity to store the two parameters from the previous stage. The advantage with respect to any full model of the antenna such as the FDTD or MoM algorithms is clear: while the cost in memory and time of the later grows exponentially with the number of fractal iterations, the iterative network model complexity grows linearly with the number of iteration stages.

In general, any symmetrical reciprocal three-port network could be used to model the triangular initiator. However, a transmission line network appears a natural approach as discussed before. In particular, the three models shown in Fig. 4.24 have been tested.

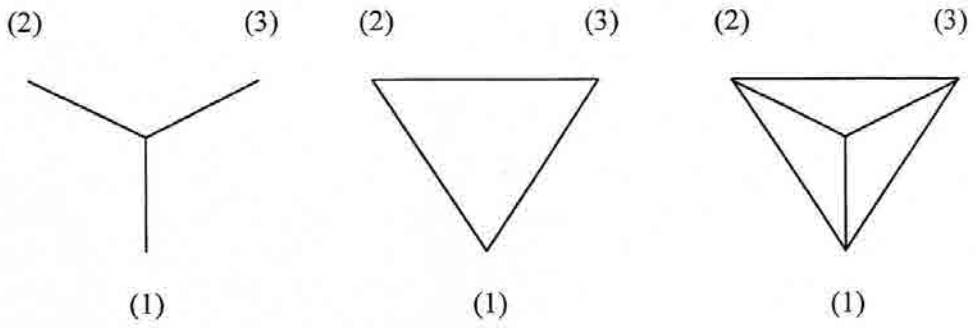

Fig. 4.24 Three simple approximate models for the triangular initiator.

The length l of the triangular side has been chosen to match the side of the measured Sierpinski antenna, i.e., l=6.423 mm, which gives a length a of the Y-branch model of a=3.7mm. In order to take into account the losses due to radiation, a finite Q has been accounted for the transmission lines by introducing an attenuation factor α such as

$$Q = \frac{\beta}{2\alpha} \tag{4.15}$$

which has been empirically adjusted to Q=10. Also the transmission line characteristic impedance has been also empirically adjusted to $5Z_o$, being Z_o the reference impedance used to compute the input reflection coefficient. Such coefficient for the whole three-port fractal structure can be calculated as

$$\Gamma_{in} = \alpha + \beta^2 \frac{\Gamma_2 + \Gamma_3 + 2(\beta - \alpha)\Gamma_2\Gamma_3}{(1-\alpha\Gamma_2)(1-\alpha\Gamma_3) - \beta^2\Gamma_2\Gamma_3} \tag{4.16}$$

where Γ_2 and Γ_3 are the normalized reflection coefficients of any couple of loads connected to ports 2 and 3 respectively. When modeling the one-port antenna network, such ports can approximately be considered to be open-circuited such that Equation (4.16) becomes

$$\Gamma_{in} = \frac{\alpha^2 + \alpha(\beta - 1) - 2\beta^2}{\alpha + \beta - 1} \tag{4.17}$$

Combining equations (4.12) through (4.17), the input reflection coefficient (Fig. 4.25) of a five iteration Sierpinski transmission line network has been computed for the three models of Fig. 4.24.

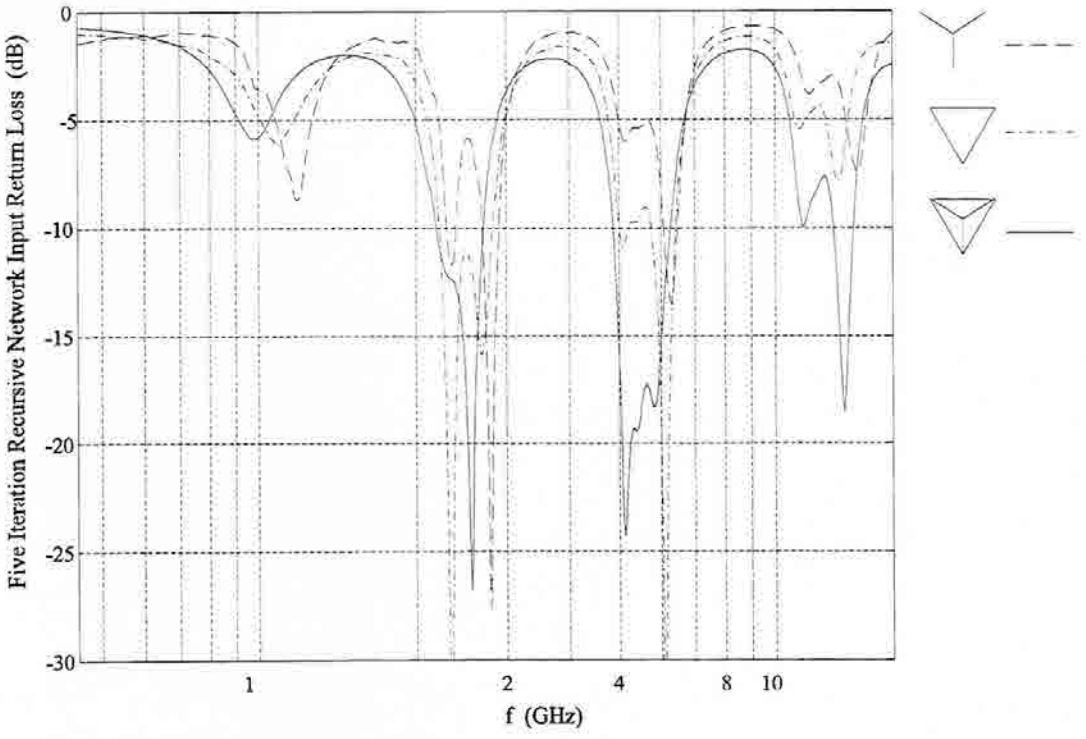

Fig. 4.25 Input reflection coefficient for a 5-iteration Sierpinski network. The three initiators yield a log-periodic behavior.

It is apparent that the three network models yield to a log-periodic behavior similar to that of the Sierpinski antenna. From these plot one could erroneously conclude that only four bands are predicted by the model instead of the expected five bands. However, as shown in Fig. 4.26, the network input impedance clearly evinces the five bands within the same frequency range. The problem here is that the finite Q transmission-line model underestimates the network losses due to radiation at lower frequencies. Thus, the input resistance is lower than the expected value from the Sierpinski antenna results and leading to a mismatch between the network and the input normalized 50Ω transmission line. If one loads the network with some resistance to take into account the additional radiation at the lowest band, the best agreement is achieved (see dashed reflection coefficient in Fig. 4.26). In particular, the Sierpinski network of Fig. 4.26 has been loaded with a frequency dependent resistance R_L such as

$$R_L \propto \left(\frac{h}{c} f\right)^2 \tag{4.18}$$

being h the whole fractal monopole size, to take into account the parabolic characteristic radiation resistance of a small monopole at low frequencies. It is interesting to notice that such an extra load does not significantly affect the performance of the higher bands since it becomes large enough there to be rather considered an open circuit. On the other hand, quite presumably the load resistance was not going to be significant at the higher bands, even if it were an arbitrary small, non-frequency dependent resistance. The current, both in the network model and in the measured antenna, becomes highly attenuated (radiated) at high frequencies before reaching the antenna tips and only the lower bands, suffering from a lower attenuation (lower radiation), would be sensitive to high reflections at the end of the antenna which would affect the input terminal behavior.

Some relevant conclusions can be extracted from the iterative model just introduced. First of all, the log-periodic behavior is directly related to the antenna fractal geometry; no matter the details of the initiator, the multiband behavior is always obtained from the recursive model. Second of all, one can conclude that the overall behavior is mostly influenced by the direct ohmic contact of the triangular clusters with their neighbors. That is, it has not been assumed anywhere any kind of mutual coupling effects between clusters, yet the model still reproduces the expected multiband behavior. Also, the transmission line based model suggests that the antenna input impedance performance is mostly influenced by electromagnetic waves being propagated and reflected from the several parts of the metallic fractal structure, which must be linked to its geometrical shape. The algorithm even predicts the double resonant behavior found within each band.

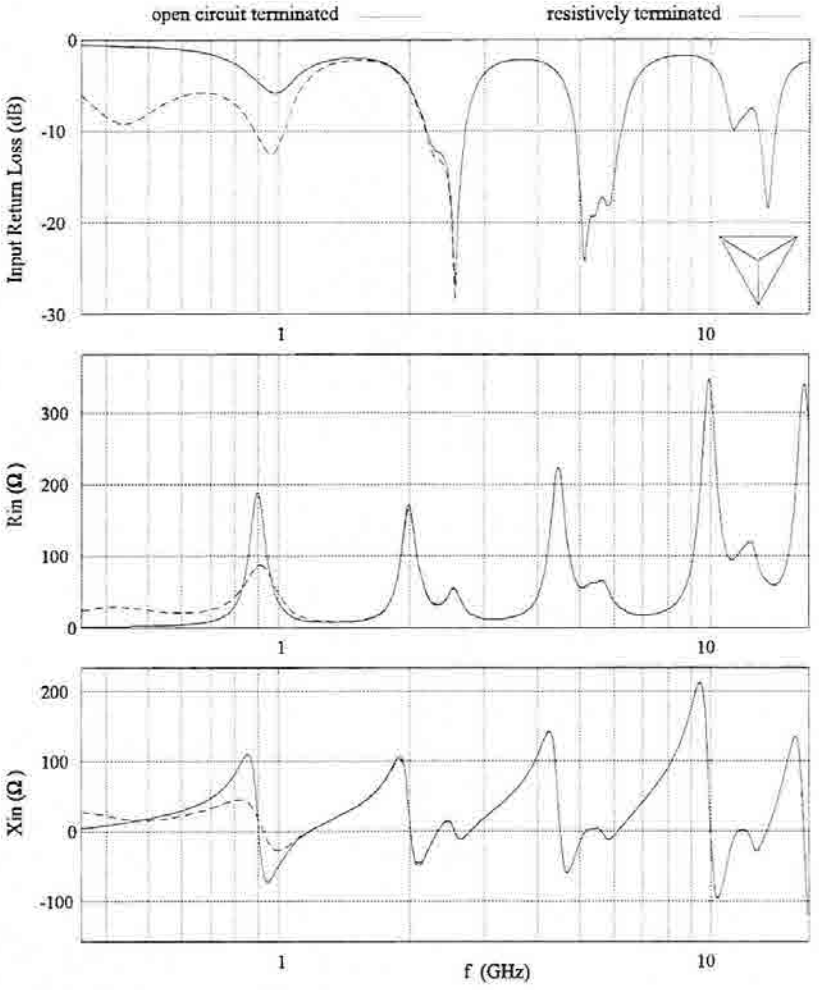

Fig. 4.26 The Sierpinski network input impedance and return loss. The solid line displays the open circuit loaded network, while the dashed line displays the behavior of the resistively loaded network.

As mentioned previously, maybe the most significant features of this model are its simplicity and high computational efficiency. For instance, the evolution of the input return loss frequency behavior with the fractal structure growing sequence can be readily simulated as shown in Fig. 4.27. Up to 12 growing stages have been included in that plot. It should be stressed that a twelve-iteration Sierpinski structure is composed by 3^{11}=177.147 triangular elements, which is by far too complex a structure to be analyzed by any other means. To keep an order of magnitude in mind, the five iteration (3^4=81 elements)

Sierpinski monopole required about 6 days running the DOTIG4 algorithm on a Sun Sparc station (which could be reduced to 2 days using a parametric estimation model [120]), or about 2 hours running the FDTD algorithm on the CM-5 parallel machine. This suggests

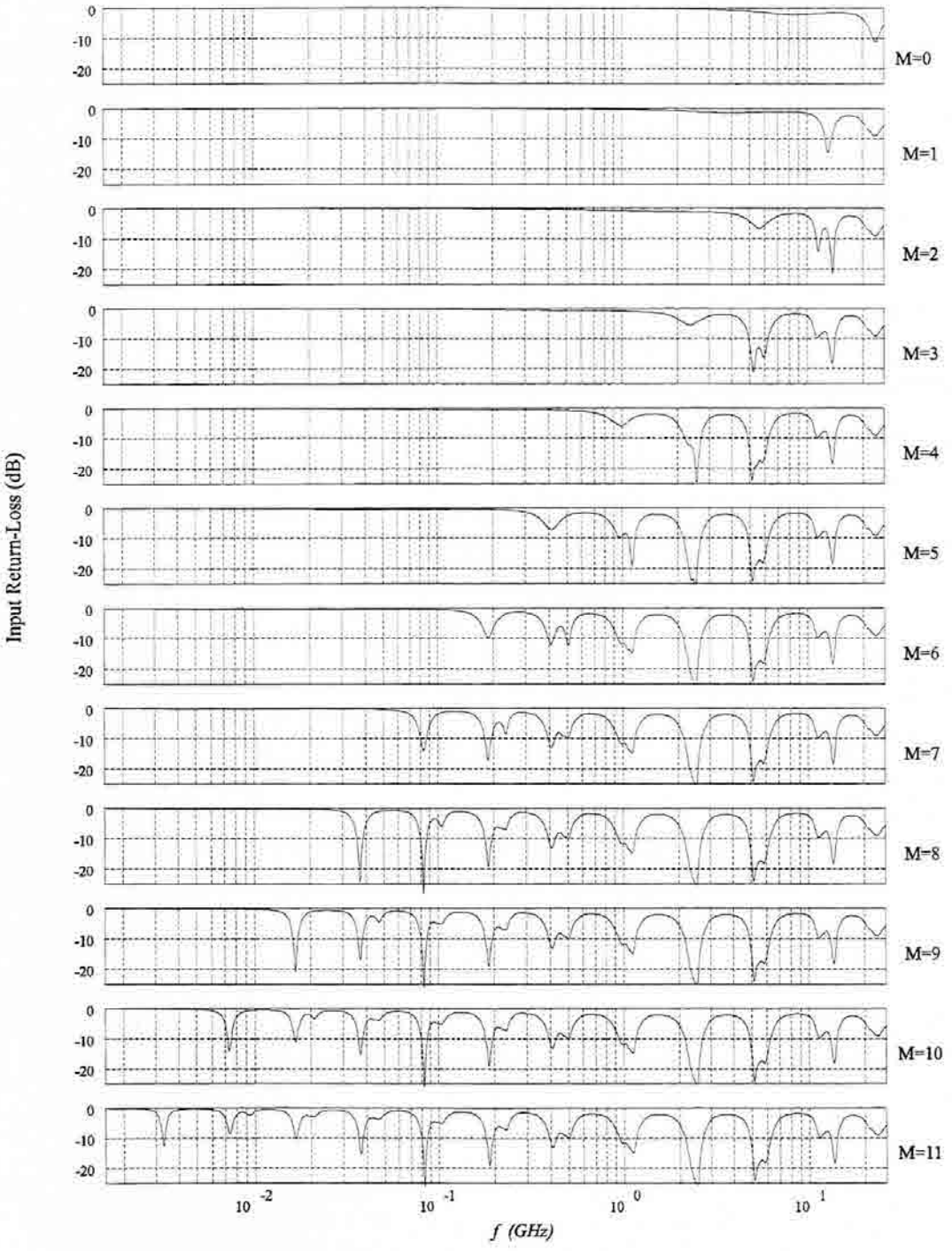

Fig. 4.27 Twelve iteration stages of the fractal network construction. Each iteration adds a new lower band since the structure grows outwards.

that such a kind of iterative algorithms, which explicitly take into account the fractal nature of the structure, should become the most appropriate for analyzing fractal antennas. A major improvement on traditional numerical methods would be achieved if they were modified to take advantage of such recursive properties when analyzing fractal structures.

It becomes manifest from Fig. 4.27 that each new stage in the fractal construction adds a new band (a log-period) to the antenna performance. Thus, one could freely design an antenna with an arbitrary number of bands by merely choosing the proper number of fractal iterations, as suggested previously. In particular, the structure is shown to expand to lower bands when growing outwards because at each iteration the overall antenna size is doubled. Conversely, the number of bands would be expanded to higher frequencies if the structure grew inwards, i.e., by using a classical contractive IFS algorithm as described in Section 2.1. Except for slight frequency shifts and input return-loss variations at the extreme bands, most of the remaining antenna behavior is kept essentially unaffected by increasing the number of bands, which makes the whole design process simpler.

4.4 - Conclusions

The first reported multiband fractal antenna has been introduced in this chapter. The antenna, which is based on the fractal Sierpinski gasket, has been shown to fulfil a multiband behavior from both the input reflection coefficient and radiation patterns points of view. Both experimental results and numerical simulations confirm such a behavior. The bands are log-periodically distributed with a spacing factor of 2, which is exactly the characteristic scale factor displayed by the geometrical fractal form. The input return-loss characteristic is essentially repeated at each band (~20% bandwidth at VSWR<2), except at the extreme bands due to the truncation effect. The link between the antenna performance and its geometrical design is also apparent on the number of bands, which is equal to the number of fractal construction iterations. A simple and efficient algorithm has been introduced to predict the antenna overall behavior at any iteration stage, which can become a powerful tool for engineering purposes.

The main goal of this chapter, which was demonstrating that fractal multiband antennas are feasible, has been achieved. Whether such a fractal shape can by modified for designing purposes is the central topic of next chapter.

5. Perturbing the Sierpinski Antenna

Once the multiband performance of the fractal Sierpinski antenna has been demonstrated, the next logical step is exploring whether the shape of the antenna can be modified to tailor the antenna performance for several application requirements. Also, it is most interesting to investigate which are the limitations on distorting the antenna shape yet not perturbing its multiband behavior. This chapter is devoted to the description of the antenna response when some variations are introduced upon its geometrical structure; mainly, by adjusting the flare angle, bending the antenna arms, changing the scale factor or essaying non-fractal variations of the antenna. The ultimate goal would be to explore the changes that would allow the antenna designer to modify the input impedance, radiation pattern, directivity, band spacing and mechanical structure of the antenna.

5.1 - Variations on the flare angle

Brown & Woodward first described in their classical work [67] the input impedance behavior of triangular and conical antennas when modifying the feeding apex angle (flare angle). Basically, they showed how both the input resistance and reactance variations decreased for large flare angles. Conical monopoles with 90° angles featured a broad-band behavior due to a fairly constant input impedance around 50Ω and a small reactance (X_{in}<10Ω) within the 90° ~ 270° electrical length range (i.e., h=λ/4 ~ h=3λ/4 being h the triangle height). Analogously, triangular antennas also displayed smaller variations upon the input impedance when opening the apex angle, however, such variations were significantly larger than those of their conical counterparts. Also, given a fixed height of the triangular arm, the antenna resonant frequencies were shifted towards longer wavelengths for large flare angles. This phenomenon can be understood if one takes into account that most of the

current propagates along the antenna edges (as shown in the FDTD current reconstruction in Chapter 4), which become larger when increasing the apex angle.

Brown & Woodward paper also included the measured E-plane co-polar radiation pattern cuts over the 60° to 270° electrical length range. All patterns displayed a characteristic two-lobe structure (similar to that of the Sierpinski antenna) when the antenna was made larger than 195 electrical degrees (i.e., $f>0.5417c/h$) and was operated well beyond the first even resonance. Although conical dipoles featured a convenient filling of the null between the two-lobe pattern for a 50° flare angle, such a behavior was not observed for the triangular antenna. Since both the pattern and the input impedance were not held constant with frequency, the antenna could not be considered frequency independent (actually, the concept of frequency-independent antennas did not come out until a few years after Brown & Woodward work).

Three Sierpinski antennas of 90°, 60° and 30° flare angles (α) (Fig. 5.1) have been constructed and measured at several frequencies, all of them having the same height. The same Cuclad 250 GT dielectric substrate has been used for the all three antennas. Their input parameters together with the radiation patterns are shown in the following sections.

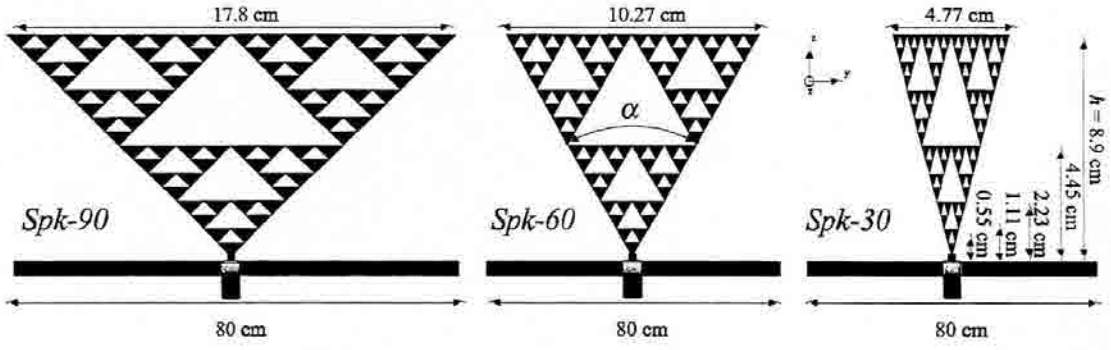

Fig. 5.1 Several configurations of the Sierpinski monopole for α=90°, α=60° and α=30° flare angles.

5.1.1 - Low frequency input parameters

The plots in Fig. 5.2 show the input parameters of the three Sierpinski monopoles, together with the same parameters for the analogous bow-tie antennas (results from [67]). The parameters are plotted with respect the antenna's electrical length ϕ, i.e.,

$$\phi = 360\frac{f.h}{c} \tag{5.1}$$

Both results, the measured Sierpinski parameters and the bow-tie ones exhibit a similar behavior at the first band (first odd and even resonances). The larger the flare angle, the smaller the input resistance and reactance variations. Also, resonant frequencies are consistently shifted towards the origin due to an overall increase of the antenna size, in particular, due to an increase on the length of the equal side edges as discussed before. In the lower frequency region ($\phi < 60°$) the similar performance of the two antenna types is more clear, which was to be expected since the contribution of the etched wholes on the Sierpinski antenna should be negligible for large enough wavelengths. Roughly speaking, the measured Sierpinski antenna works similarly to a slightly longer bow-tie antenna. Such an increase in the effective length when comparing first resonances must be related to the dielectric substrate supporting the fractal structure.

The performance of both antenna families start to significantly deviate around the first even resonance. The input resistance and reactance of the Sierpinski antenna suffer stronger variations at the third and forth resonances. Actually, this phenomenon is on account of the first Sierpinski mode operation, which becomes significant at the second band and beyond. The shift of the higher order resonant frequencies to longer wavelengths is larger than the one obtained from the dielectric coating and should be compared to that of a transmission line which has its distributed self-inductance increased (the holes on the Sierpinski structure would provide such an additional self-inductance); the additional self-inductance would reduce the phase propagation speed along the transmission line making the whole antenna to appear slightly longer.

5.1.2 - Input parameters through the bands

The input parameters of the three fractal antennas are displayed in Fig. 5.4 to show their behavior at the four upper bands. The graphic is represented in a logarithmic scale to

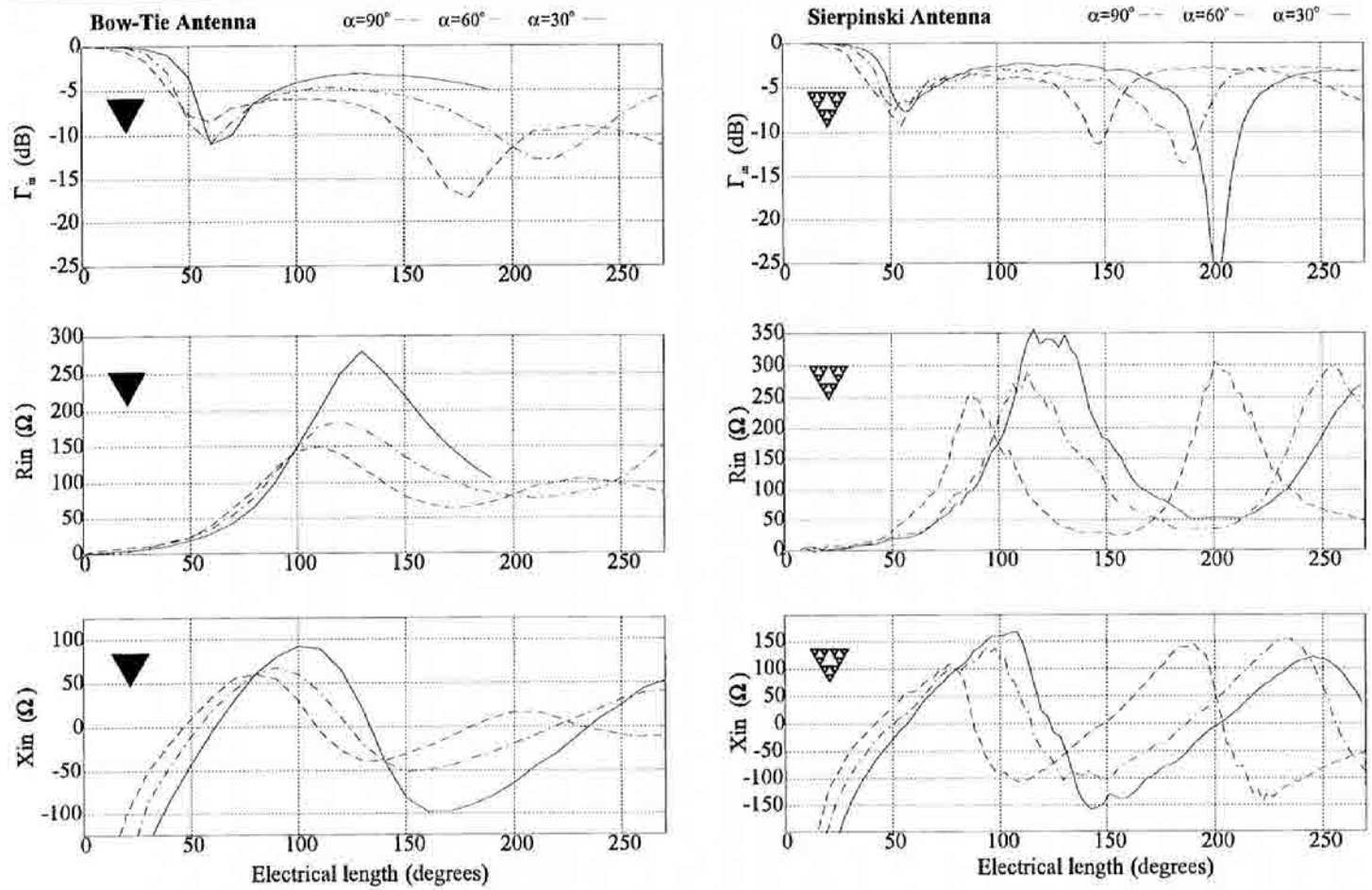

Fig. 5.2 Comparison of the input parameters of a bow-tie [67] and a Sierpinski antenna, for several flare angles (α=90°, α=60° and α=30°)

manifest the log-periodic, multiband behavior of the three antennas. As discussed before, the shift of the resonant frequencies to lower wavelengths for larger flare angles is consistent through all bands. Both features are clearly stated in Fig. 5.3. It displays the minimum VSWR frequencies as a function of the band number (n) for the three antennas. The graphic is plotted in a semi-logarithmic scale to show the exponential growing of the band frequencies. The slope m of the three curves is directly related to the log-period as

$$m = \log(\delta) \approx \log(2) \tag{5.2}$$

which again clearly evinces the link between the fractal geometry and the electromagnetic behavior of the antennas (the thin solid line corresponds to the $f=2^{n-1}$ curve and is shown for comparison). The truncation effect becomes apparent again on the slope change at the first band, where the bow-tie operation mode is dominant upon the Sierpinski modes.

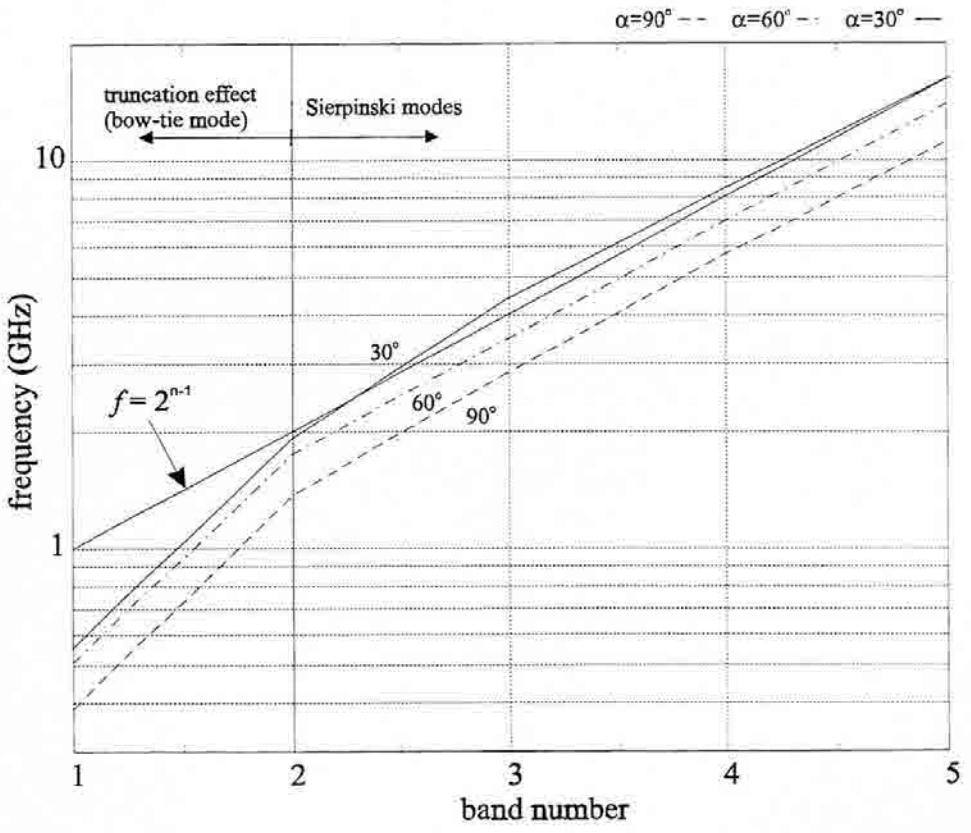

Fig. 5.3 Sierpinski band frequencies(at VSWR minimums) for several flare angles. The slope of the three curves indicate the log-period (δ=2). All three antennas had the same height (h=8.9 cm).

All antennas evince an alike behavior, with a slight tendency to reduce the amplitude of the input resistance and reactance characteristic at larger frequencies. The sharpest angle antenna performs a double resonance behavior at each band, with two resistance peaks and valleys which leads to a double frequency match within the band. This phenomenon should be related to the narrow shape of the antenna, which makes the whole structure approach the shape of a linear wire monopole, and to start deviating its

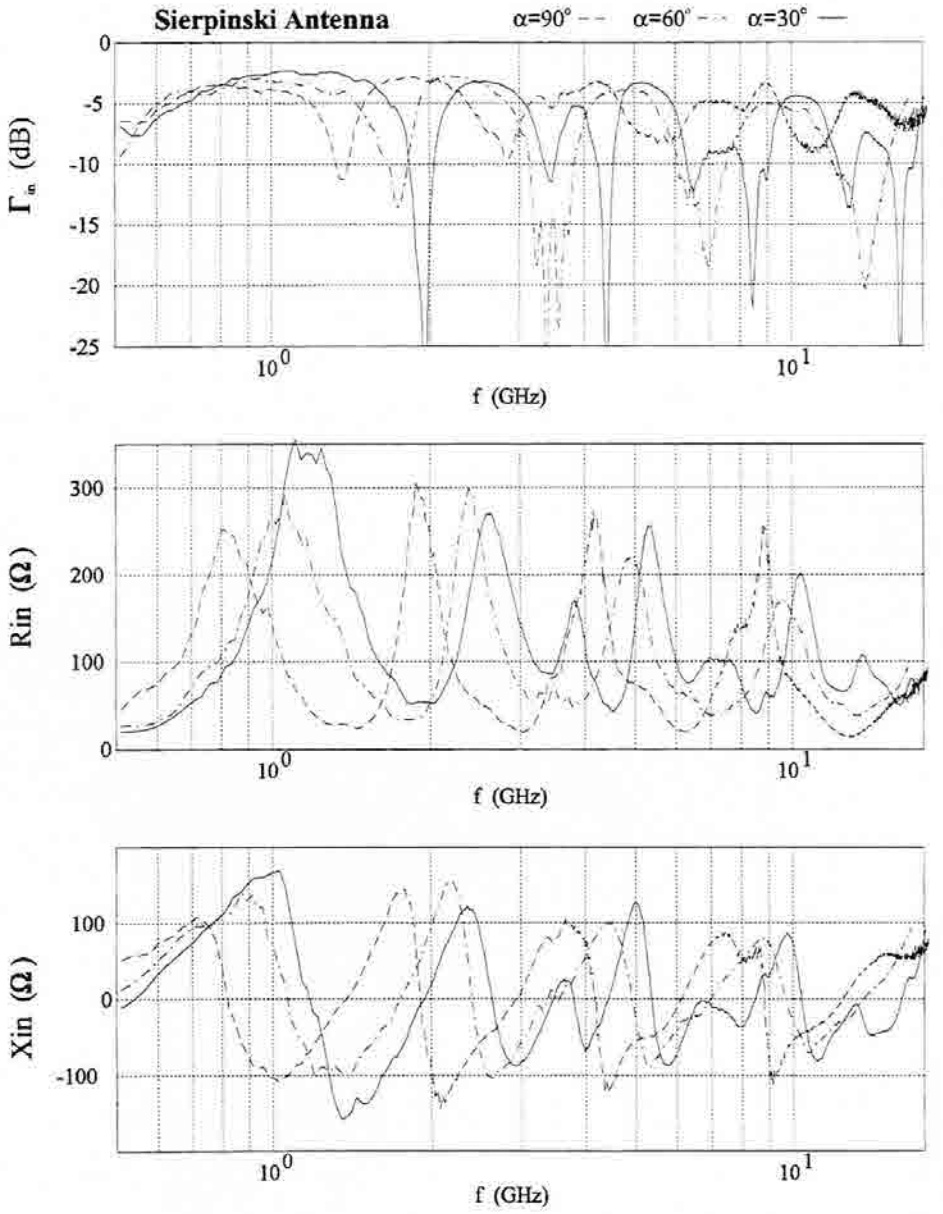

Fig. 5.4 Input parameters of the three antennas through the whole frequency range.

performance away from the ideal log-periodic one. That is, the double resonances at the upper bands tend to fill the Sierpinski antenna characteristic band-gaps that would eliminate

the periodic resonances of the classical linear monopole[1]. This issue should be related to the truncation effect as well: being the whole antenna shorter, currents would not have enough room to radiate all its power away before reaching the antenna tips. Therefore, they become reflected at the antenna ends and return to the feeding point distorting the whole antenna log-periodic behavior. The deviation of the Sierpinski-30 antenna from the log-periodic behavior is also clear in Fig. 5.3.

It is interesting to note that although the bow-tie and Sierpinski antennas work similarly at low frequencies, the fractal antenna deviates from the classical bow-tie operation mode at the upper bands. The input resistance is not kept lower for wider apex angles, nor the antennas maintain the same matching conditions. The antennas are best matched to 50Ω at odd resonances, where the input resistance attain their minimum values. Being such minimums reduced for larger flare angles, the input return-loss decreases below 10 dB in that case.

5.1.3 - The Iterative Network Model

In Section 4.3.2 an iterative transmission line network model for the Sierpinski antenna was introduced. Being extremely simple and computationally efficient, the algorithm was basically able to predict the log-periodic performance of the antenna in terms of its input parameters. An equivalent model can be derived for Sierpinski antennas based on an isosceles triangle initiator instead of the equilateral one. Due to the different size of one of the triangle sides, the equilateral symmetry of the network is broken, which must now be characterized by the following [S] matrix,

$$[S]=\begin{bmatrix} \alpha & \beta & \beta \\ \beta & \gamma & \delta \\ \beta & \delta & \gamma \end{bmatrix} \tag{5.3}$$

that is, four parameters are required to fully describe the network. The resulting mathematical relations that link the initiator parameters with those of the next iteration (see Fig. 4.23) are quite more involved than the corresponding parameters of the equilateral triangle,

[1] A sharper 15° Sierpinski antenna is described in [97] such a narrow angles the antennas almost loses all its multiband features.

$$\alpha' = \alpha + 2\beta^2\left(\alpha + \frac{\beta^2}{1-\gamma}\right)\cdot\frac{1}{1-(\gamma+\delta)\left(\alpha+\frac{\beta^2}{1-\gamma}\right)} \tag{5.4}$$

$$\beta' = \left(1+\frac{\delta}{1-\gamma}\right)\cdot\frac{\beta^2}{1-(\gamma+\delta)\left(\alpha+\frac{\beta^2}{1-\gamma}\right)} \tag{5.5}$$

$$\gamma' = \gamma + \frac{\beta(EH+G)+\delta(GB+H)}{1-EB} \tag{5.6}$$

$$\delta' = \frac{\beta(EC+F)+\delta(BF+C)}{1-BE} \tag{5.7}$$

where the auxiliary parameters B, C, E, F, G, H are defined as

$$B = \left(\gamma + \frac{\delta\alpha+\gamma\beta^2}{1-\alpha\gamma}\right)\frac{\beta}{1-\gamma^2-\frac{\beta^2(\delta+\gamma^2)}{1-\alpha\gamma}} \qquad C = \frac{\left(\delta+\frac{\beta^2\gamma}{1-\alpha\gamma}\right)}{1-\gamma^2-\frac{\beta^2(\delta+\gamma^2)}{1-\alpha\gamma}}$$

$$E = \beta\frac{\gamma+\frac{\delta(\delta\alpha+\gamma)}{1-\alpha\gamma}}{1-\alpha\gamma-\frac{\delta(\delta\alpha^2+\beta^2)}{1-\alpha\gamma}} \qquad F = \frac{\frac{\beta\delta}{1-\alpha\gamma}}{1-\alpha\gamma-\frac{\delta(\delta\alpha^2+\beta^2)}{1-\alpha\gamma}} \tag{5.8}$$

$$G = \frac{\beta\gamma+(1+\alpha)\frac{\beta\delta^2}{1-\alpha\gamma}}{1-\alpha\gamma-\frac{\delta(\delta\alpha^2+\beta^2)}{1-\alpha\gamma}} \qquad H = \frac{\delta\gamma+(1+\gamma)\frac{\beta^2\delta}{1-\alpha\gamma}}{1-\gamma^2-\frac{\beta^2(\delta+\gamma^2)}{1-\alpha\gamma}}$$

Analogously, the normalized input reflection coefficient Γ_{in} of the network described by matrix (5.3) when it is loaded by Γ_2 and Γ_3 at ports 2 and 3 respectively, is given by,

$$\Gamma_{in} = \alpha + \frac{\beta^2}{D1}\Gamma_2\left(1+\frac{\delta\Gamma_3}{1-\gamma\Gamma_3}\right)+\frac{\beta^2}{D2}\Gamma_3\left(1+\frac{\delta\Gamma_2}{1-\gamma\Gamma_2}\right) \tag{5.9}$$

where again, the auxiliary parameters *D1* and *D2* are defined as,

$$D1 = 1 - \gamma\Gamma_2 - \frac{\delta^2\Gamma_2\Gamma_3}{1-\gamma\Gamma_3} \qquad D2 = 1 - \gamma\Gamma_3 - \frac{\delta^2\Gamma_2\Gamma_3}{1-\gamma\Gamma_2} \tag{5.10}$$

Such relations have been used to compute the input return-loss of three transmission line Sierpinski networks with 30° , 60° and 90° flare angles (the same characteristic impedance $5Z_o$, quality factor Q=10, and resistive loading as those of the previous chapter have been used). In general, the results shown in Fig. 5.5 ,are consistent with the experimental data in Fig. 5.4: large flare angles shift the bands towards lower frequencies,

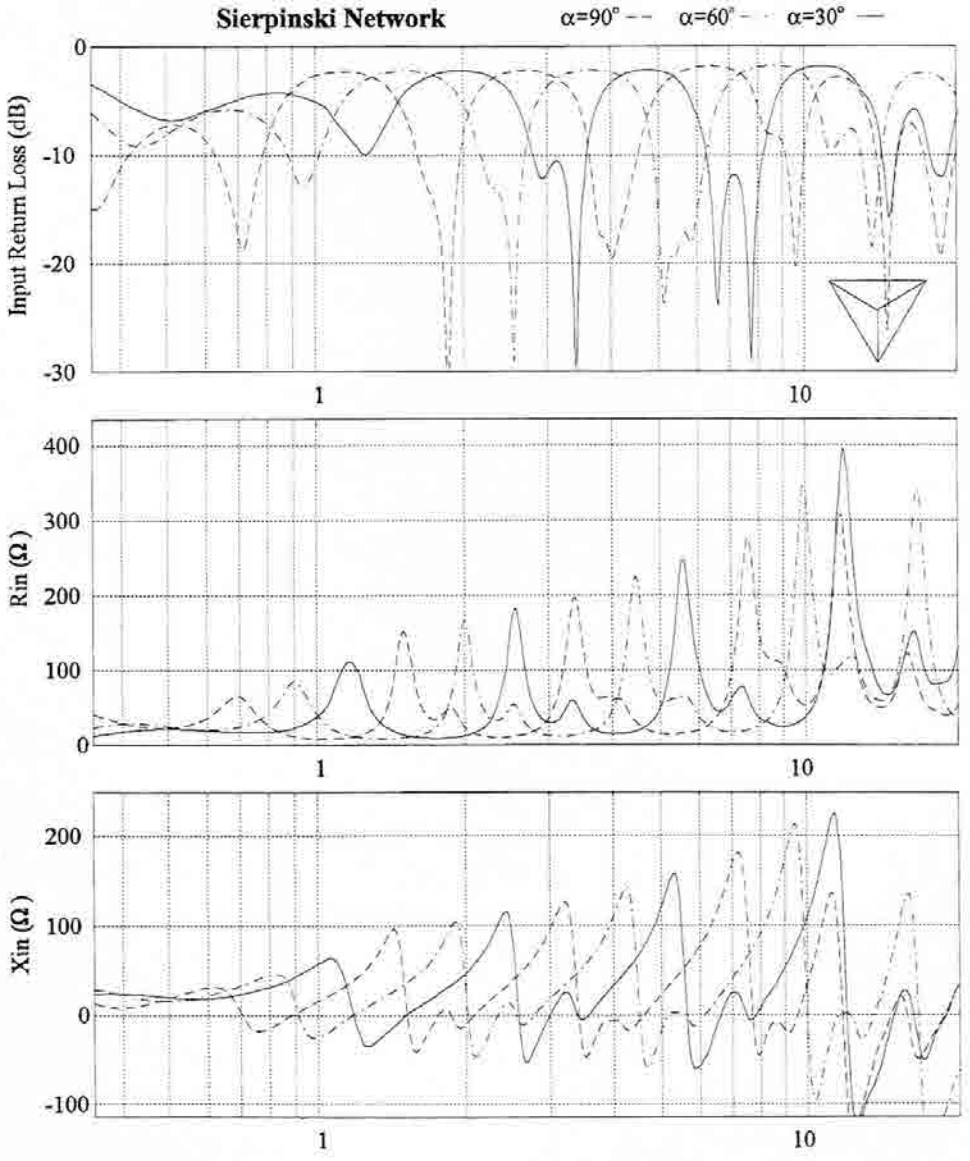

Fig. 5.5 The equivalent transmission line iterative network input parameters for the Sierpinski-30, Sierpinski-60, and Sierpinski-90 antennas.

while narrower angles tend to present a double matching characteristic within each band. The two input resistance maxima at each band become more separated for the Sierpinski-30° equivalent network, leading to such an enhanced double resonant behavior. Also, the resistance minima where the networks are best matched are higher for the narrower angle case.

5.1.4 - Sierpinski-90 and Sierpinski-30 radiation patterns

The measured Sierpinski-90 monopole radiation patterns for the E_θ and E_ϕ components are shown in figures Fig. 5.6 and Fig. 5.7, while the same patterns for the Sierpinski-30 monopole are shown in figures Fig. 5.8 and Fig. 5.9 respectively. Two cuts are displayed at each band, both around the minimum VSWR point in the Sierpinski-90 case, and one cut at each of the two band VSWR minima for the Sierpinski-30 antenna. Although the later does not keep the double matching behavior at the lower bands, the corresponding patterns at the same frequencies but scaled down by the log-period are shown for comparison as well. Only the three upper bands are shown for the Sierpinski-90 antenna because the two lower ones (f=1.4 GHz, f=0.7 GHz) where below the cutoff frequency of the anechoic chamber receiving antenna; nevertheless, no major deviations from the typical two-lobe radiation pattern should be expected at such low frequencies.

Both antennas basically agree in their polarization behavior, being the electric field mainly aligned along the θ direction, but with a significant increase of the cross-polar component on the φ=90° cut at the upper bands as described for the Sierpinski-60 equilateral prototype. However, they significantly differ upon their frequency radiation patterns dependence. While the multiband behavior appears consistent for the Sierpinski-90 case [93],[99], the Sierpinski-30 antenna clearly deviates from the multiband behavior. There is a notable increase in the number of pattern lobes at shorter wavelengths which breaks the symmetry among bands. Such a behavior is more typical of a single-band monopole or bow-tie antenna than that of a multiband fractal antenna. This phenomenon is a direct consequence of the current distribution over the antenna surface and should be related to the truncation effect. That is, being the antenna sides shorter than the other ones, the active region became severely truncated before the currents were attenuated by the radiation process. As suggested before, such a phenomenon should also explain the resonance behavior of the antenna, which is half-way between the harmonic periodic behavior of a monopole, and the log-periodic multiband behavior of the fractal Sierpinski antenna.

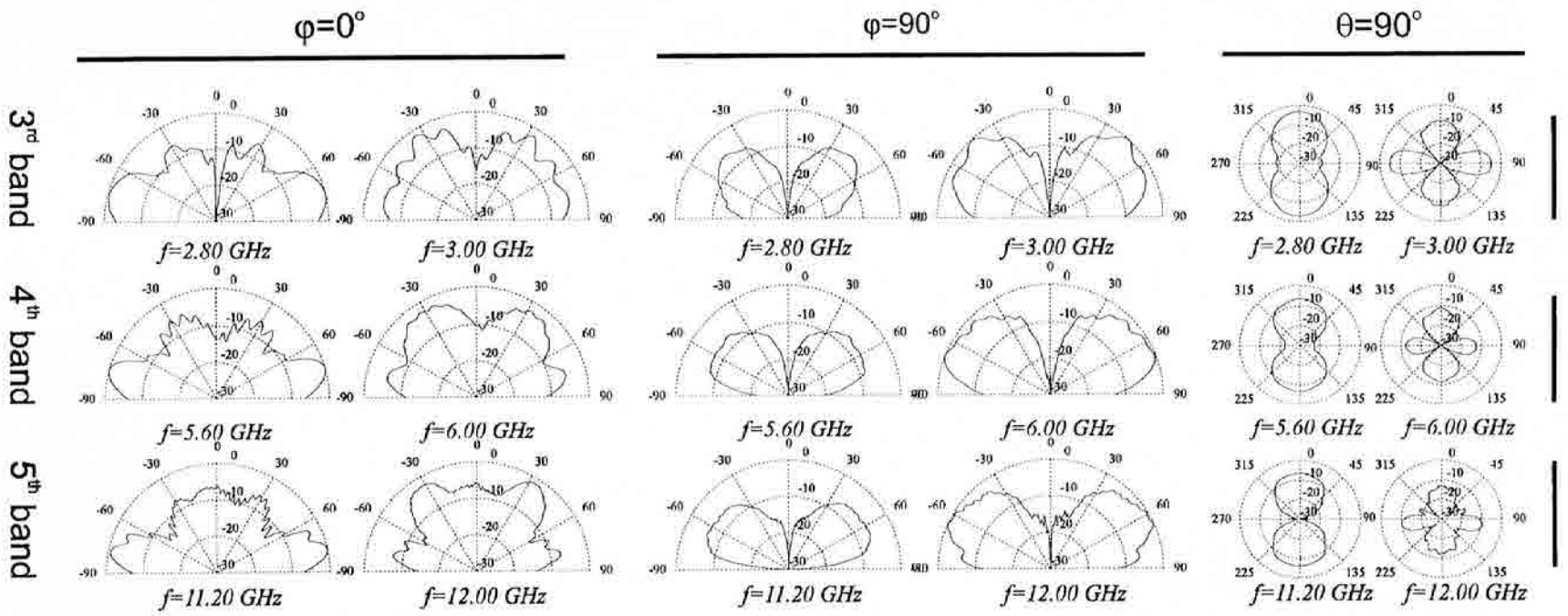

Fig. 5.6 Sierpinski-90 monopole radiation pattern main cuts (E_θ component). Two cuts are displayed for each band (rows), one at the minimum VSWR point, and the other towards the band edge. Notice the similarity among the log-periodically spaced patterns.

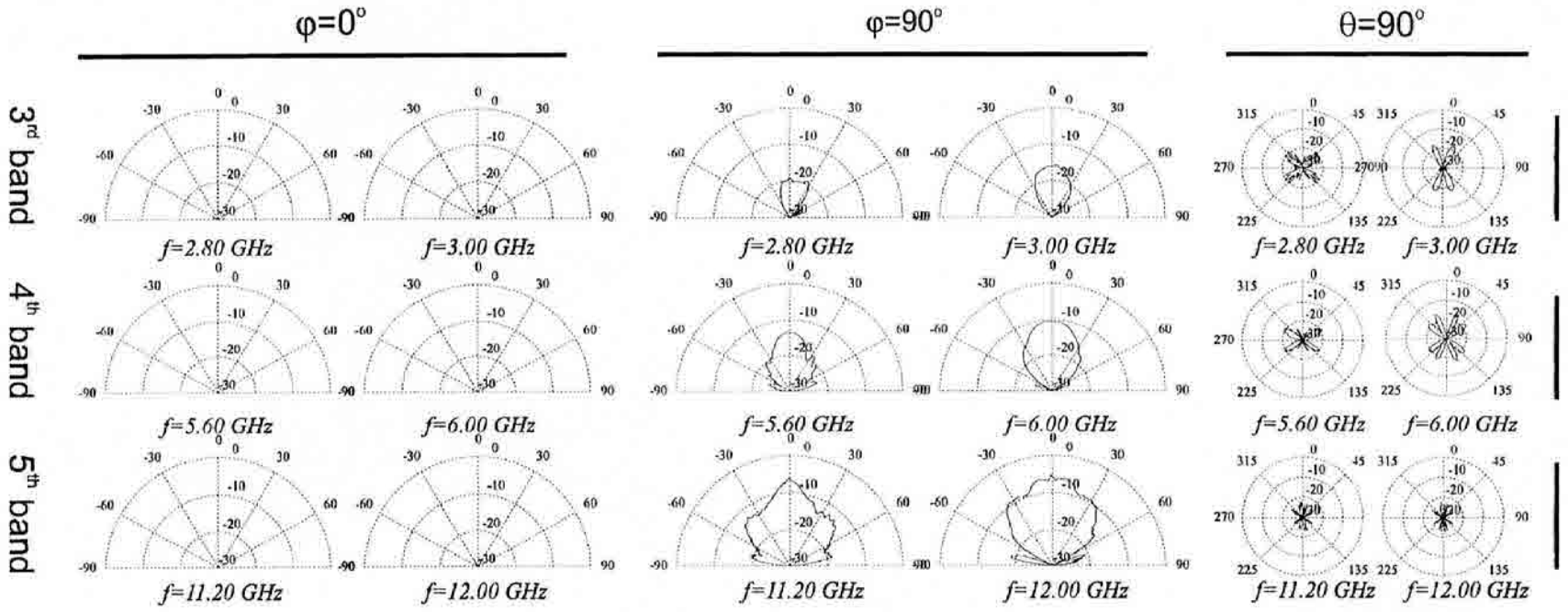

Fig. 5.7 Sierpinski-90 monopole radiation pattern main cuts for the cross-polar component (E_ϕ). Two cuts are displayed for each band (rows), one at the minimum VSWR point, and the other towards the band edge. There is a significant increase on the cross-polar component at higher frequencies for φ=90°.

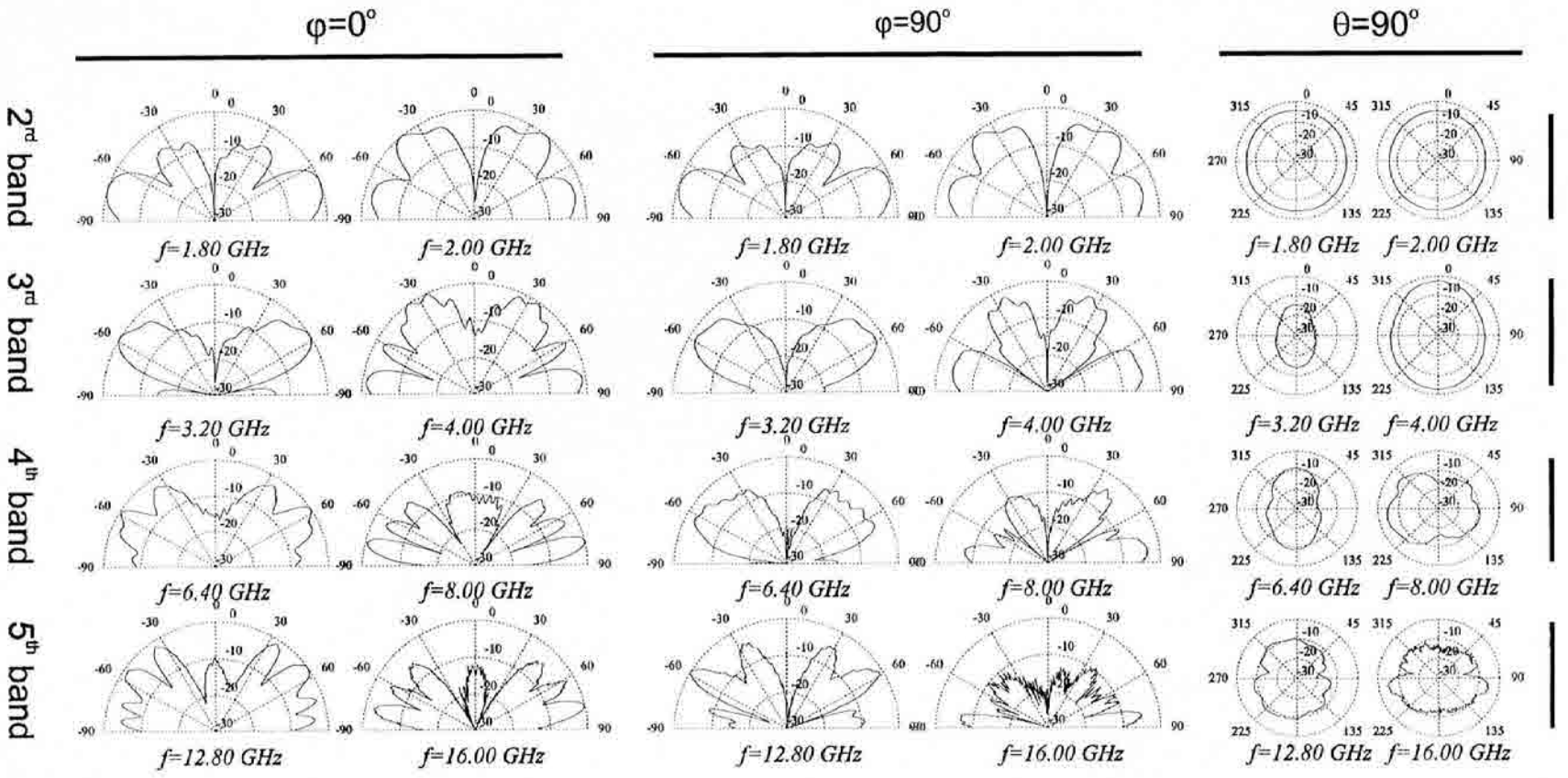

Fig. 5.8 Sierpinski-30 monopole radiation pattern main cuts (E_θ component). Two cuts are displayed at each band (rows), the one on the right column corresponds to the best matched points within the log-period, while the left ones correspond to the secondary relative VSWR minimum. It is apparent that the multiband features vanish in the Sierpinski-30 prototype.

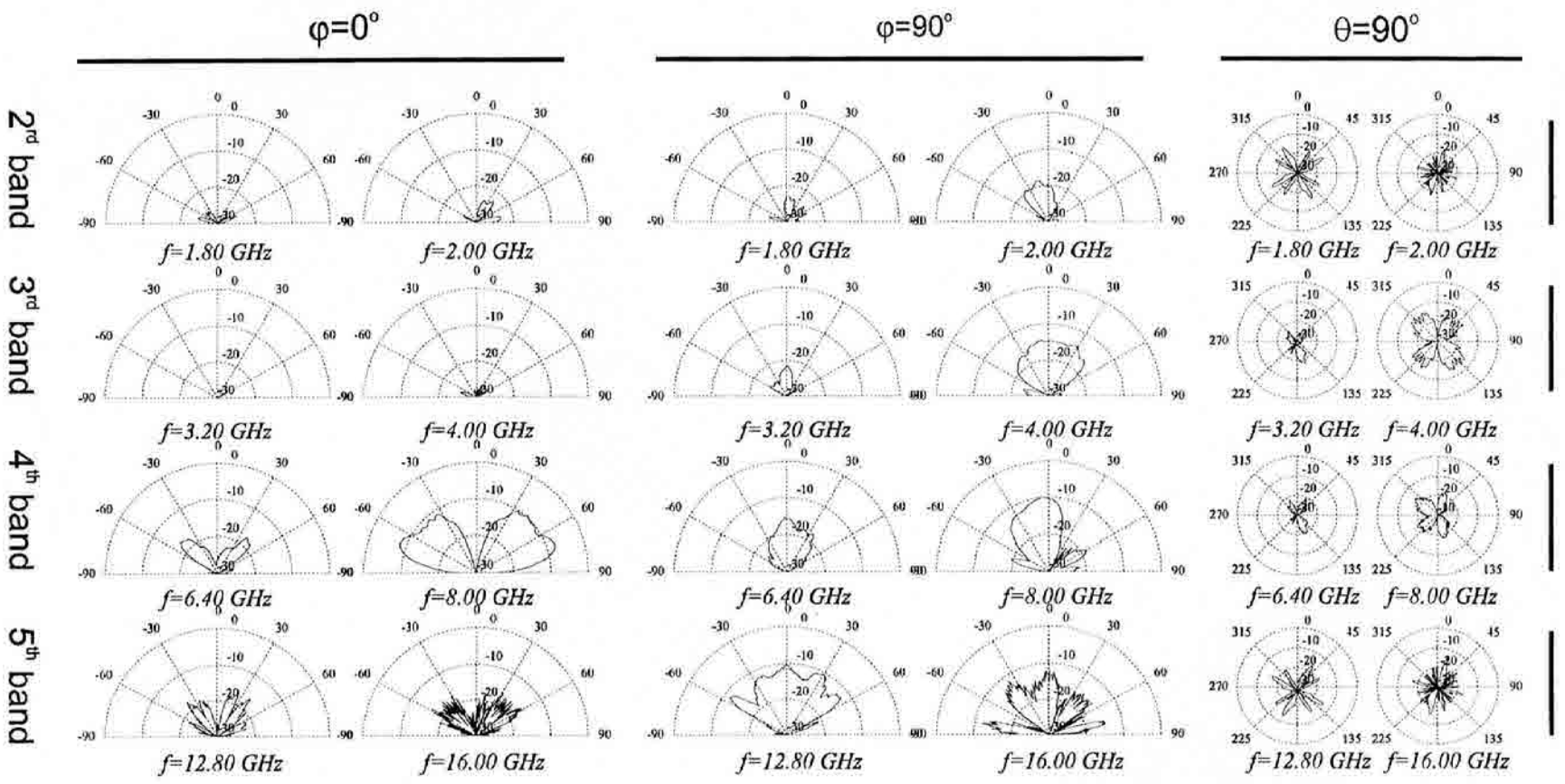

Fig. 5.9 Sierpinski-30 monopole radiation pattern main cuts (E_{ϕ} component). Two cuts are displayed at each band (rows), the one on the right column corresponds to the best matched points within the log-period, while the left ones correspond to the secondary relative VSWR minimum. It is apparent that the multiband features vanish in the Sierpinski-30 prototype.

5.1.5 - The Multiperiodic Traveling Wave V Model

It appears most interesting to investigate an approximate model that would predict the antenna response to flare angle variations. A traveling wave model looks attractive for several reasons: we know that the bow-tie antenna performs basically as a traveling wave V antenna [138] at large enough frequencies, and we assume that the Sierpinski antenna operates through a propagating wave that becomes attenuated by radiation at smaller gaskets at large enough frequencies.

5.1.5.1 - The Single V Model

The radiation vector of a uniform linear current I of length L lying on the yz plane, forming a $\alpha/2$ angle with the z-direction, is given by

$$\vec{N} = \vec{I} \cdot L \cdot e^{j\gamma L/2} \cdot \frac{\sin u}{u} \tag{5.11}$$

where u and γ are defined as

$$\gamma \equiv \gamma_z + \gamma_y \equiv k_z \cos(\alpha/2) + k_y \sin(\alpha/2) = k\cos\theta\cos(\alpha/2) + k\sin\theta\sin\varphi\sin(\alpha/2) \tag{5.12}$$

$$u \equiv \frac{\gamma L}{2} \tag{5.13}$$

Now, the radiation vector of a symmetrical V structure with flare angle α, with both current elements pointing outwards the apex angle (see Fig. 5.10), has two components N_z and N_y such as

$$N_z = I_z \cdot L \cdot \left(e^{j\gamma_1 L/2} \cdot \frac{\sin u_1}{u_1} + e^{j\gamma_2 L/2} \cdot \frac{\sin u_2}{u_2} \right) \tag{5.14}$$

$$N_y = I_y \cdot L \cdot \left(e^{j\gamma_1 L/2} \cdot \frac{\sin u_1}{u_1} - e^{j\gamma_2 L/2} \cdot \frac{\sin u_2}{u_2} \right) \tag{5.15}$$

where $I_z=I\ cos(\alpha/2)$ and $I_y=I\ sin(\alpha/2)$ account for the projections of the current element along the z and y directions respectively, and $\gamma_1=\gamma_z+\gamma_y$, $\gamma_2=\gamma_z-\gamma_y$, $u_1=\gamma_1 L/2$ and $u_2=\gamma_2 L/2$ are the γ and u parameters for the upper and lower branches of the V structure respectively.

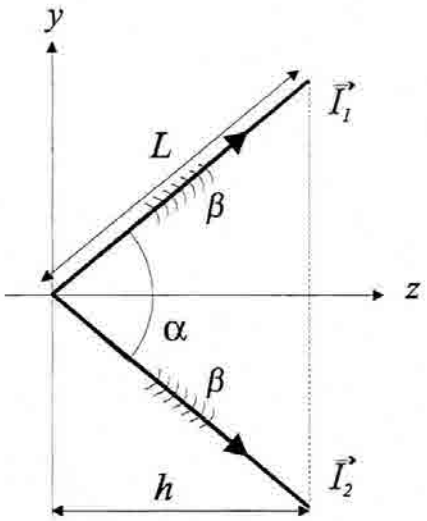

Fig. 5.10 The single V model.

When one considers that a traveling wave (instead of a uniform amplitude standing wave) is formed on each branch of the V structure, a phase progression along the wire has to be added to the current, i.e.,

$$\bar{I}_t = \bar{I} e^{-j(\beta_z z+\beta_y y)} \tag{5.16}$$

where β_z and β_y are the projections of the phase propagation constant β,

$$\begin{aligned} \beta_z &= \beta\cos(\alpha/2) \\ \beta_y &= \beta\sin(\alpha/2) \end{aligned} \tag{5.17}$$

Such a phase progression introduces a displacement on the γ parameter of the radiation vectors, such that they become

$$N_z = I_z \cdot L \cdot \left(e^{j\gamma'_1 L/2} \cdot \frac{\sin u'_1}{u'_1} + e^{j\gamma'_2 L/2} \cdot \frac{\sin u'_2}{u'_2} \right) \tag{5.18}$$

$$N_y = I_y \cdot L \cdot \left(e^{j\gamma'_1 L/2} \cdot \frac{\sin u'_1}{u'_1} - e^{j\gamma'_2 L/2} \cdot \frac{\sin u'_2}{u'_2} \right) \tag{5.19}$$

where, when both waves propagate from the apex to the tips of wire γ' and u' become

$$\begin{aligned} \gamma_i' &= \gamma_i - \beta \\ u_i' &= \frac{\gamma_i' L}{2} \qquad i = 1,\ 2 \end{aligned} \tag{5.20}$$

For the sake of simplicity but without a loss of generality, we will restrict our analysis to the radiation properties in the plane perpendicular to the V structure (the φ=0° or xz plane). For this particular case, φ=0° and k_y=0. This leads to $\gamma_1=\gamma_2$ and consequently $u_1=u_2$, which is a most logical result given the aforementioned symmetry with respect to that plane. Also the N_y component vanishes, and the remaining N_z radiation vector becomes

$$N_z = I\cos(\alpha/2) \cdot L \cdot e^{j(\gamma_z-\beta)L/2} \cdot 2 \cdot \frac{\sin((\gamma_z-\beta)L/2)}{(\gamma_z-\beta)L/2} \tag{5.21}$$

Now, by introducing $h = L\cos(\alpha/2)$ as the height of the V triangular structure, and β_α as

$$\beta_\alpha = \frac{\beta}{\cos(\alpha/2)} \tag{5.22}$$

N_z can be rewritten as

$$N_z = I \cdot h \cdot e^{j(k_z-\beta_\alpha)h/2} \cdot 2 \cdot \frac{\sin((k_z-\beta_\alpha)h/2)}{(k_z-\beta_\alpha)h/2} \tag{5.23}$$

which allows the following interpretation. In the xz plane, the V structure behaves essentially as an equivalent travelling wave current element of size h aligned along the z direction, which however propagates slower with an equivalent propagation constant β_α.

origin to $z=h/2$. The second term, i.e., the term $\sin u'/u'$ (hereafter $sinc(u')$) is the so called space factor [52],[53], which takes into account that the radiating element has a non-negligible length h. The argument of the space factor u' can only take values within the finite range,

$$u' \in \left[(-k+\beta_\alpha)h/2,(k+\beta_\alpha)h/2\right] \tag{5.24}$$

which is the so called visible range. Such concepts are analogous to their equivalents in array theory, with the main difference that the space factor is not periodic due to the continuous nature of the radiating source. The propagation constant β_α shifts the visible

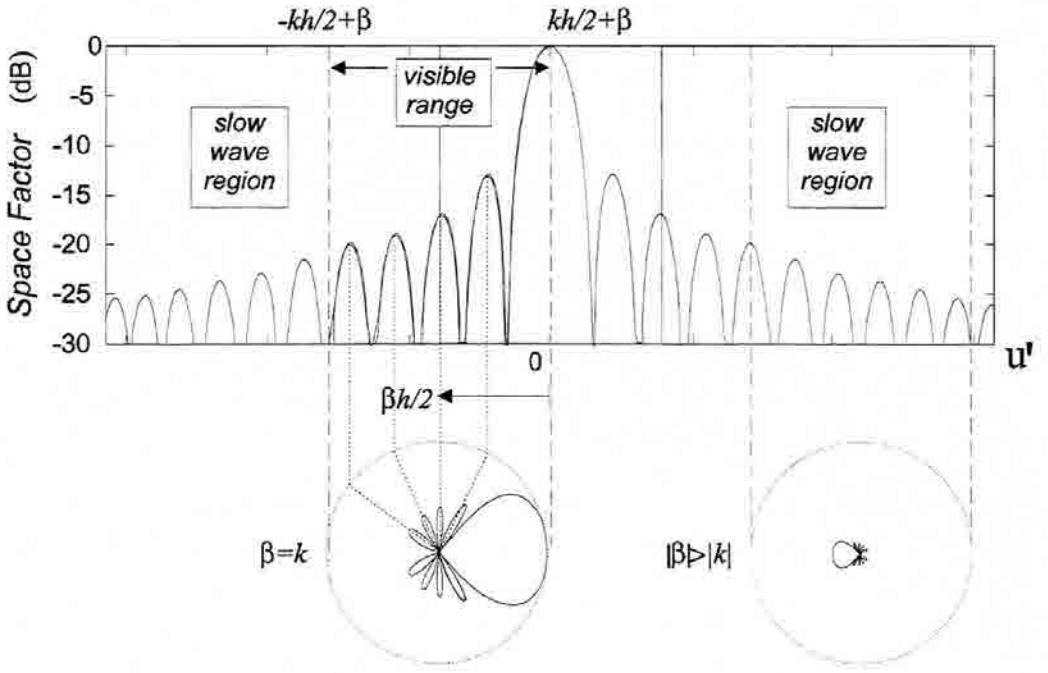

Fig. 5.11 Effect of the finite visible range on the beam tilt.

range along the u' domain Fig. 5.11, such that a tilted beam is produced, with its maximum pointing towards the θ_m direction,

$$\theta_m = \arccos\left(\frac{\beta_\alpha}{k}\right) \tag{5.25}$$

in case of $\beta_\alpha=0$, radiation is given in the broadside direction. The case $|\beta_\alpha|>|k|$ accounts for a slow wave propagating in the z-axis direction. Contrarily to what happens with a source of

infinite length, traveling slow waves indeed produce radiation for the finite source case. In the infinite case (for instance a plane surface wave traveling in an infinite media along the z direction), the space factor *sinc(u')* becomes a delta function (with null secondary lobes) and the visible range covers a null region of the spectral domain (completely out of the origin where the delta function is located) for the slow wave case. On the other hand, the finite source case always produces radiation because the *sinc(u')* function has an infinite extent. Nevertheless, radiation is held trough the lower secondary lobes of the space factor in the slow wave case, which means that the overall field strength is reduced with respect to the fast wave one (Fig. 5.11). The distinction between finite an infinite models is important here, because the flare angle α yields a slow wave in the z direction, which however radiates.

5.1.5.2 - The Balanced V Model

A balanced two-arm model is used to properly model the full Sierpinski antenna. First, we should consider both antenna arms with just one traveling current wave in both arms. Although net current is directed towards the positive $z+$ direction on both arms, waves propagate towards $z+$ in the right arm while they propagate towards $z-$ on the left one (see Fig. 5.12). Such an arrangement is consistent with the equivalent transmission line that would be formed if both arms were folded and directed to the x direction. This balanced mode yields the following radiation vector in the principal plane φ=0°, (xz),

$$N_{zo} = 2Ih \cdot e^{-j\beta_\alpha h/2} \cdot \left(e^{jk_z h/2} \frac{\sin((k_z - \beta_\alpha)h/2)}{(k_z - \beta_\alpha)h/2} + e^{-jk_z h/2} \frac{\sin((k_z + \beta_\alpha)h/2)}{(k_z + \beta_\alpha)h/2} \right) \quad (5.26)$$

where a subscript 'zo' has been added to the radiation vector to note the waves propagating outwards from the origin.

The traveling wave model just presented can be made more accurate if the equivalent V arms are loaded with an end impedance that adds the contribution of waves being reflected at the extremes. By introducing a current reflection coefficient ρ_c , the radiation vector of such equivalent reflected waves $N_{z\rho}$ would be,

$$N_{z\rho} = 2Ih \cdot \rho_c e^{-j\beta_\alpha h} \cdot e^{-j\beta_\alpha h/2} \cdot \left(e^{jk_z h/2} \frac{\sin((k_z + \beta_\alpha)h/2)}{(k_z + \beta_\alpha)h/2} + e^{-jk_z h/2} \frac{\sin((k_z - \beta_\alpha)h/2)}{(k_z - \beta_\alpha)h/2} \right) \quad (5.27)$$

where the extra phase term $e^{-j\beta_\alpha h}$ can be interpreted as the average phase delay of the waves traveling from the average $|z|=h/2$ point to the antenna tips and back towards the start up point.

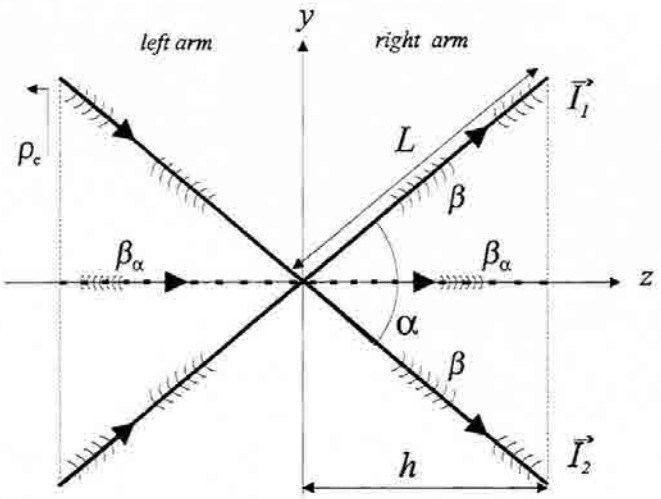

Fig. 5.12 The balanced V model.

The overall radiation vector N_z would reduce for such a full model to,

$$N_z = N_{zo} + N_{z\rho} \tag{5.28}$$

Naturally, this equivalent model yields the same result as the well known sinusoidal standing wave pattern of a linear dipole when α=90°, ρ_c=-1 and $\beta=k$.

5.1.5.3 - Propagation Through a Multiperiodic Media

Before illustrating our traveling wave V model with some examples, some considerations regarding the phase propagation constant must be taken into account. Up to now, the model reduces the Sierpinski antenna to a double V antenna model that support edge current traveling waves with a phase propagation constant β. Such a propagation constant should be $\beta=k.n_{eff}$ to take into account the dielectric antenna coatting (in previous chapter such an effective refraction index was empirically adjusted to $n_{eff} \approx 1.1$ by comparing experimental and computed results). Although this model should be enough for a continuous shape, the fractal structure appears quite distinct. Again, if propagation along the

chapter such an effective refraction index was empirically adjusted to $n_{eff} \approx 1.1$ by comparing experimental and computed results). Although this model should be enough for a continuous shape, the fractal structure appears quite distinct. Again, if propagation along the antenna edges is primarily considered, the fractal shape comes into view basically as a periodic structure (see Fig. 5.13).

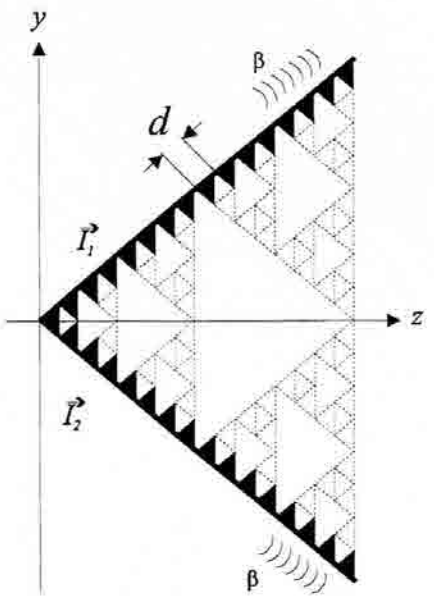

Fig. 5.13 The edge of the Sierpinski antenna is a periodic structure.

Propagation through a periodic structure is a rather particular phenomenon which is basically described in [43],[48],[55],[116]. The solution of the one-dimensional wave equation in a periodic media yields an infinite superposition of n propagating modes,

$$E(l) = \sum_{n=-\infty}^{\infty} A_n e^{-j\beta_n l} \tag{5.29}$$

with each mode characterized by a propagation constant β_n such that,

$$\beta_n = \beta_o + \frac{2\pi}{d} n \tag{5.30}$$

being d the characteristic structure period. Often, such modes are called *Hartree space harmonics* [116] or *Floquet modes* and the term corresponding to n=0 is called the *fundamental harmonic* or the *fundamental mode*. One of the most interesting aspects of this phenomenon is the fact that a slow fundamental propagation constant β_0 can yield a fast

mode propagation) or backward direction (radiation opposite to propagation). In particular, it can be seen that forward radiation is given by modes with negative n numbers such that,

$$\frac{d}{\lambda}\left(n_{eff}-1\right)<|n|<\frac{d}{\lambda}n_{eff} \qquad (forward) \tag{5.31}$$

while backward radiation is supported by modes with

$$\frac{d}{\lambda}n_{eff}<|n|<\frac{d}{\lambda}\left(n_{eff}+1\right) \qquad (backward) \tag{5.32}$$

being n_{eff} the fundamental mode effective index of refraction. Again, some interesting conclusions can derived from this relations. First of all, given a fixed period length d, there is a minimum wavelength that yields fast waves

$$\lambda<d\left(n_{eff}+1\right) \tag{5.33}$$

Such a wavelength can be thought as the cutoff wavelength of a high-pass system, which however does not imply an abrupt cease of radiation when considering finite sources as discussed previously. As a rule of thumb and neglecting coatting effects, such a cutoff wavelength is $\lambda/2=d$. Secondly, backward radiation is allowed for lower frequencies than in the forward radiation case. Forward radiation can be thought of as having a smaller cutoff wavelength $\lambda=d\cdot n_{eff}$ (roughly speaking $\lambda=d$).

With these basic ideas in mind, some striking conclusions regarding our fractal Sierpinski antenna can be drawn. One would usually think that in such case the characteristic period d is the length of the smallest triangle side. This would lead to the stunning conclusion that increasing the number of fractal iterations should lead to higher and higher cutoff frequencies that, in the ideal fractal structure, would forbidden propagation of Hartree harmonics beyond the fundamental one. However, a careful look to the fractal shape evinces that it is in fact a multiperiodic structure ! (Fig. 5.14)

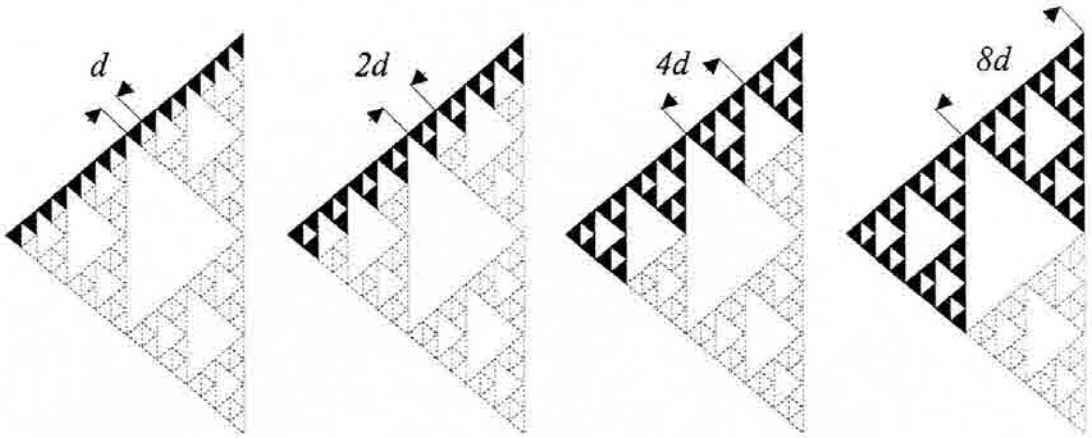

Fig. 5.14 The fractal Sierpinski gasket seen as a multiperiodic structure.

With this new picture in mind, the periods d_o, 2 d_o, 4 d_o ..., 2^m d_o become apparent, which means that wavelengths λ_o, $2\lambda_o$, $4\lambda_o$ ..., $2^m\lambda_o$ and frequencies f_o, $f_o/2$, $f_o/4$,..., $f_o/2^m$ are actually supported. Of course, there must be a longest cutoff wavelength unless the structure is made infinitely large. In fact, the finite extent of the antenna only implies that most of the contribution to radiation is held through the fundamental mode. Finally, the multiperiodic nature of the fractal shape again leads to the underlying idea of this thesis: since the ideal structure is similar with respect to many characteristic scales, it can be naturally assummed that it will offer a similar behavior with many characteristic wavelengths too, all of them related by the characteristic scale factor of the fractal shape.

5.1.5.4 - Comparison with Experimental Results

Let us now briefly reconstruct the picture of the theory just introduced. The Sierpinski antenna is schematically described by means of a balanced two-V model, which supports outward traveling waves. Such a model is completed by taking into account the proper reflected waves at the antenna tips. In the principal φ=0° plane, such a model is equivalent to a straight wire of the same size as the triangle height, aligned along the antenna axis direction (z axis). Waves propagate through this equivalent wire with a slower propagation constant β_{ez} which depends on the flare angle (see (5.22)). A multiperiodic media approach suggests that not only a phase propagation constant along the antenna edges should be considered, but also several Hartree harmonics must be taken into account. The overall propagation constant can now be anyone within the set

$$\beta_{n\alpha} = \left(\beta_o + \frac{2\pi}{d} n\right) \cdot \frac{1}{\cos(\alpha/2)} \tag{5.34}$$

depending on what space harmonic (or harmonics) is considered.

In general it is not trivial either determining how many Hartree harmonics must be included in the sum (5.29), nor their relative amplitudes A_n. However, we can test the model at low frequencies where not many modes are expected to contribute to the overall sum. The plot in Fig. 5.15 displays the result of applying the current analysis to 30°, 60°, 90° flare

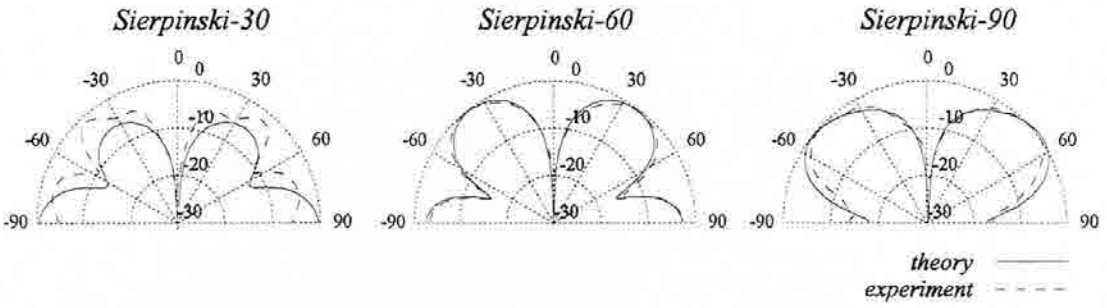

Fig. 5.15 Experimental data and theoretical analysis for the Sierpinski antenna pattern variation with changing the flare angle. The three models were tested at 2 GHz. Measured data is shown in dashed lines.

angles. All antennas had the same phyisicall parameters (h = 8.9 cm, n_{eff} = 1.1) except for the reflection coefficient at the antenna tips, which was chosen to be ρ_c = -0.8 for the two narrower antennas and ρ_c = -0.2 for the 90° one. That lower reflection coefficient for the 90° case has been empirically found to better match the non ideal null characteristic on the broadside direction of the experiments. All three antennas were tested at 2 GHz and a period equal to half of the antenna edge length was taken. It can be seen that both the theoretical model (solid line) and the experimental data (dashed) are in very good agreement in the Sierpinski-60 and Sierpinski-90 cases. The theoretical model also predicts the overall pattern shape in the Sierpinski-30 case.

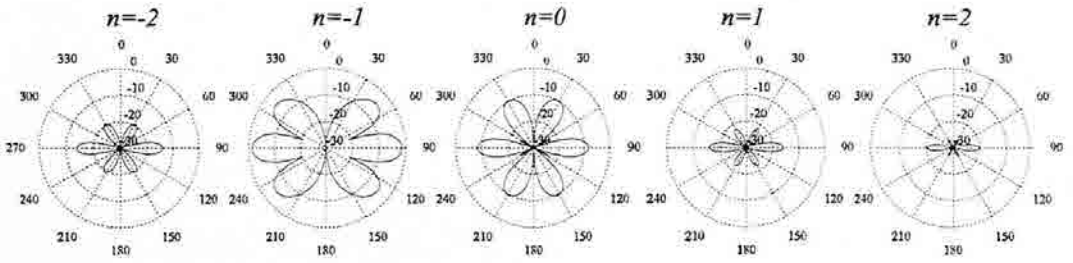

Fig. 5.16 Hartree Harmonics for the Sierpinski-60° antenna at 3.6 GHz. The harmonics for n=-1 and n=0 are predominant.

The results just presented validates the theoretical approach at low frequencies, where the fundamental mode is basically dominant. At higher frequencies one must take into account additional phenomena such as the reduction of the active region (which can be taken into account by reducing the effective antena height h), the attenuation of the traveling

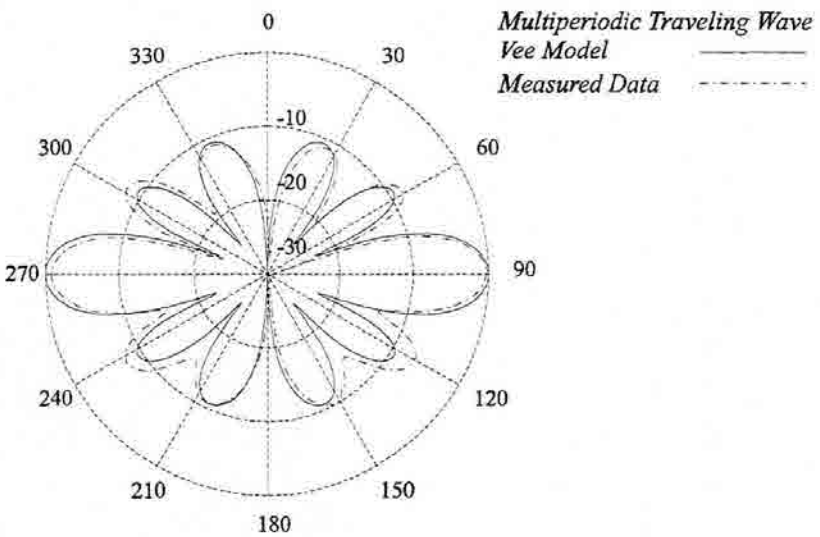

Fig. 5.17 Theoretical and experimental patterns of the Sierpinski-60° antenna at 3.6 GHz (third band). The experimental pattern is slightly assymetrical due to an imperfect balance of the balun.

wave due to radiation, and the multiperiodic nature of the system. To illustrate how the contribution of several space harmonics can modify the pattern that would predict the non-periodic model, another example is introduced. The Sierpinski-60 antenna at 3.6 GHz is now considered and space harmonics of first and second order are included. Such harmonics are shown in Fig. 5.16, all of them with the amplitude that results from evaluating (5.28) for the corresponding propagation constants given by (5.34).

The cutoff effect for the slow wave modes becomes clear now. All harmonics except the fundamental one and the first negative order one (n=-1) become rapidly attenuated, i.e., they contribute with a little amplitude to radiation. When all modes are added with a proper amplitude factor (a relative amplitude A_0=-2.43 for the fundamental mode was the only required adjustment), the resulting pattern is the one in Fig. 5.17. Again, theoretical and experimental data are found to be in good agreement except for a non ideal behavior of the tapered balun used in the experimental setup.

It is very interesting to stress that the resulting superposition of modes yields a rather different result than the fundamental mode (n=0) alone. That is, the traveling wave V model itself is not enough to predict the fractal antenna behavior at large frequencies, but requires the periodic structure approach to give an accurate result.

5.2 - Bending the arms of the Sierpinski Dipole

From the results of previous sections, one can conclude that the Sierpinski antenna operates through an active region that self-scales with wavelength. Such an active region is formed when an electromagnetic wave propagating from the apex to the tips of the antenna becomes radiated and thus attenuated when interacting with proper size fractal sub-gaskets. The existence of such a sort of propagating wave is supported by the phase current maps reconstructed through the FDTD algorithm (see Chapter 4).

Now, one should naturally wonder whether such a propagating wave would lead to a directional pattern when bending the fractal dipole antenna arms. Actually such a behavior is observed on the Euclidean version of the antenna, i.e., the bow-tie antenna, which however does not maintain the pattern lobe structure when increasing frequency (see Fig. 5.18 for the measured field patterns of the inclined-arm version of the bow-tie antenna). One should also question whether, in case that the fractal antenna displayed such directional patterns, those were going to be held similar through the bands.

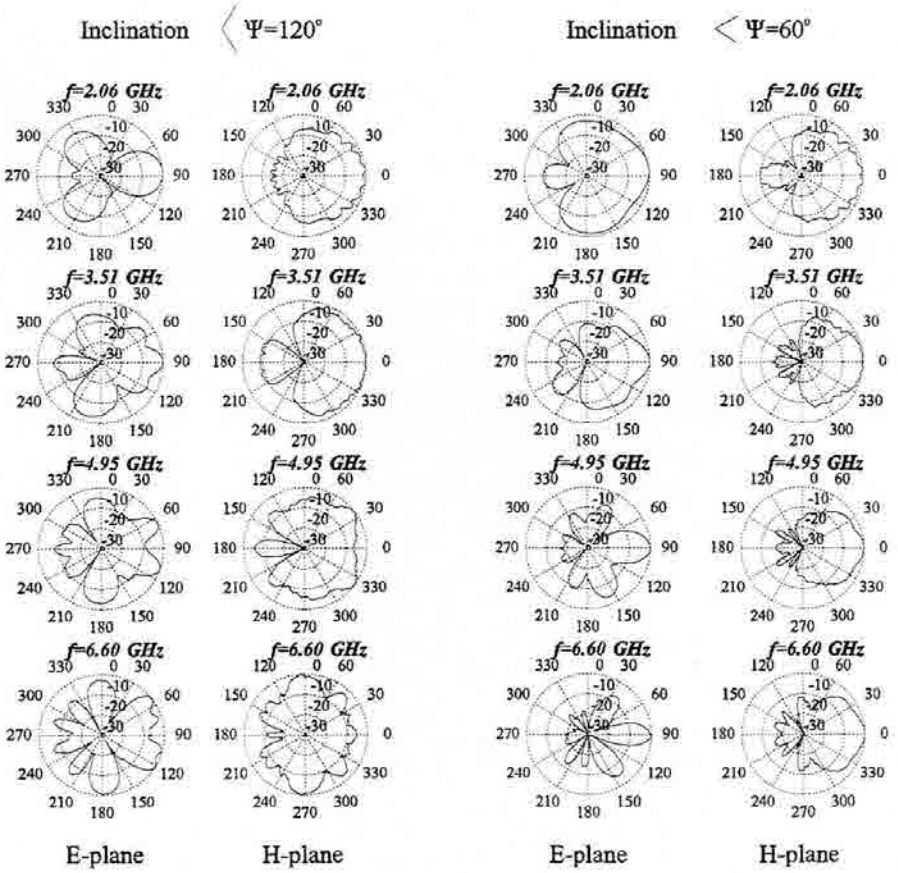

Fig. 5.18 Inclined bow-tie antenna radiation pattern cuts for Ψ=120° and Ψ=60° inclination angles

5.2.1 - Experimental Results on the Inclined Sierpinski Dipole

Two Sierpinski dipoles of 60° and 90° flare angles were constructed and fed through a tapered balun as described in the previous chapter. The arms of the antenna were inclined at angles ψ=60° and ψ=120° and measured in an anechoic chamber (see Fig. 5.19 for the antenna configuration). The results are shown in Fig. 5.20 and Fig. 5.21.

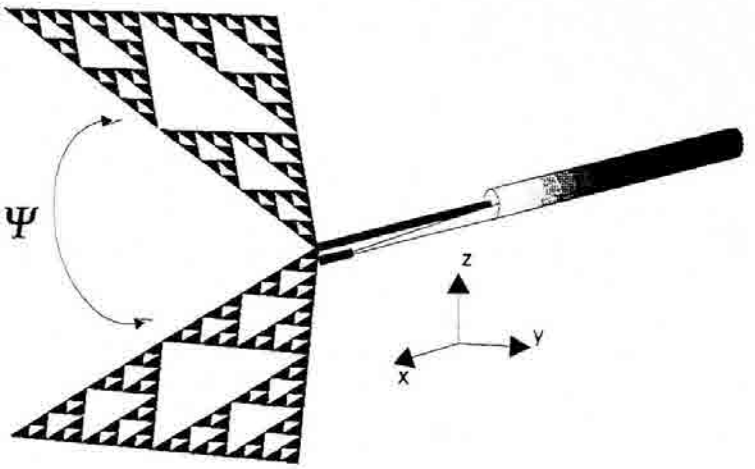

Fig. 5.19 Inclined version of the Sierpinski dipole. The arms are bent towards the x+ axis.

It can be stated from these results that the fractal properties of the antenna are still held in the inclined configuration, in the sense that the patterns still look similar through the bands. There are significant variations on the pattern shape within each band, which however become repeated when frequency is doubled.

In general, one can also state that there is a tendency on impinging directional features to the radiation patterns, which is more clear in the Sieprinski-90 prototype. However, some undesirable properties of the patterns rapidly catch the eye. Namely, the patterns display high side and back lobes, and directivity does not increase as much as one could expected when bending the antenna arms. Also, it appears quite surprising at first glance that the Sierpinski-60 tends to enhance radiation in the backward direction at the measured frequencies. Again, one should look for an explanation to this phenomenon on the multiperiodic nature of the fractal structure.

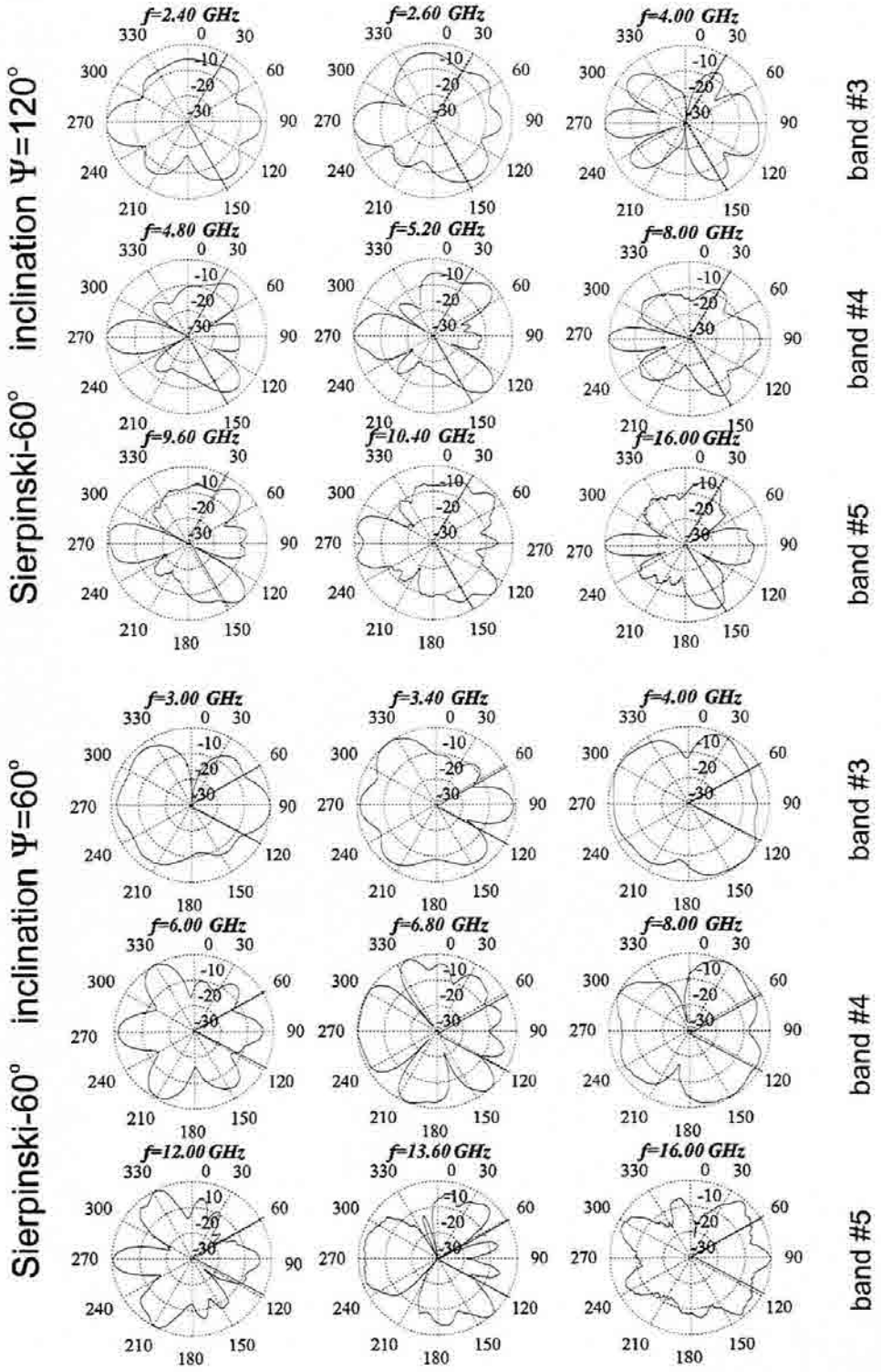

Fig. 5.20 Sierpinski-60° antenna radiation pattern E-plane cuts (φ=0°) for Ψ=120° (up) and Ψ=60° (bottom) inclination angles.

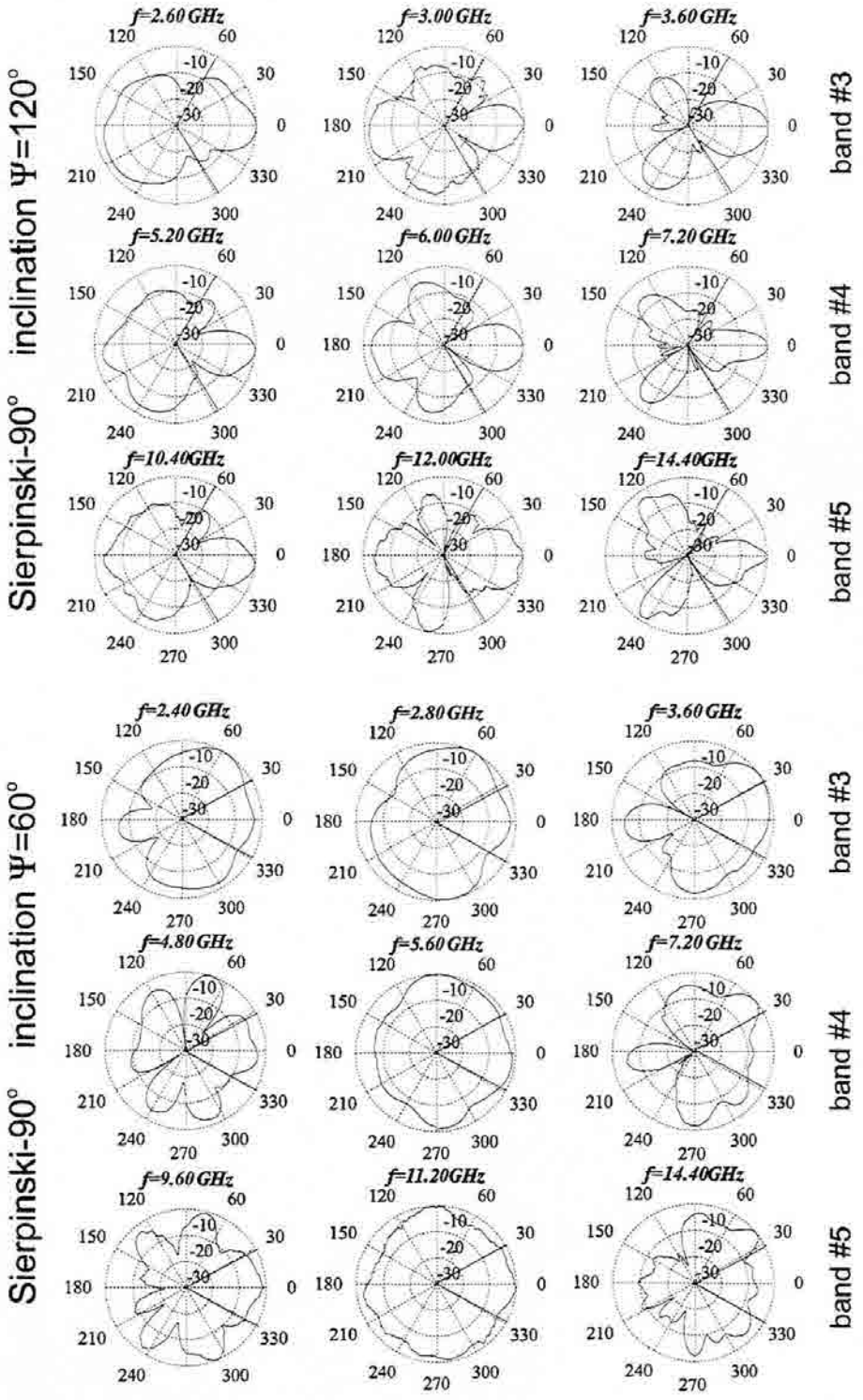

Fig. 5.21 Sierpinski-90° antenna radiation pattern E-plane cuts (φ=0°) for Ψ=120 (up) and Ψ=60° (bottom) inclination angles.

5.2.2 - The Multiperiodic Traveling Wave V Model

The V analysis of previous section can be again applied, with some slight modifications, to understand the basic behavior of the inclined antenna. For the sake of simplicity, we will consider that each arm of the antenna can be modeled as a wire current with a characterisitc propagation constant β_α. To keep the same notation as in the previous analysis, both equivalent wire will lying on the yz plane, symmetrically bended towards the $z+$ axis. It must be taken into account that both currents flow now from the bottom to the top of the antenna (Fig. 5.22).

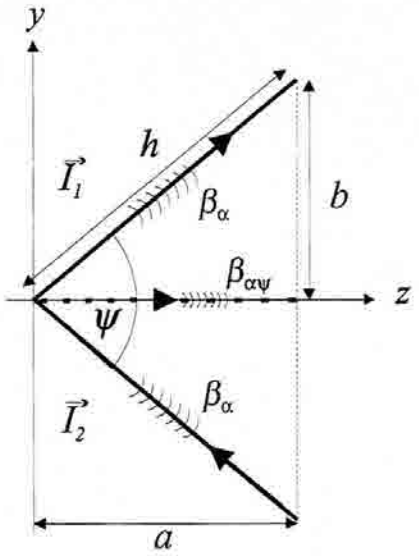

Fig. 5.22 Simple V model for the inclined version of the Sierpinski antenna.

When considering progressive waves traveling outwards from the antenna apex to the tips, the radiation vector for such currents can be written in a very similar form as that on equations (5.18) and (5.19), but with a sign reversal such that,

$$N_{zo} = I \cdot a \cdot \left(e^{j\gamma'_1 h/2} \cdot \frac{\sin u'_1}{u'_1} - e^{j\gamma_2 h/2} \cdot \frac{\sin u'_2}{u'_2} \right) \tag{5.35}$$

$$N_{yo} = I \cdot b \cdot \left(e^{j\gamma'_1 h/2} \cdot \frac{\sin u'_1}{u'_1} + e^{j\gamma'_2 h/2} \cdot \frac{\sin u'_2}{u'_2} \right) \tag{5.36}$$

where now the current wire length is the triangle height h, while a and b are the h projections upon the z and y axis respectively. Also, two auxiliary parameters γ' and u' are defined again for the upper branch (subscript '1') and the lower one (subscript '2'), as follows

$$\gamma_1 \equiv \gamma_z + \gamma_y \equiv k_z \cos(\psi/2) + k_y \sin(\psi/2) = k\cos\theta\cos(\psi/2) + k\sin\theta\sin\varphi\sin(\psi/2) \tag{5.37}$$

$$\gamma_2 \equiv \gamma_z - \gamma_y \equiv k_z \cos(\psi/2) - k_y \sin(\psi/2) = k\cos\theta\cos(\psi/2) - k\sin\theta\sin\varphi\sin(\psi/2) \tag{5.38}$$

$$\begin{aligned} \gamma_i' &= \gamma_i - \beta_\alpha \\ u_i' &= \frac{\gamma_i' h}{2} \qquad i = 1,\ 2 \end{aligned} \tag{5.39}$$

If some reflection is to be considered at the tips of the antenna, one can extend the above equations for the reflected waves by substituting the current amplitude I by I_ρ defined as

$$I_\rho = I \cdot \rho_c e^{-j2\beta_\alpha h} \tag{5.40}$$

where ρ_c is the current reflection coefficient. Also, γ' and u' parameters must be substituted by γ'' and u'' defined as,

$$\begin{aligned} \gamma_i'' &= \gamma_i + \beta_\alpha \\ u_i'' &= \frac{\gamma_i'' h}{2} \qquad i = 1,\ 2 \end{aligned} \tag{5.41}$$

Finally, the overall radiation vector considering both antenna arms, and both outward and reflected waves is just the linear superposition,

$$\vec{N} = \vec{N}_o + \vec{N}_\rho \tag{5.42}$$

In general, both N_z and N_y have to be considered to evaluate the field intensity in the φ=90° plane. Neither k_y nor k_z vanish in this plane, and a further simplification of the radiation vector expression becomes intrincate. However, one can extract some interesting conclusions upon the pattern directionality in the z axis, which states forward and backward directions, when considering radiation from outward traveling waves. In this direction k_y vanishes and the γ parameter becomes the same in the upper and lower arms. Radiation due to the z current components cancels too, and only the N_y component remains,

$$N_{yo} = 4 \cdot I \cdot b \cdot e^{-j\beta_{a\psi} a/2} e^{jk_z a/2} \cdot \frac{\sin\left(k_z - \beta_{a\psi}\right)\frac{a}{2}}{\left(k_z - \beta_{a\psi}\right)\frac{a}{2}} \tag{5.43}$$

where now, the equivalent propagation constant $\beta_{a\psi}$ is defined as,

$$\beta_{a\psi} = \frac{\beta_e}{\cos(\alpha/2)\cos(\psi/2)} \tag{5.44}$$

being β_e the phase propagation constant along the antenna edge and ψ the inclination angle. The above expression for N_{yo} can be interpreted as follows. In the z direction, the antenna behaves as a linear dipole of length $2b$, which however has its beam tilted towards z+ due to the outward traveling wave. The strength of the field is proportional to $2b$, which is maximized for ψ=180° (flat structure). On the other hand, the sinc function term accounts for a linear uniform current distribution with an equivalent length a along the z direction. As usual, the larger the length a, the narrower the sinc function and the larger the directivity. Since a and b are both projections of the triangle height h, it appears clear that there is a trade-off between field strength and pattern directivity. Narrow angles yield good directivities but poor field strengths, while the converse holds for almost flat structures.

The above is appropriate for describing, for instance, the bow-tie antenna behavior. Being current reflections at the antenna tips almost neglegible at large frequencies, the outward propagating waves yield a radiation enhancement in the z direction. However, when considering the fractal shape, its multiperiodic structure must necessarily be taken into account. As stated previously, the propagation along a periodic structure allows several space harmonics to accompany a zero order fundamental wave. For our particular case, the edge propagation constant for any particular n^{th} order mode must be expressed now as,

$$\beta_{en} = \beta_e + \frac{2\pi}{d} n \tag{5.45}$$

which yields an equivalent propagation constant in the z direction,

$$\beta_{\alpha\psi n} = \frac{\beta_e + \frac{2\pi}{d} n}{\cos(\alpha/2)\cos(\psi/2)} \tag{5.46}$$

Even when the fundamental wave propagates forward (and so does the group velocity, i.e., the energy flow velocity), the phase propagation constant of many space harmonics can be negative, yielding to backward radiation. When the fundamental wave is slow, fast waves can be easily obtained for proper values of the period d and the order number n, which will predominate in the radiation process. Actually, the backward radiation of some frequency-independent antennas such as the log-periodic dipole array is also explained through this basic space harmonics concept [39],[46].

Now, with these picture in mind, some of the inclined Sierpinski antenna features can be understood. Either forward or backward radiation can be obtained for several combinations of the flare angle (α) and frequency, which condition the size of the period d and the fundamental propagation constant β_e. This is clearly distinct to what is obtained for the bow-tie antenna which only helds forward radiation. The directivity (and related parameters such as the back lobe ratio) is increased by enlarging the triangle height h projection upon the z axis (a). Since the active region is shrunk at large frequencies in the fractal case, it is clear that the effective size projection a_{eff} will be reduced too ($a_{eff} \approx \lambda/\cos(\psi/2)$) from reconstructed FDTD currents), and this explains why, in general, patterns are less directive in the fractal case than in the Euclidean bow-tie case ($a_{eff} \approx 4.5\lambda/\cos(\psi/2)$). Nevertheless, such an effective size reduction is the price to pay if proper multifrequency operation is to be obtained. Besides this, if one takes into account that the highly uneven shape of the fractal structure can enhance reflections on the gaskets and subgaskets edges, a further distortion of the directional pattern is evinced.

5.3 - Shifting the operating bands

It appears clear from the results presented up to this point, that the multiband behavior of fractal antennas is a direct consequence of the geometric shape of the antenna body. It has been shown that the self-similarity scale factor is clearly linked to the band spacing in the log-periodic domain. For the classical Sierpinski gasket form, such a log-period was δ=2. Now, one should question whether such similarity relations would hold for other fractal shapes having different scale factors, and if one could properly modify a given fractal shape to position the operating bands where necessary.

5.3.1 - Perturbation of the Sierpinski antenna

In Chapter 4 the Sierpinski gasket was chosen as the first example to explore the feasibility of multiband operation. There, the height of the main gasket and their children gaskets (subgaskets) was associated with each operating band. Thus, it appears natural to assume that one should be able to modify the band spacing by changing the size of the children gaskets. This is precisely what has been done when designing the so called P3/5SPK and P2/3SPK antennas, which have been obtained by perturbing the original Sierpinski antenna structure.

The two novel designs are shown in Fig. 5.23 together with the original Sierpinski antenna. Both have the overall form replicated at five different scales at the base of the antenna, the smaller copy being a single triangle. The antennas are designed by means of an iterative algorithm that basically consists on subtracting a scaled triangle from the original triangular form as described in [15], which is a rather different approach than the IFS scheme. At each iteration, a reduction factor of 3/5 is found on the lower triangular cluster of the first antenna (hereafter P3/5SPK) and a reduction factor of 2/3 is found on the second one (hereafter P2/3SPK). It is interesting to notice that the two upper triangular clusters that remain after each subtraction are not proportional copies of the overall shape but are rather distorted. An affine transformation rather than a similarity one should be applied to go from the overall structure to these skewed gaskets, and hence the form is said to be self-affine [2] instead of self-similar. Nevertheless, a similarity relation holds for the lower cluster where the active region is expected to concentrate in, and hence a self-similar electromagnetic behavior can be expected for both structures.

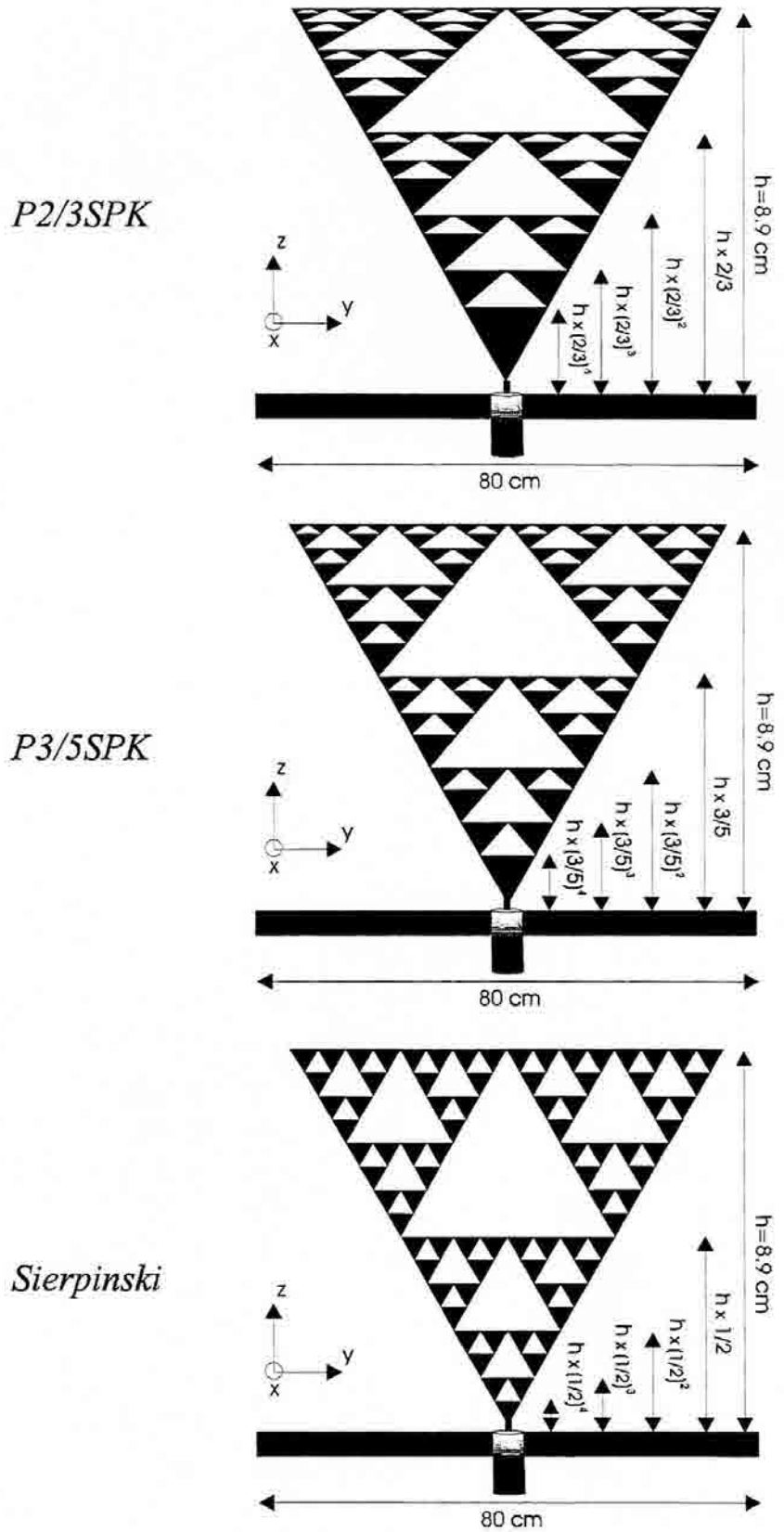

Fig. 5.23 Evolution of the original Sierpinski-60° antenna towards the P2/3SPK and P3/5SPK models.

5.3.2 - P3/5SPK and P2/3SPK Input Parameters

Both antennas were constructed following exactly the same technique as for the Sierpinski antenna. That is, the 8.9 cm height fractal shapes were printed over a Cuclad 250 GT dielectric substrate (ε_r=2.5 h=1.588 mm) and measured in the same experimental conditions. The plots in Fig. 5.24 show the input parameters of the two novel antennas together with those of the Sierpinski-60. The input reflection coefficient has been

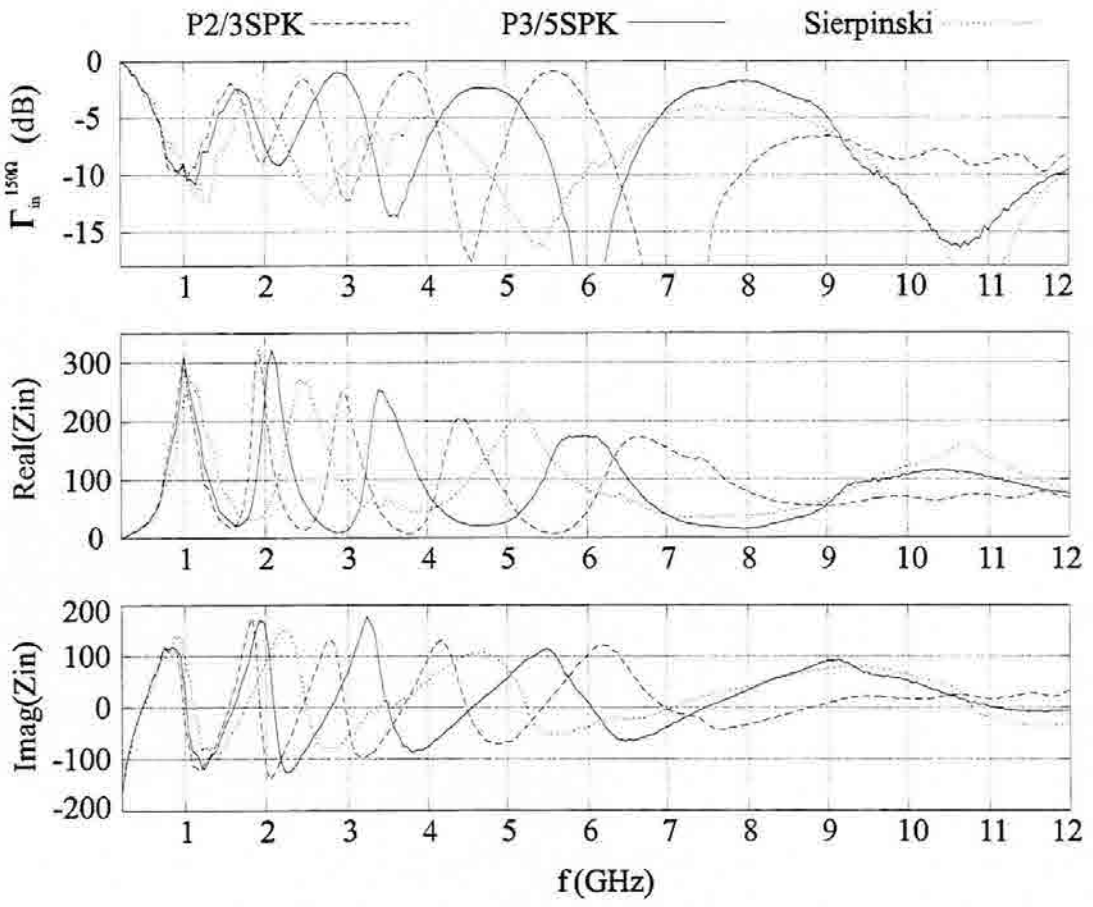

Fig. 5.24Input reflection coefficient relative to 150Ω ($\Gamma_{in}^{150\Omega}$), input resistance and reactance of the three antennas.

normalized to a 150Ω reference impedance which provides a better matching conditions than the standard 50Ω impedance. The input parameters clearly show a band compression towards the origin on the novel designs with respect to the original one. Such a compression

effect is more remarkable in the P2/3SPK case, i.e., the design displaying the most compressed geometrical structure.

The link of the frequency response with the geometrical features of the antenna is clearly evinced in Table 5.1. It lists the first five resonant frequencies (odd resonances) together with the adjacent bands frequency ratio for the three fractal antennas. Clearly, the novel designs display a characteristic log-period equal to the characteristic scale factor of the fractal shape, i.e., δ=1.66 ($1/\delta$= 3/5) for the P3/5SPK antenna, and δ= 1.5 ($1/\delta$= 2/3) for the P2/3SPK one. It is interesting noticing that once more, similarity is broken at the first band where a frequency ratio much larger ($\delta \approx 3.5$) is found between the first two odd resonances. Again, such an effect must be related to the truncation of the infinite ideal fractal structure which leads to a bow-tie mode operation at the longest wavelengths.

P2/3SPK		P3/5SPK		Sierpinski	
f_n	f_n / f_{n-1}	f_n	f_n / f_{n-1}	f_n	f_n / f_{n-1}
0.44	-	0.45	-	0.46	-
1.54	3.46	1.61	3.57	1.75	3.77
2.43	1.57	2.76	1.71	3.51	2.00
3.69	1.51	4.54	1.65	7.01	2.00
5.43	1.47	7.52	1.66	13.89	1.98

Table 5.1. Band frequencies (odd resonances, GHz) and scale factor between adjacent bands for the P2/3SPK, P3/5SPK and Sierpinski antennas.

5.3.3 - P3/5SPK and P2/3SPK Radiation Patterns

The patterns of the two novel designs were measured at the center of the four upper bands (minimum VSWR points relative to 150Ω). The main cuts display a characteristic two lobe structure similar to that of a linear monopole (Fig. 5.25). Such a reduction in the number of lobes with respect to the Sierpinski-60° antenna should be related to the relative smaller size of the full antenna with respect to the operating wavelengths.

The patterns keep a notable degree of similarity among bands with a slight increase of ripples at the highest bands mainly due to the non-ideal behavior of the ground plane. In general, the azimuth (θ=90°) cut show an almost isotropic behavior in the *H*-plane with a slight tendency to enhance radiation in the direction perpendicular to the antennas' surface, which is a common feature shared with the original Sierpinski antenna.

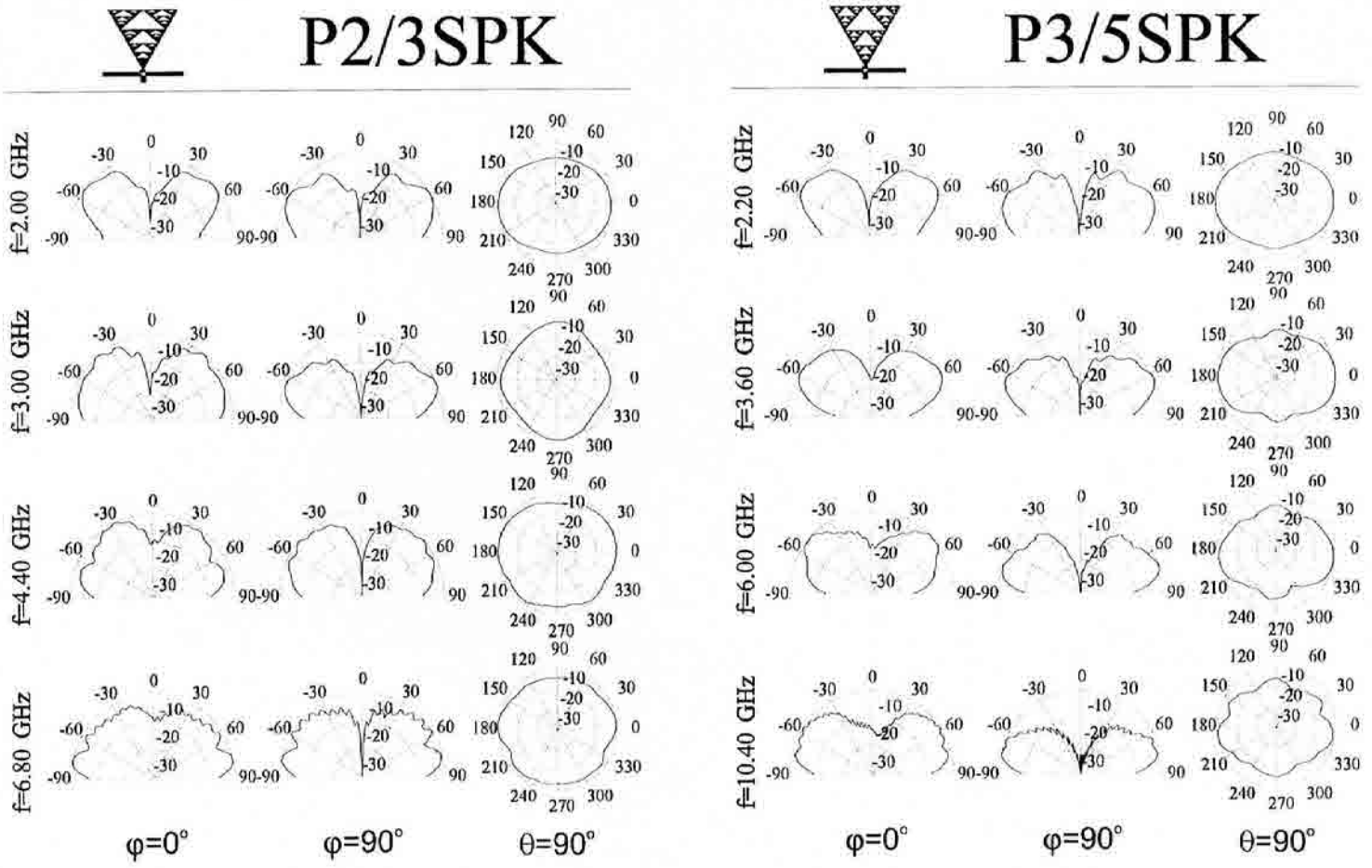

Fig. 5.25 Main cuts (φ=0°, φ=90°, θ=90°) of the radiation patterns for the P2/3SPK antenna (left), and for the P3/5SPK one (right).

As a concluding remark, we should state that the Sierpinski gasket can provide a useful multiband antenna start-point design, which can be modified to match the specific needs of different applications. The perturbation of the scaling relation among fractal iterations appears a powerful tool to fulfil band location design requirements.

5.3.4 - The Triangular Honeycomb Antenna

Since there seems to be a clear relationship between the gasket triangle height and the antenna resonant frequencies, one could be tempted to essay alternative designs exploiting such feature. Being not a fractal shape, the so called triangular honeycomb antenna (see Fig. 5.26) could display a multiband behavior if one linked the several triangle height levels within its structure with a resonant frequency.

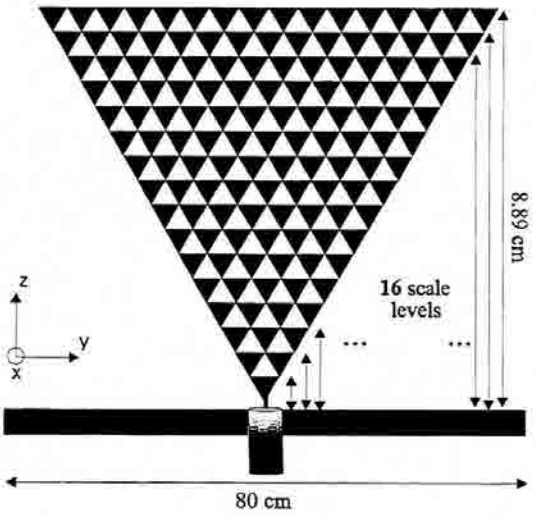

Fig. 5.26 The Triangular Honeycomb antenna.

5.3.5 - The Triangular Honeycomb Antenna Input Parameters

The experimental data upon this antenna appears quite revealing. The input reflection coefficient shows 16 minimum return-loss points within 0.1-16GHz, which is exactly the number of triangle levels within the honeycomb pattern. Although not an straightforward relationship between such height levels and the matched frequencies has been found, given the prior results regarding the Sierpinski and bow-tie antennas it seems reasonable to assume that such a relationship should exist. Thus, this could be thought of as an alternative, non-fractal way of designing a multiband antenna, provided that the similarity among the radiation patterns at the several bands is held as well.

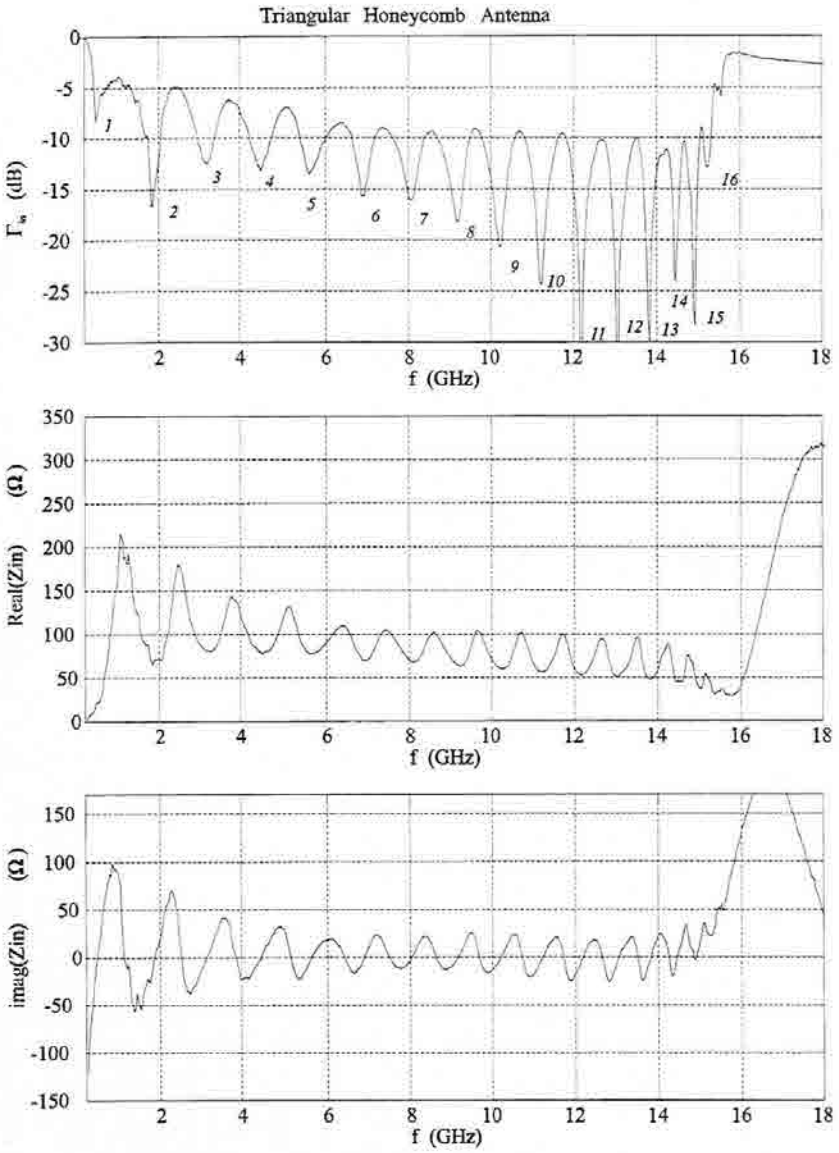

Fig. 5.27 The Triangular Honeycomb antenna input parameters.

5.3.6 - The Triangular Honeycomb Antenna Radiation Patterns

Figure 1.27 shows the φ=0° cuts of the E_θ component radiation pattern. The cuts have been measured at each one of the minimum return-loss frequency points. The pattern evolution is the typical one of a single-band antenna, with many increasing grating lobes for larger frequencies. Such a behavior is comparable to that of a linear monopole or bow-tie antenna and thus this cannot be considered a successful multiband antenna design. From the geometrical point of view, the shape of the antenna is clearly not self-similar since none of the equivalent nested triangular shapes has the same form of the overall object, even in the ideal case with an arbitrary large number of iterations. One should conclude that a

multiscale structure alone is not enough to guarantee a proper multiwavelength operation, yet there must be a strong similarity relationship among the several scales (fractal self-similarity for instance) to ensure a multiband behavior.

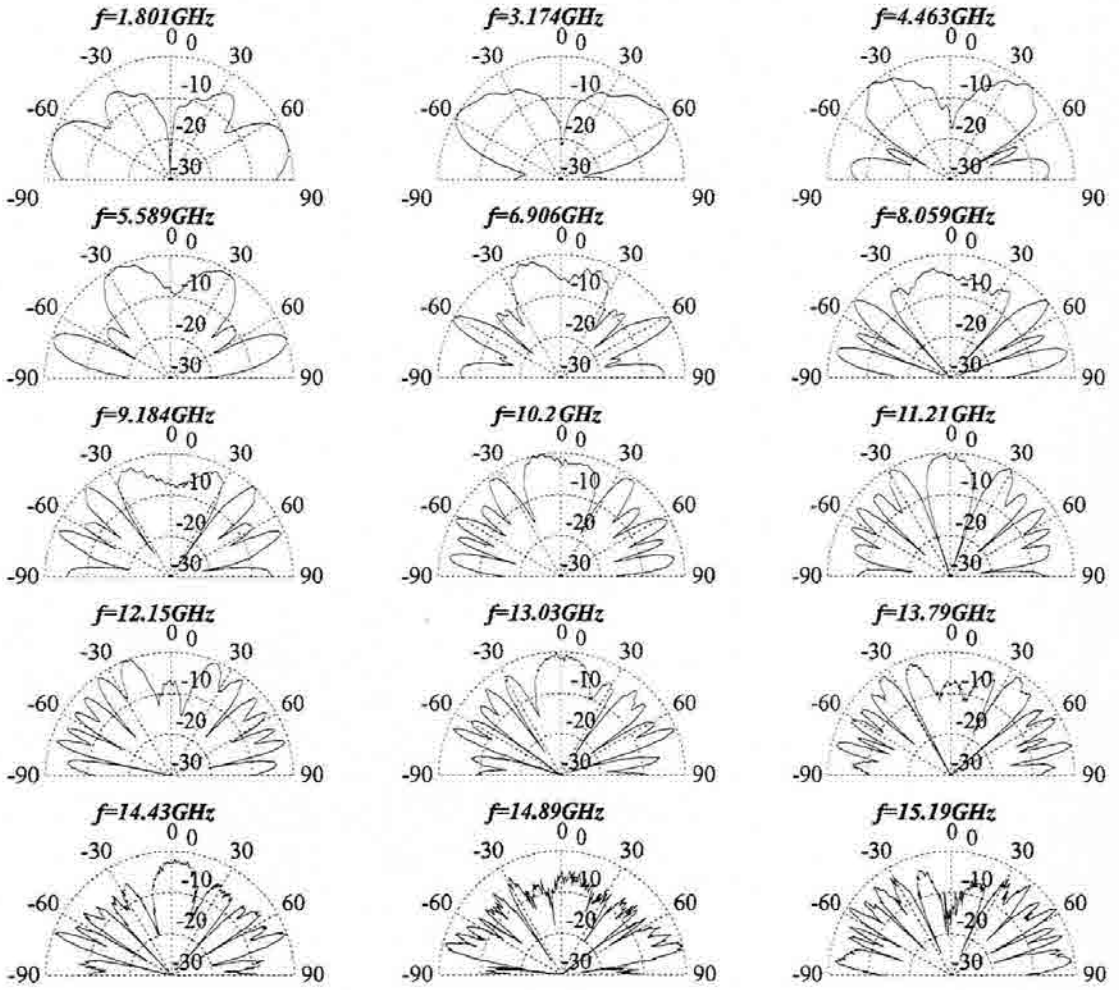

Fig. 5.28 Honeycomb antenna E-plane radiation patterns. It is not a multiband antenna.

If one assumes that currents on the Honeycomb antenna propagate mainly along the edges, it becomes clear that the periodic (but not multiperiodic) nature of its structure should be considered when analyzing its behavior. Nevertheless, it is clear that being the single period size d very small (the side length of the smaller triangles), most Hartree harmonics will be at cutoff at low frequencies. Thus, its behavior should be properly modeled at such low frequencies by just taking into account the fundamental mode on the balanced V model. Figure 5.29 displays the theoretical patterns computed following such

model at the first six matched frequency points. An empirical adjustment of the effective index of refraction (a ~6% deviation from the expected n_{eff}~ 1.1) has been applied on the theoretical model and a current reflection coefficient of ρ_c = -0.65 has been assumed.

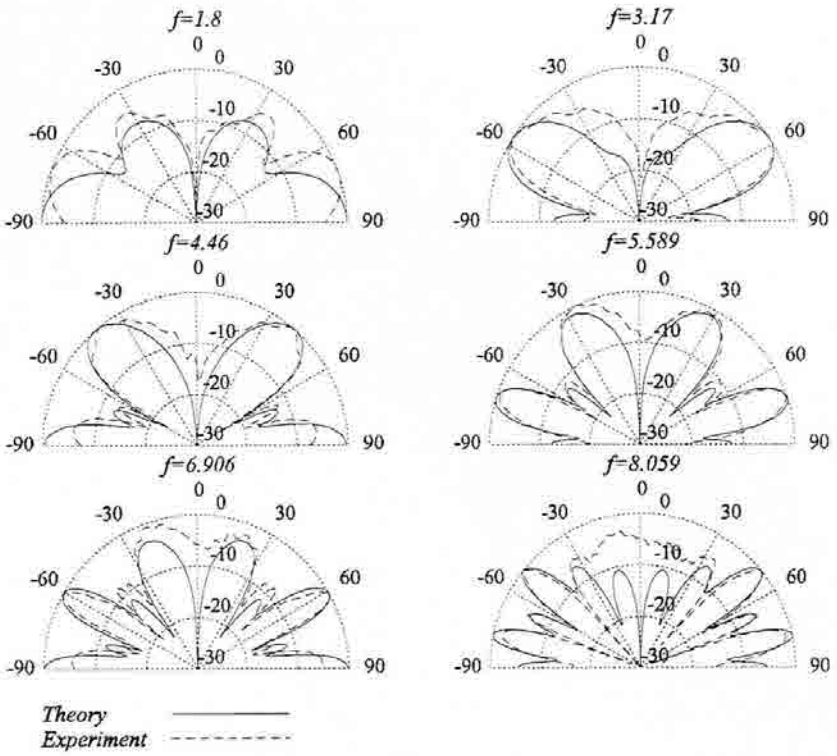

Fig. 5.29 Comparison between the measured triangular honeycomb antenna and the balanced V theoretical model radiaton patterns (φ=0°, E_θ component, frequency in GHz).

5.4 The Parany Antenna

The structure shown in Fig. 5.30 is the so called Parany antenna, which was constructed with the aim of exploring the sensitivity of the Sierpinski antenna design to significant geometrical deviations. Although long believed to be a fractal shape [121],[122], the antenna should not be considered strictly fractal[2]. Even though B.Mandelbrot [3] refused to establish a tight definition of the term fractal, and suggested that such an adjective could be used in a loose sense to name novel forms with highly irregular or self-similar shapes, he established a definition of fractal set [1] as a set whose fractal dimension is larger than its topological dimension. The Parany antenna has a self-scalable shape which, however, has both a topological and a fractal dimension D=2. This can be readily seen by considering its

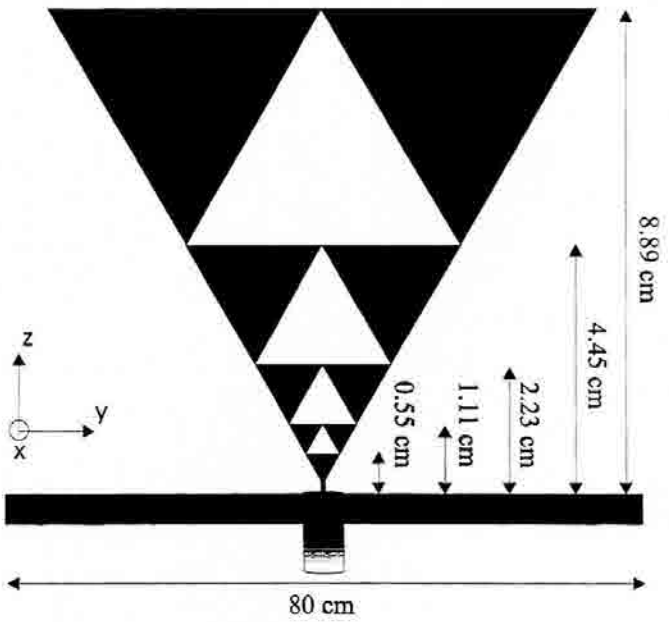

Fig. 5.30 The Parany antenna.

construction algorithm: an equilateral triangle is subtracted from the center of an inverted solid triangle in the first stage; in the following stages, a properly scaled triangle is subtracted only from the bottom remaining triangle. This way, there always remain two-dimensional surfaces on the upper part of the antenna, which will be responsible for the overall two-dimensional characteristic of the whole object.

[2] The Parany antenna is patent pending too.

On the other hand, the Parany structure is indeed a self-scalable shape, in the same sense the logarithmic spiral or the log-periodic dipole array are self-scalable too [39]. Nevertheless, there is a significant difference between the former and the later shapes. While the spiral and log-period arrays smoothly feature a continuous range of scales, the Parany antenna appears only self-scalable when the proper scale factor (i.e. δ=2 for this particular case) is chosen. This should lead to a multiband rather than frequency independent behavior similarly to what is stated for the fractal antennas considered up to this point.

5.4.1 - The Parany Antenna Input Parameters

The input parameters corresponding to the Parany antenna are shown in Fig. 5.31 together with the same parameters regarding the fractal Sierpinski-60 one. The log-periodic behavior of such an antenna is clearly shown, with a log-period $\delta = 2$ as could be anticipated from its geometrical shape. It is most remarkable the good agreement between the Parany and the Sierpinski antenna with respect to their input parameters. Such an agreement strengthens the idea that smaller details do not play a very important role at large enough wavelengths, and that the overall antenna performance at its input terminals is determined by the overall antenna shape.

However, there appears to be a consistent difference between the performance of both antennas at high frequencies. There is a significant increase in the input return-loss bandwidth in the fractal case (~40% , ~100% and ~70% at the three upper bands for L_r<10dB). If the agreement among the antenna behaviors is related to their common geometrical features, conversely the deviation on the performance should be explained through their geometrical differences. It appears sensible to assume that the high irregularity of the fractal shape should enhance radiation. Actually, the ideal Sierpinski gasket can be seen as an infinitely branched structure, as described in the introductory chapters; that is, any point in the ideal fractal shape would introduce a sudden change in the current direction. Such abrupt changes would enhance the radiation process with respect to the Parany antenna that has a smoother shape. This way, the ratio between the stored reactive energy and the radiated power, i.e., the Q factor, would be lowered and thus the overall bandwidth increased.

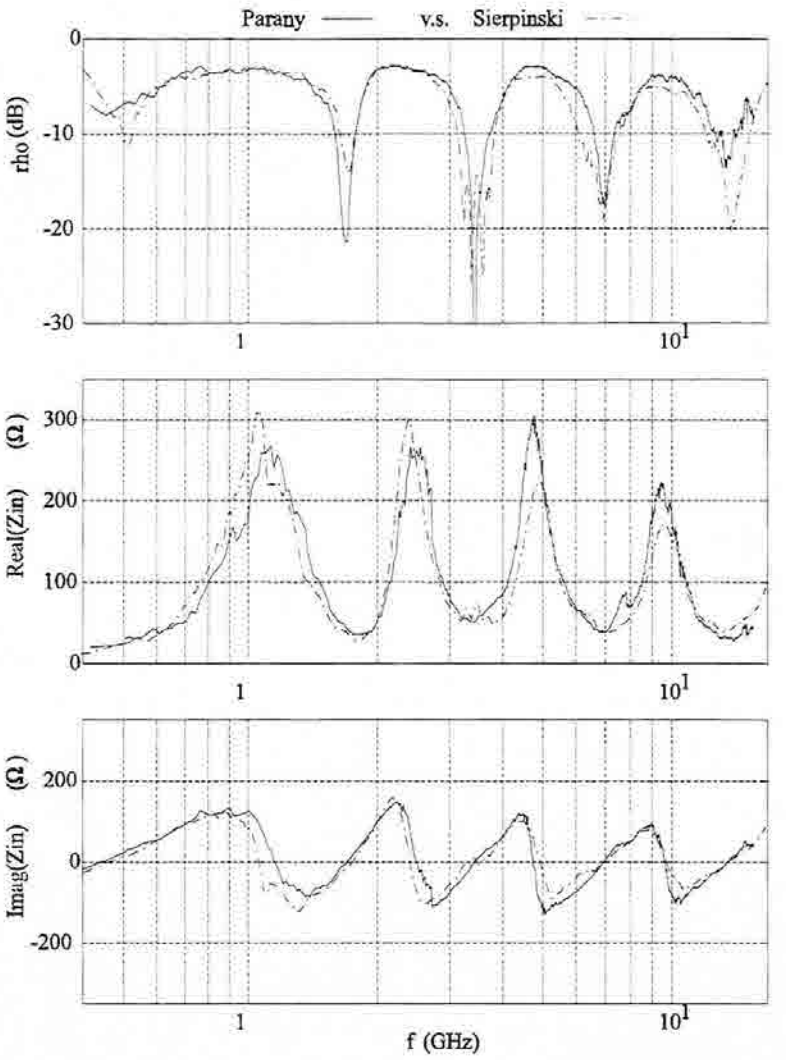

Fig. 5.31 The Parany antenna input parameters. The same parameters for the fractal Sierpinski antenna are shown in dashed lines for comparison.

5.4.2 - The Parany Antenna Radiation Patterns

The antenna radiation pattern main cuts corresponding to the three upper bands are also shown in Fig. 5.32 (E_θ component). At first glance one notices the increase in the number of lobes with respect to the fractal case. Also, the similarity among the third and the forth and fifth bands is not so clear. Both phenomena could be linked to the truncation effect in the following way: assuming that the current distribution extends further away in the Parany antenna than in the Sierpinski gasket, an increase in the number of lobes should be expected due to the larger current extent to wavelength ratio. Furthermore, a larger active region size would make more difficult a successful antenna truncation without affecting the

current distribution shape. This way, the similarities among bands would be easily lost, specially at lower frequencies. Such an argument of a smaller active region in the fractal case would be consistent with the former idea that the irregularity of its shape enhances radiation and thus introduces a stronger attenuation in the current flowing over the antenna surface.

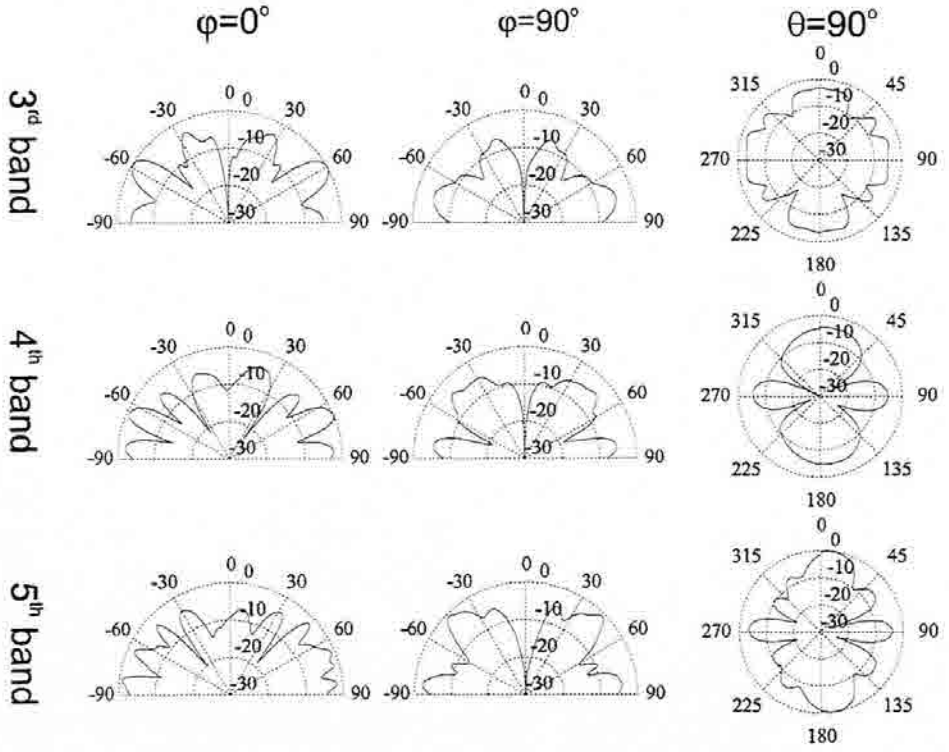

Fig. 5.32 The Parany antenna radiation patterns main cuts at the three upper bands.

Similarly, one should notice that even self-scalable, the Parany antenna can not be considered a multiperiodic structure. Although a quasi periodic analysis approach has been successfully applied to describe some log-periodic antennas [45],[48], all of them presented smooth variations on the period *d*. On the contrary, the Parany antenna has too abrupt a change in its characteristic scales and neither the periodic nor the multiperiodic approach applies. Therefore, it is not surprsing to state that, lacking of the contribution of several space harmonics, the radiation patterns of the Parany and Sierpinski antenna can become rather different. As a final conclusion, we should state that the Parany antenna does not present any remarkable advantage with respect to the Sierpinski antenna.

5.5 Conclusions

Some variations on the Sierpinski Antenna have been investigated. It has been shown that changing the antenna flare angle introduces some modifications on the resonant frequencies, impedance level and radiation patterns. In general, broader angles shift the resonant frequencies toward longer wavelengths due to the longer length of the triangle sides. Very narrow angles make the whole antenna appear closer to a linear antenna (a monpole or dipole) such that the multiband behavior tends to vanish. Such a phenomenon has been confirmed both by the input parameters and radiation patterns.

An analytical model, based on the propagation of current waves along a multiperiodic media, has been introduced to describe the Sierpinski antenna behavior. Such a model successfully predicts the variations on the pattern shape when changing, for instance, the flare angle. The model gives also an insight on the antenna behavior when the arms of the fractal dipole are inclined. Roughly speaking, the inclined version of the Sierpinski dipole features a more directional pattern, which is kept similar at the several bands. The directivity is not enhanced as much as in a bow-tie antenna due to the active region reduction effect which makes possible the multiband behavior.

It has been shown that the fractal structure of the Sierpinski antenna can be properly perturbed to shift the operating bands. Again, it has been shown that the band positions are clearly linked to the antenna geometry and its characteristic scale factor. Other non fractal configurations have been essayed, but their performance was worse than that of the fractal one.

6. *Random Fractal Tree-Like Antennas*

Previous chapters have been devoted to show that fractals can become multifrequency radiating systems, and this has been demonstrated both theoretically and experimentally. The Sierpinski antenna has been shown to operate similarly at a discrete set of frequencies and thus, it has been identified as a multiband antenna. Such feature has been shown to be clearly linked to the antenna fractal geometry, being the spacing among bands equal to the characteristic scale factor of the several fractal iterations.

One would naturally wonder what happened if such a characteristic scale factor were made arbitrarily close to unity. One might think that the several bands would become arbitrarily close and couple together into a single wide band, obtaining this way, a frequency-independent antenna. Actually, a frequency-independent antenna such as the log-periodic dipole array can be thought of as a multiscale structure, smoothly varying by means of a small scale factor from small to large sizes. Therefore, one could reasonably expect that proper fractal shapes with small scale factors would operate similarly too.

However, it is not easy to find deterministic, regular, self-similar fractal shapes with scale factors close to unity. Deterministic self-similar fractals such as the Cantor set, the Sierpinski gasket and carpet, or the Dürer pentagon [2][5], are usually highly lacunar objects presenting large gaps within substructures and abrupt scale changes among iterations. In many cases, self-similarity is broken when the scale factor δ is made $\delta<2$ and structures become at most self-affine. Among the fractal object families that allow small scale factors, the most common are random fractal shapes, and some relatives of Julia and Mandelbrot

sets obtained by iterative transformations on the complex plane [5],[87]. Random fractal forms are among those who more clearly evince a continuos set of scales within its shape. Among the several families of random fractal objects such as Brownian processes, random IFS systems, etc., maybe the most appealing are the tree-like random ones. Many natural objects, such as corals, trees, leaves, weeds and ferns have distinct fractal shapes [1],[2] with a rich scale distribution that look specially attractive for antenna design. Actually, one of the most popular fractal shapes (which however is not random), the Barnsley fern, is clearly similar to the log-periodic dipole array. Being extremely simple to feed, fractal tree-like monopoles have been chosen to investigate the feasibility of fractal wide-band or frequency-independent antennas.

There are several ways of generating fractal random branching structures. Among them, the most common is the Diffusion Limited Aggregation (DLA) process [2]. Such process can be either carried out through an experimental chemical process or by means of computer simulation. Both approaches have been followed here, and results are compared in the following sections.

6.1 - DLA Growth of Fractal Structures

The Diffusion Limited Aggregation (DLA) process describes the formation of clusters that grow from the aggregation of small particles. The general model accounts for a set of particles traveling randomly in a usually fluid medium. When the particle random-walk goes through the position of a fixed particle called the *seed*, it sticks to it becoming a seed particle too, i.e., a fixed particle that can catch the remaining flowing particles on their erratic motion. DLA is a probabilistic process that yields the formation of fractal (self-similar) clusters. The fractal nature of such aggregates has been extensively studied and characterized [9],[10],[11],[12],[123], and their self-similarity properties have been stated in a probabilistic sense.

One of the most practical ways of generating real, physical fractal aggregates is electrochemical deposition [2],[10]. In this case, the fluid media is an electrolyte solution, and the particles are usually metal ions (frequently copper or zinc). An electrostatic field is applied to the solution by means of an electrode pair such that the ions become attracted by its corresponding pole, i.e., the anode or cathode. Although this process can be carried out in a three dimensional cell where ions can move randomly in any direction, it is customary to run such experiments in a two-dimensional setting. That is, a Petri-dish is filled with a thin

layer of the aqueous solution such that particles have their movement restricted on the almost two-dimensional medium between two glass-plates (Fig. 6.1).

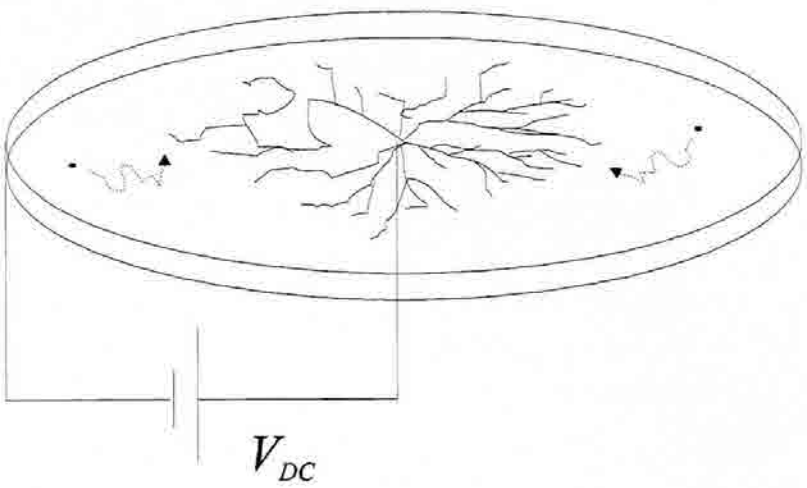

Fig. 6.1 Typical set-up of an electrochemical deposition experiment.

Depending on the shape of the electrodes, the applied electrostatic potential, the ions and their concentration, a huge variety of highly complex forms can be obtained, not all of them being fractal [10]. In general, fractal shapes are obtained when the process that predominates in the particle motion is diffusion, and hence the name of DLA fractals. When other process become predominant, more regular, dendritic-like shapes result [10]. A thorough study of the conditions that allow the formation of fractal aggregates can be found in [10]. Following such rules, the electrochemical deposition experiments that generated the fractal tree-like shapes of the antennas presented here were carried out at the Universitat de Barcelona by F.Sagués, J.Claret and M.Q.López-Salvans [9],[10] ,[11],[92].

6.2 - The Fractal Tree Antenna

6.2.1 - Structure Design and Antenna Construction

The first prototype of fractal tree antenna was designed as follows. The fractal shape was obtained by means of a quasi-two-dimensional electrodeposition experiment as described before. A deposit was grown from a thin layer of an aqueous electrolyte containing the metal ions to be deposited sandwiched between two glass plates. In this particular case, the electrochemical cell was formed by two glass plates (11 cm x 11 cm x 5 mm) separated by two copper wires of 100 μm diameter. The electrode configuration consisted of a point-like cathode located at 8 cm from the center of an 11 cm long anode, parallel to a plate side. The electrolyte solution was a non-deaderated aqueous 0.05M copper sulfate ($CuSO_4$) solution prepared with ultra pure water supplied by a Millipore-Milli Q system and Merck quality p.a. copper sulfate. The electrodeposits were grown under a voltage of 12 V between electrodes [92].

Being the fractal deposit obtained this way a good conducting structure, the idea of using it directly as an antenna looked particularly attractive, since the generation process was quite simple, inexpensive, and fast (the deposit grew in a few minutes). However, the resulting structure is often too weak to be kept standing up once the glass plates were separated, and too thin to handle a significant amount of power. Therefore, the chemical deposit had to be recorded using a CCD camera, and the resulting image processed and printed over a Cuclad 250 dielectric substrate (ε_r=2.5, h=1.588 mm) using standard printed circuit techniques. Finally, the tree was mounted up in a monopole configuration over the same 80 x 80 cm aluminum ground plane used in previous fractal antenna designs (see Fig. 6.2).

The fractal dimension of this structure (D_f) was computed by means of the MFRAC multifractal analysis software [137], leading to a value of D_f=1.71. It is interesting to notice the statistical self-similarity [2] of the tree as shown in the blow-ups in Fig. 6.2. One can

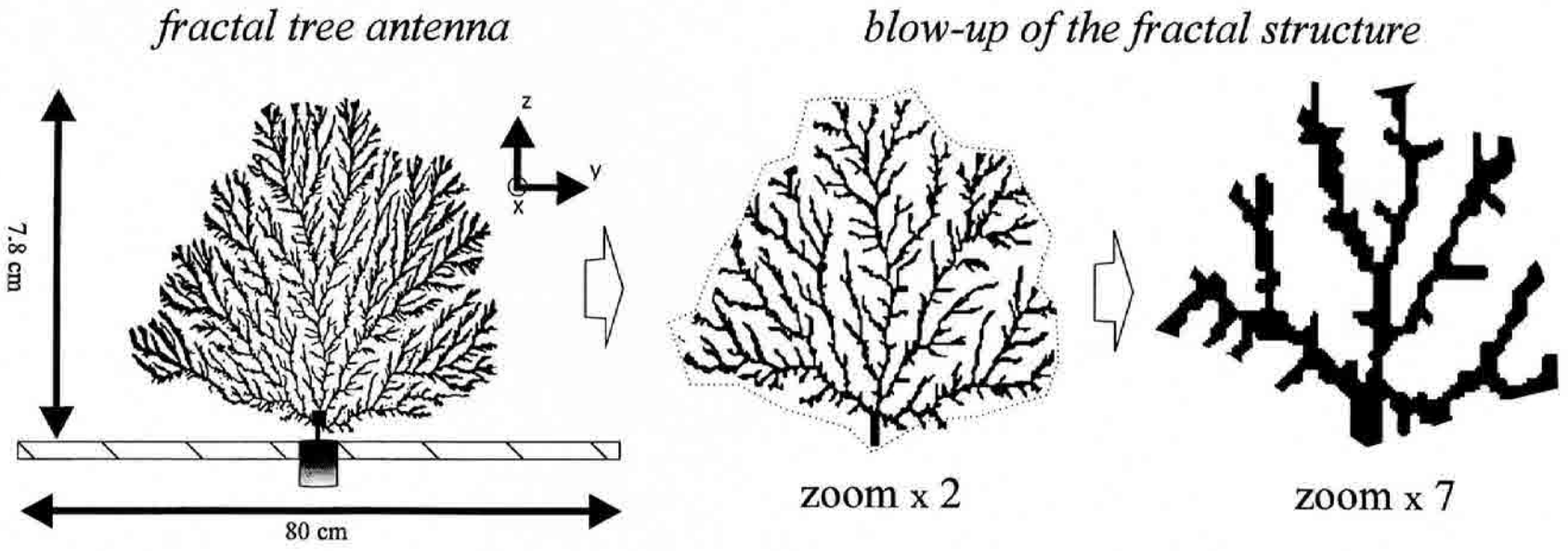

Fig. 6.2 Fractal tree antenna and blow-ups around the feeding point.

expand an inner region around the feeding point and the resulting form still keep a similar shape to the overall tree. An expansion by a factor of a 7 still holds the main features of the structure and if one neglects the contribution of the smaller parts of the body to the radiation process at longer wavelengths, a similar electromagnetic behavior might be expected at a frequency up to seven times larger than the smaller one.

6.2.2 - Input Parameters

The antenna input reflection coefficient (Γ_{in}) relative to 50Ω was measured from 900 MHz to 8 GHz using an HP8510B vector network analyzer. The resistance and reactance of the input impedance along with Γ_{in} are shown in plots (b), (c) and (d) of Fig. 6.3. The same parameters corresponding to a monopole of the same height (7.8 cm) are also plotted in dash-dotted lines for comparison. The fractal tree clearly displays a rich spectral structure with many resonant frequencies and is well matched (VSWR<2) to 50Ω at as many as 15 bands within the measured frequency range. This behavior is visibly distinct to that of the previously tested deterministic fractal shapes, since the distribution of bands is much denser, as could be anticipated from the antenna geometry. Also, the difference with the harmonic behavior of the Euclidean linear dipole is manifest. This seems to contradict the previous work developed in [125], which theoretically predicted a harmonic, periodic spectral distribution of resonant frequencies for general fractal aggregates.

On the other hand, frequency independent behavior can not be stated for the fractal tree because the antenna does not consistently keep a uniform matching characteristic in the whole frequency range. Nevertheless, the tree improves the spectral behavior of the linear monopole because both the reactance and the resistance of the fractal keep a smaller deviation from 0 and 50Ω respectively.

In order to link the spectral response of the antenna to its fractal geometry, the distribution of lengths on the structure was investigated as well. First, the recorded bitmap image of the tree had to be vectorized using a standard image segmentation software[1]. The several branches of the structure were converted this way to straight segments from which one could compute a length distribution histogram. However, such a procedure yielded rather discouraging results since the structure resulted in a large set of very short segments. The problem of identifying a length distribution over the antenna appears quite involved

[1] Corel OCR-Trace™, a trade-mark of Corel Corporation.

when relying on an automatic process, since curved branches become always decomposed on smaller straight segments. This means that larger branch lengths would not be considered and their corresponding resonant frequencies not predicted. To take into account the lengths of larger branches from its root to its tip, the antenna structure was previously manually straightened as shown in Fig. 6.4.

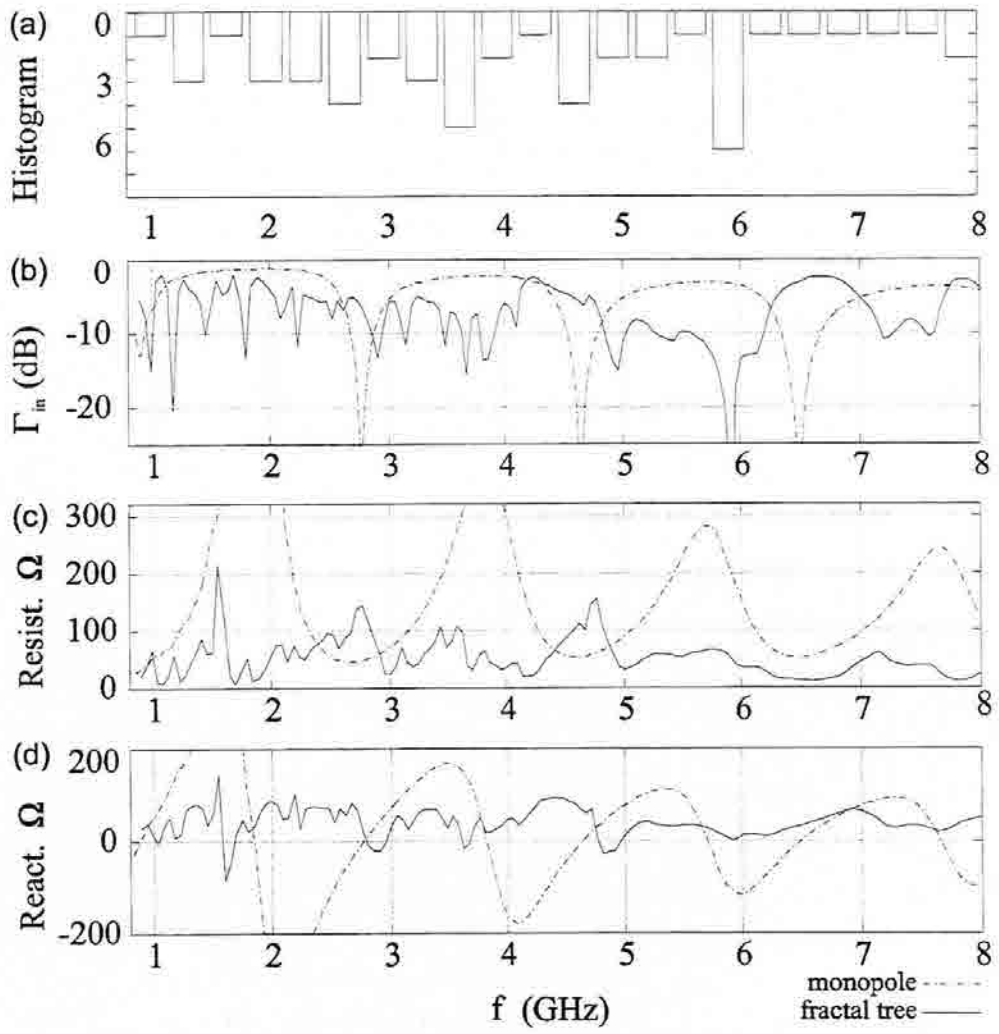

Fig. 6.3 Fractal tree antenna input parameters (b),(c),(d), and equivalent distribution of lengths (a).

Once such a simplification process had been applied, a distribution of lengths over the antenna was computed. Each length class was associated to a matched frequency by considering each segment of length l to resonate at $l \approx \lambda/4$. Finally, an histogram of the corresponding frequency distribution was computed and the result is shown in Fig. 6.3 (a). The plot basically seems to denote that a certain correlation between the length distribution

on the antenna structure and the matched frequencies exists, thus stating a link between the fractal antenna geometry and its spectral response.

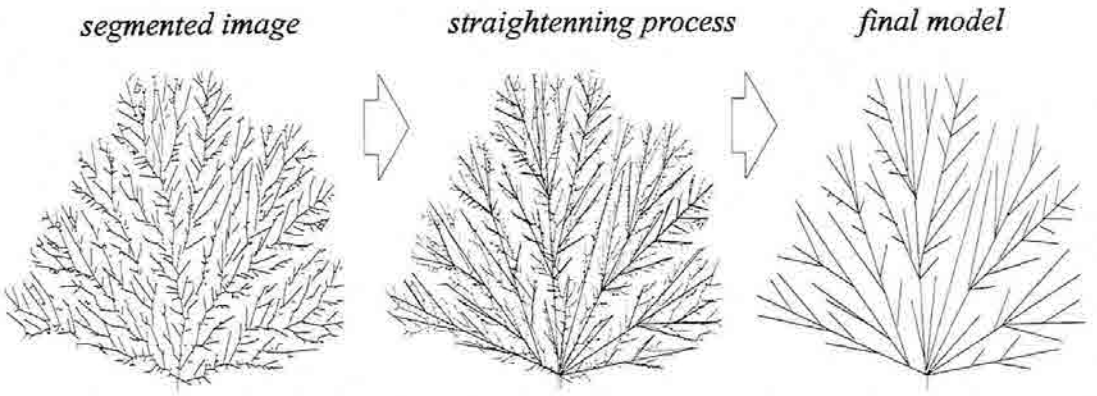

Fig. 6.4 Image segmentation and straightening prior computing the length distribution.

6.2.3 - Radiation Patterns Main Cuts

The radiation patterns were measured in an anechoic chamber at the first 15 matched bands. The main cuts φ=0° and φ=90° for the E_θ and E_φ components are shown in Fig. 6.6 and Fig. 6.7 respectively. All plots are normalized to allow a better comparison among bands. It can be seen that the E_θ φ=0° cuts hold a notable degree of similarity among them up to 5 GHz, which can be understood if one assumes a reduction on the effective current distribution size at larger frequencies. Although the patterns at 4.94, 5.44 and 7.58 GHz still keep a similar shape to the patterns at lower frequencies, they show a 10 dB dip approximately at θ=60°. On the other hand, the patterns of the φ=90° cut seem to randomly tilt from left to right through the bands, yet the number of lobes are not significantly increased at larger frequencies.

The random behavior of the patterns over the antenna plane can be related to the randomness of the fractal structure itself. That is, being the tree not symmetrical with respect to the *xz* plane, the active region would extend to a different branch configuration when a contraction or expansion is produced at the highest frequencies. That behavior was not held by the other cut due to the symmetry of the antenna with respect the *yz* plane.

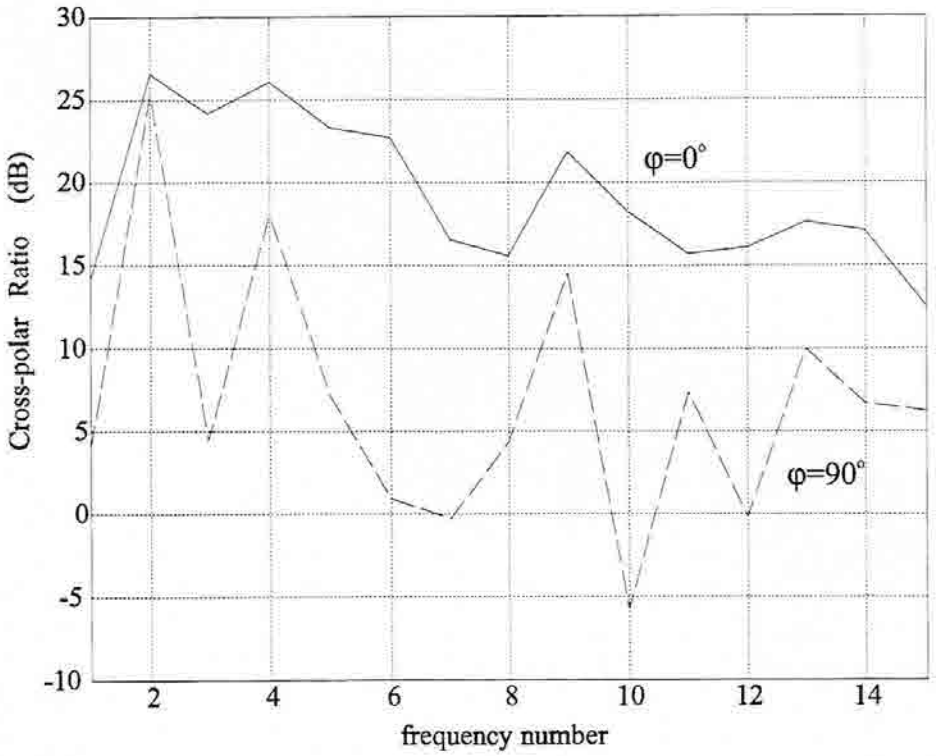

Fig. 6.5 Fractal Tree Antenna cross-polar ratio for the two main cuts.

Randomness becomes also apparent from the polarization point of view, since the cross-polar ratio is not held constant through the bands. Figure 6.5 shows the cross-polar ratio (E_ϑ/E_φ) at the fifteen measured bands for the two main cuts. Large fluctuations in the field polarization state become clear. Variations as large as 30 dB are especially remarkable at the antenna plane cut, where the randomness of the antenna shape has its main influence. Contrarily to the theoretical harmonic prediction found in [125], the randomness in the polarization state seems to basically agree with the conclusions in that particular work.

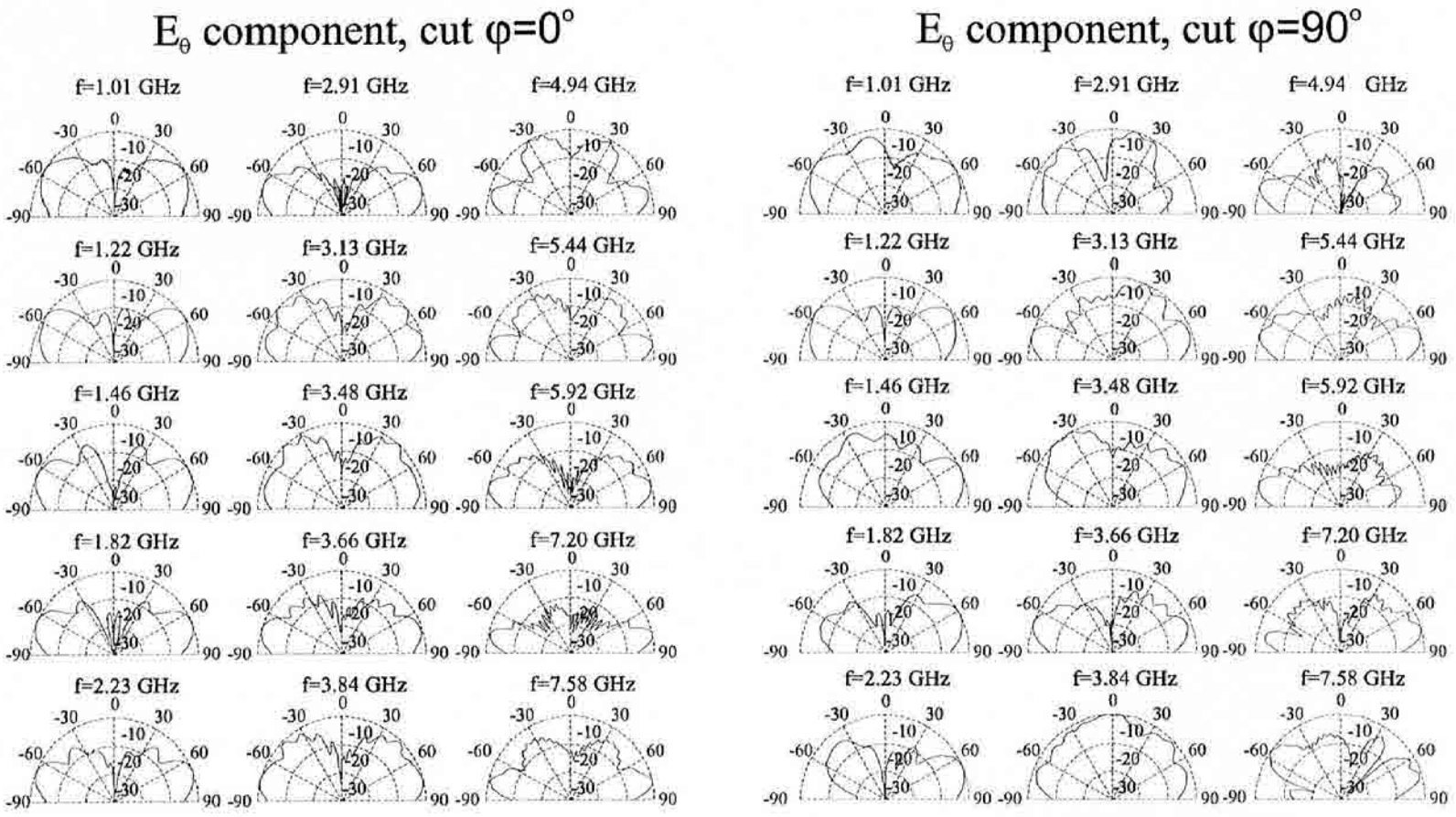

Fig. 6.6 Fractal Tree Radiation Pattern Main cuts (E_θ). The patterns are similar up to 5 GHz on the φ=0° plane.

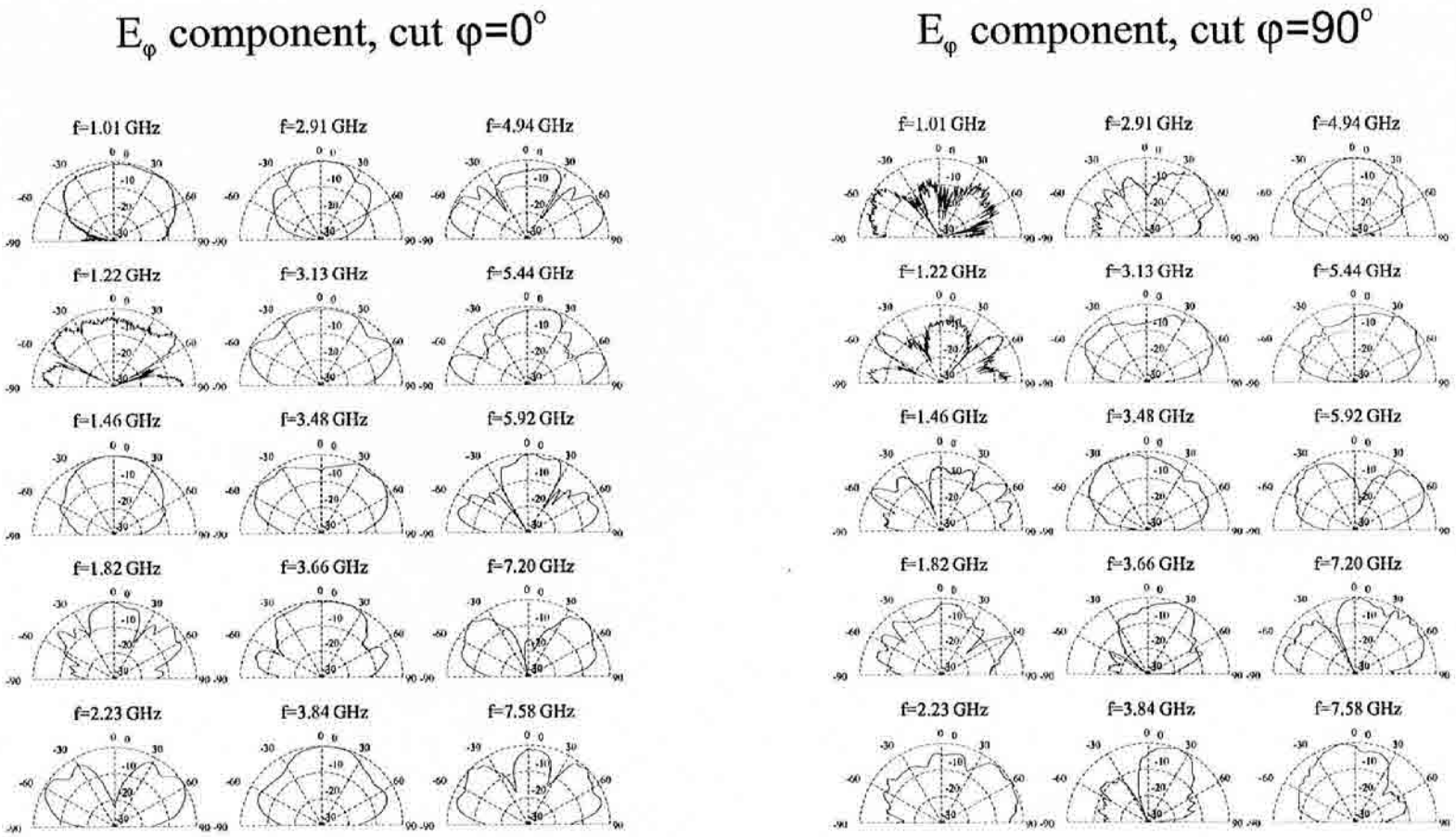

Fig. 6.7 Fractal Tree Radiation Pattern Main cuts (E_φ). The randomness effect due to the antenna shape is more clear in this case..

6.3 - The Trimmed Version of the Fractal Tree Antenna

Although some multiband features were apparent in the behavior of the fractal tree antenna of the previous section, a wide-band frequency response was not achieved. In this section, a truncated version of the previous model is essayed. One could think that some non-fractal aspects of that prototype would disturb it from a clear wide-band behavior. For instance, the coupling of the lower branches with the ground plane could store some extra reactive energy that might rise the antenna overall Q factor, impeding a successful melting of the several antenna resonances. Being such long branches almost parallel to the ground plane, a transmission-line, non radiation mode might be locally excited; since those branches are directly connected to the antenna input terminal, they might behave as parallel stubs which could modify the antenna input impedance behavior.

With this underlying idea in mind, the original antenna tree was pruned, and another version of the fractal tree antenna was constructed (Fig. 6.8).

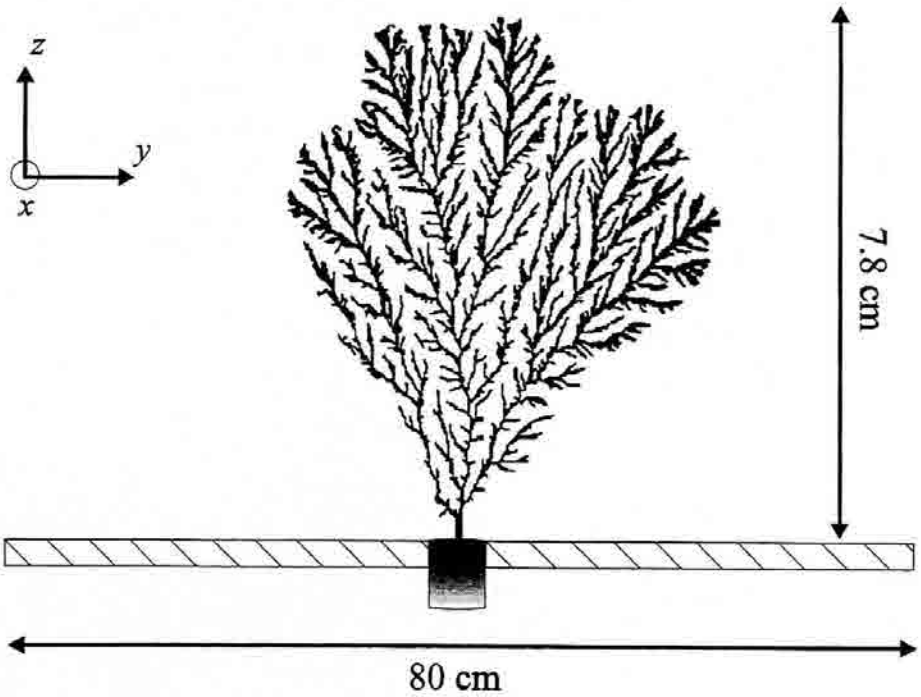

Fig. 6.8 The truncated version of the fractal tree antenna.

6.3.1 - Input Return-Loss

Contrarily to what was first expected, the truncated version of the fractal tree reduced the number of matched bands from 15 to 9, as shown in the input reflection coefficient (relative to 50Ω) of Fig. 6.9. The design still overcomes the number of resonant frequencies of the Euclidean linear dipole due to its multiscale nature, and there seems to exist a slight tendency to broaden the bands, but results are much far from what one would desire.

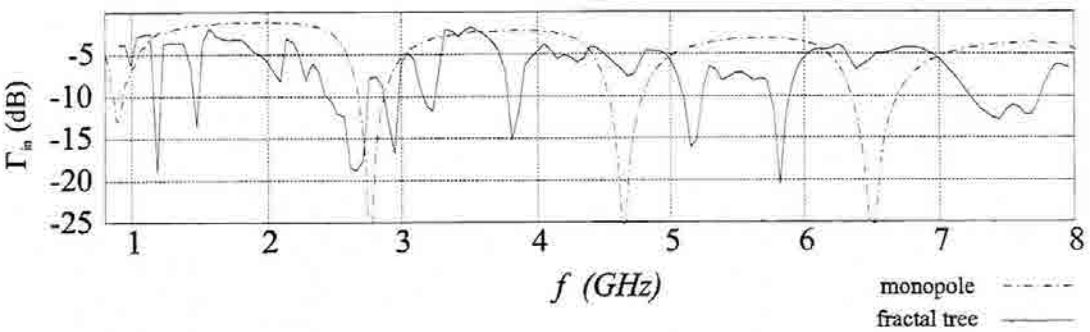

Fig. 6.9 Input reflection coefficient relative to 50Ω for the truncated version of the fractal tree.

6.3.2 - Radiation Patterns and Cross-Polar Ratio

Regarding the antenna radiation patterns, results seem to go also in the opposite direction. The E_θ component of the φ=0° and φ=90° cuts shown in Fig. 6.10 are in worse agreement than those of the previous model. The lobe structure consistently changes when increasing the operating frequency and this way, the antenna clearly deviates from a multiband operation. The cross-polar ratio is the only parameter that has been improved with respect to the previous model (Fig. 6.11), being the E_θ component the most significant one through the bands. However, this fact is mostly due to the narrower shape of the antenna rather than to a significant change on the antenna fractal nature.

One possible explanation to the band similarity loss by the current model might be found in the loss of geometrical similarity due to the trimming process (see Fig. 6.12). It is apparent that when truncated around the feeding point, the antenna body does not keep an alike shape as much as the previous model did.

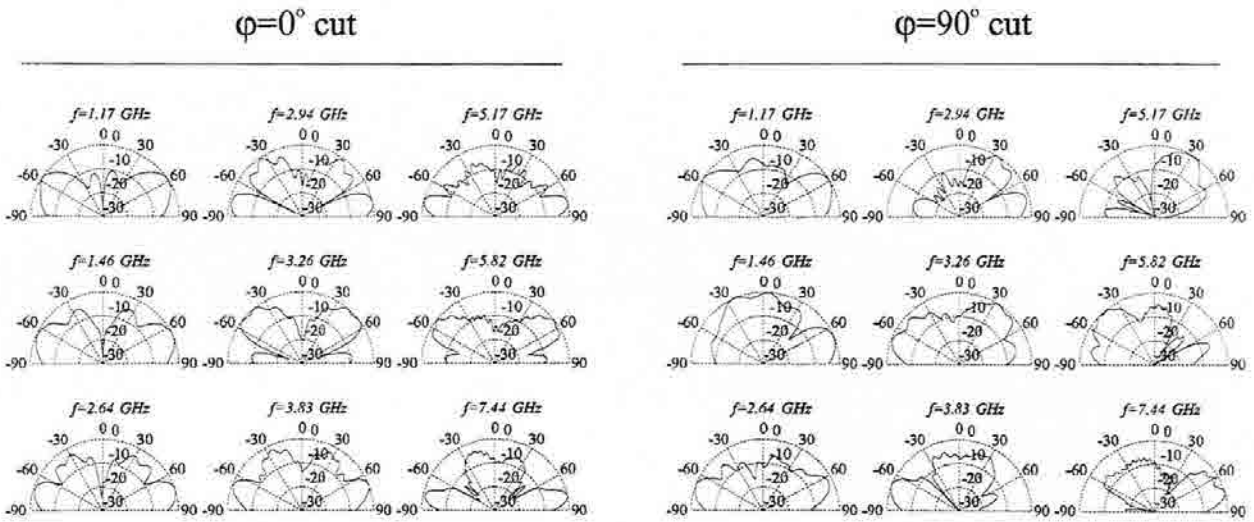

Fig. 6.10 Pruned tree radiation patterns main cuts for the E_θ component.

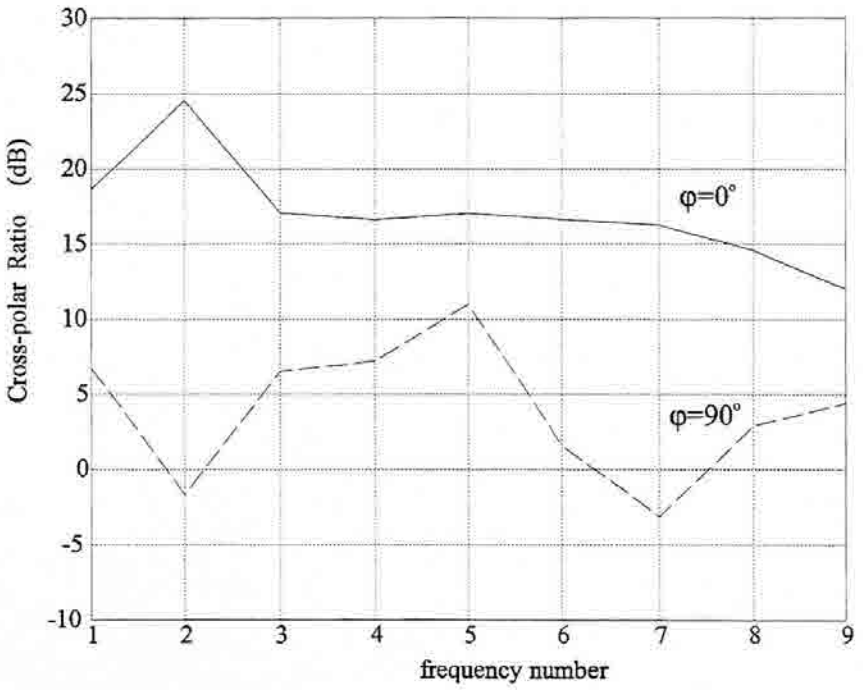

Fig. 6.11 Pruned tree antenna polarization cross-polar ratio through the matched bands.

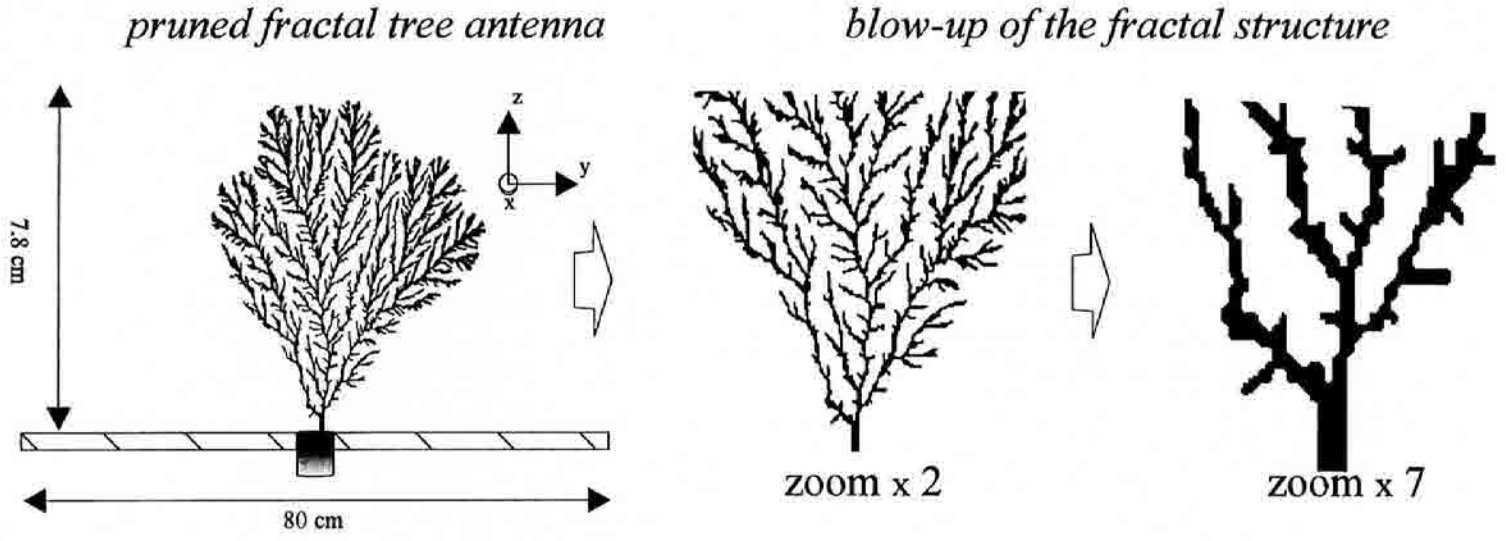

Fig. 6.12 Pruned tree structure and several blow-ups around the feeding point. The structure loses its similarity properties.

6.4 - The Simulated DLA Fractal Antenna

Even though the fractal tree antennas just introduced present some interesting features, namely a multiresonant behavior with a dens band distribution, they do not fulfill the expectations of achieving a wide-band (frequency independent) behavior. If one links the band distribution to a branch-length distribution, it could be concluded that the antenna shape does not feature a continuous enough length histogram. Also, the antenna tends to increase the pattern lobes at large frequencies, which could be related to the lacunarity of the structure, i.e., the gaps among bands. One could think that, if a denser tree structure featuring a more continuous length distribution were achieved, the fractal tree antenna behavior could be improved.

In order to get a better control on the final antenna shape, the diffusion limited aggregation process was simulated by a computer program. The DLA process can be readily simulated using a rather simple algorithm as it has been reported by many authors [2],[12]. From the mathematical point of view, the particles (ions) within the glass plates move following a Brownian motion, which can be approximated by a random-walk where each step the particle moves to any of the four neighborhood cells on a uniformly sampled two-dimensional space.

6.4.1 - SDLA Antenna Shape Design Algorithm

First of all, one has to define a finite grid of pixels where particles can be placed on and travel over. Second, a fixed point where a single sticky particle (i.e. the seed) will be placed has to be chosen as well. Such a seed point is equivalent to one of the electrodes of the experimental setup. The next step consists on delimiting a perimeter with an arbitrary shape around the seed where particles will be injected and start its random-walk. At each step, one of the four neighbor pixels is randomly chosen as the following particle position. On such a random path, the particle can either go outside of the defined perimeter and become discarded, or become stuck to the seed (with some probability) when reaching one of the its neighbor pixels. Such process would be iterated with many particles until the simulated deposit is as large as desired.

In general, one can empirically control more or less the resulting aggregate shape by modifying some of the simulation parameters such as the perimeter shape, seed position, or sticking probability. To design the new fractal tree antenna shape (hereafter Simulated

Diffusion Limited Aggregate or SDLA antenna), some special considerations have been taken into account. The limiting perimeter has been chosen to have a rectangular shape, and the seed has been placed at the center of one of its sides. By placing the seed at the edge of the simulation space, some directionality is induced on the growing process such that the final aggregate has an elongated shape with a main root through which the antenna can be conveniently fed through.

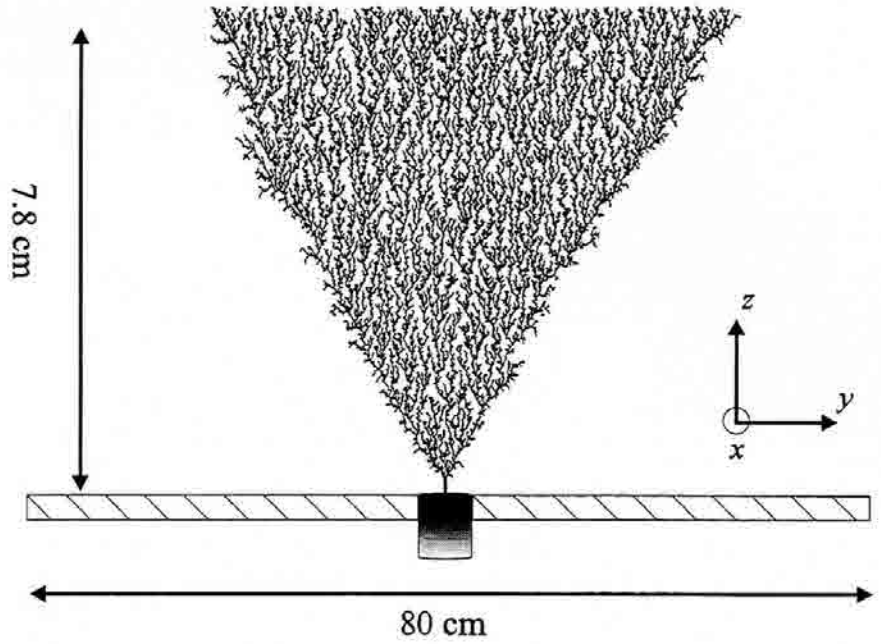

Fig. 6.13 The SDLA antenna. The fractal dimension is $D_f \approx 1.83$.

To increase the speed of the generation algorithm, two limiting perimeters were defined instead of one; the first one controls the initial position of the particles, while the second one is the limit boundary that determines when a particle must be discarded. By initially choosing a small starting point perimeter, particles begin to stick to the seed more rapidly than when considering a large initial perimeter. When the aggregate size becomes comparable to such a perimeter size, this can be conveniently re-scaled to allow a further growth. The density of the resulting deposit can be controlled by properly establishing the minimum number of stuck particles prior to the perimeter re-scaling.

Once the deposit shape had been obtained following this basic procedure, it was printed over a dielectric substrate as usual, and mounted over the ground plane in the monopole configuration (Fig. 6.13).

6.4.2 - SDLA Antenna Input Parameters

Having the same size of the other fractal tree structures, the SDLA antenna input parameters were measured on the same 0.9-8 GHz frequency range. It is clear that again (Fig. 6.14) the antenna performs in a multiresonant manner. The three input parameters evince a denser band distribution as one expected from the antenna shape. Although the antenna is not very well matched to 50Ω, up to 16 resonant frequencies (imag(Z_{in})=0) are found within the measured range, which states an improvement with respect to the previous cases. On the other hand, when one considers the input reflection coefficient with respect to an impedance Z_o=125Ω, a better input return loss characteristic is obtained (Fig. 6.15).

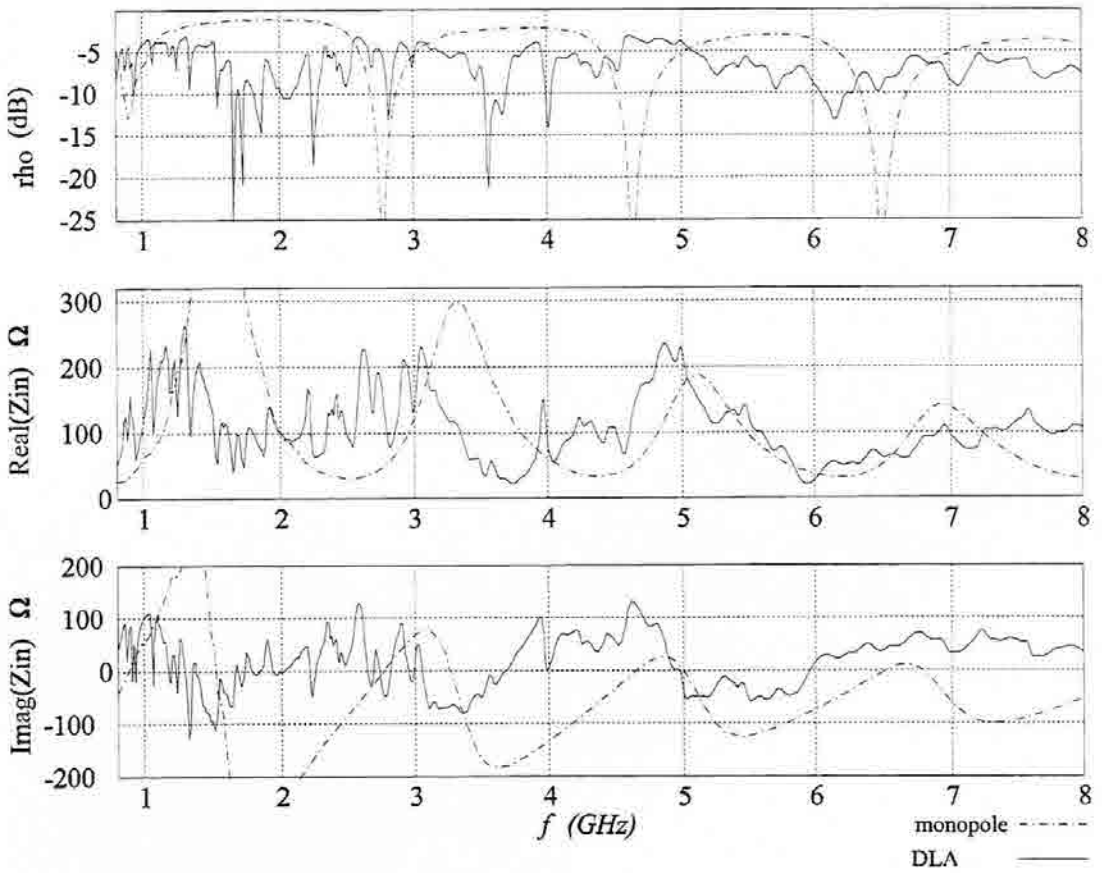

Fig. 6.14 SDLA Antenna Input Parameters.

Up to 26 VSWR minimums are obtained now, with a significant improvement on the average return-loss on the overall frequency range. However, the antenna still does not perform as one would desire. That is, instead of melting together into a single broad band, the multiple matched frequencies tend to be kept separated from the rest. Even though the denser structure yields a denser distribution of resonant frequencies too, it seems that too

much reactive energy is stored within coupled tree branches. Such an energy storage would lower the overall antenna Q factor, yielding the narrow band characteristic found at each band.

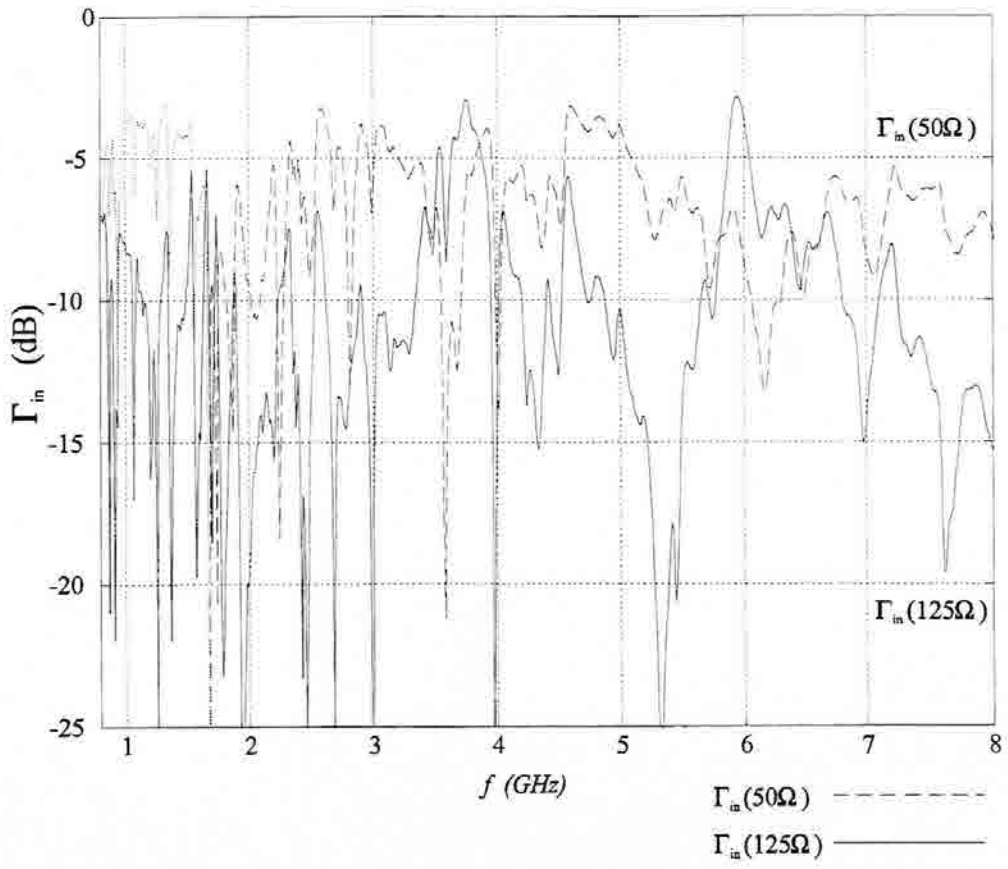

Fig. 6.15 The SDLA Antenna input reflection coefficient relative to 50Ω (dotted) and 125Ω (dashed).

6.4.3 - SDLA Antenna Patterns

Due to dense distribution of frequency VSWR minimums, the radiation pattern measurements were carried out this time by sweeping the whole frequency range. The power pattern φ=0° and φ=90° cuts are shown in Fig. 6.16, while the cross-polar ratio (E_θ/E_φ) corresponding to each pattern is shown in Fig. 6.17. In general, one might state that significant variations on the patterns are obtained when increasing the operating frequency.

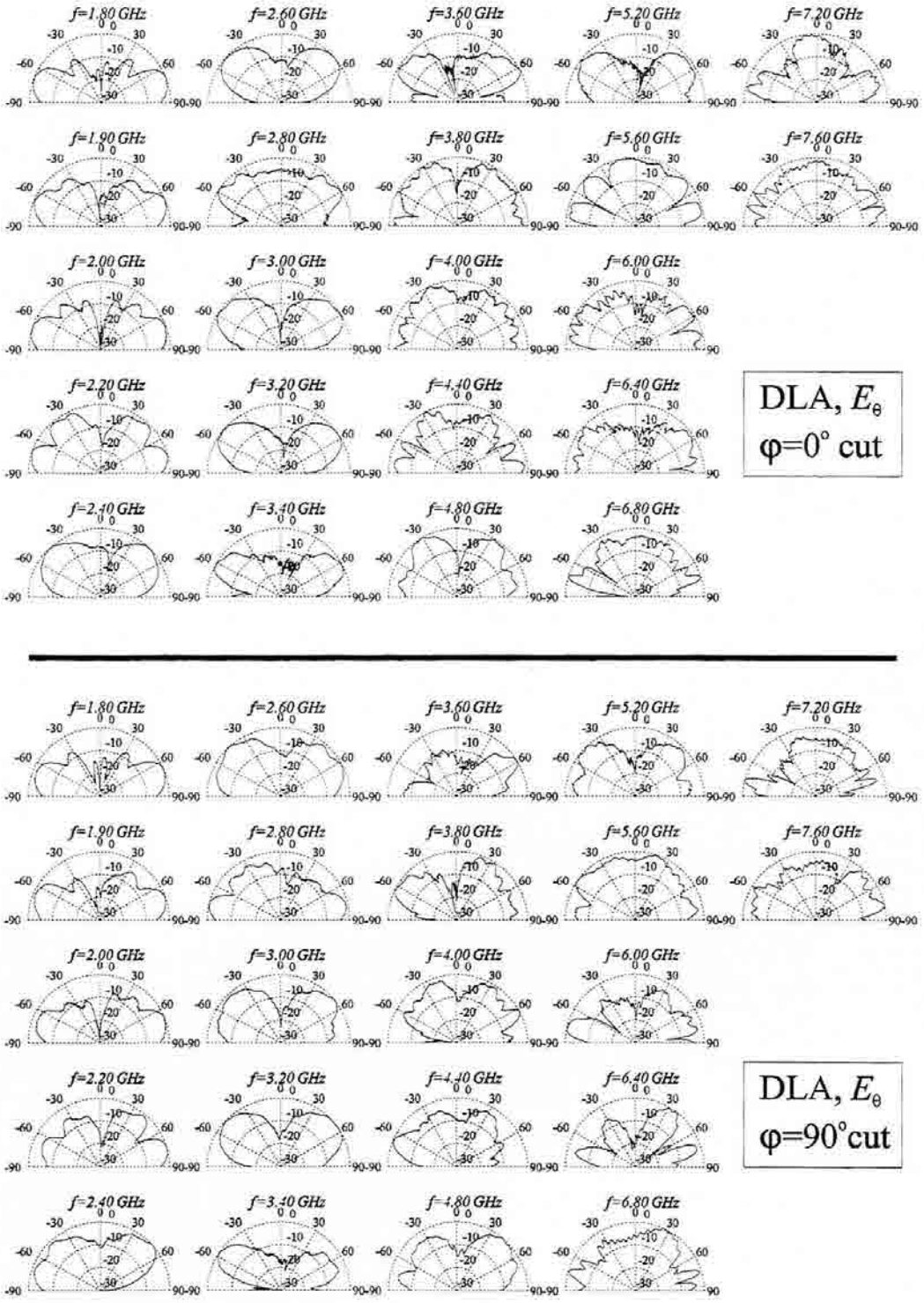

Fig. 6.16 SDLA antenna radiation pattern cuts at φ=0° and φ=90°.

Such pattern variations lead to conclude that an active region is not successfully formed on the antenna structure, most probably due to the proximity among branches that would ease the coupling and propagation of electromagnetic waves from the feeding root to the antenna

tips. Also, random pattern tilts are still observed on the φ=90° plane, which again is on account of the random antenna shape.

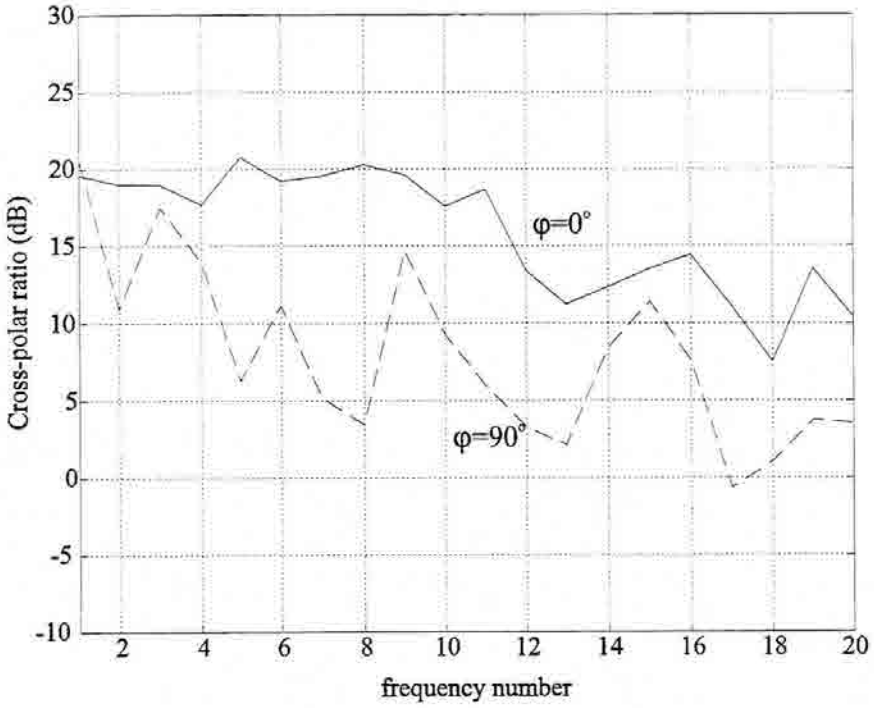

Fig. 6.17 The SDLA cross-polar ratio (E_θ/E_φ) at each of the measured bands.

The cross-polar ratio shows an improvement with respect to former designs, being the vertical component consistently above the horizontal one at low frequencies. In general, polarization suffers less variations, which should be related to the more elongated shape of the new design, rather to an improvement of its fractal properties.

6.5 Conclusions

The performance of several random fractal tree-like antennas has been experimentally investigated. The designs have shown to feature a multiple resonant characteristic from the input terminals point of view. The distribution of bands in the spectral domain is rather denser than that of the previously investigated deterministic antennas. Such feature can be linked to a smoother distribution of sizes and lengths on the antenna shape. The radiation patterns of some of the antennas keep a fair degree of similarity among bands, although some undesired features are clearly shown, mainly due to the random nature of the antenna structure. Basically, a random pattern tilt is observed on the antenna plane cut, and large variations on the cross-polar ratio are found from band to band. It has been shown that the density of the band spectrum can be modified by means of a simulated DLA antenna structure generation algorithm. Although polarization fluctuations can be improved this way too, radiation patterns seem to suffer of larger variations from band to band owing to the closer spacing of antenna branches that would ease the coupling of electromagnetic fields over the whole antenna shape.

7. *Small Fractal Antennas*

When the size of an antenna is made much smaller than the operating wavelength, it becomes highly inefficient. Its radiation resistance decreases, while proportionally the reactive energy stored in the antenna neighborhood increases rapidly. Both phenomena make small antennas difficult to match to the feeding circuit, and when matched they display a high Q, i.e., a very narrow bandwidth. The potentiality of fractal shapes for improving the efficiency of common small antennas has been recently suggested by Dr. Nathan Cohen in [100]-[103]. Based on a numerical method of moments analysis, he observed that fractal Minkowski loops presented a low resonant frequency, relative to their electric size. Also, numerical results upon the so called Cohen dipole evinced that the directivity of some common antennas such as linear dipoles and Yagi antennas could be improved.

Many fractal curves such as the Koch, Minkowski, Peano and Hilbert curves [2] can be fitted in a finite area although they have an infinite length. Such a striking property should lead to question many common assumptions regarding Euclidean antennas. For instance, might such long structures support arbitrarily large wavelengths and couple them efficiently to free space ? Fractal curves are highly uneven curves, being their fractal dimension a good parameter for their roughness characterization. Since it is well known that sharp shapes, sudden bends and discontinuities tend to enhance radiation, might fractal shapes improve the radiation properties of common antennas ? For instance, could fractal shapes increase the low radiation resistance of a small dipole or loop ? Actually, Nathan

Cohen observed in [100],[101] that some small fractal loops presented an unusual large input resistance. Even though their area was very small, their perimeter was not, which led him to think that some assumptions upon small antennas might not necessarily hold for fractal shapes. For instance, the radiation resistance of a small Euclidean circular loop can be consistently written either in terms of its area (A) or its perimeter (C) as [52],

$$R_r = \eta\left(\frac{2\pi}{3}\right)\left(\frac{kA}{\lambda}\right)^2 = 20\pi^2\left(\frac{C}{\lambda}\right)^4 \tag{7.1}$$

Obviously, such a description is not correct for fractal loops, since area and perimeter are not as simply linked to each other as they are in Euclidean loops, and the two approaches would lead to completely different conclusions.

On the other hand, one of the main limiting features of small antennas is their narrow bandwidth due to its large Q factor. When operated below resonance, the input reactance of an small antenna increases rapidly, which together with the fast decrease of the radiation resistance yields a poor Q factor and thus such a narrow bandwidth. Again, some fractal loops might have surprisingly small resonant frequencies due to their large perimeters, which together with their larger radiation resistance might lead to a broader bandwidth than common antennas.

This chapter is devoted to investigating some aspects regarding small fractal antennas. Firstly, some theoretical considerations upon the fundamental limits on small antennas are done for fractal shapes, secondly some experimental and numerical results upon a particular case of a small fractal antenna are introduced and discussed.

7.1 - Some theoretical considerations upon small fractal antennas

Several authors have extensively worked upon the fundamental limits of small antennas [58]-[64],[118],[119],[127],[128] being Chu's [118] and Wheeler's work [58] among the ones that have most influenced further investigations on such topic. An antenna is said to be small when it can be enclosed into a radiansphere, i.e., an sphere with radius $a=\lambda/2\pi$ [58],[59],[61]. For such antennas, Chu established a fundamental limitation on their Q factor based in the following argumentation.

7.1.1 - Fundamental Limitations on Small Antennas

For any arbitrary current distribution and antenna structure, the field outside the radiansphere can be written as a linear combination of orthogonal spherical waves propagating radially outwards [118],[119]. When considering circularly symmetrical, linearly polarized fields, only TM_{no} modes are required to fully describe them [118]. That is,

$$H_{\varphi} = \sum_{n} A_n P_n^{1}(\cos\theta) h_n(kR)$$
$$E_{\theta} = j\eta \sum_{n} A_n P_n^{1}(\cos\theta) \times \frac{1}{kR}\frac{d}{dR}\left[R h_n(kR)\right] \tag{7.2}$$

where $P_n^{1}(\cos\theta)$ is the first associated Legendre polynomial of order n, $h_n(kR)$ is the spherical Hankel function of the second kind and order n, k is the free space wave number and R the distance from the coordinate origin where the antenna is located. From this result, one can freely interpret that space outside an sphere of an arbitrary radius a essentially behaves as an equivalent transmission line where each of the orthogonal spherical waves is an independent propagating mode. Equivalent voltage and current waves, with amplitudes proportional to the electric and magnetic fields on the sphere surface, can be defined for such an equivalent transmission line. A characteristic impedance can be associated to the n^{th} propagating mode such as

$$Z_n = j\frac{\frac{d}{d\rho}(\rho h_n(\rho))}{\rho h_n(\rho)} \tag{7.3}$$

where ρ is defined as $\rho=ka$,. Using the recurrence formulas of spherical Bessel functions, such impedance can be written as [118],

$$Z_n = \frac{n}{j\rho} + \cfrac{1}{\cfrac{2n-1}{j\rho} + \cfrac{1}{\cfrac{2n-3}{j\rho}}} \ddots \cfrac{1}{\cfrac{3}{j\rho} + \cfrac{1}{\cfrac{1}{j\rho}+1}} \tag{7.4}$$

which can be interpreted as an equivalent high-pass ladder filter network as shown in Fig. 7.1.

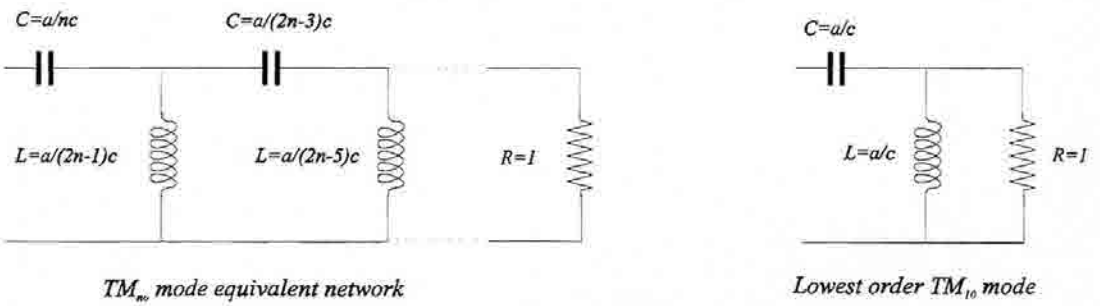

Fig. 7.1 Chu's equivalent ladder network for spherical TM_{no} modes (left) and for the fundamental, lowest order mode TM_{10} (right).

Essentially, the antenna can be also reinterpreted as the coupling network inside the sphere that draws power from the generator and delivers it to such an equivalent ladder filter network outside the sphere, i.e., to free space. Since it is a high-pass filter, the larger the frequency, the larger the power coupled to the terminal resistance which takes into account power dissipation due to radiation. Actually, the product *ka* (i.e. the operating frequency times the sphere radius) rather than frequency alone is what determines the pass-band, which means that the larger the sphere radius, the lower the frequencies that can become efficiently radiated.

The Q factor of the whole system is proportional to the stored reactive energy to the radiated power ratio. Assuming that the whole network operation around a particular

frequency can be approached by a series *RLC* circuit, the Q factor of the n^{th} mode (Q_n) can be computed. Since the propagating modes constitute an orthogonal set, the whole stored energy and radiated power can be computed as the sum of the individual stored energies and radiated powers from each mode [119]. That is,

$$Q = \frac{\sum_n A_n^2 \left(\frac{1}{2n+1}\right) Q_n(ka)}{\sum_n A_n^2 \left(\frac{1}{2n+1}\right)} \tag{7.5}$$

It is shown in [118],[119] that the quality factor of all modes increases very rapidly when $ka<n$, being the lowest order TM_{10} mode the one with the smaller Q. Assuming that higher order modes only contribute to rise the overall Q factor, one can conclude that the lowest achievable Q is that of an antenna exciting only such mode. The equivalent ladder network is reduced this way to a second order network (see Fig. 7.1). Its Q factor is given by,

$$Q = \frac{1}{k^3 a^3} + \frac{1}{ka} \tag{7.6}$$

which establishes the lower, fundamental limit of the Q factor that can be achieved by a linearly polarized antenna. Several authors have reported such result as well [52],[59] leading to a slightly different expression for equation (7.6). Recently, J. Mc Lean [62] has reviewed some of these concepts concluding that (7.6) yields actually the correct expression. He also showed that the fundamental limit upon circularly polarized antennas is on the order of a half that of the linearly polarized ones [62].

It is important to state that this limit is established regardless of the antenna current distribution inside the sphere. Actually, the current distribution inside the sphere is not uniquely determined by the field distribution outside the sphere [118] so several current distributions can lead to the same Q factor. In practice, such a fundamental limit has not ever been reached, being the Goubau antenna [52],[60] with $Q \approx 1.5 \cdot Q_{min}$ one of the lowest Q reported antennas. Achieving a low Q antenna, basically depends on how efficiently it uses the available volume inside the radiansphere.

It must be stressed that Chu's definition of the Q factor is a general concept that applies even when the antenna is not resonant. Since the Q definition is valid for a resonant system, it is implicitly assumed that the extra amount of unbalanced reactive energy of a non resonant antenna is externally compensated by a proper inductor or capacitor at the

input terminals. Therefore, depending on the nature of the predominating energy the out of resonance Q factor has to be defined as,

$$Q = \omega \frac{2W_e}{P_r} \qquad W_e > W_m \tag{7.7}$$

$$Q = \omega \frac{2W_m}{P_r} \qquad W_m > W_e \tag{7.8}$$

where W_m and W_e are the stored and magnetic energies and P_r is the average radiated power. Of course, both definitions are equivalent if the antenna is self-resonant, which is not usual for small antennas.

Prior to Chu's work, Wheeler introduced the Power Factor (PF) concept to characterize small antennas [58],[61],[117]. He assumed that any small reactive antenna could be reduced to an equivalent first order network when operating at low frequencies. Such a network would be either a serial RC network or a parallel RL one depending on whether electric of magnetic stored reactive energy predominates at low frequencies. He defined the PF for such networks as

$$PF_e = \frac{G}{B} = \frac{G}{\omega C} \qquad W_e > W_m \tag{7.9}$$

$$PF_m = \frac{R}{X} = \frac{R}{\omega L} \qquad W_m > W_e \tag{7.10}$$

being G and R the radiation conductance and resistance respectively. Actually, such definition can be reinterpreted as $PF \approx 1/Q$, provided that only the radiation resistance or conductance is taken into account, and that the contribution of only one of the reactive components of the antenna input impedance is significant to the overall antenna performance. Also, he stated that the lowest achievable PF is that of an spherical coil filling the volume inside the radiansphere, that is,

$$PF = \left(\frac{2\pi a}{\lambda} \right)^3 = k^3 a^3 \tag{7.11}$$

which is in agreement with the limit established in Equation (7.6), provided that the sphere enclosing the antenna is much smaller than the operating wavelength.

7.1.2 - Small Fractal Antennas and the Fundamental Limit

Before describing some experimental results regarding small fractal antennas, some theoretical considerations should be taken into account. First of all, Chu's theory is based on the fact that any antenna current distribution can be developed in a series of orthogonal spherical functions. Although this is strictly correct for common antennas, it has not yet been proved to hold for fractal shapes. Field expansion into a series of orthogonal spherical modes has been proved to converge for well-shaped distributions in the same sense Fourier series do. That is, the series converge provided that the distribution is piecewise continuous and has a piecewise derivative [110],[111],[112]. Often considered 'mathematical monsters', many fractal curves are among those 'pathological' cases of curves which do not have a piecewise continuous derivative. Therefore, one should conclude that the fundamental limit is not formally proven for hypothetical fractal antennas.

A similar problem arises when one analytically deals with the radiation vector of a uniform linear current on a fractal wire monopole. It is computed as a line integral with respect to the arch length along the wire as,

$$\bar{N}(k) = \int_C \bar{I}(l')e^{jk\bar{l}'}dl' \tag{7.12}$$

again, a line integral is defined for rectifiable curves [110], and many fractal curves are non-rectifiable, i.e., they cannot be approached by a finite length polygonal curve. In other words, the radiation vector expressed in (7.12) might yield, for instance, an infinite value. This would give an infinite electrical field even when a finite current amplitude over the antenna is considered, which would mean an infinite radiation resistance. It is important to stress that such an arbitrarily large radiation resistance would be achieved with a finite size fractal antenna that could be fitted in an arbitrarily small volume, but that would have an infinite wire length.

The radiation resistance of an arbitrarily shaped loop has been demonstrated to be proportional to the square of the enclosed area to the operating wavelength ratio [53]. Such proof is based on applying Stoke's theorem to the line integral along the antenna perimeter to derive an expression of an equivalent magnetic dipole radiating the same electric fields. Stoke's theorem assumes integration along a closed curve (the loop perimeter in this case)

which has a piecewise continuous derivative. Many fractal loops such as the Minkowski loop and the Koch snowflake loop do not have a piecewise continuous derivative, so one must be very careful on assuming that Stoke's theorem can be applied as done for Euclidean shapes.

Of course, one could argue that such considerations would only apply to the ideal fractal shapes, for instance, fractal loops and monopoles with infinite lengths. Any feasible implementation of a fractal antenna would necessary have a finite length, and a finite number of segments with a continuous derivative. Such a derivative might become arbitrarily large at some sharp corners of the structure, but never infinite or undetermined. However, one must take into account that an ideal fractal shape, i.e., the fractal attractor, can always be thought as a limit object from an infinite succession of non strictly fractal objects, which can approach the ideal one up to an accuracy as good as desired. That is, an infinite Koch curve could not ever be obtained, yet it might be approached by a finite but arbitrarily long, highly uneven Koch-like curve. With this idea in mind, it would be sensible to assume that given a limit on the performance of the ideal shape (which might not be the same as the one established by the Chu-Wheeler theory or it might not even exist), the non-ideal fractal curves on the succession would approach the ideal performance as much as one would desire. It should be clear that in this case a technological limit (the resolution of our fabrication process when approaching the fractal attractor) rather than a fundamental one would be the main limiting factor on the antenna performance, which is a completely different approach than the classical one.

7.1.3 - An Example: Simple Analysis of the Minkowski Loop.

The Minkowski loop was chosen by N. Cohen as the first example of small fractal antenna presenting an anomalously large radiation resistance [100],[101]. It is interesting to notice that the whole loop area decreases as $(5/9)^n$ while its perimeter increases as $(5/3)^n$, being n the fractal iteration number. Thus, we have the striking characteristic of a vanishing area loop which however has an infinite perimeter (see Fig. 6.19).

If one assumes a uniform current distribution along the antenna perimeter, the antenna can be analytically described as follows. At the n^{th} iteration the antenna structure is composed of 5^n identical square loops (the fractal *initiator*), each one having a side length $l/3^n$, being l the side length of the square enclosing the loop. The radiation vector of the whole structure at the n^{th} iteration can be written, as usual, as the product of the element factor (the small squared loop initiator) with the array factor. The whole array structure can

be thought as an infinite series of convolutions similarly to what was described for the Cantor array of Chapter 3. That is, a five-delta generator is convolved with a scaled version of itself as many times as iterations in the fractal construction, being the scale factor at each iteration $\delta = 1/3$. The associated array factor can be then written as an infinite product succession of the individual five-element generator array factor. Therefore, the whole radiation vector for the Minkowski loop at the n^{th} iteration can be written as,

$$\vec{N}_n(k_x,k_y) = \vec{N}_n^{loop}(k_x,k_y)\cdot\prod_{m=1}^{n}\left(1+4\cos\left(k_x l/3^m\right)\cos\left(k_y l/3^m\right)\right) \tag{7.13}$$

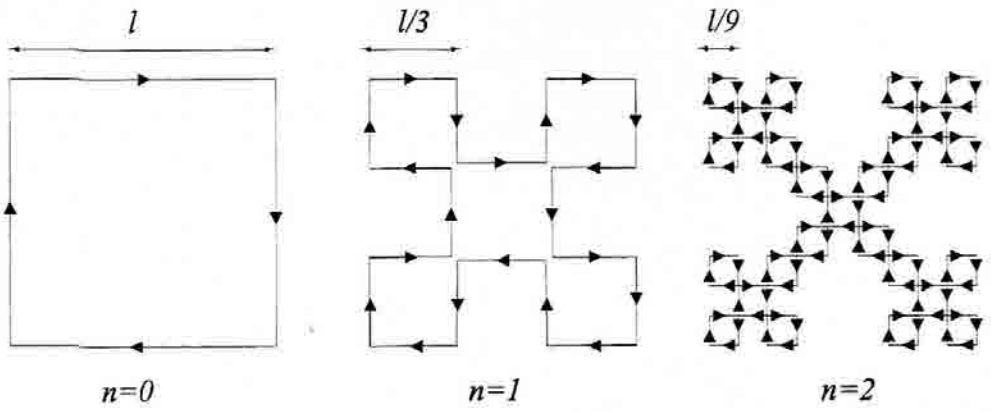

Fig. 7.2 First iterations on the Minkowski loop.

When considering that the square loop initiator is much smaller than the operating wavelength ($l<<\lambda$), its radiation vector can be written, at the n^{th} iteration as,

$$\vec{N}_n^{loop}(k_x,k_y) = \frac{1}{3^{2n}} I\cdot l^2(k_x\hat{x}-k_y\hat{y}) = \frac{1}{3^{2n}}\vec{N}_0^{loop}(k_x,k_y) \tag{7.14}$$

Also, following that approximation the five generator elements overlap into a single one, such that the whole radiation vector can be expressed as,

$$\vec{N}_n(k_x,k_y) \approx \frac{1}{3^{2n}}\vec{N}_0^{loop}(k_x,k_y)\cdot\prod_{m=1}^{n}(1+4) = \vec{N}_0^{loop}(k_x,k_y)\cdot\left(\frac{5^n}{9^n}\right) \tag{7.15}$$

which leads to the conclusion that the radiation resistance of such a Minkowski loop (R_r^n) is related to the radiation resistance of the square loop enclosing the antenna (R_r^0) as

$$R_r^n = R_r^0\left(\frac{5}{9}\right)^{2n} \xrightarrow[n\to\infty]{} 0 \tag{7.16}$$

That is, the radiation resistance vanishes for the ideal fractal shape. The decrease ratio $(5/9)^{2n}$ is due to the area reduction at each iteration, and since the limit object has a null area, the final loop has a null radiation resistance as well. This seems to be in contradiction with the original idea that the fractal shape might have a larger radiation resistance than expected. However, in such a simple analysis one has not taken into account that when traveling along an infinite length wire, phase shifts along the perimeter might occur even for arbitrarily large wavelengths. For example, one could consider the picture described in Fig. 7.3. That is, for a particular wavelength, a 180° phase shift might be introduced such that currents on the opposite side of the loop become in phase instead of the common out of phase situation. Now, the radiation vector has to be modified. The initiator loop element factor has changed yielding,

$$\vec{N}_n^{loop'}(k_x,k_y) = 2\frac{I\cdot l}{3^n}\left(\cos\left(\frac{k_x l}{2\cdot 3^n}\right)\hat{x} + \cos\left(\frac{k_y l}{2\cdot 3^n}\right)\hat{y}\right) \approx 2\frac{I\cdot l}{3^n}(\hat{x}+\hat{y}) = \frac{\vec{N}_0^{loop}(k_x,k_y)}{3^n} \tag{7.17}$$

where as usual, it has been assumed that $l<<\lambda$. This assumption might seem to be in contradiction to the initial supposition that a phase reversal on the small loop existed, however one must remember that when considering a fractal loop there is an arbitrarily large path between any two points on the fractal perimeter. Here, a square loop has been taken as the initiator to simplify the analysis; nevertheless, a Minkowski loop could be taken instead and such loop might be fitted into a square much smaller than the wavelength but with an arbitrarily large side length.

The overall radiation vector can be readily calculated now by just taking into account the sign reversal on the central loop, i.e.,

$$\vec{N}_n'(k_x,k_y) = \vec{N}_0^{loop'}(k_x,k_y)\frac{1}{3^n}\cdot\prod_{m=1}^{n}\left(-1+4\cos\left(k_x l/3^m\right)\cos\left(k_y l/3^m\right)\right) \tag{7.18}$$

Again by following the approximation $l<<\lambda$ one gets,

$$\vec{N}_n'(k_x,k_y) = \vec{N}_0^{loop'}(k_x,k_y)\frac{1}{3^n}\cdot\prod_{m=1}^{n}(3) = \vec{N}_0^{loop'}(k_x,k_y) = 2\Pi(\hat{x}+\hat{y}) \tag{7.19}$$

that is, the radiation resistance of the null area, ideal fractal loop is the same as the original initiator,

$$R_r^n = R_r^0 \tag{7.20}$$

Now, rather than behaving as a conventional loop, the antenna performs as an equivalent linear dipole of length $2^{1/2}l$ aligned along the $y=x$ direction. This means that the radiation resistance of such a fractal loop decreases as the square of the length to wavelength ratio instead of the forth power as common Euclidean loops.

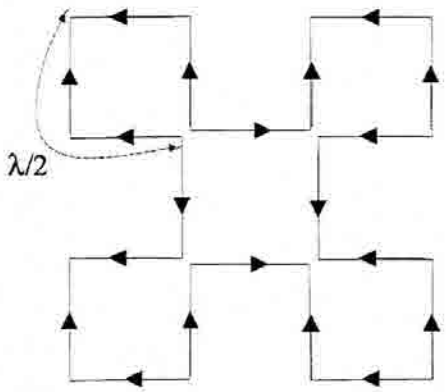

Fig. 7.3 The Minkowski Loop current distribution taking into account a proper current phase reversal.

Of course, neither the first analysis, nor the second one perfectly describe the behavior of such a hypothetical loop. Mutual coupling between loops have not been taken into account (which might shorten the electrical path along the perimeter), and an unlikely uniform current distribution has been considered. In practice, the current distribution would be much similar to a sinusoidal one, and even if an unusually large radiation resistance were obtained, the reactive energy stored among the antenna loops might increase the overall antenna Q. Such complex antennas require a computer model together with some experimental data to give a proper insight on their true behavior; this is the approach carried out in the following section. Nevertheless, the former analysis becomes useful to stress that one should take special care before considering that some common assumptions supported by classical Euclidean antennas hold for fractal antennas as well.

7.2 - The Small Koch Monopole

First thought of as a candidate to become a simple multiband antenna, the Koch monopole is an effective example to illustrate that fractals can improve some features of common Euclidean shapes. Being ideally a non rectifiable curve (its length grows as $(4/3)^n$), the Koch curve has neither a piecewise continuous derivative. Actually, it is nowhere differentiable, which means that its shape is highly rough and uneven. Thus, it appears as a good candidate for becoming an efficient radiator.

7.2.1 - Antenna Description

The classical Koch curve construction algorithm was described in Chapter 2. Initially constructed for a straight segment of height h, an IFS algorithm can be applied to generate the succession of curves that converge to the ideal fractal shape. When analyzing the fractal antenna behavior, it looks specially interesting to compare it with that of the closest Euclidean version, i.e., a straight monopole. We will name such a straight monopole as *K0* (the zeroth iteration of the fractal construction), while the remaining objects of the iterations will be referred as *K1,K2* ... *KN*. Although the fractal shape might look too convoluted to be of practical application, it can be easily printed over a dielectric substrate using standard printed circuit techniques. The fabrication complexity in this case is exactly the same for the Euclidean antennas and for almost all fractal ones. Since one is interested in examining the low frequency behavior, a high performance (low-loss) microwave dielectric substrate is no longer required.

Up to five iterations of the fractal succession were constructed, all of them of the same overall height and using the same substrate. The six antennas (*KO...K5*) where mounted over an 80 x 80 cm ground plane and measured over a 0.1 to 2 GHz frequency range. The antennas were also numerically analyzed using the frequency domain method of moments algorithm, written in a MATLAB™ code and run on an HP workstation (i.e., the same code used to analyze the wire Sierpinski antenna in Chapter 4). Figure 7.21 shows the five iteration version of the Koch monopole (i.e. *K5*), which has an overall height h=6 cm, but a whole length of $l = h \cdot (4/3)^5 = 25.3$ cm.

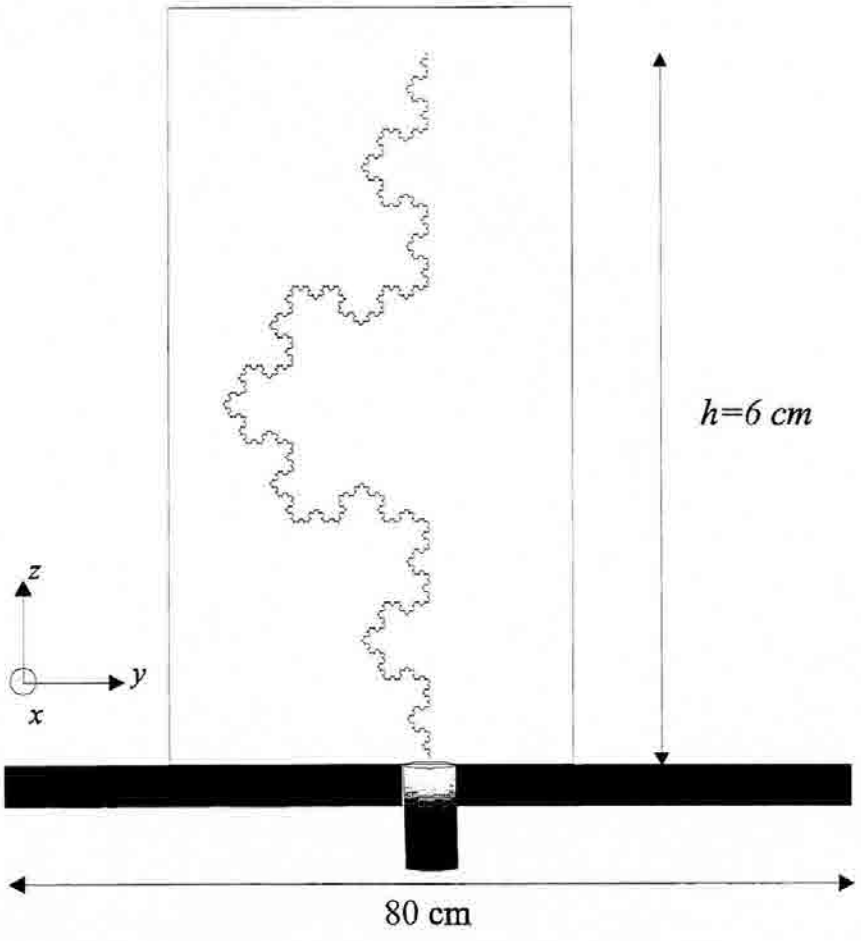

Fig. 7.4 The five-iteration fractal Koch monopole (K5).

7.2.2 - Input Parameters

The input resistance and reactance of the five measured Koch monopoles, together with the same parameters for a linear monopole (*K0*) are shown in Fig. 7.5. All antennas had the same height h=6 cm, but of course a different length l. The method of moments data corresponding to the Euclidean antenna (*K0*) and the first three iterations of the fractal one (*K1,K2,K3*) are also shown for comparison. The copper etched wire had approximately a rectangular cross-section of width w=200μm and thickness t=35μm, except for the *K5*

model where the wire width was reduced to w=150μm. To get the best match between experimental and numerical data, an equivalent radius of a=120μm was considered following the equivalent radius approach outlined in [52]. Also, an equivalent input resistance due to ohmic losses was computed at each frequency by integrating the square of the current distribution over the whole antenna length. The skin effect was also taken into account there by assuming an equivalent cylindrical wire cross-section as described in [52] too. It is apparent that a good match between numerical and experimental data is obtained.

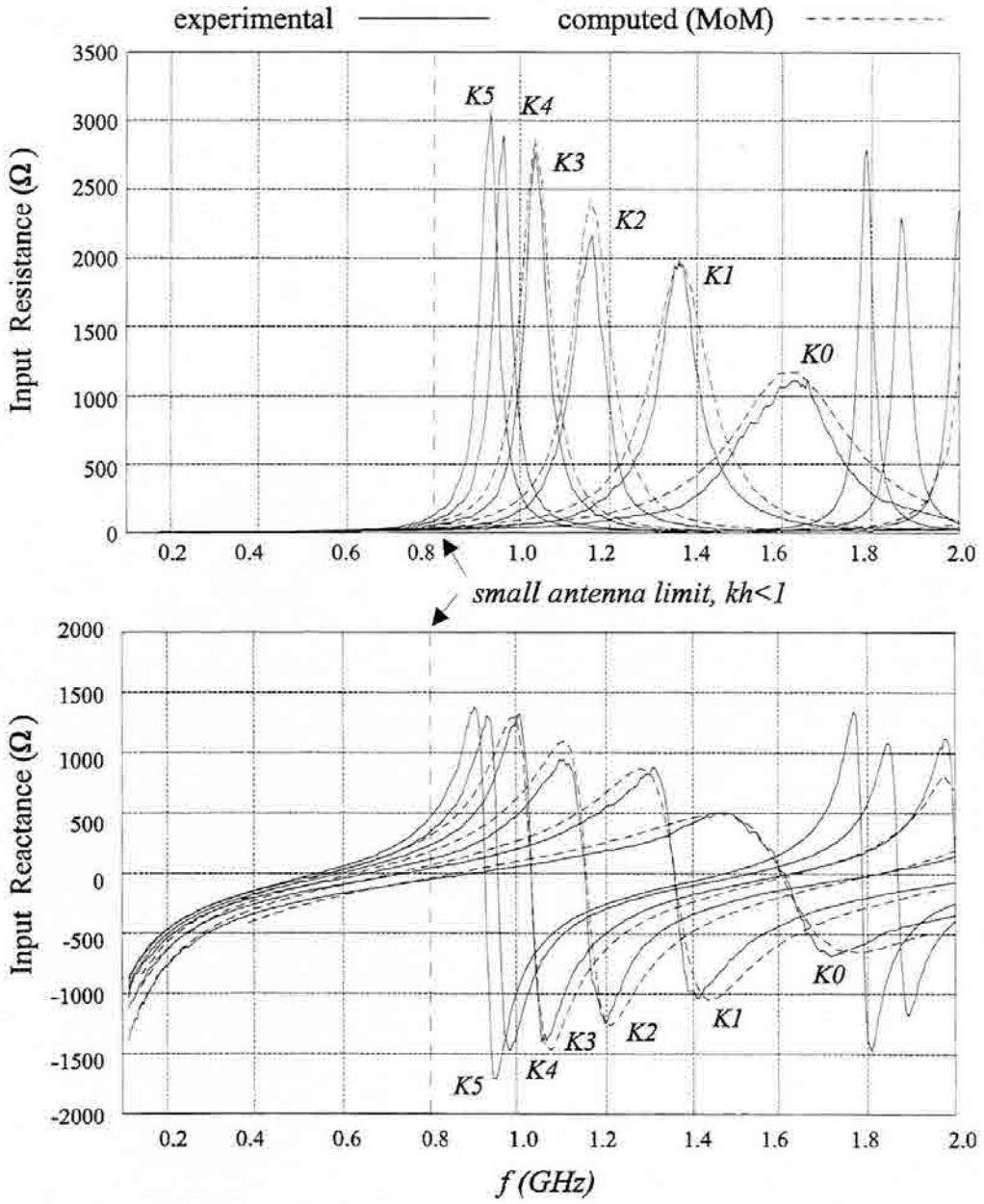

Fig. 7.5 The Koch monopole input parameter evolution for several fractal iterations.

Some interesting conclusions can be derived from the input parameters plot. First of all, in the low frequency region the input resistance increases with the number of iterations when comparing the six characteristics at a given frequency. While the linear monopole input resistance becomes very small below the first resonance (0.9 GHz), the *K5* model is about its input resistance maximum value. Figure 7.23 shows such a drive resistance increase with growing fractal iterations for a fixed frequency (the first monopole resonant frequency has been chosen in this case).

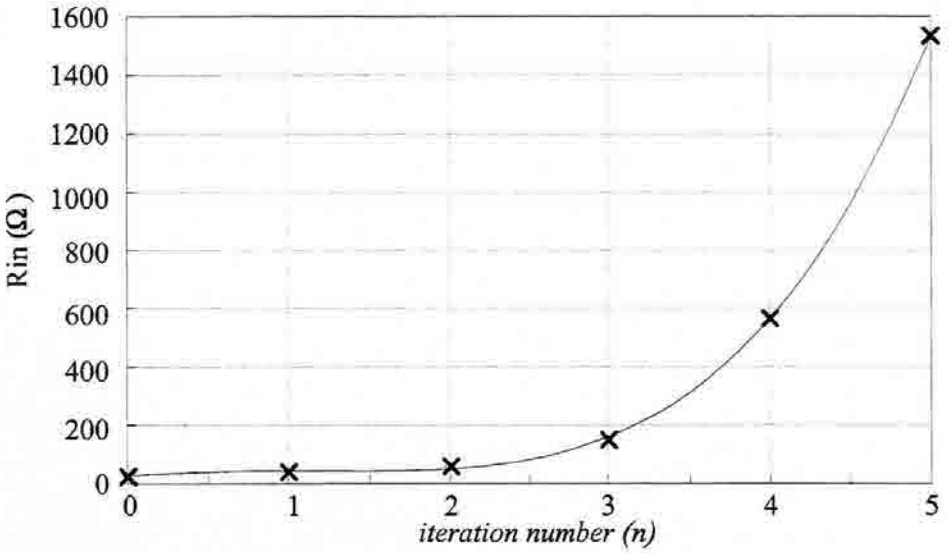

Fig. 7.6 Input resistance of the linear monopole and the first 5 fractal iteration antennas, measured at the monopole's first resonant frequency.

Analogously, the input reactance plot evinces that resonant frequencies are consistently shifted towards the lower frequency region at each fractal iteration. In particular, even though all the Koch models can be considered small antennas (kh = 1) below $f \approx 0.8$ GHz, they are self-resonant, i.e., they have a vanishing input reactance without the need of an external compensating reactive element. The longest antenna (*K5*) reaches its second at resonance about the same frequency where the linear dipole has its first resonance.

The peculiar behavior of the Koch monopole must be linked to its geometrical shape. It is apparent that even though all models have the same size, they perform as longer antennas than what would be predicted from their height alone. It seems that the electrical current propagates along the whole wire length despite of its shape such that, the longer the whole wire, the lower the resonant frequencies regardless of the antenna size (height). This

supports the idea, expressed in the theoretical considerations of Section 7.1, that a sinusoidal-like current distribution along the whole wire should be considered. Such a distribution would introduce some phase shifts along the antenna that would enhance radiation with respect the uniform current case where the contributions from some parts of the antenna might cancel.

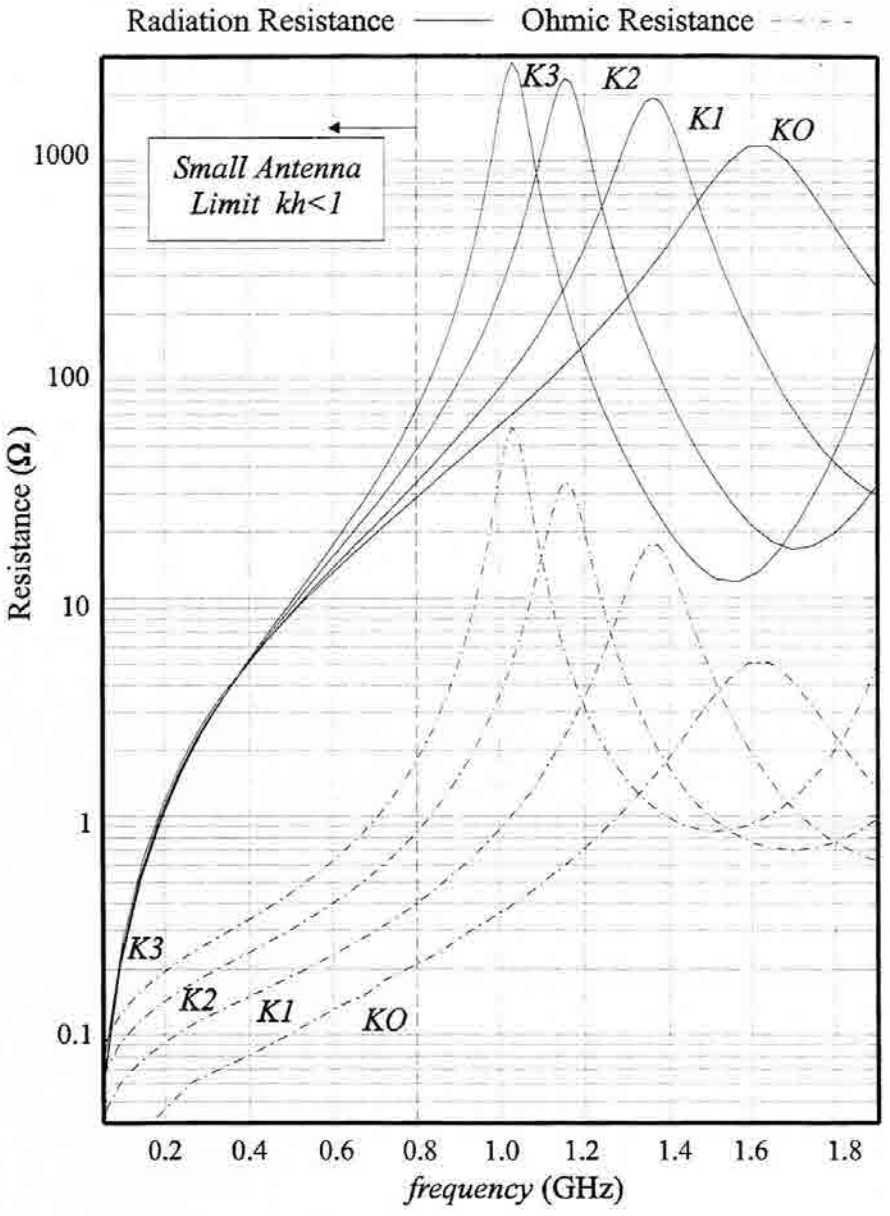

Fig. 7.7 Frequency evolution of drive resistance radiation and ohmic loss components (K0..K3). Both features have been computed using the MoM technique.

7.2.3 - Drive Resistance and Antenna Efficiency

It is important to stress that the input resistance increase is not due to an increase on the input loss-resistance with the wire length. Both the resistance due to radiation and ohmic losses behave similarly with frequency, being the ohmic resistance consistently below the radiation one, as shown in Fig. 7.7. Here, both resistances have been computed using the MoM technique as outlined before.

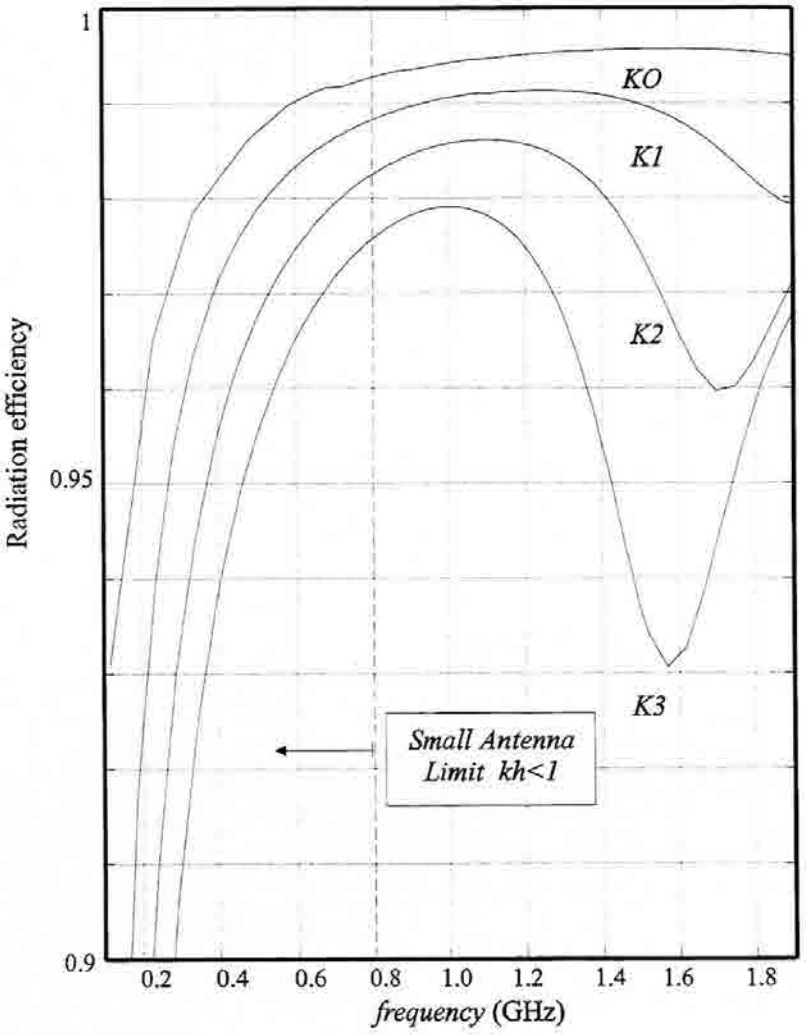

Fig. 7.8 K0...K3 antenna efficiency evolution with frequency.

The antenna efficiency can also be computed from both resistance components. Figure 7.25 displays the evolution with frequency for the *K0...K3* models. Even though there is a decrease on the overall antenna efficiency for larger iteration numbers, it is kept within rather acceptable values over the 0.1 - 1.9 GHz frequency range. Nevertheless, at very low

frequencies the efficiency of all four antennas decreases rapidly as one might expect from the finite size and length of the antennas.

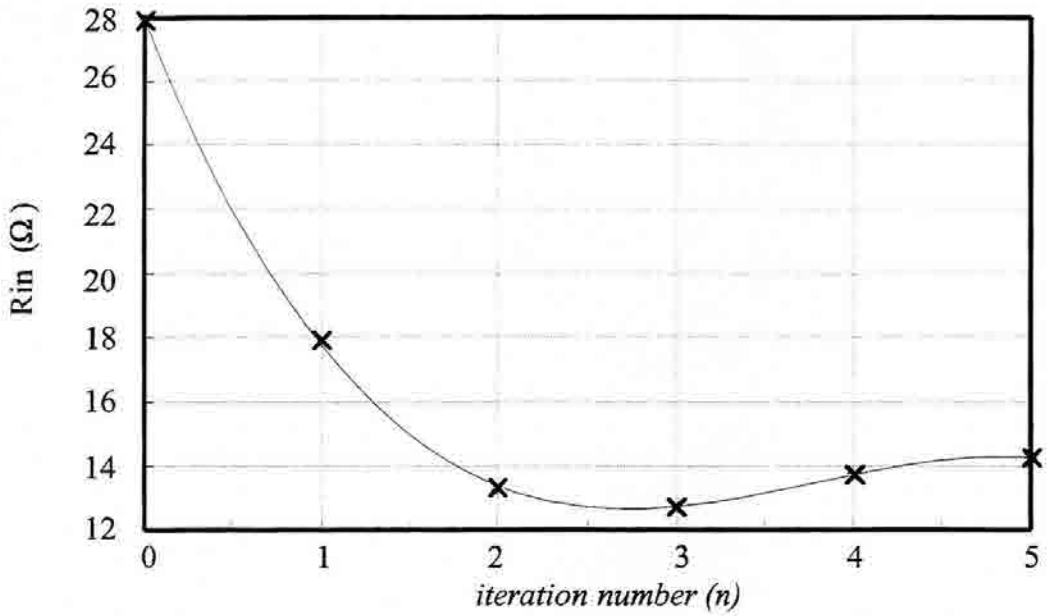

Fig. 7.9 Antenna drive resistance at resonance for the K0..K5 models.

Also, one must take into account that although resonant frequencies can be shifted towards longer wavelengths, that does not mean that the whole antenna behavior is shifted to the frequency origin too. For instance, the drive resistance at resonance is not kept around that of the linear monopole when increasing the number of iterations. That is, although the fractal prototypes drive resistance is always larger for a given frequency than that of the linear monopole, it decreases with the resonant frequency reduction. Such feature is apparent in Fig. 7.9, where the drive resistance at resonance is plotted with respect to the fractal iteration stage number.

7.2.4 - Antenna Size Compression Features

One might be tempted to extract some striking conclusions from the plots in Fig.7.5. For instance, one might think that an arbitrarily small resonant frequency could be obtained by increasing the number of fractal iterations as much as desired (or at least up to the technological limitations). The following figures give an insight on some of these issues. Figure 7.27 shows the evolution of the normalized effective electrical length (l_e) as a function of the normalized physical antenna length (l_p). The later is the total wire length normalized by the antenna height h, while the former is the normalized physical length that

should have a linear monopole to resonate at the same frequency the fractal antennas do. That is,

$$l_e = \frac{l}{h} \cdot \frac{f_r^{K0}}{f_r^{KN}} = l_p \cdot \frac{f_r^{K0}}{f_r^{KN}} \tag{7.21}$$

where f_r^{KO} and f_r^{KN} are the measured first resonant frequencies of the linear monopole and the n^{th} fractal antenna respectively. The curve in dotted lines shows what could be considered the ideal case, that is, an electrical length increase equal to the physical wire length increase (l_e=l_p).

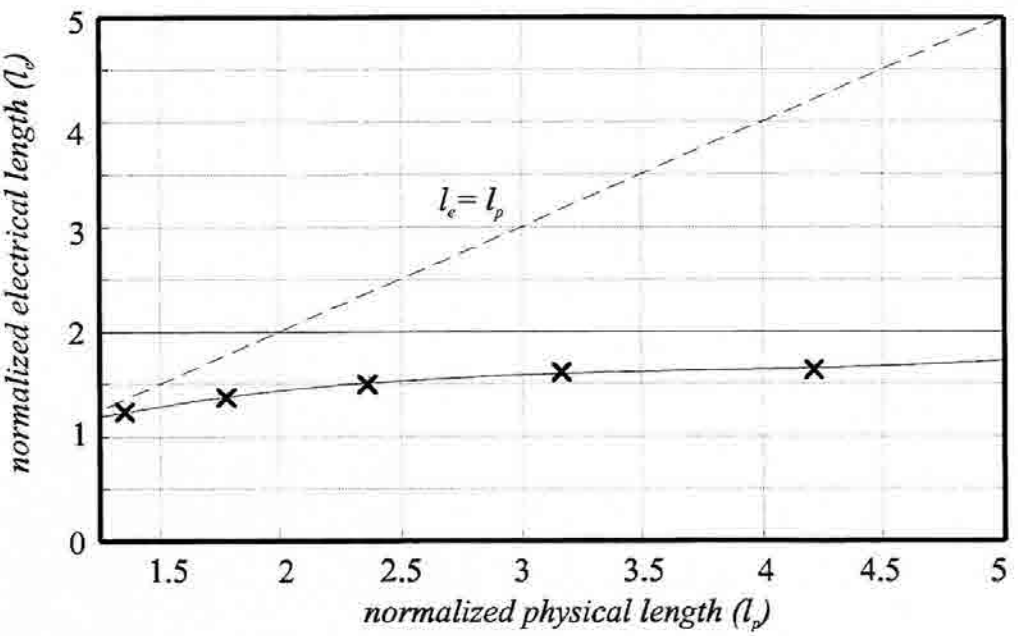

Fig. 7.10 Normalized electrical length with respect to physical wire length (solid line). The l_e=l_p line is shown for comparison (dashed).

It becomes apparent that, although the effective antenna length is increased at each fractal iteration, it does not grow at the same rate as l_p does. It even seems that a saturation might occur for arbitrarily large iteration numbers. In fact, it is difficult to extract conclusions on the antenna performance for such large fractal iteration numbers. The number of segments increases exponentially with the fractal growth which holds up the computer numerical analysis. From the experimental point of view, effectively increasing the antenna length becomes complicated for the actual antenna size. The resolution on the fabrication process was limited around a 100μm strip width, which means that the triangular bends on the antenna structure can become rounded beyond the forth and fifth iteration. This

way, the whole antenna shape is made smoother than desired, making the physical copper path shorter than what would be obtained for arbitrarily narrow strips. Therefore, one should take into account that the plots in Fig. 7.10 might underestimate the maximum achievable electrical length.

Instead of considering a fixed antenna size, one might think on the fractal shaping of monopoles as a technique for antenna size reduction. In that case, one would be interested on how much the classical linear monopole might be shrunk. The graphic in Fig. 7.11 represents the length compression factor (*CF*) as a function of the iteration number. Analogously to the perimeter compression factor defined by Cohen for the Minkowski loops [100], *CF* is obtained from comparing the first resonant frequencies of the Euclidean and the fractal antennas at the several iterations.

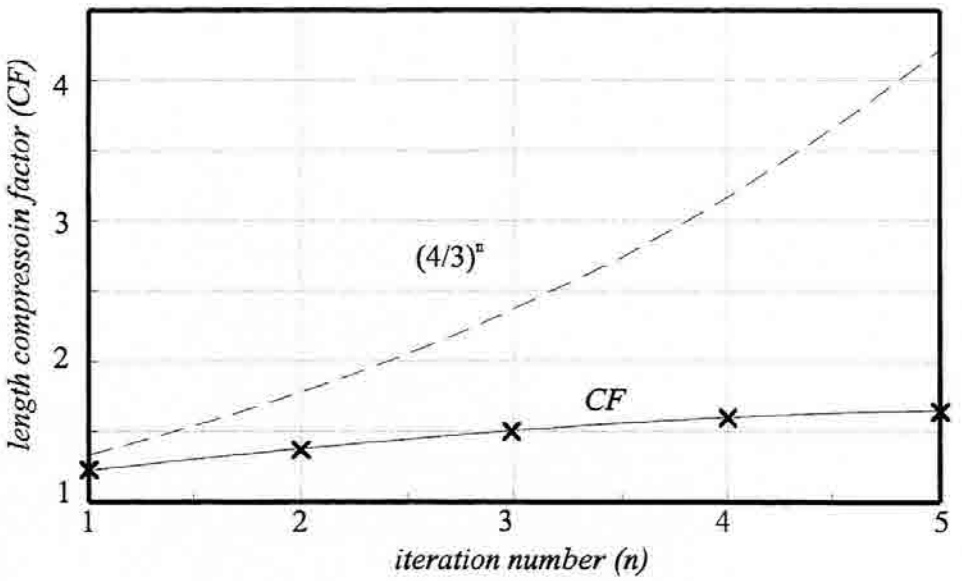

Fig. 7.11 The length compression factor for the first five fractal iterations. The $(4/3)^n$ characteristic is shown for comparison.

Again, the compression factor consistently increases with the number of iterations. Although far from the ideal $(4/3)^n$ physical length expansion characteristic, the graph shows that a conventional monopole can be shrunk by a factor of ~1.65 and still operate under the resonance condition. Whether such a compression factor can be further improved by increasing the number of iterations beyond n=5 appears as a most interesting question which would require further investigation to be answered.

7.2.5 - The Quality Factor

It has been shown that the fractal Koch antenna improves some features of a classical linear monopole when operating as a small antenna. Namely, resonant frequencies are shifted towards the longer wavelengths at each fractal growth iteration, making the antenna to be resonant even below the small antenna limit. Such a frequency shift makes the input resistance to appear consistently larger in the fractal case than in the linear monopole one. However, one must take into account that not only the input resistance is raised, but also that the input reactance is increased. Actually, a figure of merit of the small antenna is its Q factor, which can be loosely estimated as the input reactance (X_{in}) to radiation resistance (R_r) ratio.

The Koch antennas Q factor have been computed from both experimental and numerical data. The Q factor rather than the Wheeler's power factor (PF) [58] has been chosen to check the antenna performance because the later might lead to some wrong conclusions in this case. Both parameters are equivalent at the very low frequency range when the antenna is operated far from resonance. At such a low frequency region, the contribution to the input impedance of either the equivalent input inductor or capacitor almost vanishes and either PF and Q can be computed from the input impedance data as,

$$Q \approx \frac{1}{PF} \approx \frac{X_{in}}{R_r} \tag{7.22}$$

In such a very low frequency range, the Wheeler cap method [61],[63] can be used to estimate the antenna ohmic resistance and subtract it from the input resistance to evaluate the true antenna radiation resistance. However, even though the measured Koch antennas can be considered small, neither the Wheeler cap method can be applied, nor its PF computation is straightforward. Since the fractal monopoles are resonant, the contribution of the inductive component to the input impedance extends well beyond the small antenna limit. If one directly applied (7.22), one would get the wrong conclusion that a zero Q (and an infinite PF) were achieved at resonance. Also, the Wheeler cap method might lead to a wrong radiation resistance measurement since the metallic cap would slightly shift the antenna resonant frequencies where fast variations on the input parameters are obtained.

To properly evaluate the antenna Q, one must find a proper way to estimate either the average stored electric or magnetic energy and apply the definitions in equations (7.7) and (7.8). It is shown in [119] that the average stored electric and magnetic energies of a

loss-less one-terminal microwave network can be related to the input reactance (X_{in}) and susceptance (B_{in}) as,

$$W_e = \frac{|I|^2}{8}\left(\frac{dX_{in}}{d\omega} - \frac{X_{in}}{\omega}\right) = \frac{|V|^2}{8}\left(\frac{dB_{in}}{d\omega} + \frac{B_{in}}{\omega}\right) \tag{7.23}$$

$$W_m = \frac{|I|^2}{8}\left(\frac{dX_{in}}{d\omega} + \frac{X_{in}}{\omega}\right) = \frac{|V|^2}{8}\left(\frac{dB_{in}}{d\omega} - \frac{B_{in}}{\omega}\right) \tag{7.24}$$

where I and V are the input terminals current and voltage respectively. Since the power dissipated by the antenna is

$$P_L = \frac{1}{2}|I|^2 R_{in} = \frac{1}{2}|V|^2 G_{in} \tag{7.25}$$

the Q factor as defined in (7.7) and (7.8) can be computed as

$$Q = \frac{\omega}{2R_{in}}\left(\frac{dX_{in}}{d\omega} - \frac{X_{in}}{\omega}\right) \qquad W_e > W_m \tag{7.26}$$

$$Q = \frac{\omega}{2R_{in}}\left(\frac{dX_{in}}{d\omega} + \frac{X_{in}}{\omega}\right) \qquad W_m > W_e \tag{7.27}$$

or equivalently as,

$$Q = \frac{\omega}{2R_{in}}\left(\frac{dX_{in}}{d\omega} + \left|\frac{X_{in}}{\omega}\right|\right) \tag{7.28}$$

One must remind that (7.23) and (7.24) only strictly apply to one-port loss-less network, but they become a good approximation for low loss, high Q networks, which is the case of small antennas. Actually, the definition in (7.26) is the same L.J.Chu uses in his paper [118] to derive the antenna Q fundamental limit.

Equation (7.28) has been applied to compute the Q factor over the low frequency range for the Euclidean and Koch fractal antennas (Fig. 7.12). Both experimental and numerical data have been used. In the later case, ideal loss-less Koch antennas have been considered to evaluate the antenna Q, that is, only considering power dissipation due to

radiation. This has been done because the experimental data includes the ohmic resistance that lowers the overall Q, which might lead us to the wrong conclusion that the Q reduction were only due to an increase of the ohmic losses.

The plot in Fig. 7.12 clearly evidences that the fractal antenna not only presents a lower resonant frequency and a larger radiation resistance, but it also improves the Q factor

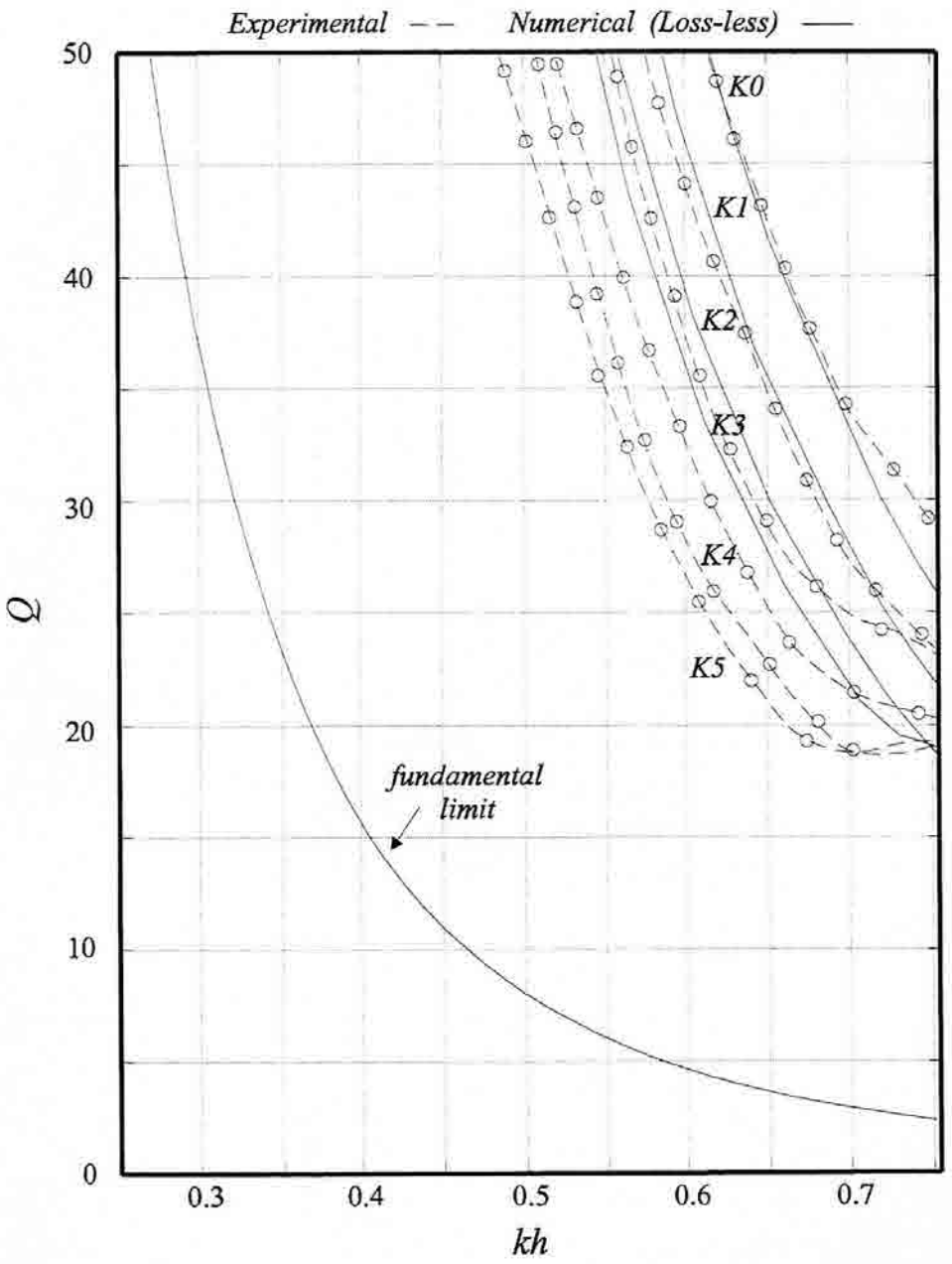

Fig. 7.12 Q factor of the linear monopole and Koch antennas computed from numerical (solid lines) and experimental data (dashed lines). The Chu fundamental limit curve is shown for comparison.

of the linear monopole. In a loose sense, such Q can be interpreted as the inverse of the fractional bandwidth, which means that the fractal antenna features a broader bandwidth than the Euclidean one. Up to ~1.6 bandwidth improvement factor is obtained when comparing the ideal loss-less monopole and *K3* antenna, while up to a ~2.25 factor bandwidth enhancement is obtained when comparing the monopole with the *K5* antenna, which however has the contribution of larger ohmic losses. Anyway, it is clear that the Q factor is reduced at each fractal growth iteration and that, the larger the number of iterations, the closer the Q to the fundamental limit (the fundamental limit expressed in (7.6) is also shown for comparison). It is commonly understood that an antenna Q factor depends on how efficiently it uses the available volume inside the radiansphere. As stated by Hansen in [59], being the linear dipole a one-dimensional object ($D = 1$), it inefficiently exploits such a radiansphere volume. Thus, it is not surprising that a fractal curve, featuring a fractal dimension $D > 1$ ($D \approx 1.262$ for the Koch monopole), can become a more efficient small antenna. Actually, fractal dimension is commonly loosely interpreted as a measure of the space filling properties of the fractal object. Therefore, one should conclude again that there exists a relation between the fractal geometric properties and the electromagnetic behavior of the antenna, and that such properties can be readily employed to design antennas with some useful properties.

7.2.6 - Current Distributions

The method of moments analysis allows the reconstruction of the current distribution over the antenna. Figure 7.30 shows such a current distribution for the linear monopole and the *K3* antenna. The fractal structure has been unfolded such that the current is shown over the whole antenna wire length. The wire length of both antennas has been normalized to the shorter one such that the further point on the longer current distribution yields the relative physical length, that is, $l^{K3}=(4/3)^3 l^{K0}=2.37 \cdot l^{K0}$.

Both currents have been computed at four different frequencies. The first one corresponds to the first fractal resonance; the second one coincides with the small antenna limit; the third one is computed at the first linear monopole resonance, while the fourth one is about where the radiation pattern of the Koch antenna start to become asymmetrical. It is clear that the current distribution over the Koch antenna is very similar to that of a linear antenna with a length 2.37 times its height. Boundary conditions at the antenna tip force current to vanish and the wave propagating along the antenna wire becomes reflected towards the feeding point. Roughly speaking, a typical standing wave sinusoidal pattern is formed, which makes the input impedance oscillate more or less as it does in a typical

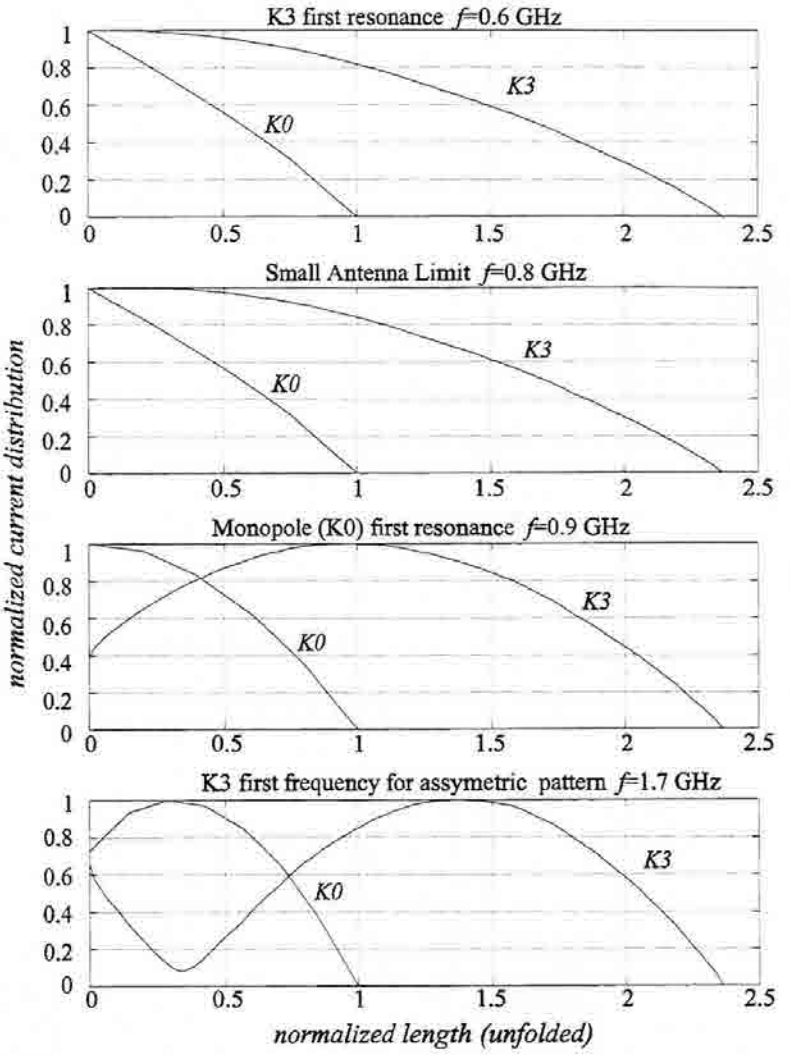

Fig. 7.13 Current distributions over the monopole and Koch antenna (K3). From top to bottom, the currents have been computed at the first K3 resonance, the small antenna limit, the first monopole resonance, and the pattern asymmetry boundary. Length and current amplitude are normalized.

transmission line. For instance, it is apparent that while the linear monopole still features an almost triangular current distribution, the sinusoidal pattern is already formed in the fractal case. At the first monopole's resonance, the current over the *K3* antenna is about to reach its minimum value, i.e., the maximum impedance point. In the last case, the current amplitude over *K3* starts to raise above the minimum point, and a π radian phase shift on the current distribution is obtained in the nearby of the feeding point. These results corroborate the idea outlined in the Minkowski antenna discussion, that the length increase in the fractal case might induce some phase shifts over the structure that would enhance radiation, making the fractal antenna a good small antenna.

7.2.7 - Radiation Patterns

The power radiation patterns shown in Fig. 7.14 have been computed at the same frequencies as the current distributions of the previous section. Euclidean and fractal patterns are represented in the same plot for comparison. It is clear that the Koch and linear monopole patterns are basically the same below the small antenna limit. At the first monopole resonant frequency the fractal pattern starts to appear slightly narrower. At the

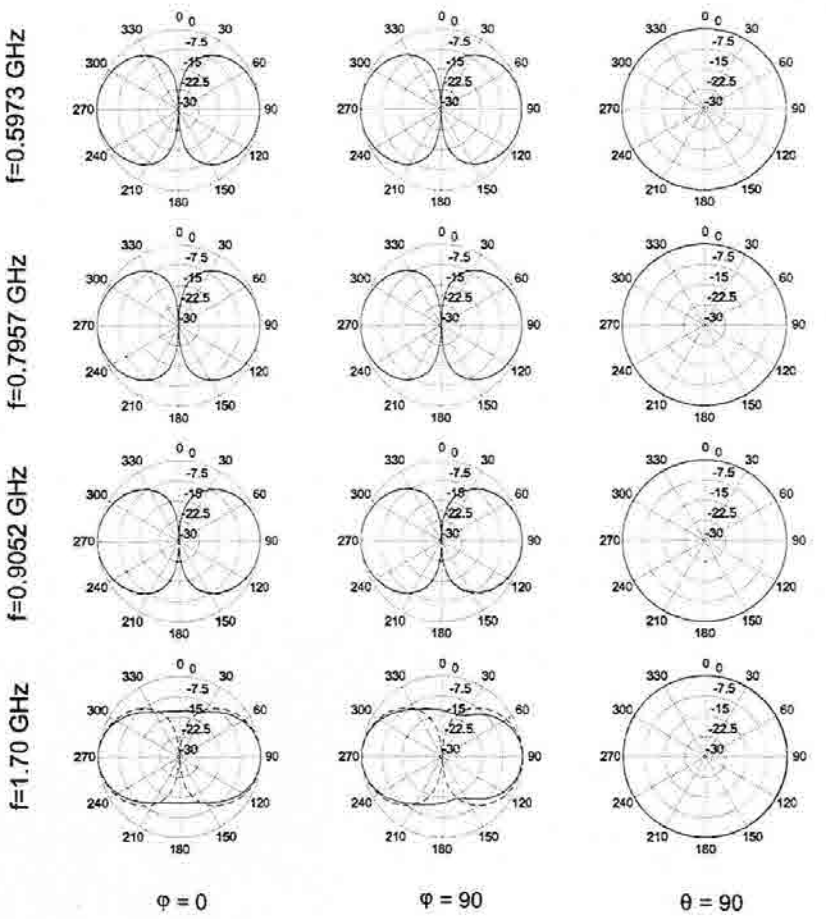

Fig. 7.14 Radiation pattern main cuts of the fractal Koch antenna(solid line) and the linear monopole (dashed line) at the same frequencies as the current reconstructions in Fig.7.13. The Koch antenna performs basically as a typical small antenna from the radiation pattern point of view.

last frequency, symmetry is broken in the antenna plane, basically due to the asymmetrical shape of the antenna structure and the phase shifts on the current distribution. Also, the null in the zenith direction is filled up mainly due to the contribution of the cross-polar component. Such contribution manifests that horizontal currents do not completely canceled, which can be explained through the phase delay introduced by the long antenna structure.

7.3 - The Large Koch Monopole

Given the results of previous chapters it might be reasonable to expect a multiband behavior for a large Koch monopole, i.e., a Koch monopole operating through a wide range of short wavelengths in terms of the antenna size. The fractal shape is indeed self-similar since the lower third of the Koch monopole is also a Koch curve scaled down by a factor of three. So are the three remaining parts of the antenna. Hence, if multiband, the antenna should feature a band spacing equal to the scale factor δ=3.

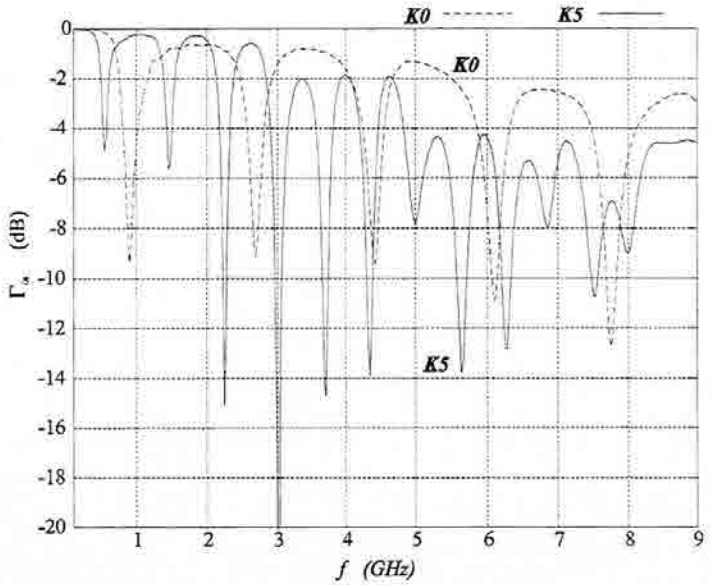

Fig. 7.15 Large Koch antenna input reflection coefficient. It is not a multiband antenna.

However, Fig. 7.15 clearly evinces that the Koch monopole does not perform a multiband behavior (the *K5* and the linear monopole input reflection coefficients are shown for comparison). The antenna input parameters perform in a harmonic fashion rather than in a log-periodic one. Nevertheless, such a result is not surprising given the current reconstruction previously introduced. It seems that current easily follows the antenna wire path from the feeder to the tip, yielding to a standing wave pattern when current is reflected at the antenna end. Self-similarity is not enough to guarantee a multiband performance since the truncation principle must be fulfilled too. Since current seems to extend over all antenna length, that principle is not held by the Koch antenna and the multiband operation can not be supported. Actually, we saw in Chapter 5 that very narrow Sierpinski antennas did not fulfill that principle either, so it is not surprising that a wire antenna such as the Koch monopole does not either.

On the other hand, it appears reasonable to think that if the number of fractal iterations were sufficiently large such that the antenna length (not height) were large enough too, current attenuation due to radiation might help to follow the truncation principle. It is possible, therefore, that in such case and for very large frequencies the antenna performed a true multiband operation.

7.4 - The Small Zig-Zag Antenna

Some other space-filling curves can be considered for designing broadband small antennas. Usually designed as a large, directive antenna [130], a zig-zag curve my be thought as a potential good small antenna given prior results (see Fig. 7.16). Given a fixed height, the antenna wire length can be increased by reducing the pitch angle. If again one assumes that current propagates all along the antenna wire, an antenna size reduction might be expected as in the Koch antenna case.

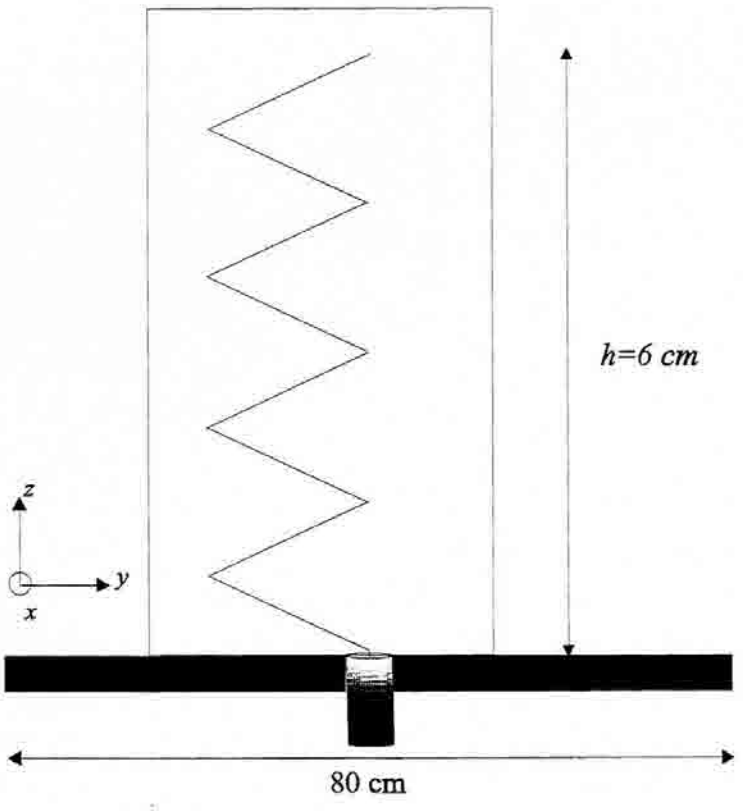

Fig. 7.16 The Zig-Zag monopole.

Three zig-zag monopoles (*Z1..Z3*) with the same wire length and dimensions as the *K1*, *K2* and *K3* antennas have been simulated using the MoM algorithm. The antennas were designed to fit exactly in the same rectangular area any of the fractal Koch antennas can be

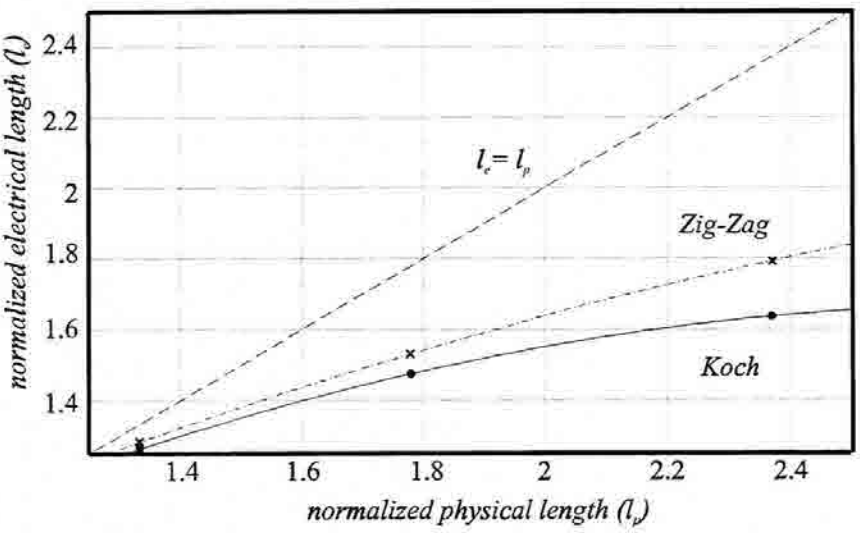

Fig. 7.17 Electrical length versus physical wire length for the K3 and Z3 antennas.

fitted in (6 cm x 1.73 cm). As previously done in the Koch antenna case, the electric length (Fig. 7.17) and antenna size compression (Fig. 7.18) factor has been computed. Also, the *Q* factor of the three antennas has been calculated and the results are compared for both kinds of antennas in Fig. 7.19.

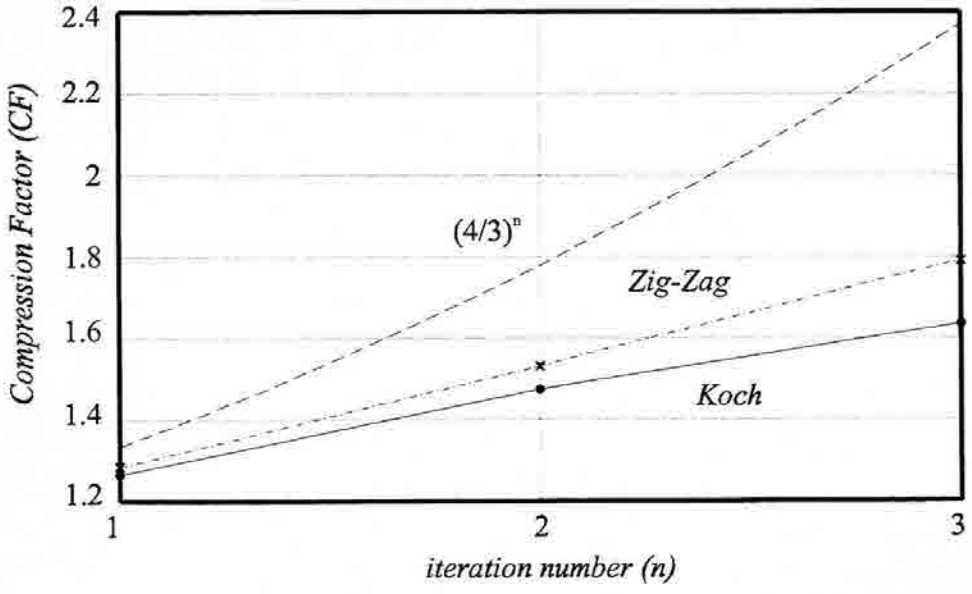

Fig. 7.18 Zig-zag antenna (Z3) size compression factor. The same feature for the K3 antenna, together with the ideal case is shown for comparison.

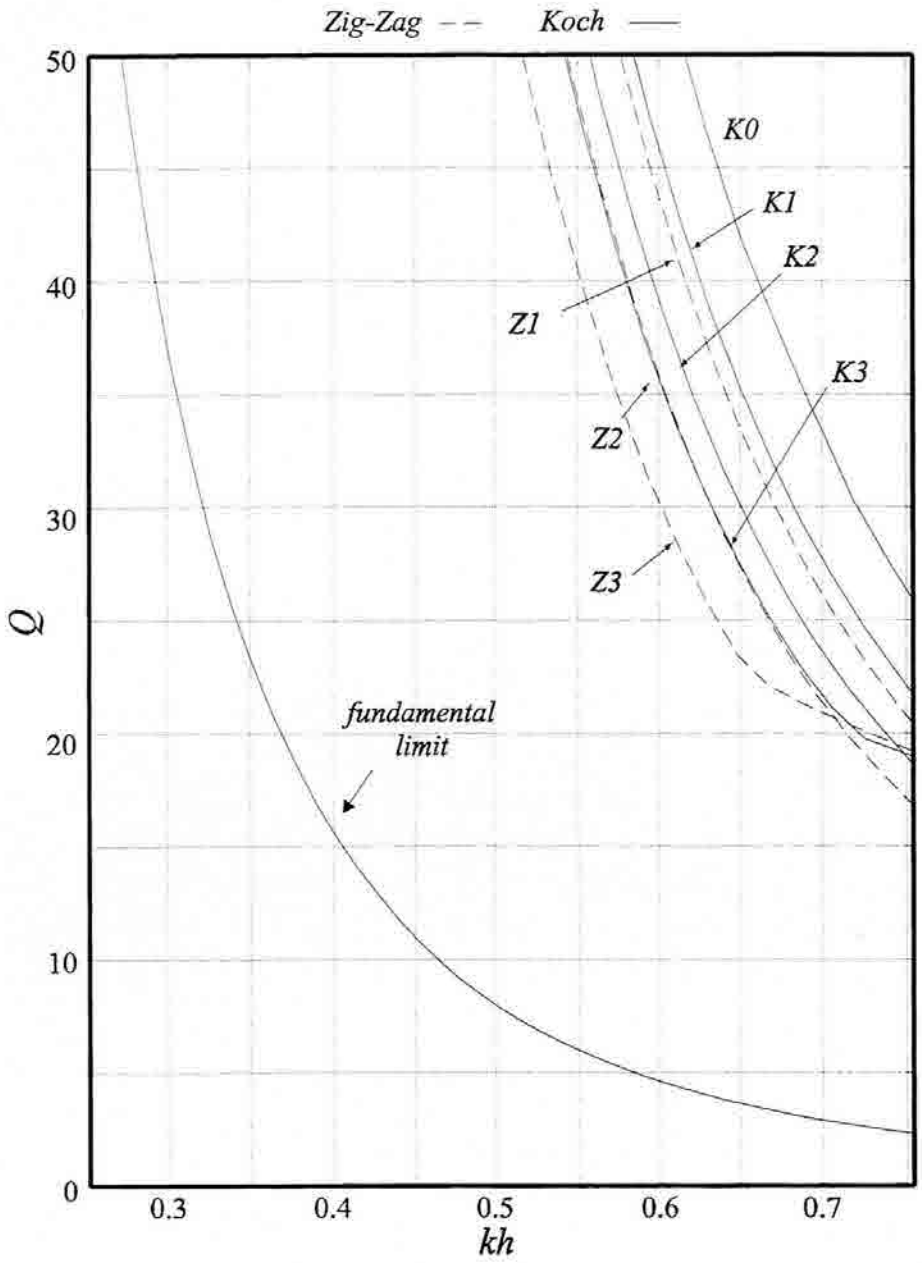

Fig. 7.19 Zig-zag antenna (solid) and Koch antenna (dashed) quality factor evolution. The fundamental limit is shown for comparison.

It is apparent that similar results as those of the Koch antenna are obtained. The zig-zag antenna even slightly improves the features of the Koch antenna, in terms of compression and quality factor. One must notice that the zig-zag curve can not be considered a fractal one: it is not self-similar and it holds the same value for the topological and fractal dimensions (D = 1). One might search the reason of the performance improvement in that the zig-zag curve tends to fill the two dimensional space better than the Koch curve. Actually the zig-zag antenna approaches a plane filling curve (D=2) while the

fractal one (D=1.26) is closer to a linear object than to a surface one. The only objection to the non-fractal antenna performance is rather theoretical: while the number of iterations can be increased as much as desired in the fractal case, the zig-zag structure does not converge to any limit object and it is not a truly space filling curve [2]. Also, the length increase is obtained by reducing the antenna pitch angle, which might be translated into an increase of the reactive energy due to coupling among turns, as well as into an efficiency decrease due to radiation cancellation at the narrow V-shaped segments. On the contrary, the Koch curve always keep a minimum 60° angle at any bend, no matter the number of iterations and wire length.

7.5 - Conclusions

The potentiality of fractal antennas to become low-Q resonant small antennas has been proved through experimental and numerical results. The Koch monopole improves bandwidth, radiation resistance and reactance of those of a linear monopole of the same size. Equivalently, it can be thought that the size of a common monopole can be reduced by fractally shaping the wire. The antenna performance enhancement can be linked to the irregularity of the fractal shape, as well to its plane filling characteristic. Featuring a fractal dimension larger than unity, it can be thought that the fractal antenna better fills the available volume inside the radiansphere that establishes the small antenna limit size. Another non-fractal but space-filling like curve, the zig-zag antenna, has been shown to improve the linear monopole features as well.

It has been also shown too that it cannot be readily assumed that Chu's theoretical fundamental limit on small antennas also applies for ideal fractal antennas. One might think that the arbitrarily long length of the later might yield an arbitrarily large radiation resistance even for arbitrarily small antennas. However, experimental and numerical results show that it is rather difficult to achieve a performance improvement beyond certain limits, and that both the electrical length, compression factor and radiation resistance enhancement characteristics seem to saturate. For fractal shapes, it seems that such limit should be related to the fractal dimension D since it describes the space filling properties of the fractal object, but not a straightforward relation between D and such a theoretical limit has been derived. If so, some highly convoluted cloud-like current distributions featuring a fractal dimension D>3 [5] might theoretically overcome the performance of any other Euclidean small antenna.

8. Conclusions

Fractal antennas and arrays have been investigated throughout this thesis. Experimental, numerical and theoretical results have confirmed that fractals can indeed become effective antennas. Due to the self-similarity property of fractals, it has been theoretically shown that ideal fractal attractors should behave exactly the same way at an infinite set of discrete frequencies. Such feature is valid for both fractal antennas and fractal arrays.

It has been shown that ideal fractal arrays feature a multifrequency array factor. Rather than relying on a current distribution reconfiguration at each frequency, ideal fractal arrays holding a fixed current distribution feature a constant array factor through the bands due to their self-similar spatial arrangement. Fractal Iterated Function Systems have been introduced as a design tool for such arrays, and some design rules concerning the band spacing and Side-Lobe Ratio (SLR) have been presented.

Although finite size arrays still hold some similarity properties at as many frequencies as fractal construction iterations, it has been shown that a truncation effect breaks the equality among bands. Fractal array factors have been suggested as an alternative scheme to design multiband arrays. Contrarily to fractal arrays, fractal array factor arrays do keep an almost constant lobe width, directivity and pattern shape at the several bands. Again, such feature is achieved with a current distribution that does not change with frequency, which however does not guarantee a constant field intensity through the bands. In such arrays, the number of elements grows exponentially with the number of bands, but some low side-lobe fractal generators have been shown to provide a useful mean to drastically reduce the number of elements without a significant degradation on the array features.

Some of the theoretical considerations regarding the multiband operation of fractal radiating systems have been confirmed experimentally by the Sierpinski antenna behavior. The antenna features a multiband operation at as many bands as fractal iterations used in its construction algorithm. The bands are log-periodically spaced by the characteristic scale factor of the fractal geometrical shape. The multiband operation has been shown to be consistent from both the radiation pattern and input impedance points of view. It has been unveiled that a self-scaling current active region allows such a multiband operation. Such an active region is analogous to that of the previously described spiral and log-periodic dipole array frequency-independent antennas. However, due to the rather large characteristic scale factor in the fractal case, bands become separated such that significant variations on the antenna behavior are held within each band, and hence, a frequency independent behavior is not attained.

The sensitivity of the fractal Sierpinski antenna to structural perturbations has been investigated as well. Large flare angles and inclined arms have appeared useful to reduce the antenna height or to modify its radiation pattern, yet still keeping a multiband behavior; an analytical model has been introduced to explain the antenna response to some of those changes. Similarly, variations on the characteristic geometrical scale factor have been tried, leading to the conclusion that the antenna can be successfully modified to reallocate the operating bands. Several non-fractal configurations have been essayed as well, which featured a less constant behavior through the bands. One should conclude that, although fractally shaping might not be the only way of achieving a multiband performance, it somehow provides a consistent, robust mean to get it.

A frequency-independent operation of fractal antennas has been essayed by designing some random fractal tree-like antenna shapes. Featuring a rich variety of geometrical scales, one hoped that the several bands melted into a single broad one. Such antennas did feature a denser, richer distribution of bands, but not a frequency independent behavior. Radiation patterns were kept fairly similar at several bands in some designs, but the randomness of their shape introduced some undesired features, namely, pattern lobe random tilts and cross-polarization fluctuations.

Fractal small antennas can improve the features of some common small antennas. The space filling properties of some planar fractal curves seem to play a key role on taking advantage of the small volume occupied by such tiny antennas. For instance, the Koch monopole featuring a fractal dimension larger than one has shown to provide a superior performance than the classical one dimensional monopole. It has been explained, through some theoretical considerations, that one should be specially careful on assuming that classical constrains apply to small fractal antennas as well. As a matter of fact, it has been

shown that the fractal Koch antenna tends toward the fundamental quality factor limit when increasing the antenna length (not the size) on the recursive approach of the ideal shape. However, experimental results seem to point out that some limits to the antenna feature improvement actually occur. Other planar, non-fractal space filling like curves appeared as good small antennas too, which might suggest that fractal antennas not necessarily outcome the properties of all Euclidean shapes, at least for fractal dimensions smaller than three.

As a final conclusion to this work, we should stress that one should not be tempted to think on fractals as 'the solution' on the design of multiband and small antennas. However, fractals have been successfully proven to be a new useful, alternative approach to antenna design.

9. References

[1] B.B. Mandelbrot, The Fractal Geometry of Nature, W.H. Freeman and Company, 1983.

[2] H.O. Peitgen, H.Jürgens, D.Saupe, *Chaos and Fractals, New Frontiers of Science*, Springer-Verlag, 1990.

[3] B.B.Mandelbrot,*Los Objetos Fractales*, Tusquets Editores, Barcelona, 1975.

[4] H.Koch, "Sur une courbe continue sans tangente, obtenue par une construction géometrique élémentaire," Arkiv för Matematik 1, pp.681-704,1904.

[5] M.F. Barnsley , R.L. Devaney, B.B. Mandelbrot, H.O. Peitgen, D. Saupe, R.F. Voss, Y. Fisher, M. Mc Guire, *The Science of Fractal Images*, Springer Verlag, 1988.

[6] W.Sierpinski, "Sur une courbe dont tout point est un point de ramification", C.R.Acad. Paris 160, p.302,1915.

[7] K.Falconer, *Fractal Geometry, Mathematical Foundations and Applications*, Wiley, NewYork, 1990.

[8] H. Jones, D.E. Reeve, D. Saupe, *Fractals and Chaos*, A.J. Crilly, R.A. Earnshaw and H. Jones, Editors; Springer-Verlag, 1990.

[9] L.López-Tomàs, J.Claret, F.Mas, F. Sagués, "Aggregation under a forced convective flow", Physical Review B, vol. 46, no.18, pp. 11 495-11 500, November 1992.

[10] F.Sagués, L.López-Tomàs, J.March, R.Reigada, P.P.Trigueros, E.Vilaseca, J.Claret, F.Mas, "Disordered Grown Systems: Generation and Fractal Analysis. Electrodeposition", Int. Journal of Quantum Chemistry, vol.52, pp.375-394,1994.

[11] L.López-Tomàs, J.Claret, F.Sagués, "Quasi Two-Dimensional Electrodeposition under Forced Fluid Flow", Physical Review Letters, vol. 71, no. 26, pp.4373-4376, December 1993.

[12] R.F.Voss, "Multiparticle diffusive fractal aggregation", Phyiscal Review B, vol.30, no.1, pp.334-337, July 1984.

[13] A.Lakhtakia, N.S. Holter, R. Messier, V.K.Varadan, V.V. Varadan, "On the Spatial Fourier Transforms of the Pascal-Sierpinski Gaskets", J.Phys.A: Math.Gen. 19, pp.3147-3152, 1986.

[14] D.L.Jaggard, "On Fractal Electrodynamics," in *Recent Advances in Electromagnetic Theory*, H.N.Kritikos, pp. 183-224, D.L.Jaggard Editors; Springer Verlag, 1990.

[15] D.L.Jaggard, "Prolog to special section on Fractals in Electrical Engineering," Proceedings of the IEEE, vol. 81, no. 10, pp. 1423-1427, October 1993.

[16] Y.Kim and D.L.Jaggard, "The Fractal Random Array", Proc. of the IEEE, vol.74, no. 9, pp.1278-1280, September 1986.

[17] D.L.Jaggard and Y.Kim, "Diffraction by Bandlimited Fractal Screens," J.Opt.Soc.Am.A4, 1055-1062 (1987).

[18] Y.Kim and D.L.Jaggard, "A Bandlimited Fractal Model of Atmospheric Refractivity Fluctuation," J.Opt.Soc.Am.A5, pp. 475-480, (1988).

[19] Y.Kim and D.L.Jaggard, "Optical Beam Propagation in a Bandlimited Fractal Medium," J.Opt.Soc.Am.A5, pp. 1419-1426, (1988).

[20] D.L.Jaggard, X.Sun, "Scattering from Bandlimited Fractal Fibers," IEEE Trans. Ant. and Propagat., vol.37, pp.1591-1597 (1989).

[21] D.L.Jaggard, X.Sun, "Scattering by Fractally Corrugated Surfaces,"J.Opt.Soc.A7, pp.1131-1139, (1990).

[22] X.Sun and D.L.Jaggard, "Wave Scattering from Non-Random Fractal Surfaces" Opt.Comm. 78, pp.20-24, (1990).

[23] D.L.Jaggard, X.Sun, "Rough Surface Scattering: A Generalized Rayleigh Solution", J.Appl.Phys. 68, pp.5456-5462, December 1990.

[24] D.L.Jaggard, X.Sun, "Reflection from Fractal-Layers," Optics Let. 15, pp. 1428-1430 (1990).

[25] D.L. Jaggard and T.Spielman, "Triadic Cantor Target Diffraction," Microwave and Optical Technology Letters, vol. 5, no. 9, pp. 460-466, August 1992.

[26] D.L.Jaggard, T.Spielman, X.Sun, "Fractal Electrodynamics and Diffraction by Cantor Targets", AP-S/URSI Comission B Meeting, London, Ontario, June 1991.

[27] X.Sun, D.L.Jaggard, "Wave interactions with generalized Cantor bar fractal multilayers," J. Appl. Physics, 70 (5), pp. 2500-25007, September 1991.

[28] D.L.Jaggard, X.Sun, "Reflection from Fractal Multilayers", Optics Letters, vol.15, no.24, December 1990.

[29] M.M.Beal, N.George, "Features in the optical transforms of serrated apertures and disks", *J. Opt.Soc.Am.*, vol. 6, no. 12, pp. 1815-1826, December 1989.

[30] Y. Kim, H. Grebel, D.L. Jaggard,"Diffraction by fractally serrated apertures", *J.Opt.Soc.Am.*, vol. 8, no. 1, pp. 20-26, January 1991.

[31] D.L.Jaggard, "Fractal Electrodynamics: Wave Interactions with Discretely Self-Similar Structures," chapter 5 in Electromagnetic Symmetry, C.Baum and H.Kritikos, eds., Taylor and Francis Publishers, 1995.

[32] M.V.Berry, "Diffractals", J.Phys.A: Math.Gen.12, pp.781-797, (1979).

[33] M.V.Berry, T.M.Blackwell, "Diffractal Echoes", J.Phys.A:Math.Gen.14, pp.3101-3110, 1981.

[34] C.Allain, M.Cloitre, "Optical Fourier Transforms of Fractals," in Fractal Physics, L.Pietronero and E.Tossatti, editors, North-Holland, New York, 1986.

[35] S.D.Bedrosian, X.Sun, "Theory and Application of Pascal-Sierpinski Gasket Fractals", Circuits Syst., Sig.Processing 9, pp.147-159, (1990).

[36] S.D.Bedrosian, X.Sun, "Pascal-Sierpinski Gasket Fractal Networks: Some Resistance Properties", J.Franklin Inst.326, pp.503-509, (1989).

[37] T.Falco,F.Francis,S.Lovejoy,D.Schertzer, B.Kerman, M.Drinkwater, "Universal Multifractal Scaling of Synthetic Aperture Radar Images of Sea-Ice", IEEE Transactions on Geoscience and Remote Sensing, vol.34, no.4, July 1996.

[38] C.V.Stewart, B.Moghaddam, K.J.Hintz and L.M.Novak, "Fractional Brownina Motion Models for Synthetic Aperture Radar Imagery Scene Segmentation," Proc. IEEE, vol.81, pp. 1511-1522, 1993.

[39] P.E.Mayes, "Frequency-Independent Antennas and Broad-Band Derivatives Thereof", Proc. of the IEEE, vol. 80, no. 1, January 1992.

[40] J.D.Dyson, "The Equiangular Spiral Antenna," IRE Trans. Antennas Propag., vol. AP-7, pp. 181-187, October 1959.

[41] J.D.Dyson, "The Unidirectional Equiangular Spiral Antenna," IRE Trans. Antennas Propag., vol. AP-7, pp. 329-334, October 1959.

[42] D.E.Isbell, "Log-Periodic Dipole Arrays, " IRE Trans. Antennas Propagation, vol.8, pp. 260-267, May 1960.

[43] P.E.Mayes, G.A. Deschamps, and W.T. Patton, "Backward-wave radiation from periodic structures and application to the design of frequency-independent antennas," Proc. IRE, vol. 49, pp. 962-963, May 1961.

[44] G.A. Deschamps, J.D. Dyson, "The Logarithmic Spiral in a Single-Aperture Multimode Antenna System," IEEE Transactions on Antennas and Propagation, vol. ap-19, no. 1, January 1971.

[45] V.H.Rumsey, *Frequency-Independent antennas*, Academic Press, 1966.

[46] R.L. Carrel, "Analysis and Design of the log-periodic dipole antenna," Doctoral Thesis at the Dep. of Electrical Engineering of the University of Illinois at Urbana-Champaign, 1961.

[47] R.S.Elliot, "A View of Frequency-Independent Antennas," The Microwave Journal, pp.61-68, December 1962.

[48] P.E.Mayes, *Advanced Antenna Theory*, ECE 477 course, Dept. of Electrical Engineering, University of Illinois, Urbana-Champaign, 1993.

[49] H.G.Booker, "Slot Aerials and Their Relation to Complementary Wire Aerials," J.Inst.Elec.Engrs., pt III A, pp.620-626, 1946.

[50] S.Egashira, T.Tanaka, A.Sakitani, "A Design of AM/FM Mobile Telephone Triband Antenna", IEEE Trans. on Antennas and Propagation, vol.42, no.4, pp.538-540, April 1994.

[51] H. Jasik, *Antenna Engineering Handbook*, pp. 2.10-2.13, Mc Graw Hill, 1961.

[52] C.A.Balanis, *Antenna Theory, Analysis and Design*, John Wiley & Sons, New York, 1982.

[53] A.Cardama, Ll.Jofre, J.M.Rius, J.Romeu, S.Blanch, *Antenes,* Edicions UPC, Barcelona, September 1993. (*in catalan or spanish*)

[54] W.L.Stutzman, G.A.Thiele, *Antenna Theory and Design*, Wiley & Sons, New York, 1981.

[55] S.Ramo, J.R.Whinnery,T.Van Duzer, *Fields and Waves in Communication Electronics*, 2nd edition, John Wiley & Sons, New York, 1984.

[56] J.R.Mosig, R.C.Hall, "Integral Equations in Frequency Domain", in *Recent Advances in Numerical Techniques for Electromagnetics*, course at the Applied Physics Dept., University of Granada, September 1995.

[57] W.J.R. Hoefer, "The Transmission Line Matrix (TLM) Technique", in *Recent Advances in Numerical Techniques for Electromagnetics*, course at the Applied Physics Dept., University of Granada, September 1995.

[58] H.A.Wheeler, "Fundamental Limitations of Small Antennas," Proc. IRE, pp. 1479-1488. December, 1947.

[59] R.C.Hansen, "Fundamental Limitations in Antennas", Proc. IEEE, vol.69, no.2, February 1981.

[60] G.Goubau, "Multi-Element Monopole Antennas", Proc. Workshop on Electrically Small Antennas ECOM, Ft. Mammouth, N.J., pp.63-67, May 1976.

[61] H.A.Wheeler, "Small Antennas", IEEE Transactions on Antennas and Propagation, vol. 23, no.4,pp. 462-469, July 1975.

[62] J.S. McLean, "A Re-Examination of the Fundamental Limits on the Radiation Q of Electrically Small Antennas", IEEE Trans. on Antennas and Propagation, Vol.44, no.5, May 1996.

[63] C.H.Walter, "Electrically Small Antenna Studies at OSU", Proc. Workshop on Ellectrically Small Antennas ECOM, Ft. Mammouth, N.J., pp.25-34, May 1976.

[64] K.Fujimoto, A.Henderson, K.Hirasawa, J.R.James, *Small Antennas*, Research Studies Press Ltd., West Sussex, February 1988.

[65] A.Rubio, A.Salinas,R.Gómez,I.Sánchez,"Time Domain Analysis of Dielectric-Coated Wire Antennas and Scatterers," *IEEE Trans. on Antennas and Propagation*, Vol.42, no.6, June 1994.

[66] A.Rubio, R.Gómez, I.Sánchez, "Time-Domain Analysis of Magnetic-Coated Wire Antennas", IEEE Trans. Antennas and Propagation, Vol.43, no.6, pp.591-596, June 1995.

[67] G.H.Brown,O.M.Woodward, "Experimentally Determinded Radiation Characteristics of Conical and Triangular Antennas", RCA Review, pp. 425-452, December 1952.

[68] C.E.Smith, C.M.Butler, K.R. Umashankar, "Characteristics of a Wire Biconical Antenna", Microwave Journal, September 1979.

[69] K.L.Shlager, G.S.Smith, J.G.Maloney, "Optimization of Bow-Tie Antennas for Pulse Radiation", IEEE Trans. on Antennas and Propagation, vol.42, no.7, July 1994.

[70] J.W.Duncan, V.P. Minerva, "100:1 Bandwidth Balun Transformer" Proc. of the IRE,pp.156-164, February 1960.

[71] G.Burke, A.Pogio, "Numerical Electromagnetics Code (NEC)-Method of Moments", NIST # TD116, NSIT, Springfield, Virginia, 1981.

[72] G.Mur, "Absorbing Boundary Conditions for the Finite-Difference Approximation of the Time-Domain Electromagnetic-Field Equations,"*IEEE Transactions on Electromagnetic Compatibility*. Vol. EMC-23, pp. 377-382, November 1981.

[73] D.M.Pozar, "Microstrip Antennas", Proc. of the IEEE, vol.80, no.1, January 1992.

[74] J.R.James, P.S.Hall, C.Wood, *Microstrip Antenna Theory and Design*, IEE Electromagnetic Waves Series 12, Peter Peregrinus Ltd., Stevenage, 1981.

[75] I.J. Bahl, P.Bhartia, *Microstrip Antennas*, Artech House, Dedham, 1980.

[76] N.Kumprasert, W.Kiranon, "Simple and Accurate Formula for the Resonant Frequency of the Equilateral Triangular Microstrip Patch Antenna", IEEE Trans. on Antennas and Propagation, vol.42, no.8, pp.1178-1179, August 1994.

[77] J.F. Zürcher, F.E.Gardiol, *Broadband Patch Antennas*, Artech House, Boston, 1995.

[78] K.C.Gupta, M.D.Abouzahra, *Analysis and Design of Planar Microwave Components*, IEEE Press, Piscataway, 1994.

[79] R.W.P.King, *Arrays of Cylindrical Dipoles*, Cambridge at the University Press, London, 1968.

[80] S.Amari, M.Gimersky, J. Bornemann, "Imaginary Part of Antenna's Admittance from its Real Part Using Bode's Integrals", IEEE Trans. on Antennas and Propagation, vol.43, no.2, pp.220-223, February 1995.

[81] M.A. Tilston, K.G. Balmain, "A Multiradius, Reciprocal Implementation of the Thin-Wire Moment Method", IEEE Trans. on Antennas and Propagation, vol.38, no.10, October 1990.

[82] J.H.Richmond, N.H.Geary, "Mutual Impedance Between Coplanar-Skew Dipoles", IEEE Trans.Antennas and Propagation, pp.414-416, May 1970.

[83] J.H.Richmond, N.H. Geary, "Mutual Impedance of Nonplanar-Skew Sinusoidal Dipoles", IEEE Trans.Antennas and Propagation,pp. 412-414, May 1975.

[84] W.A.Imbriale, "Method of Moments Applied to Wire Antennas", Chapter 2 in *Numerical and Asymptotic Techniques in Electromagnetics*, R. Mittra editor, Springer Verlag, New York, 1975.

[85] R.F.Harrington, *Field Computation by Moment Methods*, IEEE Press, Piscataway, 1993.

[86] A.Driouach, A.Rubio,R.Gómez, "Application of parametric models to inverse scattering problems", IEE Proc.-Microw. Antennas Propag., vol. 143, no. 1, February 1996.

[87] C.Puente, "Fractal Design of Multiband Antenna Arrays", Elec. Eng. Dept. Univ. Illinois, Urbana-Champaign, ECE 477 term project, Dec.1993.

[88] C.Puente, R.Pous,"Fractal Design of Multiband and Low Side-Lobe Arrays", *IEEE Trans. Antennas and Propagation*, vol. 44, no. 5, pp. 1-10, May 1996.

[89] C.Puente, J.Romeu, R.Pous, X.Garcia, F.Benitez, "Fractal multiband antenna based on the Sierpinski gasket", *IEE Electronics Letters*, vol. 32, no.1, pp.1-2, January 1996.

[90] C.Puente,J.Romeu,R.Bartolomé,R.Pous, "Perturbation of the Sierpinski antenna to allocate the operating bands," IEE Electronics Letters, vol. 32, no.24, pp. 2186-2188, November 1996.

[91] C.Puente, J.Romeu, R.Pous, A.Cardama, "On the Behavior of the Sierpinski multiband fractal antenna," IEEE Trans. on Antennas and Propagation, (Submitted October 1996).

[92] C.Puente, J.Claret, F.Sagués, J.Romeu, M.Q.López-Salvans, R.Pous, "Multiband properties of a fractal tree antenna generated by electrochemical deposition," IEE Electronics Letters, vol. 32, no. 25, pp. 2298-2299, December 1996.

[93] X.Garcia, "Aplicació d'estructures fractals al disseny d'antenes multifreqüència", C.Puente director, Engineer Degree Final Project at the ETSETB, Universitat Politècnica de Catalunya (UPC), June 1995 (*in catalan*).

[94] F.Benítez, "Simulació i Anàlisi d'una Antena Fractal amb el Mètode FDTD", R.Pous director, Engineer Degree Final Project at the ETSETB, Universitat Politècnica de Catalunya (UPC), June 1995 (*in catalan*).

[95] R.Bartolomé, "Medida y Análisis de Antenas Fractales. Modificaciones sobre la Antena de Sierpinski", C.Puente director, Engineer Degree Final Project at the ETSETB, Universitat Politècnica de Catalunya (UPC), June 1995 (*in spanish*).

[96] LL.Milà, "Disseny, Implementació i mesura d'una antena triangular fractal multibanda de 60 graus", C.Puente director, Technical Engineer Degree Final Project at the EUPBL, Universitat Politècnica de Catalunya (UPC), September 1995 (*in catalan*).

[97] F.X.Fernández, "Disseny, Implementació i Mesura d'una Antena Fractal Multibanda", C.Puente director, Technical Engineer Degree Final Project at the EUPBL, Universitat Politècnica de Catalunya (UPC), September 1995 (*in catalan*).

[98] A.Seguí, "Diseño, Implementación y Medida de una Antena Fractal Multibanda (III)", C.Puente director, Technical Engineer Degree Final Project at the EUPBL, Universitat Politècnica de Catalunya (UPC), September 1995 (*in spanish*).

[99] A.Medina, "Diseño, Medida y Caracterización de la Antena Fractal y Microstrip Triángulo de Sierpinski", C.Puente director, Technical Engineer Degree Final Project at the EUPBL, Universitat Politècnica de Catalunya (UPC), September 1996 (*in spanish*).

[100] N.Cohen, "Fractal Antennas: Part 1", Communications Quarterly, pp.7-22, Summer 1995.

[101] N.Cohen, R.G.Hohlfeld, "Fractal Loops And The Small Loop Approximation", Communications Quarterly, pp.77-81, Winter 1996.

[102] N.Cohen, "Fractal and Shaped Dipoles", Communications Quarterly, pp. 25-36, Spring 1996.

[103] N.Cohen, "Fractal Antennas: Part 2", Communications Quarterly, pp. 53-66, Summer 1996.

[104] C.Goutelard, "Fractal theory of large arrays of lacunar antennas," Electromagnetic Wave Propagation Panel Symposium (AGARD-CP-528), pp. 35/1-15, June 1992 (*in french*).

[105] A.Lakhtakia, V.K. Varadan, V.V. Varadan, "Time-harmonic and time-dependent radiation by bifractal dipole arrays", Int. J. Electronics, 1987, vol. 63, no. 6, pp.819-824, 1987.

[106] C.Allain, M.Cloitre, "Spatial spectrum of a general family of self-similar arrays", Physical Review A, vol.36, no.12, pp.5751-5757, December 1987.

[107] A.V.Oppenheim, A.S.Willsky, I.T.Jones, *Signals and Systems*, Prentic-Hall, U.S., 1983.

[108] A.Papoulis, *Signal Analysis*, McGraw Hill, New York 1977.

[109] R.M.Eisberg, L.S. Lerner, *Physics: Foundations and Applications, Volume II*, McGraw-Hill, New York, 1981.

[110] T.M.Apostol, *Calculus, One-Variable Calculus, with an Introduction to Linear Algebra*, Blaisdell Publishing Company, Waltham, Massachussets, 1967.

[111] T.M.Apostol, *Calculus, Multi-Variable Calculus and Linear Algebra, with Application to Differential Equations and Probability*, Blaisdell Publishing Company, Waltham, Massachussets, 1967.

[112] M.R.Spiegel, *Mathematical Handbook of Formulas and Tables*, Schaum's Outline Series, McGraw-Hill, New York, 1992.

[113] K.S.Yee, "Numerical solution of initial boundary value problems involving Maxwell's equations in isotropic media." IEEE Transactions on Antennas and Propagation, vol.AP-11, pp.302-307, May 1966.

[114] G. Mur, "Absorbing Boundary Conditions for the Finite-Difference Approximation of the Time-Domain Electromagnetic-Field Equations". IEEE Transactions on Electromagnetic Compatibilityk. vol.EMC-23, pp. 377-382, November 1981.

[115] K.S.Kunz,R.J.Luebbers, The Finite Difference Time Domain Method for Electromagnetics. CRC Press, 1993.

[116] A.Ishimaru, *Electromagnetic Wave Propagation, Radiation, and Scattering*, Prentice-Hall, New Jersey 1991.

[117] J.D.Krauss, *Antennas*, McGraw-Hill, New York, 1988.

[118] L.J.Chu, "Physical Limitations on omni-directional antennas", J.Appl.Phys., vol. 19, pp.1163-1175, December 1948.

[119] R.F.Harrington, "Time-Harmonic Electromagnetic Fields", McGraw-Hill, New York,1961.

[120] J.Fornieles, A.Rubio,R.Gómez, "On the application of parametric models to the transient analysis of resonant and multiband antennas", to appear in IEEE Trans. Antennas and Propagation.

[121] S.Blanch, "Diagnóstico y Caracterización de Antenas y Entornos de Medida", Ph.D. Dissertation at the Universitat Politècnica de Catalunya, February, 1996. (*in spanish*)

[122] N.Duffo, "Análisis de Problemas Electromagnéticos Mediante Elementos de Contorno", Ph.D. Dissertation at the Universitat Politècnica de Catalunya, February, 1996. (*in spanish*)

[123] Evert, B.B.Mandelbrot, L.Wag, "Variability of the form and of the harmonic measure for small off-off- latice diffusion limited aggregates", Phys. Rev. A 45, pp. 5798, 1992.

[124] B.B.Mandelbrot, C.J.G.Evertsz, "The potential distribution around growing fractal clusters", Nature 348, pp.143-145, 1990.

[125] T.Robin, B.Souillard, "Electromagnetic Properties of Fractal Aggregates", Europhysics Letters, vol.21, pp.273-278, January 1993.

[126] Schellkunhoff, S.A., "A Mathematical Theory of Linear Arrays", Bell System Technical Journal, 22, 80.

[127] R.L.Fante, "Quality Factor of General Ideal Antennas," IEEE Transactions on Antennas and Propagation, vol. AP-17, no.2, pp.151-155, March 1969.

[128] R.E.Collin, S.Rothschild, "Evaluation of Antenna Q", IEEE Transactions on Antennas and Propagation, pp.23-27, January 1964.

[129] J.E.Aitken,"Swept-frequency microwave Q-factor measurement," Proc. IEE, vol.123, no.9, pp.855-861, September 1976.

[130] D.L.Sengupta, "The Radiation Characteristics of a Zig-Zag Antenna", IRE Trans. on Antennas and Propagation, pp.191-195, April 1958.

[131] C.Puente, R.Pous, "Diseño Fractal de Agrupaciones de Antenas", IX Simposium Nacional de la URSI, vol.1, Las Palmas de Gran Canaria, September 1994. (*in spanish*)

[132] C.Puente, J.Romeu, R.Pous, A.Cardama, "Multiband Fractal Antennas and Arrays", Fractals in Engineering Conference (FE'97), INRIA Rocquencourt, Arcachon, France, June 1997.

[133] C.Puente, J.Romeu, R.Pous, A.Cardama, "Multiband Fractal Antennas and Arrays", Fractals in Engineering Conference, Springer Verlag, June 1997.

[134] C.Puente, R.Pous, J.Romeu, X.Garcia, "Antenas Fractales o Multifractales", patent application number P-9501019, presented at the Oficina Española de Patentes y Marcas, May 1995. (*in spanish*)

[135] C.Puente, R.Pous, J.Romeu, "Antenas Fractales de Sierpinski", presented at the Oficina Española de Patentes y Marcas, December 1996. (*in spanish*)

[136] X.Liang, W. Zhensen, W.Wenbing, "On the synthesis of fractal patterns from the concentric-ring array," IEE Electronics Letters, vol.32, pp.1940-1941, October 1996.

[137] Mach, J., Mas, F., "MFRAC V1.0 software for fractal and multifractal indices calculation'. Departament de Química Física, Universitat de Barcelona, http://www.qf.ub.es/area5/jordi/mfrac.html, Barcelona 1996.

[138] C.Puente, A.Hijazo, F.Benitez, D3-Electromagnetics and Photonics Engineering group URL at the WWW; http://www-tsc.upc.es.